MODELING OF MULTI-LAYER THICKNESS MODE UNDERWATER ACOUSTIC TRANSDUCERS

by

William August Hoiles

B.A.Sc. (Engineering Physics), University of British Columbia, 2010

Thesis submitted in partial fulfillment
of the requirements for the degree of

Master of Applied Science

in the
School of Engineering Science
Faculty of Applied Science

SIMON FRASER UNIVERSITY

Spring 2012

APPROVAL

Name: William August Hoiles

Degree: Master of Applied Science

Title of Thesis: Modeling of Multi-Layer Thickness Mode Underwater Acoustic Transducers

Examining Committee:

Chair: **Dr. Paul Ho**
Professor

Dr. John Bird
Senior Supervisor
Professor

Dr. Andrew Rawicz
Supervisor
Professor

Dr. Behraad Bahreyni
Internal Examiner
Assistant Professor
School of Engineering Science

Date Approved: 14 March 2012

Partial Copyright License

Abstract

This thesis develops distributed models for determining steady state and transient performance characteristics of multi-layered underwater acoustic transducers operating in thickness mode. This important class of transducers is usually modeled using lumped circuit or distributed models with only a couple of layers. Distributed models are preferred for design purposes since lumped circuit models are generally not defined by material parameters. Distributed models are developed and closed form expressions are obtained for key steady-state performance characteristics including, the electrical impedance/admittance, receive sensitivity, transmit sensitivity, and efficiency. The impedance/admittance and receive sensitivity models are verified using experimental measurements. Expressions for transient performance are determined using the Laplace transform and are validated using theoretical and experimental methods. A novel method is derived for outputting desired pressure waveforms by pre-shaping the input drive voltage. The distributed models developed in this thesis accurately predict the performance of existing transducers and are valuable for transducer design.

Keywords: underwater acoustic transducers; transient characteristics; steady-state characteristics; drive voltage design method

Acknowledgments

I would like to thank my senior supervisor, Dr. John Bird. He gave me the support and freedom necessary to complete this thesis. His love of science and research has been an inspiration throughout my graduate studies.

A special thank you to Sabir Asadov for his attention to detail and patience when helping me conduct experimental measurements of the transducers. If it were not for the transducers he designed and built, this thesis would not have been possible.

I would like to express my sincerest appreciation to all my family members for supporting me throughout my academic career. You taught me the importance of doing my best and providing me with the supportive environment in which to achieve my goals. Without the help of each of you, I would not be where I am today.

Finally, but by no means least, I would like to thank my friends and colleagues for their discussions, sustenance, and most importantly their camaraderie and understanding.

Dedication

. . . to my family; Bill, Tiiu, Harley, Endla, and my grandparents

Table of Contents

List of Tables

List of Figures

Glossary Terms

Symbol	Definition	Units
V	Voltage	$[V]$
F	Force	$[N]$
ξ	Particle Displacement	$[m]$
u	Particle Velocity	$[m/s]$
ρ	Density	$[kg/m^3]$
k	Wave-Number	$[1/m]$
c, v	Acoustic Velocity	$[m/s]$
Z	Impedance	$[kg/s]$
L	Length	$[m]$
T	Stress	$[Pa]$
S	Strain	$[\ \ ]$
E	Electric Field	$[V/m]$
D	Electric Displacement Field	$[C/m^2]$
c^D	Stiffness Coefficient under Constant Electrical Displacement	$[Pa]$
h	Piezoelectric Constant	$[V/m]$
K^S	Clamped Permttivity under Constant Strain	$[\ \ ]$
ε_o	Vacuum Permittivity	$[F/m]$
ε_r^S	Relative Clamped Permittivity	$[F/m]$
β^S	Clamped Impermittivity Coefficient	$[m/F]$
ω	Radian Frequency	$[1/s]$
f	Frequency	$[Hz]$
I	Current	$[A]$

Symbol	Definition	Units
N	Electromechanical Turns Ratio	$[FV/m]$
C_o	Clamped Capacitance	$[F]$
η	Efficiency	[ ]
TTF	Transmit Transfer Function	$[F/V]$
TVR	Transmit Voltage Response	$[Pa/V]$
M	Sensitivity	$[V/Pa]$
A_o	Area of Transducer Active Face	$[A_o]$
J_s	Spherical-Wave Reciprocity Parameter	$[m^4s/kg]$
S	Transmit Current Response	$[Pa/A]$
Q	Charge on Surface	$[C/m^2]$
P	Pressure	$[Pa]$
s	Laplace Domain Parameter	$[1/s]$
t	Time Domain Parameter	$[s]$
$POVI$	Transfer Function of Transmit Transducer	$[Pa/V]$
$TPOVI$	Transient Pressure Output resulting from Voltage Input	$[Pa]$
$TVOPI$	Transient Voltage Output resulting from Pressure Input	$[V]$
DVDM	Drive Voltage Design Method	$[V]$
SADM	Syntactic Acoustic Damping Material	

1. Introduction

This thesis focuses on modeling multi-layer underwater acoustic transducers operating in thickness mode. These types of transducers are used as transmitters, receivers, or both. As a transmitter, the transducer is used to convert an electrical drive signal into a pressure signal in a propagation medium. As a receiver, it is used to convert an incoming pressure signal into an electrical signal. However, when a transducer acts as both, it alternates between the role of a transmitter and a receiver.

The operation of a transmitting transducer, T, and receiving transducer, R, is presented in figure 1.1. The transmitting transducer is driven by a commonly employed finite cycle sinusoid (Drive Signal). The pressure produced by T propagates through the medium (Transmitted Signal). As seen, the Transmitted Signal contains both steady-state (SS_1) and transient sections (T_1, T_2). T_1 is the rise time of the Transmitted Signal associated with the amount of time it takes for the Transmitted Signal to reach its SS_1 value. T_1 exists because of the pressure waves interacting with the material and the geometry of the transducer. T_2 is a result of the residual pressure waves still active in the transducer after the drive signal has stopped and is known as the ring time of the Transmitted Signal.

The Received Signal contains the rise time, T_3, ring time, T_4, and the steady-state section SS_2. T_3 is larger than T_1 because it contains the effects of the Transmitted Signal and the pressure wave interactions of R. T_4 is larger than T_2 because it contains the effects of the residual pressure wave interactions of T after the Drive Signal has stopped and the residual pressure wave interactions of R after the Transmitted Signal has stopped.

Transducers are used for a number of applications in the fields of oceanographic and hydro-geographic surveys, seismic exploration, marine research, environmental monitoring, navigation, communication, target tracking, etc. To construct a transducer for a specific application, the designer must understand the relationship between the Drive Signal and Transmitted Signal, and the relationship between the Transmitted Signal and Received Signal. The transducer model is used to describe

these relationships.

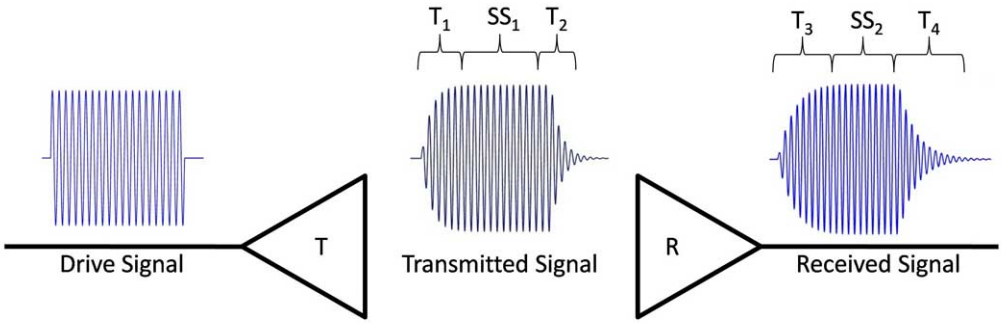

Figure 1.1: Basic Operation of an Acoustic Transducer

A typical multi-layer thickness mode underwater acoustic transducer is composed of a stack of piezoelectric and non-piezoelectric elements. These elements are shielded from the external environment by the transducer housing. The internal structure of the transducer is presented in figure 1.2.

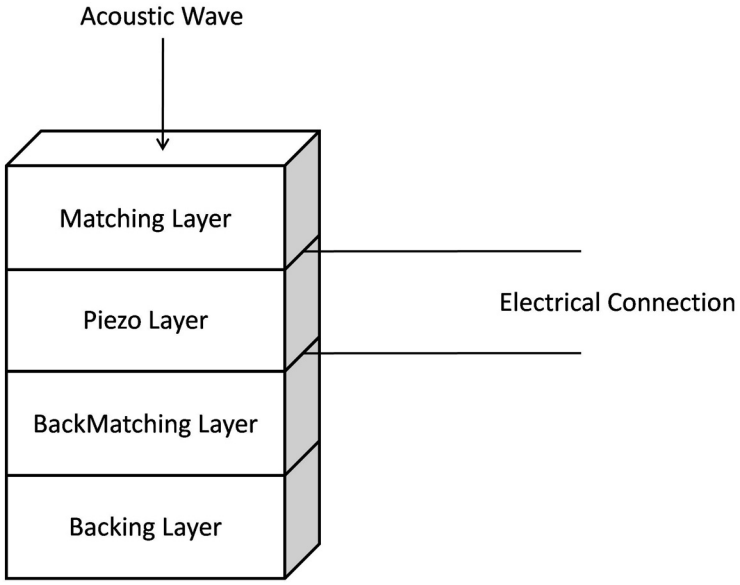

Figure 1.2: Basic Mechanical Structure of Multi-Layer Acoustic Transducer Operating in Thickness Mode

The Matching Layer is designed to allow the largest amount of energy from an acoustic pressure wave to enter the transducer. The Piezo Layer converts acoustic waves into electrical signals. The BackMatching Layer mechanically supports the

Piezo Layer and is also used to adjust the performance characteristics of the transducer. The Backing Layer supports the BackMatching Layer.

The design of multi-layered acoustic transducers operating in thickness mode is far from trivial. Failure of the designer to understand the effect material parameters and geometric construction have on the complex acoustical wave interaction in the transducer severely limits the performance of the resulting transducer. A designer requires a set of performance characteristics to understand the effect material parameters and geometry have on the performance of the transducer. Unfortunately, performance characteristics for a multi-layer acoustic transducer operating in thickness mode are difficult to gather or obtain. Therefore, comprehensive models are developed for the steady-state and transient performance characteristics of transducers.

The steady-state performance characteristics presented in this thesis include the input electrical impedance, acoustical impedance, efficiency, sensitivity, and transmit voltage response (TVR). The input electrical impedance is used to model the transducer as an electrical impedance, whereas, the acoustical impedance is the mechanical impedance looking into the transducer from the transmitting acoustic face. The efficiency is a ratio of the output acoustic power to the input electrical power, and the sensitivity is the ratio of the input acoustic pressure to the voltage that is obtained at the electrical terminals of the transducer. The TVR is the ratio of the pressure output of the transducer to a drive voltage.

The transient performance characteristics presented include the transient voltage output resulting from a pressure input ($TVOPI$), the transient pressure output resulting from a voltage input ($TPOVI$), and the voltage response resulting from a drive voltage input.

In addition to changing the material parameters and geometry of a transducer to obtain certain performance characteristics, it is also possible to design the input drive voltage to obtain a pre-determined output pressure waveform. A novel design paradigm used to output custom pressure waveforms from a multi-layer acoustic transducer operating in thickness mode is theoretically developed in this thesis.

In order to find the steady-state performance characteristics of a transducer, it is easiest to model the transducer using an equivalent electromechanical circuit. Since the elements in a thickness mode transducer are made to vibrate in a single direction, the models associated with the transducer are one-dimensional by design.

A classical circuit model used for a transducer is the lumped circuit model, specifi-

cally the Butterworth-Van Dyke (BVD) model [1, 2]. The BVD model is used because it provides an explanatory and straightforward method of gaining deeper insight into the behavior of the transducer. It is known that the BVD model is not generally appropriate for modeling a multi-layer transducer's steady-state or transient characteristics. The limitations of the BVD model include the inability to obtain the parameter values used by the BVD from the material and geometric parameters of the transducer, the inaccuracy of the model when the frequency analysis is far away from the mechanical resonance frequency of the transducer, and the failure of the model to account for the characteristics of the transducer introduced by its multi-layered structure. The limitations of the BVD model are discussed further in section 2.1.

State-of-the art equivalent circuit models of the transducer rely on the use of the distributed circuit model developed by Mason [3]. Distributed models are more complex than the BVD model but provide a complete representation of both the piezoelectric and non-piezoelectric elements. If arranged correctly, the distributed models provide a complete representation of the multi-layer underwater acoustic transducer operating in thickness mode.

In chapter 2, the steady-state performance characteristics of the multi-layer transducer are developed in detail. Although not new generally, the models presented in this thesis are new in that they are tailored for multi-layer acoustic transducers operating in thickness mode. In chapter 2, Mason's distributed model of the piezoelectric and non-piezoelectric elements is used to construct distributed models of multi-layer acoustic transducers operating in thickness mode. These distributed models are developed to solve the constraints associated with using the BVD model. An in depth development of the distributed model of the piezoelectric and non-piezoelectric elements is completed in sections 2.2 and 2.3. In section 2.7, the distributed models are used to obtain the steady-state performance characteristics of both, the commonly employed Matched transducer as well as the novel Cross-Talk Minimization (XTM) transducer.

The Matched transducer is composed of a Matching Layer, Piezo Layer, and a Backing Layer, whereas the XTM transducer is composed of a Piezo Layer, Back-Matching Layer, and a Backing Layer. This XTM transducer is a significant step forward in transducer design in that the BackMatching Layer is tailored to obtain certain performance characteristics. The BackMatching Layer allows the XTM transducer to be used for a wide range of applications. The models presented in chapter 2

facilitate the analysis and subsequent optimization of multi-layered acoustic transducers operating in thickness mode.

For any model to be useful, it must provide accurate results. Therefore, verification of the steady-state models developed must be made through the use of well designed experiments. In chapter 3, verification of the impedance takes place by comparing the experimental and theoretical impedance values for a number of transducers with varying element thicknesses and materials.

In order to find the theoretical impedance, a good estimate of the material parameters and geometric dimensions of the transducer is required. Although the geometric dimensions are easy to obtain, it is generally difficult to obtain all the material parameters necessary to use the theoretical impedance model. To find the material parameters, transducer designers rely on fitting the theoretical impedance to the experimentally measured impedance values [4, 5]. In this thesis, the material parameters and validation of the theoretically determined impedance values are performed using the same experimentally measured impedance. To ensure the material parameters do not interfere with the validation of the theoretical impedance, constraints are introduced on the allowable values of the material parameters. This restriction ensures that the material parameters cannot be adjusted to fit the impedance values without being reasonably close to the actual material parameters of the transducer. In section 3.1, it is validated that the theoretical impedance can be used to obtain the material parameters of the transducer. This is performed by conducting a constrained non-linear fit to determine the material parameters from synthetically produced impedance curves. Therefore, it is shown that the introduction of material constraints allows the validation of the theoretical impedance using the measured experimental impedance without a priori knowledge of the material parameters of the transducer.

Measuring the impedance of a transducer is a relatively simple task. However, making a sensitivity measurement requires the use of a complex experimental setup as well as taking a considerable amount of time to complete. These are the primary driving factors for the development of a theoretical sensitivity model for multilayer acoustic transducers operating in thickness mode. The sensitivity model developed affords practical, cost-effective and convenient alternative to the design-through-experimentation process. The sensitivity measurement of an XTM transducer is validated and a comprehensive analysis of the theory used to conduct the sensitivity

measurement is presented in chapter 4. Furthermore, the experimental setup and sources of error that are commonly encountered when conducting a sensitivity measurement are discussed in detail for completeness.

In order to find the transient characteristics of a multi-layer acoustic transducer operating in thickness mode, Laplace domain equations describing the particle speed, pressure, and force in a piezoelectric and non-piezoelectric element were used. The equation describing the voltage on the electrodes of the piezoelectric element in the Laplace domain is used as well. These equations were first developed by Redwood and Stuetzer for the transient analysis of a single piezoelectric element and are presented at the beginning of chapter 5 [6, 7]. Subsequent study of the single piezoelectric element was done in [8, 9].

The distributed model is generally not used to find the transient characteristics of a multi-layer acoustic transducer operating in thickness mode because of the intrinsic complexity of the Laplace domain expressions and finding the inverse transform. In order to solve this complexity problem, state-of-the-art Laplace domain inversion routines are used to find the time domain solutions. This marks a leap forward in our ability to determine the transient performance characteristics of the transducer. In turn, facilitating novel transducer designs customized to enhance the transducer's transient performance. Section 5.2 focuses on the development of the *TVOPI*, *TPOVI*, and voltage response of a single element transducer.

Recently, transducer drive electronics have been developed that can output an arbitrary drive voltage. This has spurred the development of software capable of shaping the drive voltage to output specific pressure waveforms from a transducer. Current work in this area is focused on the use of lumped circuit models to obtain a finite cycle sinusoidal pressure outputs with low transients [10, 11, 12, 13, 14]. However, this method is useful only when the frequency content of the desired pressure waveform is close to the mechanical resonance frequency of the transducer and does not account for the multi-layered structure of the transducer. Other researchers have focused on finding the transfer function of the transducer by measuring the pressure output caused by a known drive voltage [15, 16, 17]. Using the transfer function of the transducer, techniques of *Inverse Filtering* are applied to determine the necessary drive voltage. But, the problem with the transfer function method is that it requires a difficult to obtain high accuracy measurement of the output pressure waveform. A major issue with both of these methods is the need to perform experimental measure-

ments on the transducer in order to obtain the parameters needed to design the drive voltage.

The development of a new drive voltage design method which eliminates the restrictions or obstacles associated with the lumped circuit model and the use of the transfer function of the transducer is presented in section 5.3. Since no experimental measurements are required to determine the drive voltage, the design of the transducer can be optimized to output a complex pressure waveform with a simple drive voltage. This method also facilitates the utilization of existing transducers for new cutting edge applications where sophisticated output pressure waveforms are required.

Having developed the expressions that describe the transient characteristics of a multi-layer acoustic transducer operating in thickness mode, these expressions need to be validated. The focus of chapter 6 is on the validation of these expressions using theoretical and experimental methods. For the first time, it is shown that distributed model based transient theory can be utilized to model the transient behavior of a piezocomposite element.

Having established the steady-state and transient performance characteristics of a multi-layer acoustic transducer operating in thickness mode, chapter 7 presents an application example and the concluding summary of the thesis.

2. Steady-State Transducer Modeling

An in depth development of the distributed models and the steady-state performance characteristics of multi-layer acoustic transducers operating in thickness mode is presented in this chapter.

A commonly used transducer model is the lumped circuit model, however, this method does not accurately model the characteristics of a multi-layer acoustic transducer operating in thickness mode. A discussion of the weaknesses associated with using the lumped circuit model is presented in section 2.1.

Sections 2.2 and 2.3 present a comprehensive development of the distributed equivalent circuit models of the non-piezoelectric and piezoelectric elements, these being the fundamental components used in building the distributed equivalent circuit models of a transducer.

In any practical application, the transducer is connected to electrical circuitry using an electrical cable. The cable can effect the steady-state performance characteristics of the transducer. A steady-state model of the cable is therefore presented in section 2.5 which can be used with the distributed equivalent circuit model of the transducer to account for any effects the cable may have on the performance characteristics.

The steady-state performance characteristics of multi-layer acoustic transducers operating in thickness mode are developed using the distributed equivalent circuit models. In section 2.6, the distributed equivalent circuit models of the novel XTM transducer and the Matched transducer are presented. Section 2.7 focuses on the development of the following performance characteristics that include: the electrical impedance, acoustic impedance, efficiency, sensitivity, and transmit voltage response of the XTM and Matched transducers. A discussion of the resonance frequency of a transducer is presented in section 2.7.6.

2.1. Lumped Circuit Model of Transducer

The lumped circuit representation of a single element electroacoustic transducer is extensively used to find the steady-state performance characteristics. The model itself is known as the Extended Butterworth-Van Dyke (EBVD) model [18]. There are a number of issues associated with using this model to obtain the performance characteristics of a transducer. To see this, a brief description of the model is presented.

The EBVD model is based on representing the transducer as a simple mechanical system, illustrated in figure 2.1 [3].

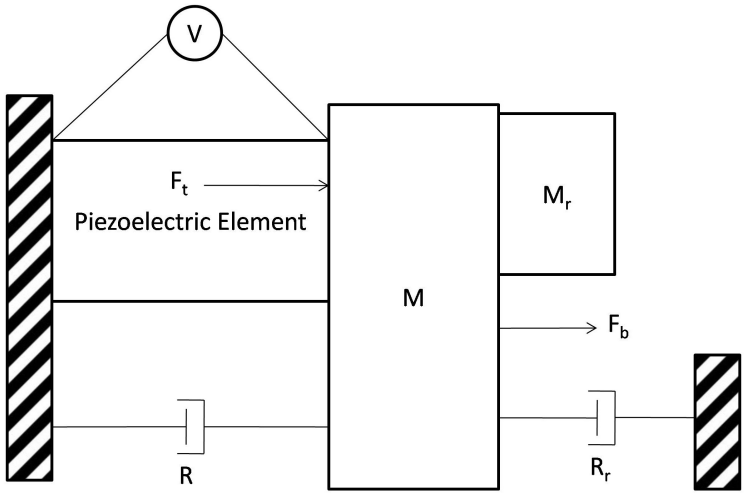

Figure 2.1: Mechanical Model of Transducer with Rigid Backing

The dashed blocks represent rigid objects. The parameters are defined as follows: R_r is the radiation resistance, M_r is the radiation mass, M is the effective mass of the piezoelectric element, F_t is the force produced by the piezoelectric element, and F_b is an external acoustic force applied to the transducer. V is the drive voltage of the transducer element. It is assumed that the backing material is rigid. Notice that no consideration is made if the transducer is composed of a multi-layered structure.

The development of the equivalent circuit model is presented in [3]. The input admittance of the transducer, Y_{eq}, is given by equation 2.1. Note that to find Y_{eq}, the external force being applied to the transducer is set to zero, F_b=0.

$$
\begin{aligned}
C_o &= \frac{A_o \varepsilon_{33}^S}{L} \\
N &= h_{33} C_o \\
C &= \frac{L}{A_o[c_{33}^D - h_{33}^2 \varepsilon_{33}^S]} \\
Y_{eq} &= j\omega C_o + \frac{1}{R_o} + \frac{N^2}{j\omega(M + M_r) + (R + R_r) + \frac{1}{j\omega C}}
\end{aligned} \tag{2.1}
$$

h_{33} is the piezoelectric constant of the element, ε_{33}^S is the permittivity of the element, R_o is the dielectric loss term, A_o is the surface area of the transmitting face of the element, L is the thickness of the element, and c_{33}^D is the stiffness coefficient of the element. The equivalent circuit model representation of equation 2.1 is presented in figure 2.2. Notice that the parameters $\{R, M, M_r, R_r\}$ are the same parameters used in figure 2.1.

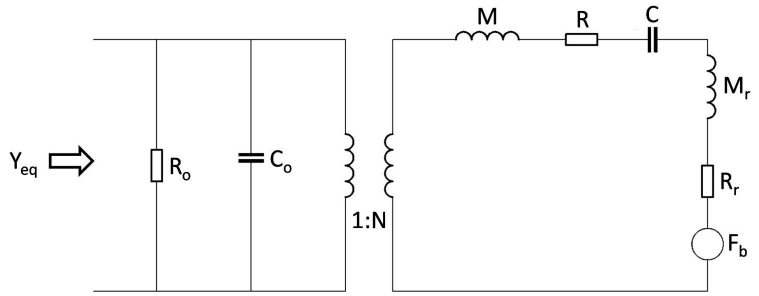

Figure 2.2: Electrical Model of Transducer with Rigid Backing

Using the circuit diagram in figure 2.2 it is possible to find the output pressure of the transducer resulting from an input drive voltage. In addition, one can find the open-circuit output voltage resulting from an input drive force on the face of the transducer.

An important feature to be aware of when using the lumped circuit model for a general transducer is that the parameters $\{R_o, C_o, N, M, R, C, M_r, R_r\}$ do not, in general, have closed form analytic solutions that can be calculated from the material parameters and dimensions of the transducer [18]. Unlike the single element case, the parameters $\{R_o, C_o, N, M, R, C, M_r, R_r\}$ must be determined from experimental measurements. For example, to determine the values for R_r and M_r. It is assumed that the transducer face moves with a fixed velocity u_o. Equation 2.2 is the radiation

impedance of the transducer used to find R_r and M_r [3].

$$\begin{aligned} Z_r &= \frac{1}{u_o u_o^*} \iint_S p(\vec{r}) u^*(\vec{r}) dS \\ &= R_r + jX_r \\ &= R_r + j\omega\Big(\frac{X_r}{\omega}\Big) \\ &= R_r + j\omega M_r \end{aligned} \tag{2.2}$$

The surface integral 2.2 is evaluated on the surface of the transducer. This requires knowledge of the near-field pressure pattern, which almost always requires the use of finite numerical techniques.

Another issue with this model is that it is only accurate near the mechanical resonance of the transducer. It is clear the development of a more rigorous model to accommodate the need to do analysis off resonance, with transients, and to have the parameters of the model depend only on the material properties and dimensions of the transducer is necessary. This can be done if a distributed model is used.

2.2. Distributed Model for a Non-Piezoelectric Element

In this section a detailed development of the distributed model of a non-piezoelectric solid element is given. The development follows what is presented in [3], but is expanded to provide the reader with a clear understanding of how the model is developed.

All transducers are composed of solid elements used for impedance matching, mechanical support, or to provide protection from the environment. The distributed model is developed to model one-dimensional longitudinal wave motion in a solid element. The term distributed model is used because the assumption is made that the mass and stiffness are spread continuously throughout the element. This development involves first analyzing the distributed theory of a single solid element without any loses present. From this analysis, an equivalent circuit model is constructed. It it shown that the single element case can easily be extrapolated to a multi-element case. The last part of this section focuses on taking losses into account.

2.2.1. Mechanical Impedance of a Solid Non-Piezoelectric Element

In this section, a presentation of the theory needed for longitudinal wave motion in a solid element is made. Using the theory developed, the mechanical impedance of a solid element with cross sectional area A_o is found. The final product of the theory is the lossless line transmission formula given by equation 2.3. Figure 2.3 shows how equation 2.3 is related to the physical structure of the element.

$$Z_{in} = \frac{Z_o[Z_L + jZ_o tan(kL)]}{Z_o + jZ_L tan(kL)} \tag{2.3}$$

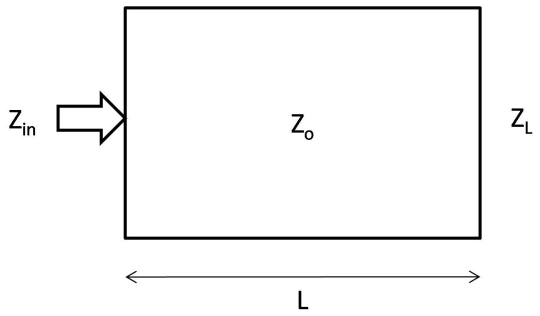

Figure 2.3: Mechanical Representation of Non-Piezoelectric Element

Z_L is the impedance at the end of the element, and $Z_o = \rho c A_o$ is the impedance of the material in the element. The parameter $k = \frac{2\pi f}{c}$ is the wave number of the element material, and L is the length of the element in the thickness mode direction. A number of approximations are necessary in order for this formula to be valid, as shown in the next section.

2.2.2. Derivation of the Mechanical Impedance of a Solid Non-Piezoelectric Element

In this section the input mechanical impedance of a solid non-piezoelectric element is developed. The element is sub-divided into very small elements, and each of these elements is modeled using a lumped spring-mass representation. Lateral forces on the element are assumed negligible. With this assumption, the developed impedance formula is not able to model gases or liquids since they do not obey the free lateral boundary conditions. Gases and liquids are almost never used in an underwater trans-

ducer, therefore, there is no loss in generality by excluding these from the analysis. The assumption is made that there is no energy loss on the interface of the element or any energy loss in the element itself.

The length of each small element is Δz with cross-sectional area A_o. The mass of each element is $M = \rho A_o \Delta z$, and the stiffness is $K = Y A_o / \Delta z$. The parameter Y is Young's Modulus and ρ is the density of the material in the element. The longitudinal displacement of the i^{th} element is denoted ξ_i. Each of the elements on either side of the i^{th} element produces an opposing force due the stiffness which hinders its motion. The displacement of the i^{th} element can be modeled with the following formula.

$$M\frac{\partial^2 \xi_i}{\partial t^2} = -K(\xi_i - \xi_{i-1}) - K(\xi_i - \xi_{i+1}) \tag{2.4}$$

The equations for M and K are now substituted into the above expression.

$$\rho A_o \Delta z \frac{\partial^2 \xi_i}{\partial t^2} = -\frac{Y A_o}{\Delta z}(\xi_i - \xi_{i-1}) - \frac{Y A_o}{\Delta z}(\xi_i - \xi_{i+1}) \tag{2.5}$$

Re-arranging the above equation gives.

$$\frac{\partial^2 \xi_i}{\partial t^2} = \frac{Y}{\rho \Delta z^2}[(\xi_{i+1} - \xi_i) - (\xi_i - \xi_{i-1})] \tag{2.6}$$

Now if the limit as $\Delta z \to 0$ is taken, the following equation is obtained.

$$\frac{\partial^2 \xi}{\partial t^2} = (\frac{Y}{\rho})\frac{\partial^2 \xi}{\partial z^2} \tag{2.7}$$

Equation 2.7 is known as the one-dimensional lossless wave equation. In most cases, the frequency response solution to this equation is of interest. This can be obtained by making the following substitution $\xi(z,t) = \xi(z)e^{j\omega t}$, where ω is the frequency of the sinusoidal driving force. As well, noting that the speed of an acoustic wave in the material is $c = \sqrt{Y/\rho}$, after substitution, the following equation is obtained.

$$\frac{\partial^2 \xi}{\partial z^2} + (\frac{\omega}{c})^2 \xi = 0 \tag{2.8}$$

If $k = \omega / c$, the general solution to this differential equation is:

$$\xi(z,t) = (Ae^{-jkz} + Be^{jkz})e^{j\omega t} \tag{2.9}$$

The input impedance of the element Z must be found. This is equal to the ratio

of the force F, and the particle velocity, u; where F and u are related to ξ through the following formulas: .

$$F = -A_o Y \frac{\partial \xi}{\partial z} = -A_o Y jk(-Ae^{-jkz} + Be^{jkz})e^{j\omega t} \tag{2.10}$$

$$u = \frac{\partial \xi}{\partial t} = j\omega(Ae^{-jkz} + Be^{jkz})e^{j\omega t} \tag{2.11}$$

To solve for Z, the general solution 2.9 is plugged into the expressions for F and ξ above. After algebraic manipulation, the following formula for Z is obtained.

$$Z(z) = Z_o \frac{Ae^{-jkz} - Be^{jkz}}{Ae^{-jkz} + Be^{jkz}} \tag{2.12}$$

The two impedance boundary conditions $Z(0) = Z_{in}$ and $Z(L) = Z_L$ are imposed since the impedance looking into the element is to be determined. The constants A and B may then be solved. Z_{in} is the impedance looking into the element, and Z_L is the impedance at the end of the element. Plugging these boundary conditions into equation 2.12, and simplifying, the equation for Z_{in}, given by equation 2.13, is obtained.

$$Z_{in} = \frac{Z_o[Z_L + jZ_o tan(kL)]}{Z_o + jZ_L tan(kL)} \tag{2.13}$$

Equation 2.13 is the lossless line transmission formula for a non-piezoelectric element.

2.2.3. Equivalent Circuit Model for a Solid Non-Piezoelectric Element

Since the transducer is, in general, connected to electrical equipment, it would be ideal if equation 2.13 for mechanical impedance, could be transformed into an electrical circuit equivalent. This is done by relating force F and particle velocity u, to voltage V and current I. The fundamental equation for electrical impedance is given by $V = Z_e I$, where $_e$ is the electrical impedance. The fundamental equation for mechanical impedance is given by $F = Z_m u$, where Z_m is the mechanical impedance. Using the electrical and mechanical impedance equations, it is found that F is related to V, and u is related to I.

In order to convert the mechanical impedance into an electrical impedance, the following trigonometric identities need to be used as well as the parameters Z_a and

Z_b, defined in equations 2.17 and 2.18.

$$tan(\frac{kL}{2}) = \frac{1-cos(kL)}{sin(kL)} \tag{2.14}$$

$$sin(kL) = \frac{2tan(\frac{kL}{2})}{1+tan^2(\frac{kL}{2})} \tag{2.15}$$

It is useful to re-write equation 2.13 into the following form. The reason this is done is to allow the parameters Z_a and Z_b to be easily substituted into the expression for Z_{in}.

$$\begin{aligned} Z_{in} &= \frac{Z_o[Z_L + jZ_o tan(kL)]}{Z_o + jZ_L tan(kL)} \\ &= \frac{Z_o Z_L + jZ_o^2 tan(kL)}{Z_o + jZ_L tan(kL)} \\ &= \frac{-j\frac{Z_o Z_L}{tan(kL)} + Z_o^2}{-j\frac{Z_o Z_L}{tan(kL)} + Z_L} \end{aligned} \tag{2.16}$$

The parameters Z_a and Z_b are given by:

$$Z_a = jZ_o tan(kL/2) \tag{2.17}$$

$$Z_b = -jZ_o/sin(kL) \tag{2.18}$$

Combinations of Z_a and Z_b are used to represent Z_o^2 and $-jZ_o/tan(kL)$ as shown below:

$$\begin{aligned} Z_a^2 + 2Z_a Z_b &= -Z_o^2 tan^2(\frac{kL}{2}) + \frac{2Z_o^2 tan(\frac{kL}{2})}{sin(kL)} \\ &= -Z_o^2 tan^2(\frac{kL}{2}) + 2Z_o^2 tan(\frac{kL}{2})[\frac{1+tan^2(\frac{kL}{2})}{2tan(\frac{kL}{2})}] \\ &= -Z_o^2 tan^2(\frac{kL}{2}) + Z_o^2 + Z_o^2 tan^2(\frac{kL}{2}) \\ &= Z_o^2 \end{aligned} \tag{2.19}$$

$$
\begin{aligned}
Z_a + Z_b &= jZ_o tan(\frac{kL}{2}) - \frac{jZ_o}{sin(kL)} \\
&= jZ_o \frac{1 - cos(kL)}{sin(kL)} - \frac{jZ_o}{sin(kL)} \\
&= -jZ_o \frac{cos(kL)}{sin(kL)} \\
&= -\frac{jZ_o}{tan(kL)}
\end{aligned} \tag{2.20}
$$

The equation for $Z_a^2 + 2Z_aZ_b$ and $Z_a + Z_b$ are substituted into equation 2.16 to determine the circuit equivalent representation of Z_{in}.

$$
\begin{aligned}
Z_{in} &= \frac{(Z_a + Z_b)Z_L + 2Z_aZ_b + Z_a^2}{Z_a + Z_b + Z_L} \\
&= \frac{Z_b(Z_a + Z_L) + Z_a(Z_a + Z_b + Z_L)}{Z_a + Z_b + Z_L} \\
&= \frac{Z_b(Z_a + Z_L)}{Z_a + Z_b + Z_L} + Z_a \\
&= \frac{1}{\frac{Z_a + Z_b + Z_L}{Z_b(Z_a + Z_L)}} + Z_a \\
&= \frac{1}{\frac{1}{Z_b} + \frac{1}{Z_a + Z_L}} + Z_a \\
&= Z_b//(Z_a + Z_L) + Z_a
\end{aligned} \tag{2.21}
$$

From equation 2.21, the equivalent circuit model of the input impedance of the element is constructed, shown in figure 2.4.

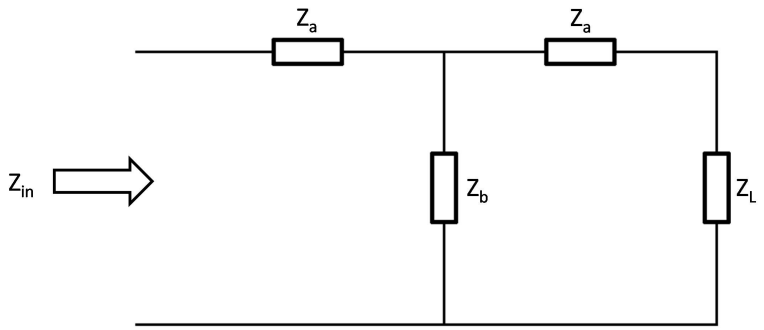

Figure 2.4: Distributed Circuit Equivalent of a Solid Bar

Note that Z_L is the impedance at the end of the element.

2.2.4. Mechanical Impedance for a Series of Non-Piezoelectric Elements

In many cases it is necessary to find the input impedance of a series of non-piezoelectric elements. To do this, the following recursive formula is utilized.

$$Z_{i+1} = \frac{Z_{o,i}[Z_i + jZ_{o,i}tan(k_iL_i)]}{Z_{o,i} + jZ_itan(k_iL_i)} \tag{2.22}$$

It is easiest to see how this formula is used if the input impedance Z_{in} of the following two element structure is to be determined.

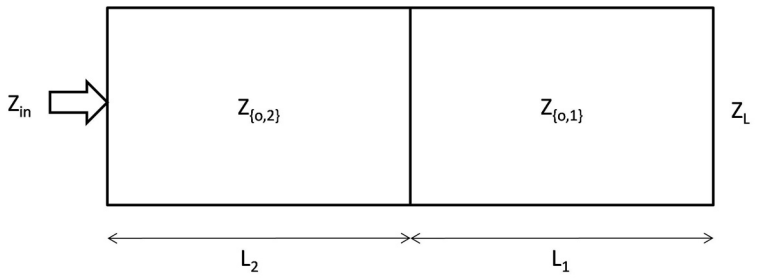

Figure 2.5: Two Non-Piezoelectric Element Structure

$$Z_2 = \frac{Z_{o,1}[Z_L + jZ_{o,1}tan(k_1L_1)]}{Z_{o,1} + jZ_Ltan(k_1L_1)}$$

$$Z_{in} = \frac{Z_{o,2}[Z_2 + jZ_{o,2}tan(k_2L_2)]}{Z_{o,2} + jZ_2tan(k_2L_2)} \tag{2.23}$$

It is straightforward to see how equation 2.22 can be used to find the input impedance for an N element non-piezoelectric structure.

2.2.5. Modeling for a Lossy Solid Non-Piezoelectric Element

If the medium in the element is absorbing, then the only quantity that changes in the above equations is the mechanical acoustic velocity in the element. The mechanical loss is accounted for by introducing a complex positive constant. Normally these losses are negligible if the material does not have a large value of L or if the loss is small. The discussion of losses is presented in section 2.4.

2.3. Distributed Model for a Piezoelectric Element

A model suitable for modeling a piezoelectric element is presented in this section.There are four primary types of models that are used for modeling the piezoelectric element: the Segmented 33 Bar, Un-segmented 31 Bar, Length Expanded Bar, and the Thickness-Mode Plate [3]. The theory for the Thickness-Mode Plate is the only one presented here because the analysis is conducted on a thickness mode transducer. The development of the piezoelectric element model follows what is presented in [3], and is expanded where necessary to explicitly show how the final results are obtained.

2.3.1. Approximations to the Phenomenological Equations for Piezoelectric Element

The phenomenological constitutive equations linearly relate the stress T, strain S, electric field E, and electric displacement D in a piezoelectric element with crystal structure C_{6v}. These are presented in matrices 2.24 and 2.25 [19]. Matrices 2.24 and 2.25 are used to construct the distributed model of the piezoelectric element.

$$\begin{pmatrix} T_1 \\ T_2 \\ T_3 \\ T_4 \\ T_5 \\ T_6 \end{pmatrix} = \begin{pmatrix} c_{11}^D & c_{12}^D & c_{13}^D & 0 & 0 & 0 \\ c_{12}^D & c_{11}^D & c_{13}^D & 0 & 0 & 0 \\ c_{13}^D & c_{13}^D & c_{33}^D & 0 & 0 & 0 \\ 0 & 0 & 0 & c_{44}^D & 0 & 0 \\ 0 & 0 & 0 & 0 & c_{44}^D & 0 \\ 0 & 0 & 0 & 0 & 0 & 2(c_{11}^D - c_{12}^D) \end{pmatrix} \begin{pmatrix} S_1 \\ S_2 \\ S_3 \\ S_4 \\ S_5 \\ S_6 \end{pmatrix} - \begin{pmatrix} 0 & 0 & 0 & 0 & h_{15} & 0 \\ 0 & 0 & 0 & h_{15} & 0 & 0 \\ h_{31} & h_{31} & h_{33} & 0 & 0 & 0 \end{pmatrix} \begin{pmatrix} D_1 \\ D_2 \\ D_3 \end{pmatrix} \tag{2.24}$$

$$\begin{pmatrix} E_1 \\ E_2 \\ E_3 \end{pmatrix} = - \begin{pmatrix} 0 & 0 & 0 & 0 & h_{15} & 0 \\ 0 & 0 & 0 & h_{15} & 0 & 0 \\ h_{31} & h_{31} & h_{33} & 0 & 0 & 0 \end{pmatrix} \begin{pmatrix} S_1 \\ S_2 \\ S_3 \\ S_4 \\ S_5 \\ S_6 \end{pmatrix} + \begin{pmatrix} \beta_{11}^S & 0 & 0 \\ 0 & \beta_{11}^S & 0 \\ 0 & 0 & \beta_{33}^S \end{pmatrix} \begin{pmatrix} D_1 \\ D_2 \\ D_3 \end{pmatrix} \tag{2.25}$$

The goal is to make assumptions to the equations in 2.24 and 2.25 to obtain a formula that retains a good representation of the physical system, that is also tractable.

First, the polarization direction of the piezoelectric element is in the 3 direction, which is parallel to the thickness dimension of the element. It is assumed that no energy is lost in the piezoelectric element. In general, the piezoelectric material being used has a high dielectric constant; therefore, the fringing effects are negligible. This enables D to be set to $D_1 = D_2 = 0$. As well, since the material is composed of a non-conductive dielectric with no free charges, $\nabla \bullet D = 0 \implies \partial D_3(z)/\partial z = 0$. Another assumption made is that the electrode surfaces of the piezoelectric element are at equipotential such that $E_1 = E_2 = 0$ on the electrode surfaces. In addition, fringing of the field is ignored so that $E_1 = E_2 = 0$ throughout the material. Only the longitudinal electric field E_3 is considered because it is assumed that this electric field does not cause any shear stresses in the material. This enables T to be set to; $T_4 = T_5 = T_6 = 0$. Other assumptions made are is that no loading forces exist on the material, and that no internal loading of the material in the 1 and 2 directions (directions perpendicular to the thickness mode dimensions) occurs enabling T to be set to; $T_1 = T_2 = 0$ on the surface and inside the element.

Using these assumptions, the following set of equations are left:

$$T_3 = c_{33}^D S_3 - h_{33} D_3 \tag{2.26}$$

$$E_3 = -h_{33} S_3 + \beta_{33}^S D_3 \tag{2.27}$$

In the next section, particle velocity, force, current, and voltage in the piezoelectric element are related using equations 2.26 and 2.27.

2.3.2. Relating Particle Velocity, Force, Current, and Voltage in the Piezoelectric Element

In this section u and F are related to V and I using equations 2.26 and 2.27.

Note that the following relations for strain $S_3 = \partial\xi/\partial z$ and stress $\partial T_3/\partial z = \rho\partial^2\xi/\partial t^2$ exist. By taking the spacial derivative of equation2.26, these relations can be directly plugged in to obtain the following expression.

$$\rho\frac{\partial^2\xi}{\partial t^2} = c_{33}^D\frac{\partial^2\xi}{\partial z^2} - h_{33}\frac{\partial D_3}{\partial z} \tag{2.28}$$

Assuming that $\partial D_3(z)/\partial z = 0$ the following equation is obtained.

$$\rho\frac{\partial^2\xi}{\partial t^2} = c_{33}^D\frac{\partial^2\xi}{\partial z^2} \tag{2.29}$$

Dividing both sides of this equation by ρ, the familiar wave equation is obtained.

$$\frac{\partial^2\xi}{\partial t^2} = (\frac{c_{33}^D}{\rho})\frac{\partial^2\xi}{\partial z^2} \tag{2.30}$$

When $\xi(z,t) = \xi(z)e^{j\omega t}$, the general solution to this differential equation is given by the following equation.

$$\xi(z,t) = \Big[Ae^{jkz} + Be^{-jkz}\Big]e^{j\omega t} \tag{2.31}$$

The constants A and B need to be determined from the mechanical boundary conditions of the piezoelectric element. A schematic drawing of the piezoelectric element is presented figure 2.6.

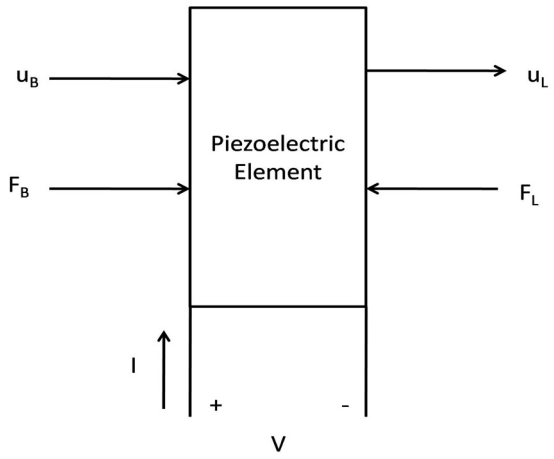

Figure 2.6: Piezoelectric Element

The mechanical boundary conditions associated with this piezoelectric element are given by the following equations:

$$u_B = \left.\frac{\partial \xi}{\partial t}\right|_{z=0} \tag{2.32}$$

$$u_L = \left.\frac{\partial \xi}{\partial t}\right|_{z=L} \tag{2.33}$$

$$F_B = \left. -A_o T_3 \right|_{z=0} \tag{2.34}$$

$$F_L = \left. -A_o T_3 \right|_{z=L} \tag{2.35}$$

The parameters u_B and u_L are the particle speeds on the face of the piezoelectric element. F_B and F_L are the associated forces on the face of the piezoelectric element. Figure 2.6 of the piezoelectric element indicates the directions of these quantities relative to the piezoelectric element. The boundary conditions are used to obtain the following set of equations which are used to solve for the constants $\{A, B\}$:

$$\begin{aligned} u_B &= \left.\frac{\partial \xi}{\partial t}\right|_{z=0} \\ &= j\omega \left[A e^{jkz} + B e^{-jkz} \right] e^{j\omega t} \Big|_{z=0} \\ &= j\omega \Big[A + B \Big] e^{j\omega t} \end{aligned} \tag{2.36}$$

$$
\begin{aligned}
u_L &= \frac{\partial \xi}{\partial t}\Big|_{z=L} \\
&= j\omega\Big[Ae^{jkz} + Be^{-jkz}\Big]e^{j\omega t}\Big|_{z=L} \\
&= j\omega\Big[Ae^{jkL} + Be^{-jkL}\Big]e^{j\omega t}
\end{aligned} \tag{2.37}
$$

$$
\begin{aligned}
F_B &= -A_o T_3\Big|_{z=0} \\
&= -A_o[c_{33}^D S_3 - h_{33} D_3]\Big|_{z=0} \\
&= -A_o[c_{33}^D \frac{\partial \xi}{\partial z} - h_{33} D_3]\Big|_{z=0} \\
&= -A_o[c_{33}^D jk(Ae^{jkz} - Be^{-jkz})e^{j\omega t} - h_{33}\frac{I}{j\omega A_o}]\Big|_{z=0} \\
&= -A_o c_{33}^D jk(A-B)e^{j\omega t} + \frac{h_{33}}{j\omega} I
\end{aligned} \tag{2.38}
$$

$$
\begin{aligned}
F_L &= -A_o T_3\Big|_{z=L} \\
&= -A_o[c_{33}^D S_3 - h_{33} D_3]\Big|_{z=L} \\
&= -A_o[c_{33}^D \frac{\partial \xi}{\partial z} - h_{33} D_3]\Big|_{z=L} \\
&= -A_o[c_{33}^D jk(Ae^{jkz} - Be^{-jkz})e^{j\omega t} - h_{33}\frac{I}{j\omega A_o}]\Big|_{z=L} \\
&= -A_o c_{33}^D jk(Ae^{jkL} - Be^{-jkL})e^{j\omega t} + \frac{h_{33}}{j\omega} I
\end{aligned} \tag{2.39}
$$

In the above equations the fact that $D_3 = I/j\omega A_o$ is used. The above boundary conditions are used to solve for F_B and F_L as functions of u_L and u_B. After doing the algebraic manipulation and simplification, the following set of equations for F_B and F_L are obtained:

$$
F_L = -\frac{\rho c A_o}{jtan(kL)} u_L + \frac{\rho c A_o}{jsin(kL)} u_B + \frac{h_{33}}{j\omega} I \tag{2.40}
$$

$$F_B = -\frac{\rho c A_o}{jsin(kL)} u_L + \frac{\rho c A_o}{jtan(kL)} u_B + \frac{h_{33}}{j\omega} I \tag{2.41}$$

Equation 2.27 is used to relate V to I, u_B, and u_L. To do this, the following expressions are used:

$$D_3 = \frac{Q}{A_o} \tag{2.42}$$

$$E_3(z) = \frac{\partial V}{\partial z} \tag{2.43}$$

$$u = \frac{\partial \xi}{\partial z} \tag{2.44}$$

$$I = \frac{\partial Q}{\partial t} = A_o \frac{\partial D_3}{\partial t} \tag{2.45}$$

$$\frac{\partial V}{\partial t} = j\omega V \tag{2.46}$$

Q is the charge on the surface of the electrode, ω is the frequency of the sinusoidal voltage between the electrodes of the piezoelectric element, and A_o is the surface area of the electrode.

V is now related to I, u_B, and u_L. To begin, the expression for $E_3(z)$ is substituted into equation 2.27 to obtain.

$$\frac{\partial V}{\partial z} = -h_{33} \frac{\partial \xi}{\partial z} + \beta_{33}^S D_3 \tag{2.47}$$

Then, the integral with respect to z is found on both sides of the above equation from 0 to L, where L is the length of the piezoelectric element.

$$\int_{z=0}^{L} \frac{\partial V}{\partial z} dz = -h_{33} \int_{z=0}^{L} \frac{\partial \xi}{\partial z} dz + \int_{z=0}^{L} \beta_{33}^S D_3 dz \tag{2.48}$$

After evaluating the above integral, the following result is obtained.

$$V = -h_{33}[\xi(L) - \xi(0)] + \beta_{33}^S D_3 L \tag{2.49}$$

Using equation 2.45, the time derivative is found on both sides of equation 2.49 in order to introduce I, as shown below:

$$\begin{aligned}
\frac{\partial V}{\partial t} &= -h_{33}[\frac{\partial \xi(L)}{\partial t} - \frac{\partial \xi(0)}{\partial t}] + \beta_{33}^S \frac{\partial D_3}{\partial t} L \\
j\omega V &= -h_{33}[u_L - u_B] + \beta_{33}^S \frac{I}{A_o} L \\
I &= \frac{A_o}{L\beta_{33}^S}[j\omega V + h_{33}[u_L - u_B)]] \\
&= j(\frac{A_o \omega}{L\beta_{33}^S})V + \frac{A_o h_{33}}{L\beta_{33}^S}[u_L - u_B]
\end{aligned} \tag{2.50}$$

For convenience, the parameter C_o is introduced into equation 2.50. C_o is the clamped capacitance of the piezoelectric element and is given by the following formula.

$$C_o = \frac{A_o}{L\beta_{33}^S} = \frac{A_o \varepsilon_{33}^S}{L} \tag{2.51}$$

After introducing C_o, the following formula is obtained which relates V to I, u_B, and u_L.

$$V = \frac{h_{33}}{j\omega}[-u_L + u_B] + \frac{1}{j\omega C_o} I \tag{2.52}$$

Equations 2.40, 2.41, and 2.52 provide the information necessary to construct the equivalent circuit model of the piezoelectric element. These equations can be compactly combined in matrix form as presented in 2.53.

$$\begin{pmatrix} F_L \\ F_B \\ V \end{pmatrix} = \begin{pmatrix} -\frac{\rho c A_o}{jtan(kL)} & \frac{\rho c A_o}{jsin(kL)} & \frac{h_{33}}{j\omega} \\ -\frac{\rho c A_o}{jsin(kL)} & \frac{\rho c A_o}{jtan(kL)} & \frac{h_{33}}{j\omega} \\ -\frac{h_{33}}{j\omega} & \frac{h_{33}}{j\omega} & \frac{1}{j\omega C_o} \end{pmatrix} \begin{pmatrix} u_L \\ u_B \\ I \end{pmatrix} \tag{2.53}$$

2.3.3. Equivalent Circuit Representation for a Piezoelectric Element

The equations presented in 2.53 give the relations between F, u, V, and I for a piezoelectric element. There are a number of different equivalent circuits that can be obtained using these relations, some of which include the Mason, Redwood, and KLM equivalent circuit models. In this section the focus is on the development of the Mason Model, but any of the others could have been used as well.

In order to construct the equivalent circuit model of the piezoelectric element, the

use is made of the equation of $Z_a + Z_b$, given by equation 2.20, and the parameters Z_o and N given by the following equations:

$$Z_o = \frac{1}{j\omega C_o} \tag{2.54}$$

$$N = C_o h_{33} \tag{2.55}$$

After plugging $Z_a + Z_b, Z_o$, and N into 2.53, the following matrix of relations is obtained which is then used to develop the equivalent circuit model of a piezoelectric element.

$$\begin{pmatrix} F_L \\ F_B \\ V \end{pmatrix} = \begin{pmatrix} -(Z_a + Z_b) & Z_b & Z_o N \\ -Z_b & (Z_a + Z_b) & Z_o N \\ -Z_o N & Z_o N & Z_o \end{pmatrix} \begin{pmatrix} u_L \\ u_B \\ I \end{pmatrix} \tag{2.56}$$

To construct an equivalent circuit that satisfy the relations in 2.56, the equations need to be in a form allowing the circuit topology to be realized. The algebraic manipulations necessary to do this are presented below:

$$NV = Z_o N^2 (u_B - u_L) + Z_o I N \tag{2.57}$$

$$Z_o I N = NV - Z_o N^2 (u_B - u_L) \tag{2.58}$$

$$\begin{aligned} F_B &= Z_b(u_b - u_L) + Z_a u_B + Z_o I N \\ &= Z_b(u_b - u_L) + Z_a u_B + NV - Z_o N^2 (u_B - u_L) \\ &= (Z_b - Z_o N^2) NV - Z_o N^2 (u_B - u_L) + Z_a u_B + NV \end{aligned} \tag{2.59}$$

$$\begin{aligned} F_L &= Z_b(u_b - u_L) - Z_a u_L + Z_o I N \\ &= Z_b(u_b - u_L) - Z_a u_L + NV - Z_o N^2 (u_B - u_L) \\ &= (Z_b - Z_o N^2) NV - Z_o N^2 (u_B - u_L) - Z_a u_L + NV \end{aligned} \tag{2.60}$$

To use 2.59 and 2.60 to create an equivalent circuit model, note that Force is analogous to Voltage, and Current is analogous to Particle Velocity, and that the Mechanical Impedance and Electrical Impedance are equivalent. From these analogies, and equations 2.59 and 2.60, these equations are represented by the equivalent circuit

model given in figure 2.7.

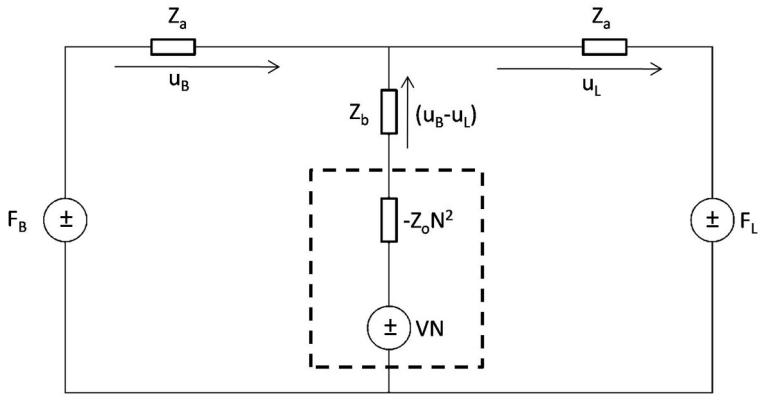

Figure 2.7: Distributed Circuit Equivalent of a Piezoelectric Element

It is convenient to convert the boxed section of the circuit into an equivalent form using the properties of an ideal transformer, as shown in figure 2.8.

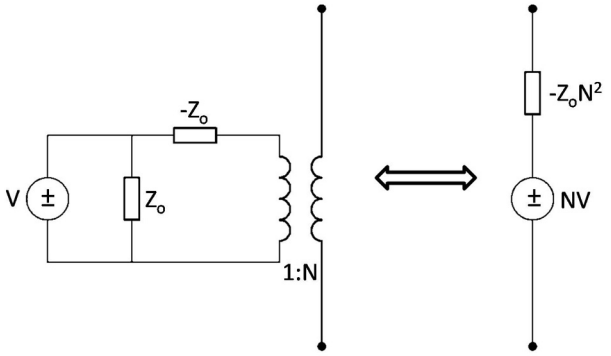

Figure 2.8: Transformation using Ideal Transformer Theory

Using this topology transform, as well as making the substitution $Z_B = F_B/u_B$ and $Z_L = F_L/u_L$, Mason's Model is obtained for the distributed equivalent circuit model of a piezoelectric element operating in thickness mode. This is presented in figure 2.9.

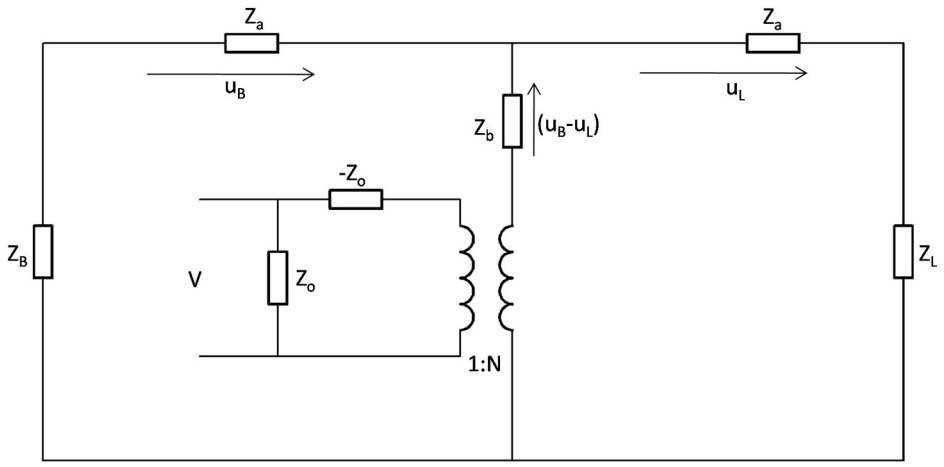

Figure 2.9: Mason's Model of Thickness Mode Piezoelectric Element

In the Mason Model, $Z_a = j\rho cA_o tan(kL/2)$, $Z_b = -j\rho cA_o/sin(kL)$ and $N = h_{33}C_o$. Z_B and Z_L are the backing and load impedance of the piezoelectric element. Note that $k = \omega/c$, ω is the frequency, c is the acoustic wave velocity in the piezoelectric element, and ρ is the density of the piezoelectric element.

2.4. Accounting for Material Losses in the Piezoelectric Element

In the development above the loss mechanisms that are present in the piezoelectric element have been omitted. This omission is valid for single crystal piezoelectric elements because the loss in single crystal elements such as quartz, is sufficiently small [20]; however, for most underwater acoustic transducers, the piezoelectric element is made of piezoceramic materials, such as PZT, or a piezocomposite material. These materials contain large losses as compared with quartz, consequently neglecting the loss terms causes significant effects on the theoretical values obtained for the performance characteristics [5, 20, 21] .

How to introduce losses in the distributed model of a piezoelectric element is shown in section 2.4.1. Following this, a discussion of each of the loss parameters is provided in section 2.4.2. The last section discusses how to find the values of the loss parameters.

2.4.1. Theoretical Discussion of how to Introduce Loss Parameters

It should be noted that no physical explanation of losses in the piezoelectric element has yet been clearly established. There have been a number of theories developed, and it seems as though there are four primary mechanisms in which loss can take place in a piezoelectric transducer. A good physical discussion of these loss mechanisms and the effects on the impedance is given in [22]. The four primary portions of loss in a piezoelectric element are due to the domain wall portion, fundamental lattice portion, microstructure portion, and conductivity portion. Losses in piezoelectric elements are generally due to dielectric, mechanical, or piezoelectric losses [23]. In order to account for these losses in the developed model of the piezoelectric element, the following equations are introduced [24].

$$\varepsilon_{33}^{S*} = \varepsilon_{33}^{S}(1 + j\delta_e) \tag{2.61}$$

$$c_{33}^{D*} = c_{33}^{D}(1 + j\delta_m) \tag{2.62}$$

$$h_{33}^{*} = h_{33}(1 + j\delta_p) \tag{2.63}$$

Each of the δ terms represents a specific loss. δ_e represents the dielectric loss, δ_m represents the mechanical loss, and δ_p represents the piezoelectric losses. As seen, the introduction of complex constants into the material parameters is how the losses are introduced into the distributed models.

2.4.2. Theoretical Discussion of Loss Parameters

These loss terms may be substituted into the equations developed for the equivalent circuit model by making the following changes $\varepsilon_{33}^{S*} \rightarrow \varepsilon_{33}^{S}$, $c_{33}^{D*} \rightarrow c_{33}^{D}$, and $h_{33}^{*} \rightarrow h_{33}$. From an energetics argument, it is shown that the following results must hold for the loss terms $\delta_e, \delta_m, \delta_p$ [24].

$$\delta_e \leq 0 \tag{2.64}$$

$$\delta_m \geq 0 \tag{2.65}$$

It is also expect that $|\delta_p| \leq |\delta_m|, |\delta_e|$. In the following paragraphs, a discussion of what the loss terms actually represent for the piezoelectric element. In order to better understand the cause of the losses, the microscopic structure of the piezoelectric

material is analyzed.

Mechanical Loss δ_m

Mechanical loss δ_m can be caused by a number of effects such as thermal conductivity, domain and grain boundary effects, interstitial atomic diffusion, scattering, and the motion of dislocations [25]. A number of models have been developed for the mechanical dispersion and how to model c_{33}^D which account for dispersion relationships in elastic materials. A number of the phenomenological loss models proposed are frequency dependent and involve the relaxation times of the displacement of an element to an applied stress and strain [25].

Dielectric Loss δ_e

The dielectric loss occurs because when an electric potential is applied to the electrodes of the piezoelectric material, the molecules of the dielectric fail to align instantaneously to the applied field, so a phase is introduced. In essence, a delay is introduced between the applied electric field and the polarization of the dielectric medium. A large amount of research has gone into the development of various models to account for the dielectric loss. Some common models for dielectric loss include the Debye relaxation, Cole-Cole equation, Cole-Davidson Equation, and Havriliak-Negami relaxation.

Piezoelectric Loss δ_e

Smits presented a connection between the laws of irreversible thermodynamic processes and statistical mechanics applied to domain wall motion and jumping defects, such as lattice defects, in order to show that the piezoelectric losses can, in fact, be represented by δ_p [26]. Smits also shows that the piezoelectric loss term is fully determined if the dielectric and mechanical loss terms are known, in which case he shows that $\delta_m \delta_e \propto \delta_p^2$. It is worth noting that Smits results are in complete agreement with what Holland found from a purely energetics argument [24]. From Smit's results, it can be seen that it is possible to use a Debye formula to represent the piezoelectric losses.

2.4.3. Finding the Complex Values

There are a number of methods for determining the complex material coefficients of the piezoelectric element [4, 5, 21, 22, 23, 27]. Some of the methods involve the measurement of the impedance of the piezoelectric element at a few select frequen-

cies, while others involve a range of frequency measurements. In all the impedance measurements conducted in this thesis, the impedance data is obtained over a range of frequencies. Therefore, a best fit approach to match the experimental data with the theoretical data is used to determine the complex loss factors, as explained in chapter 3.

2.5. Cable Model

In this section, the effect of a cable on the performance characteristics of the transducer are analyzed. These effects are especially important if the cable is long or if the operational frequency of the transducer is high. The transmission line equation from circuit theory can be utilized to take into account the effects caused by the cable.

The characteristic impedance of a transmission line is defined by Z_{tl}, given by the equation 2.66 [28].

$$Z_{tl} = \sqrt{\frac{R + j\omega L}{G + j\omega C}} \tag{2.66}$$

With this equation, the assumption is made that the drive voltage along the cable is sinusoidal with a frequency given by ω. A circuit equivalent representation of equation 2.66 is provided in figure 2.10.

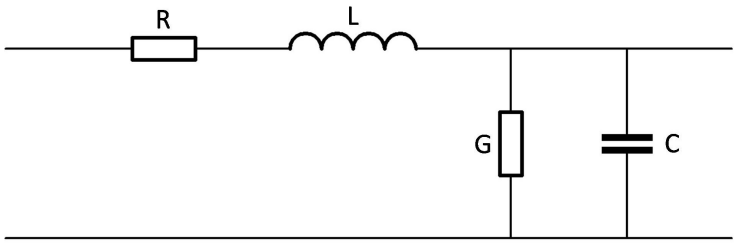

Figure 2.10: Circuit Equivalent Representation of Cable

R is the cable resistance per unit length, L is the inductance per unit length, G is the conductance of the dielectric per unit length, and C is the capacitance per unit length of the cable.

The sinusoidal input impedance for an electrical transmission line is given by the following formula [28].

$$Z_{in} = Z_{tl}\frac{Z_l + jZ_{tl}tanh(\gamma l)}{Z_{tl} + jZ_l tanh(\gamma l)} \tag{2.67}$$

$$\gamma = \sqrt{(R + j\omega L)(G + j\omega C)} \tag{2.68}$$

l is the length of the electrical line, Z_l is the impedance at the end of the electrical line, and Z_{in} is the impedance looking into the electrical line. In most cases, the cables used for transducers have a very low R and G value. For this analysis, it is assumed that the effects of R and G are small enough that they can be neglected such that the following equation for γ is obtained.

$$\gamma \approx j\omega\sqrt{LC} \tag{2.69}$$

Plugging γ into equation 2.67 for the impedance of an electrical transmission line, the following equation is obtained.

$$Z_{in} = Z_{tl}\frac{Z_l + jZ_o tan(\omega\sqrt{LC}l)}{Z_{tl} + jZ_l tan(\omega\sqrt{LC}l)} \tag{2.70}$$

Assuming that the cable lengths and frequencies are small enough; $\omega\sqrt{LC}l \ll 1$. Using this assumption, the following approximation can be made $tan(\omega\sqrt{LC}l) \approx \omega\sqrt{LC}l$. This gives the following formula for the impedance of the line.

$$\begin{aligned} Z_{in} &= Z_{tl}\frac{Z_l + jZ_{tl}\omega\sqrt{LC}l}{Z_{tl} + jZ_l\omega\sqrt{LC}l} \\ &= \frac{Z_l + jZ_{tl}\omega\sqrt{LC}l}{1 + j\frac{Z_l}{Z_{tl}}\omega\sqrt{LC}l} \end{aligned} \tag{2.71}$$

Since R and G are of negligible size, by assumption, $Z_{tl} = \sqrt{L/C}$, the following result for the line impedance

$$Z_{in} = \frac{Z_l + j\omega Ll}{1 + jZ_l\omega Cl} \tag{2.72}$$

Now, if $\omega Ll \ll 1$, the following result is found, which is identical to what would be found if only the line capacitance per unit length C was used.

$$Z_{in} \approx \frac{Z_l}{1 + j\omega C l Z_l}$$
$$\approx \frac{Z_l}{1 + (\omega C l Z_l)^2} - j\frac{\omega C l Z_l^2}{1 + (\omega C l Z_l)^2} \tag{2.73}$$

2.6. Complete Electrical Equivalent Transducer Model

Now that equivalent circuit models of the non-piezoelectric element, piezoelectric element, and the cable, have been developed, all of these are combined to build the complete electrical equivalent circuit model of a transducer. In this thesis, two primary types of transducers are analyzed. The first is the novel XTM transducer, which has the mechanical layout presented in figure 2.11.

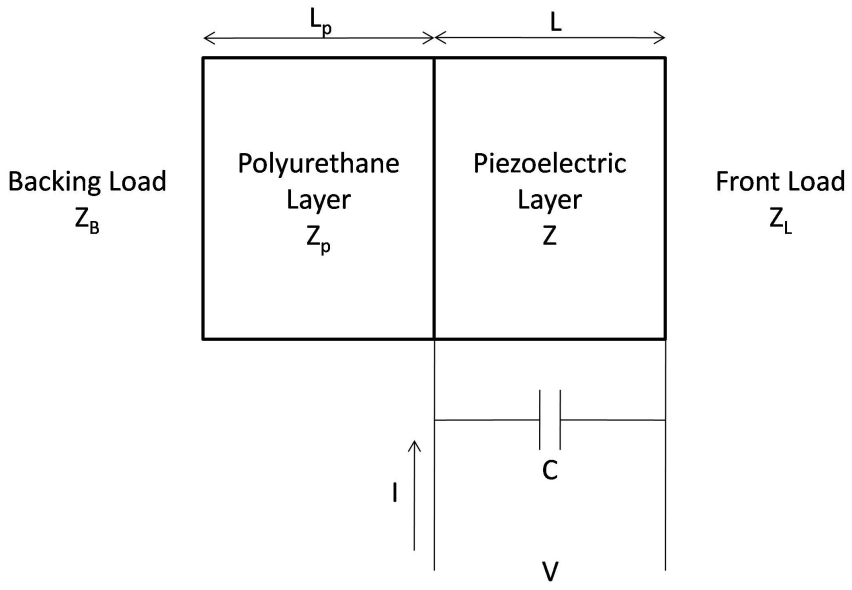

Figure 2.11: Mechanical Representation of the XTM Transducer

This cross sectional representation along with the area of each element gives enough information to develop the equivalent circuit model of the XTM transducer, given in figure 2.12.

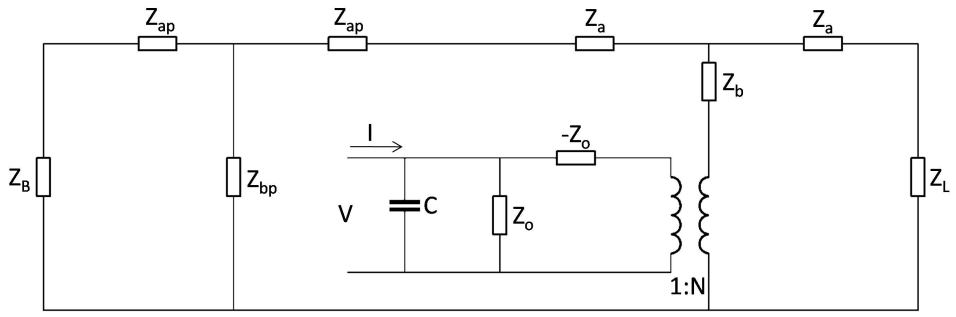

Figure 2.12: Electrical Equivalent Representation of the XTM Transducer

The second type of transducer is the Matched transducer, of which a mechanical diagram is presented in figure 2.13.

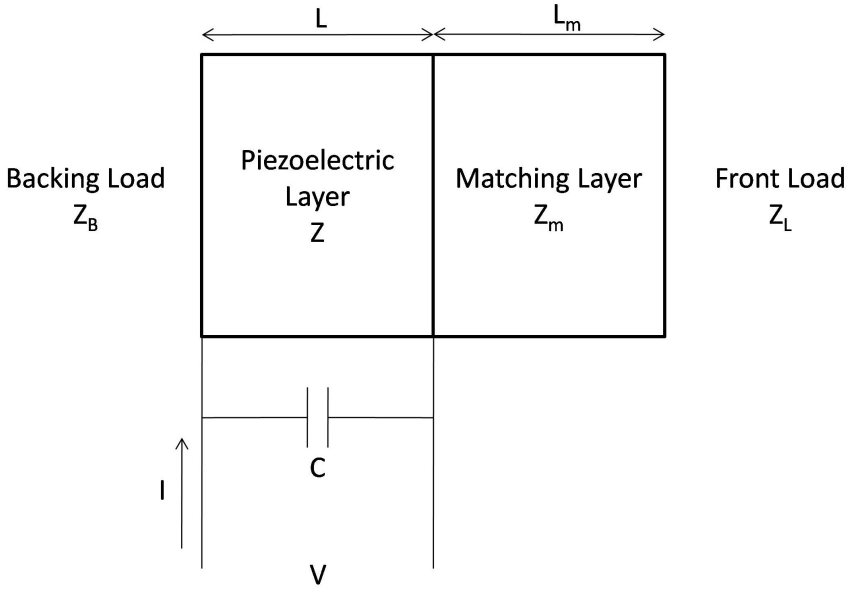

Figure 2.13: Mechanical Representation of the Matched Transducer

The corresponding electrical circuit model of the Matched transducer in figure 2.13, is provided in figure 2.14.

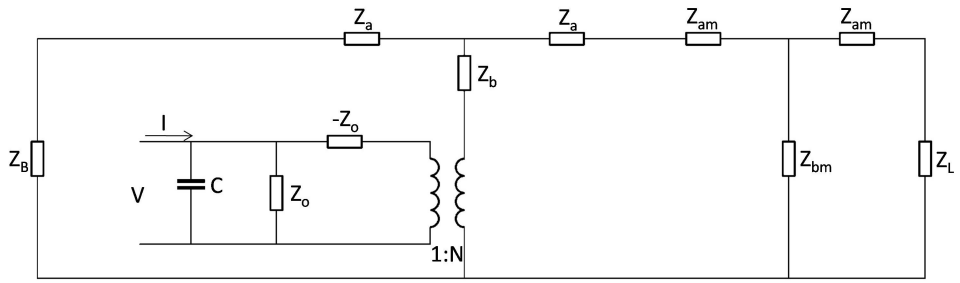

Figure 2.14: Electrical Equivalent Representation of the Matched Transducer

The circuit diagrams in figures 2.12 and 2.14 are utilized to determine a number of performance characteristics for both transducers.

2.7. Transducer Performance Characteristics

In this section the steady-state performance characteristics of the XTM and Matched transducers are determined including the electrical impedance, acoustical impedance, efficiency, sensitivity, and the TVR. With these characteristics, a designer can construct metrics of performance based on the materials and dimensions of the transducer. Since these performance characteristics depend only on the material properties and dimensions of the transducer, it is possible to rapidly test a number of configurations to meet specific design goals thereby reducing both the cost and time inherent if a purely experimental design validation is conducted.

2.7.1. Electrical Impedance

The electrical impedance of a transducer can be used to find the resonance frequency, anti-resonance frequency, bandwidth, and material parameters of the transducer. In this section the input electrical impedance of the transducer presented in figure 2.15 is determined.

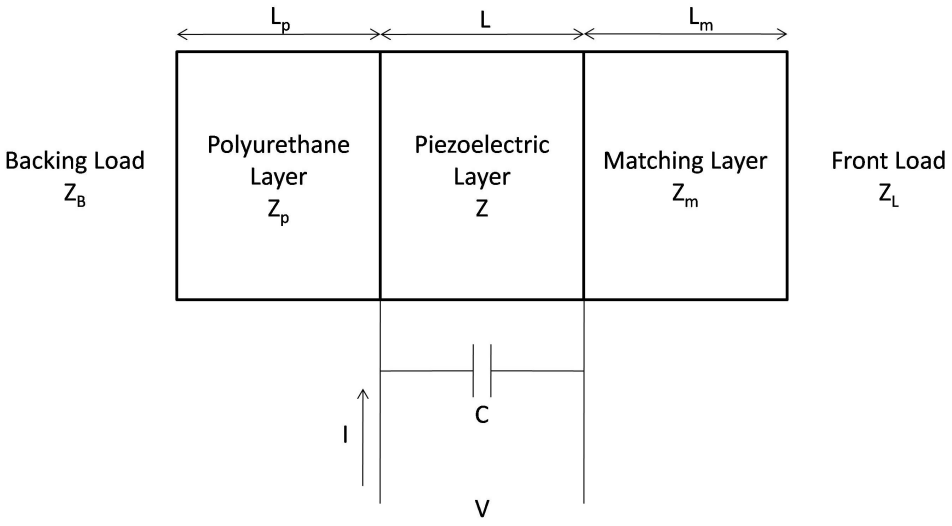

Figure 2.15: Mechanical Structure of Transducer

Notice that the input electrical impedance of the XTM transducer may be obtained L_m is set to; $L_m = 0$. If the input electrical impedance of the Matched transducer is desired instead, then L_p is set to; $L_p = 0$. The parameter C, in the above diagram, is used to account for the cable capacitance. The equivalent circuit model of the transducer shown in figure 2.15 is presented in figure 2.16.

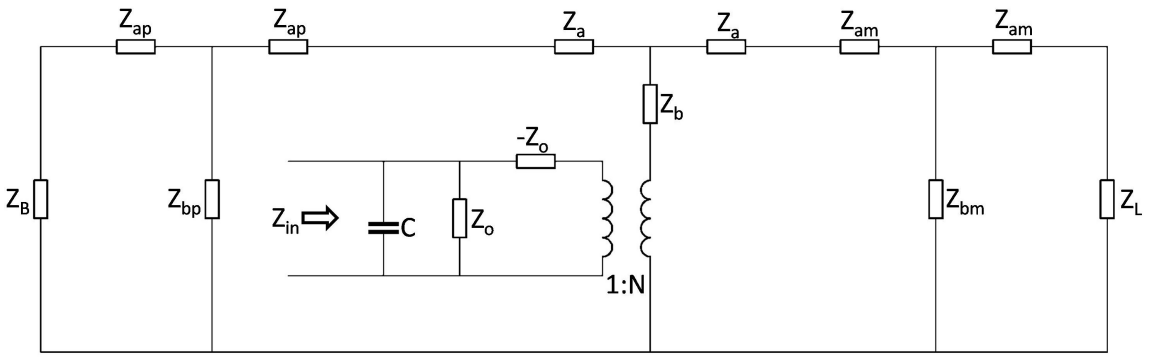

Figure 2.16: Distributed Circuit Equivalent of Above Transducer

Now basic circuit theory is applied to obtain an expression for Z_{in}, the input electrical impedance of the transducer. The solution for Z_{in} is given by the following equations:

$$Z_B = \rho_B v_B A_o \tag{2.74}$$

$$Z_p = \rho_p v_p A_o \tag{2.75}$$

$$k_p = \frac{\omega}{v_p} \tag{2.76}$$

$$\begin{aligned} Z_{backing} &= (Z_B + Z_{ap})//Z_{bp} + Z_{ap} \\ &= \frac{Z_p[Z_B + jZ_p tan(k_p L_p)]}{Z_p + jZ_B tan(k_p L_p)} \end{aligned} \tag{2.77}$$

$$k_p = \frac{\omega}{v_p} \tag{2.78}$$

$$Z_p = \rho_p v_p A_o \tag{2.79}$$

$$Z_{ap} = jZ_p tan(k_p L_p/2) \tag{2.80}$$

$$Z_{bp} = -jZ_m/sin(k_p L_p) \tag{2.81}$$

$$k_m = \frac{\omega}{v_m} \tag{2.82}$$

$$Z_m = \rho_m v_m A_o \tag{2.83}$$

$$Z_{am} = jZ_m tan(k_m L_m/2) \tag{2.84}$$

$$Z_{bm} = -jZ_m/sin(k_m L_m) \tag{2.85}$$

$$\begin{aligned} Z_{face} &= (Z_L + Z_{am})//Z_{bm} + Z_{am} \\ &= \frac{Z_m[Z_L + jZ_m tan(k_m L_m)]}{Z_m + jZ_L tan(k_m Lm)} \end{aligned} \tag{2.86}$$

$$k = \frac{\omega}{v} \tag{2.87}$$

$$Z_a = j\rho v A_o tan(kL/2) \tag{2.88}$$

$$Z_b = -j\rho v A_o/sin(kL) \tag{2.89}$$

$$Z_{eq} = [\frac{(Z_a + Z_{face})//(Z_a + Z_{backing}) + Z_b}{N^2} - Z_o]//Z_o \tag{2.90}$$

$$N = \frac{\varepsilon_{33}^S A_o h_{33}}{L} = C_o h_{33} \tag{2.91}$$

$$C_o = \frac{\varepsilon_{33}^S A_o}{L} \tag{2.92}$$

$$Z_o = \frac{1}{j\omega C_o} \tag{2.93}$$

$$Z_{in} = \frac{Z_{eq}}{1 + j\omega C Z_{eq}} \tag{2.94}$$

Z_{face} is the impedance looking out of the face of the transducer, and $Z_{backing}$ is the impedance looking out the backing of the transducer. // indicates that the impedances are in parallel. Although the system of equations looks very complicated, it can be easily implemented on any standard computer. Notice that if all the terms are plugged into the above expression for Z_{eq}, the following compact expression is obtained.

$$Z_c = \rho c A_o \tag{2.95}$$

$$Z_{eq} = \frac{1}{j\omega C_o} + \left(\frac{h_{33}}{\omega C_o}\right)^2 \frac{(Z_{face} + Z_{backing})sin(kL) + j2Z_c(1 - cos(kL))}{Z_c(Z_{face} + Z_{backing})cos(kL) + j(Z_c^2 + Z_{face}Z_{backing})sin(kL)} \tag{2.96}$$

2.7.2. Input Acoustic Impedance

The acoustic impedance, Z_{ac}, of a transducer is the ratio of the pressure on the transmitting face of the transducer, P, to the particle velocity of the transmitting face, u. From the equivalent circuit model, Z_{ac} is found as the impedance looking into the transducer from the transmitting face of the transducer. Notice that the XTM transducer and Matched transducers have different expressions for Z_{ac}.

First, Z_{ac} is found for the XTM transducer. The mechanical setup to find Z_{ac} for the XTM transducer is presented in figure 2.18.

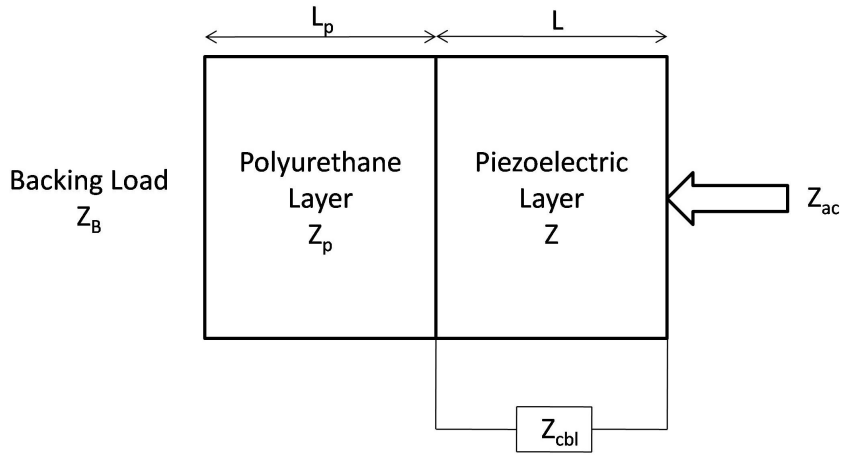

Figure 2.17: Mechanical Setup to find Acoustic Impedance for XTM Transducer

The value Z_{cbl} represents the cable impedance connected to the electrical port

of the piezoelectric element. The mechanical setup presented in figure 2.18 is converted into an equivalent electrical setup to find the expression for Z_{ac}, as shown in figure 2.18.

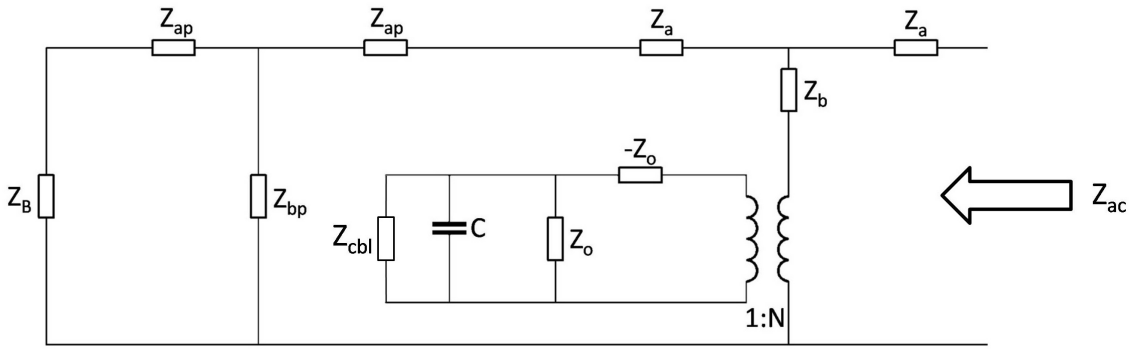

Figure 2.18: Mechanical Setup to find Acoustic Impedance for XTM Transducer

The expression for Z_{ac}, determined from the circuit diagram provided in figure 2.18, for the XTM transducer is presented below.

$$Z_{ac} = (Z_{backing} + Z_a)//(Z_b + N^2(Z_{cbl}//Z_o - Z_o)) + Z_a \tag{2.97}$$

An expression for Z_{ac} for the Matched transducer is determined next. The mechanical representation and equivalent circuit diagram for the Matched transducer are presented in figure 2.19.

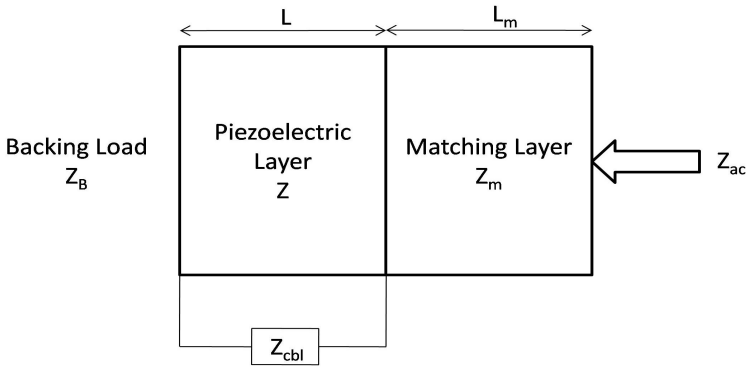

(a) Mechanical

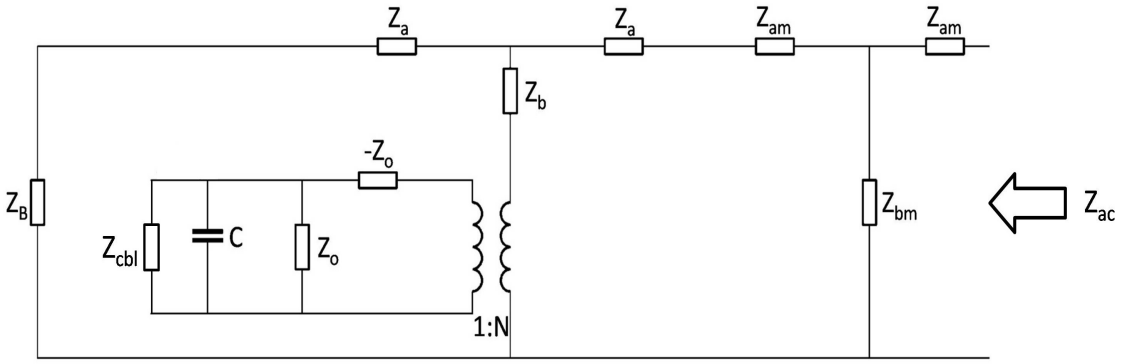

(b) Electrical

Figure 2.19: Mechanical and Electrical Model of Matched Transducer to find Acoustic Impedance

Using the circuit diagram in figure 2.19(b), the following expression is found for the acoustic impedance of the Matched transducer.

$$Z_{ac} = [(Z_B + Z_a)//(Z_b + N^2(Z_{cbl}//Z_o - Z_o)) + (Za + Z_{am})]//Z_{bm} + Z_{am} \qquad (2.98)$$

2.7.3. Efficiency

The efficiency of a transducer is equal to the ratio of the acoustic power emitted from the face of the transducer to the electrical power that is delivered to the transducer. The efficiency is represented by η. η can be found using equation 2.99, where P_a is the acoustic power emitted and P_e is the electrical power delivered to the transducer.

$$\eta = \frac{P_a}{P_e} = \frac{acoustic\ power}{electrical\ power} \tag{2.99}$$

Figure 2.20 illustrates the diagram used to find the efficiency of the transducer.

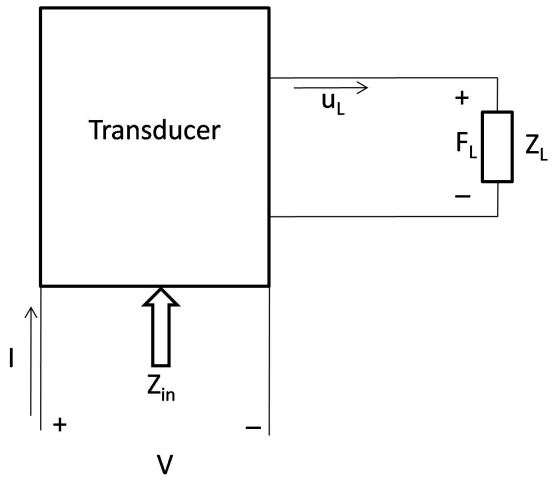

Figure 2.20: Diagram used to find Efficiency η

Z_L is the impedance of the loading medium and Z_{in} is the input electrical impedance of the transducer. F_L is the force on the face of the transducer. V is the sinusoidal voltage being delivered to the transducer, and I is the sinusoidal current being delivered to the transducer. With these terms defined, the expressions for P_a and P_e are found using the following formulas.

$$\bar{P_e} = VI \tag{2.100}$$

$$\begin{aligned} P_e &= \frac{1}{2} Re[VI^*] \\ &= \frac{1}{2}|V||I|cos(<V, I>) \\ &= \frac{1}{2}|V||\frac{V}{Z_{in}}|cos(<V, \frac{V}{Z_{in}}>) \\ &= \frac{1}{2}\frac{|V|^2}{|Z_{in}|}cos(\phi_{in}) \end{aligned} \tag{2.101}$$

$$\bar{P}_a = F_L u_L \tag{2.102}$$

$$\begin{aligned} P_a &= \frac{1}{2} Re[F_L u_L^*] \\ &= \frac{1}{2}|F_L||u_L| cos(< F_L, u_L >) \\ &= \frac{1}{2}|F_L||\frac{F_L}{Z_L}| cos(< Z_L u_L, u_L >) \quad \text{with} \quad Im[Z_L] = 0 \\ &= \frac{1}{2}\frac{|F_L|^2}{Z_L} \end{aligned} \tag{2.103}$$

Notice that P_a and P_e are the average powers which are found from the complex powers $\bar{P}_a$ and $\bar{P}_e$, as shown. Note that the function $< a, b >$ is defined as the angle measure between the parameters a and b. Now substituting P_a and P_e into equation 2.99 determines the expression for efficiency.

$$\begin{aligned} \eta = \frac{P_a}{P_e} &= \frac{1}{2}\frac{|F_L|^2}{Z_L}\frac{2|Z_{eq}|}{|V|^2 cos(\phi_{in})} \\ &= \frac{|TTF|^2}{Z_L}\frac{|Z_{in}|}{cos(\phi_{in})} \end{aligned} \tag{2.104}$$

The term TTF is the transmission transfer function of the transducer and is defined as $TTF = F_L/V$. ϕ_{in} is the phase angle associated with the input electrical impedance Z_{in}. The TTF can be found from the transmit voltage response of the transducer's TVR, which is developed for the XTM and Matched transducer in section 2.7.5.

2.7.4. Sensitivity

The sensitivity of a transducer is obtained by finding the open-circuit output voltage resulting from a given input pressure on the face of the transducer.

Sensitivity is represented using the parameter M. The value e_o corresponds to the open-circuit output voltage of the transducer, and the applied sinusoidal pressure is equal to $P = F/A_o$, where F is the sinusoidal force on the face of the transducer and A_o is the surface area of the face of the transducer.

Since the analysis is performed using the equivalent circuit model, the applied force F is represented by a voltage source of equal value F. With this substitution, it is possible to find the output voltage e_o at the open-circuit output terminals of the transducer as a function of input pressure, noting that $F = PA_o$. Also, keep in mind

that the pressure P and the voltage e_o are being applied with a sinusoidal frequency of $\omega = 2\pi f$.

In this section, the sensitivity is developed for the XTM transducer and the Matched transducer. Since equations for the sensitivity are different for each type of transducer, each is treated separately in the following sections.

Sensitivity for XTM Transducer

The electrical equivalent circuit of the XTM Transducer is presented in figure 2.21.

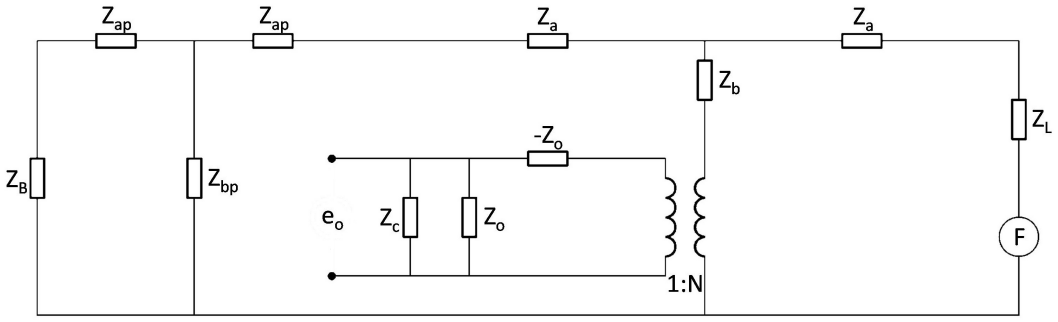

Figure 2.21: Distributed Circuit Equivalent of an XTM Transducer to find Sensitivity

The parameters used in this model are defined by the following equations:

$$k_p = \frac{\omega}{v_p} \tag{2.105}$$

$$Z_p = \rho_p v_p A_o \tag{2.106}$$

$$Z_{ap} = jZ_p tan(k_p L_p/2) \tag{2.107}$$

$$Z_{bp} = -jZ_m/sin(k_p L_p) \tag{2.108}$$

$$Z_a = j\rho v A_o tan(kL/2) \tag{2.109}$$

$$Z_b = -j\rho v A_o/sin(kL) \tag{2.110}$$

$$N = C_o h_{33} \tag{2.111}$$

$$Z_o = \frac{1}{j\omega C_o} \tag{2.112}$$

$$Z_c = \frac{1}{j\omega C} \tag{2.113}$$

Note that Z_L and Z_B are the load and backing impedances of the XTM transducer respectively. Using nodal analysis and the transformation of an ideal transformer, an

expression is obtained for e_o/F using the circuit in figure 2.21. The final result is presented in equation 2.114.

$$\begin{aligned} Z_{backing} &= \frac{Z_p[Z_B + jZ_p tan(k_p L_p)]}{Z_p + jZ_B tan(k_p L_p)} \\ A_1(\omega) &= \frac{Z_a + Z_{backing}}{2Z_a + Z_{backing} + Z_L} \\ A_2(\omega) &= (Z_a + Z_L)//(Z_{backing} + Z_a) + Z_b \\ \frac{e_o}{F} &= \frac{(Z_o//Z_c)NA_1(\omega)}{[(Z_o//Z_c - Z_o)N^2 + A_2(\omega)]} \end{aligned} \tag{2.114}$$

Notice that the expression for e_o/F is a complex quantity, therefore the absolute value of this quantity must be used in order to obtain a measurable expression. It is convenient to express the hydrophone sensitivity by the quantity M, which is given by equation 2.115.

$$\begin{aligned} M &= 20log(|\frac{e_o}{F}A_o|) - 120 \\ &= 20log(|\frac{e_o}{P}|) - 120 \end{aligned} \tag{2.115}$$

M has units of decibel-volts per micro-pascal $[dB//V/\mu Pa]$. Note that the pressure P is in units of Pascals, and e_o is in units of Volts.

Sensitivity for Matched Transducer

In this section the sensitivity for the Matched transducer is presented. The equivalent circuit model of the Matched transducer is given by the circuit diagram in figure 2.22.

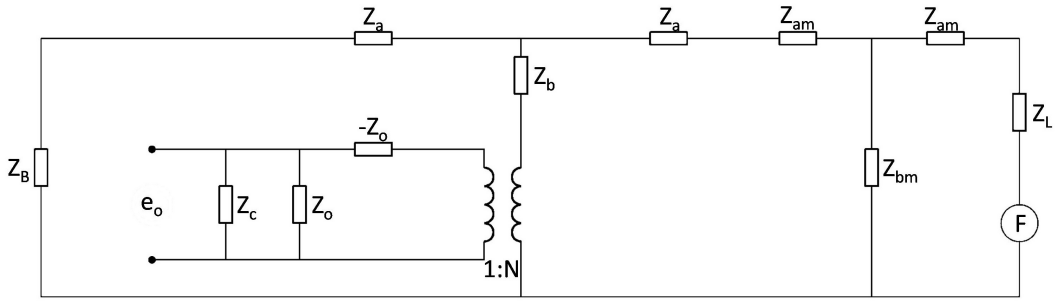

Figure 2.22: Distributed Circuit Equivalent of a Matched Transducer to find Sensitivity

The parameters used in this model are defined by the following equations.

$$Z_{am} = j\rho_m v_m A_o tan(k_m L_m/2) \tag{2.116}$$
$$Z_{bm} = -j\rho_m v_m A_o / sin(k_m L_m) \tag{2.117}$$
$$k_m = \frac{\omega}{v_m} \tag{2.118}$$
$$Z_a = j\rho c A_o tan(kL/2) \tag{2.119}$$
$$Z_b = -j\rho c A_o / sin(kL) \tag{2.120}$$
$$N = C_o h_{33} \tag{2.121}$$
$$Z_o = \frac{1}{j\omega C_o} \tag{2.122}$$
$$Z_c = \frac{1}{j\omega C} \tag{2.123}$$

Nodal analysis and the transformation of an ideal transformer are used to obtain an expression for e_o/F for the Matched transducer, which is presented in equation 2.124.

$$\begin{aligned} Z_{ll} &= ((Z_L + Z_{am})//Z_{bm} + Z_a + Z_{am})//(Z_a + Z_B) + Z_b \\ A_1(\omega) &= \left[\frac{Z_{am}+Z_L}{Z_{bm}} + \frac{Z_{am}+Z_L}{Z_{am}+Z_a} + 1\right]\left[\frac{Z_{am}+Z_a}{Z_a+Z_B} + 1\right] - \frac{Z_{am}+Z_L}{Z_{am}+Z_a} \\ \frac{e_o}{F} &= \left[\frac{N(Z_c//Z_o)}{A_1(\omega)[Z_{ll} - Z_o N^2 + (Z_c//Z_o)N^2]}\right] \end{aligned} \tag{2.124}$$

As in the previous section, it is standard practice to represent the sensitivity using the units of decibel-volts per micro-pascal $[dB//V/\mu Pa]$. Equation 2.125 is the sensitivity for the Matched transducer case.

$$\begin{aligned} M &= 20log(|\frac{e_o}{F}A_o|) - 120 \\ &= 20log(|\frac{e_o}{P}|) - 120 \end{aligned} \tag{2.125}$$

2.7.5. Finding the Transmission Voltage Response

The Transmission Voltage Response (TVR) is the ratio of the pressure output from the face of the transducer to the drive voltage of the transducer. Measurement of the TVR is done at steady-state with a sinusoidal input voltage of frequency ω.

In this section the TVR is developed for both the XTM transducer and the Matched transducer.

TVR for XTM Transducer

The TVR of the XTM transducer can be found from the equivalent distributed circuit model of the XTM transducer in figure 2.23.

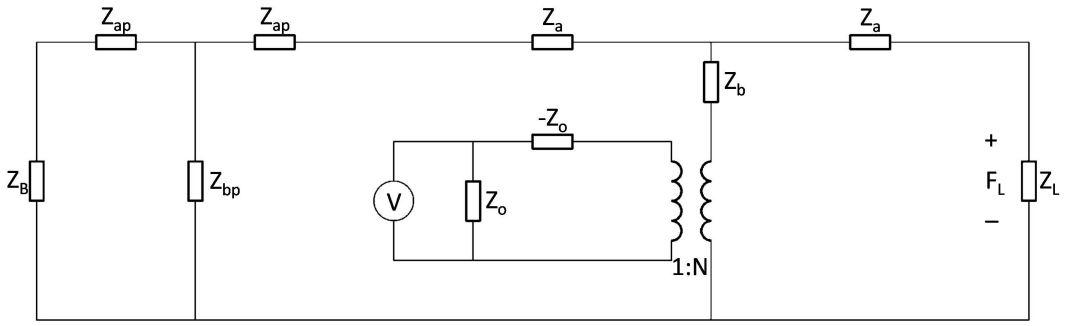

Figure 2.23: Distributed Circuit Equivalent of an XTM Transducer to find the TVR

The definitions of the terms in figure 2.23 are given in the XTM sensitivity section 2.7.4. Using circuit theory the expression for F_L/V is determined and given by the following formula.

$$\frac{F_L}{V} = \left[\frac{Z_L N}{Z_a + Z_L}\right]\left[\frac{(Z_a + Z_{backing})//(Z_a + Z_L)}{(Z_a + Z_{backing})//(Z_a + Z_L) + (Z_b - Z_o N^2)}\right] \tag{2.126}$$

By convention the TVR has units of $[dB//\mu Pa/V]$. Equation 2.127 is the TVR for the XTM transducer in units of $[dB//\mu Pa/V]$.

$$\begin{aligned} TVR &= 20log(|\frac{F_L}{VA_o}|) + 120 \\ &= 20log(|\frac{P}{V}|) + 120 \end{aligned} \tag{2.127}$$

Note that P is in units of Pascals and V is in units of Volts.

TVR for Matched Transducer

To find the TVR of the Matched transducer, the following distributed circuit model of the Matched transducer given in figure 2.24 is used.

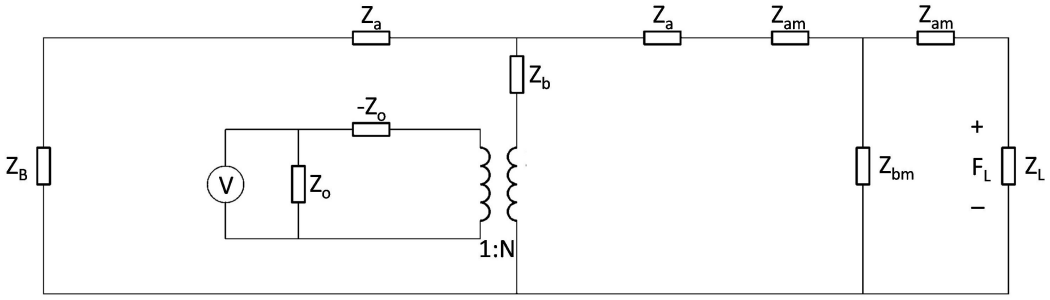

Figure 2.24: Distributed Circuit Equivalent of a Matched transducer to find TVR

The definitions of the parameters in the above circuit can be found in section 2.7.4 for the Matched transducer. Circuit theory is used to develop an expression for F_L/V from the circuit diagram in figure 2.24. The expression for F_L/V is presented below.

$$\begin{aligned} A_1(\omega) &= \left[1 + \frac{Z_a + Z_{am}}{Z_{bm}} + \frac{Z_a + Z_{am}}{Z_{am} + Z_L}\right] \\ A_2(\omega) &= \left[\frac{1}{Z_b - Z_o N^2} + \frac{1}{Z_a + Z_{am}} + \frac{1}{Z_B + Z_a}\right] A_1(\omega) - \frac{1}{Z_L + Z_{am}} \\ \frac{F_L}{V} &= \left[\frac{Z_L}{Z_{am} + Z_L}\right]\left[\frac{N}{(Z_b - Z_o N^2) A_2(\omega)}\right] \end{aligned} \tag{2.128}$$

As in the previous section, the TVR has units of $[dB//\mu Pa/V]$ and is given by the following formula.

$$\begin{aligned} TVR &= 20log(|\frac{F_L}{V A_o}|) + 120 \\ &= 20log(|\frac{P}{V}|) + 120 \end{aligned} \tag{2.129}$$

Note that P is in units of Pascals and V is in units of Volts.

2.7.6. Resonance Frequency Modes

The resonance frequency of a transducer can be determined by finding the minimum value of the input electrical impedance. In general, this is done numerically because

it is very difficult to analytically obtain an expression for the minimum of the input electrical impedance given its transcendental nature.

As an example of how to find the resonance frequency using the impedance, assume that a single piezoelectric element that is unloaded is being analyzed. The input electrical impedance for this element is given by the following formula.

$$Z_{in} = Z_o//(\frac{Z_b + 0.5Z_a - N^2 Z_o}{N^2}) \tag{2.130}$$

Substituting in the values for Z_a, Z_b, N, Z_o and simplifying, the following formula for the input impedance is obtained.

$$\begin{aligned} Z_{in} &= \frac{1}{j\omega C_o} - \frac{2sin(kL)N^2}{\rho c A_o \omega C_o (1 + cos(kL))} \\ &= -\frac{1}{C_o \omega}[j + \frac{2N^2 tan(\frac{kL}{2})}{\rho c A_o}] \end{aligned} \tag{2.131}$$

This expression of Z_{in} is used to find the expression for $|Z_{in}|^2$, which is presented below.

$$|Z_{in}|^2 = (\frac{1}{C_o})^2 \frac{1}{\omega^2} + (\frac{4N^4}{\rho c A_o}) tan^2(\frac{kL}{2}) \tag{2.132}$$

In order to find the minimum of this expression, numerical methods must be used. As seen from this simple analysis of a single piezoelectric element, it is difficult to obtain a good estimate of the resonance frequency of the transducer without resorting to numerical methods.

2.8. Conclusion of Transducer Modeling

The development of the distributed equivalent circuit models of the piezoelectric and non-piezoelectric elements of a transducer operating in thickness mode were presented in this chapter. In addition, the equivalent circuit model was utilized to model the cable that connects the transducer to the electrical systems that drive and receive the signals from the transducer. These models were developed assuming the transducer is operating in steady-state.

It was shown how to introduce mechanical, dielectric, and piezoelectric losses in both piezoelectric and non-piezoelectric element models by the addition of complex

constants to certain material parameters. The expressions for a number of performance characteristics including the electrical impedance, acoustic impedance, efficiency, sensitivity, and TVR, as well as how to find the resonance frequency of a transducer are presented. Although the performance characteristics are found for the specific cases of the XTM and Matched transducers, the theory may be expanded to any acoustic transducer operating in thickness mode.

3. Experimental Validation of Distributed Impedance Model

The focus of this chapter is on the experimental validation of the impedance model developed in section 2.7.1. This is accomplished by making a comparison between the theoretically and experimentally determined impedance curves for a number of transducers with varying material types and geometric dimensions.

The impedance is one of the easiest steady-state performance characteristics to measure experimentally, so the validation of the theoretical impedance is used to provide validation of the circuit models developed in chapter 2.

Although the impedance is one of the easiest performance parameters to measure, the validation of the impedance model is not trivial. The complexity arises because access is limited to a number of the material parameters of the non-piezoelectric and piezoelectric elements. It is rare for a manufacturer to provide all the material data of a piezoelectric element, and even if they do, the variability in the material parameters can be as high as $\pm 20\%$. Therefore, before the experimental analysis begins, it must be determined if the impedance curves can be used to obtain the material parameters.

In section 3.1, an intricate analysis is conducted to determine the accuracy of the material parameters obtainable from an impedance curve, in theory. The equations of the impedance curves and experimental setup used to conduct the accuracy analysis are presented in section 3.1.1. The analysis is conducted by producing synthetic experimental impedance data and subsequently utilizing a constrained nonlinear minimization on an error function to obtain the original material parameters from the synthetic impedance data. The constraints are introduced because there are physical limitations on the values of the material parameters. The constraints for a general piezoelectric element are presented in section 3.1.3. The analysis shows that it is possible, assuming that the developed theoretical impedance model is correct, to find the material parameters of the transducer from the impedance curves.

Having established that the material parameters can be determined from the

impedance curves, it becomes possible to validate the theoretical impedance using the experimentally measured impedance, without the need to have every material parameter of the transducer defined. The fits of the theoretical impedance are done by hand because it is computationally difficult to obtain a suitable estimate of the material parameters using a standard constrained nonlinear minimization routine on the experimental data obtained. The allowable values of the piezoelectric material parameters are bounded using the constraints presented in section 3.1.3. For non-piezoelectric elements, the density and acoustic velocity can be obtained with good accuracy without the use of complex measurements.

The experimental setup used to measure the impedance is presented in section 3.1.1 and the impedance curves analyzed include the magnitude of the impedance, resistance, reactance, admittance, conductance, and susceptance. The experimental verification of the impedance measurements is conducted in section 3.2.

3.1. Accuracy of Material Parameters Obtained from Impedance Measurement

This analysis focuses on determining if the material parameters of a single piezoelectric element in air can be accurately determined from the measured impedance data.

The experimental setup used to conduct the impedance measurements is presented in section 3.1.1. The errors associated with the measurements and how to synthetically produce them are discussed in section 3.1.2. The routine used to determine the accuracy of the material parameters from the synthetically produced impedance data is presented in section 3.1.5 and the final results of the analysis are given in section 3.1.6. It is clearly demonstrated that the material parameters of a single piezoelectric element can be determined with good accuracy using measured impedance data.

3.1.1. Experimental Setup used to Measure Impedance

The experimental setup used to measure the impedance of a transducer is presented in figure 3.1.

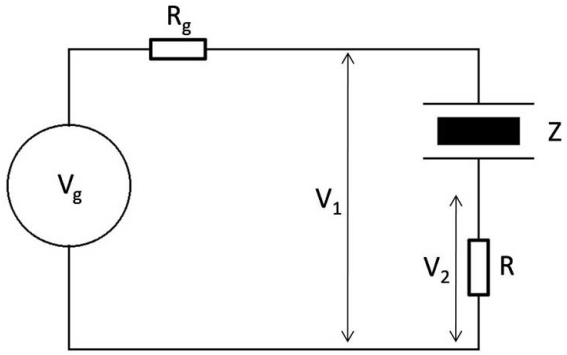

Figure 3.1: Schematic of Impedance Measurement System

V_g is the output voltage of the generator, R_g is the internal resistance of the voltage generator, R is a high precision resistor, and Z represents the transducer's input impedance. The voltages V_1 and V_2 are measured using a TDS-3034B Tektronix Oscilloscope. V_g is used to drive the system with a pure sinusoidal waveform with a frequency $\omega = 2\pi f$. The magnitudes, V_1 and V_2 as well as the phase difference between V_1 and V_2, $\phi_1 - \phi_2 = \phi_{12}$, are measured. These values provide sufficient information to determine the impedance and admittance of the transducer Z, given by equations 3.1 and 3.2.

$$Z(f) = R\Big[\frac{V_1(f)}{V_2(f)}e^{i(\phi_{12}(f))} - 1\Big] \tag{3.1}$$

$$Y(f) = \Big(\frac{1}{R}\Big)\Big[\frac{V_2(f)}{V_1(f)e^{i(\phi_{12}(f))} - V_2(f)}\Big] \tag{3.2}$$

Equations 3.1 and 3.2 are used to obtain the expression for the magnitude of the impedance, resistance, magnitude of admittance, conductance, and susceptance as shown below:

$$z(f) = |Z(f)| \qquad \text{Magnitude of Impedance} \tag{3.3}$$

$$R(f) = Re[Z(f)] \qquad \text{Resistance} \tag{3.4}$$

$$X(f) = Im[Z(f)] \qquad \text{Reactance} \tag{3.5}$$

$$y(f) = |Y(f)| \qquad \text{Magnitude of Admittance} \qquad (3.6)$$

$$G(f) = Re[Y(f)] \qquad \text{Conductance} \qquad (3.7)$$

$$B(f) = Im[Y(f)] \qquad \text{Susceptance} \qquad (3.8)$$

3.1.2. Estimate of Errors in Impedance Measurement

A method for introducing inaccuracies in the voltage and phase measurements of V_1, V_2, and ϕ_{12} is introduced in this section. Referring to the manual of the TDS-3034B Tektronix Oscilloscope, a $\pm 2\%$ error exists on the vertical resolution which must be introduced into V_1 and V_2. The phase angle ϕ_{12} has an assumed error of $\pm 0.5\%$, which is added to ϕ_{12}. Since only the ratio of V_1 and V_2, and the relative phase angle between the two waveforms is important, it is possible to set $V_2 = 1$ and $\phi_2 = 0$ without loss of generality. If Z is known, then the following formula can be used to obtain V_1 and ϕ_1.

$$V_1(f)e^{i\phi_1(f)} = \frac{Z(f)}{R} + 1 \qquad (3.9)$$

In this analysis, the values $V_1(f), V_2(f)$ and $\phi_{12}(f)$ are known. It is possible, therefore, to introduce the errors using the following normal distributions where $\sim \mathcal{N}(\mu, \sigma^2)$ indicates a normal distribution with mean μ and variance σ^2.

$$V_1(f) \sim \mathcal{N}(V_1(f), ((0.02)V_1(f))^2) \qquad (3.10)$$

$$V_2(f) \sim \mathcal{N}(V_2(f), ((0.02)V_2(f))^2) \qquad (3.11)$$

$$\phi_{12}(f) \sim \mathcal{N}(\phi_{12}(f), ((0.005)\phi_{12}(f))^2) \qquad (3.12)$$

3.1.3. Constraints on Allowable Material Parameters for a Piezoelectric Element

From the analysis of a number of manufacturing sources and literature, it is determined that the following constraints can be used to bound the values of the material parameters. These constraints account for nearly every piezoelectric material used in an underwater acoustic transducer. The constraints for the material constants $\{\rho, c_{33}^D, K_{33}^S, h_{33}\}$ are presented in equation 3.13.

$$c_{const} = \begin{cases} 3000 \leq \rho \leq 8000 & [\text{kg}] \\ 50 \leq Re[c_{33}^{D}] \leq 140 & [\text{Pa}] \\ 0 \leq Im[c_{33}^{D}] \leq 25 & [\text{Pa}] \\ 200 \leq Re[K_{33}^{S}] \leq 1300 & [\ ] \\ -400 \leq Im[K_{33}^{S}] \leq 0 & [\ ] \\ 1 \leq Re[h_{33}] \leq 4 & [\text{GV/m}] \\ 0 \leq Im[h_{33}] \leq 0.5 & [\text{GV/m}] \end{cases} \tag{3.13}$$

3.1.4. Error Function used to Determine Accuracy of Material Parameters

The error function used to determine the accuracy of the material parameters is given by equation 3.26. Notice that the size of the admittance data is scaled relative to the size of the impedance data. This is done to ensure that the impedance values, $\{z, R, X\}$, do not dominate the value of the Error function.

$$\vec{y}^{scl} = \vec{y} * (\frac{max(\vec{z})}{max(\vec{y})}) \tag{3.14}$$

$$\vec{G}^{scl} = \vec{G} * (\frac{max(\vec{R})}{max(\vec{G})}) \tag{3.15}$$

$$\vec{B}^{scl} = \vec{B} * (\frac{max(\vec{X})}{max(\vec{B})}) \tag{3.16}$$

$$\vec{y_m}^{scl} = \vec{y_m} * (\frac{max(\vec{z_m})}{max(\vec{y_m})}) \tag{3.17}$$

$$\vec{G_m}^{scl} = \vec{G_m} * (\frac{max(\vec{R})}{max(\vec{G_m})}) \tag{3.18}$$

$$\vec{B_m}^{scl} = \vec{B_m} * (\frac{max(\vec{X_m})}{max(\vec{B_m})}) \tag{3.19}$$

$$Z_e = |\vec{z} - \vec{z_m}|^2 \tag{3.20}$$

$$R_e = |\vec{R} - \vec{R_m}|^2 \tag{3.21}$$

$$X_e = |\vec{X} - \vec{X_m}|^2 \tag{3.22}$$

$$Y_e = |\vec{y}^{scl} - \vec{y_m}^{scl}|^2 \tag{3.23}$$

$$G_e = |\vec{G}^{scl} - \vec{G_m}^{scl}|^2 \tag{3.24}$$

$$B_e = |\vec{B}^{scl} - \vec{B_m}^{scl}|^2 \tag{3.25}$$

$$Error = Z_e + R_e + X_e + Y_e + G_e + B_e \tag{3.26}$$

The values $\{\vec{z_m}, \vec{R_m}, \vec{X_m}, \vec{y_m}, \vec{G_m}, \vec{B_m}\}$ indicate the measured data and $\{\vec{z}, \vec{R}, \vec{X}, \vec{y}, \vec{G}, \vec{B}\}$ are the estimated values obtained using the expected material parameters of the transducer. Note that the vector symbol $\rightarrow$ above any parameter indicates that it is a set of values, each of which is defined at a specific frequency.

3.1.5. Routine Used to Determine Accuracy of Material Parameters found from Impedance Measurement

The routine used to determine the accuracy of the obtainable material parameters is summarized by the following steps.

0. Define the surface area A_o, thickness of the element L, and the resistance value R. For this analysis, $A_o = 111.95\text{mm}^2, L = 5.12\text{mm},$ and $R = 55\Omega$.

1. Randomly select realistic values of $\{K_{33}^S, c_{33}^D, h_{33}, \rho\} = x_{opt}$ using normal distributions.

2. Use x_{opt} to find $\vec{Z}$, and then use $\vec{Z}$ to find $\{\vec{V_1}, \vec{V_2}, \vec{V_3}\}$.

3. Introduce the measurement errors into the values of $\{\vec{V_1}, \vec{V_2}, \vec{V_3}\}$ to obtain $\{\vec{V_1}^e, \vec{V_2}^e, \vec{V_3}^e\}$.

4. Use $\{\vec{V_1}^e, \vec{V_2}^e, , \vec{V_3}^e\}$ to find $\{\vec{z_m}, \vec{R_m}, \vec{X_m}, \vec{y_m}, \vec{G_m}, \vec{B_m}\} = X_{IA}^e$.

5. Conduct a constrained nonlinear minimization of the Error function to obtain an estimate of the original material parameters using the data in X_{IA}^e. The estimated material parameters are defined by $\{_{est}K_{33}^S, _{est}c_{33}^D, _{est}h_{33}, _{est}\rho\} = x_{est}$.

6. If the constrained nonlinear minimization was successful, then find the percent error between the values in x_{opt} and x_{est}.

In step one, each material parameter is found using a constrained uniform distribution, with the limits of the distribution determined by the constraints present in equation 3.13.

In step two, the material parameters x_{opt} are used to find the impedance of the transducer for a number of frequency values defined by $\vec{f} = \{f_1, f_2, \ldots, f_N\}$. Here the study is conducted using $\vec{f} = \{100\text{kHz}, 101\text{kHz}, \ldots, 700\text{kHz}\}$. Equation 2.131 is used to find the impedance $\vec{Z} = \{Z(f_1), Z(f_2), \ldots, Z(f_N)\}$. The calculated $\vec{Z}$ is then used to obtain the values of $\{\vec{V_1}, \vec{V_2}, \vec{\phi_{12}}\}$ using equation 3.9 and noting that $V_2 = 1$ and $\phi_2 = 0$. Note that the vector symbol $\rightarrow$ above any parameter indicates that it is a set of values, each of which is defined at a specific frequency, ie. $\vec{V_1} = \{V_1(f_1), V_1(f_2), \ldots, V_1(f_N)\}$.

In step three, equations 3.10 to 3.12 are used to introduce the inaccuracy of the measurement into the values of $\{\vec{V_1}, \vec{V_2}, \vec{\phi_{12}}\}$. The voltage and phase angle measurements containing measurement error are given by $\{\vec{V_1}^{\,e}, \vec{V_2}^{\,e}, \vec{\phi_{12}}^{\,e}\}$.

In step four, equations 3.1 to 3.8 are used to find the parameters of X_{IA}^e using the values from $\{\vec{V_1}^{\,e}, \vec{V_2}^{\,e}, \vec{\phi_{12}}^{\,e}\}$.

In step five, a constrained nonlinear minimization is conducted using the Error function given by equation 3.26 and the constraints defined in equation 3.13. The data supplied to the Error function is $\{\vec{f}, X_{IA}^e\}$. The task of the minimization routine is to find values of $x_{est} = \{_{est}K_{33}^S, _{est}c_{33}^D, _{est}h_{33}, _{est}\rho\}$ that are close to x_{opt}. The function used to implement the minimization routine is the MATLAB routine **fmincon** with the option 'active-set' specified.

In step six, the determination of the validity of the results obtained from the constrained nonlinear minimization is performed. To do this, the value of the Error function is found using the values x_{est} and X_{IA}^e. For this analysis, if the Error function is less than or equal to $1 * 10^9$, then the minimization routine was successful.

If the fit is good, then the percent error between the parameters in x_{opt} and x_{est} are determined. As an example, the percent error for the real part of K_{33}^S is presented below.

$$\%E[Re[K_{33}^S]] = \left(\frac{Re[K_{33}^S] - Re[_{est}K_{33}^S]}{Re[K_{33}^S]}\right) * 100 \tag{3.27}$$

3.1.6. Conclusion of Accuracy Analysis

The accuracy routine in section 3.1.5 was run for 3000 successful trials. After analysis of the percent errors obtained, it was found that the estimated values of ρ and c_{33}^D had the largest inaccuracies of the obtained material parameters. On the other hand, the estimated acoustic velocity, $v = \sqrt{c_{33}^D/\rho}$ had the highest accuracy of the obtained material parameters. The following list summarizes a rough estimate of the percent error of the material parameters obtained from an in air measurement of the impedance and admittance of a single piezoelectric element.

$$\%E[Re[v]] = \pm 0.02\% \qquad \%E[Im[v]] = \pm 0.05\%$$
$$\%E[Re[K_{33}^S]] = \pm 2\% \qquad \%E[Im[K_{33}^S]] = \pm 0.2\%$$
$$\%E[Re[h_{33}]] = \pm 15\% \qquad \%E[Im[h_{33}]] = \pm 0.5\%$$
$$\%E[Re[c_{33}^D]] = \pm 25\% \qquad \%E[Im[c_{33}^D]] = \pm 35\%$$
$$\%E[\rho] = \pm 25\%$$

The analysis presented in this thesis shows that the material parameters of a transducer can be determined using its impedance and admittance curves if the geometric dimensions of the transducer are known. This is a very beneficial result as far as transducer design is concerned, substantially improving design efficiency. Note that the parameter ρ is generally available from literature for standard materials, or can be determined with high accuracy using a standard analytical balance.

3.2. Experimental Verification of the Impedance and Admittance Model

Verification of the steady-state impedance from section 2.7.1 is validated in this section using a number of different transducers. The experimentally measured impedance and admittance data is compared with the theoretically determined impedance and admittance data to perform the validation. The experimental measurement system used to obtain the impedance/admittance data is presented in section 3.1.1.

3.2.1. Piezoelectric Transducer

In this section the impedance/admittance curves for the transducer shown in figure 3.2 are determined experimentally. To find the impedance/admittance of this transducer theoretically, the impedance model of the XTM transducer presented in section 2.7.1 is used.

Figure 3.2: XTM 214kHz Piezoelectric Transducer

The XTM transducer is composed of 3 Layers. The first and third layers are polyurethane layers that provide electrical shielding and mechanical support for the piezoelectric element. The second polyurethane layer differs in thickness from the first layer. Both polyurethane layers have the same impedance as water. The layer in between the polyurethane layers is the piezoelectric element. The backing material, as shown in figure 2.15, is composed of synctactic acoustic damping material (SADM). This is a novel transducer design in that the third layer is a quarter wave layer of polyurethane between the piezoelectric element and the SADM material. This geometry is used as it seems to reduce the crosstalk between neighboring piezoelectric elements in a transducer composed of a number of thickness mode structures arranged in a planar array pattern. The material parameters found for this transducer are shown below:

$A_o = 445.16$	$[mm^2]$
$\rho_{load} = 1000$	$[kg/m^3]$
$v_{load} = 1500$	$[m/s]$
$\rho_m = 1000$	$[kg/m^3]$
$v_m = 1500$	$[m/s]$
$L_m = 4.445$	$[mm]$
$L = 7.65$	$[mm]$
$\rho = 7750$	$[kg/m^3]$
$c_{33}^D = (121 + 2j)$	$[GPa]$
$K_{33}^S = (710 - 10j)$	$[\quad]$
$h_{33} = (2.68 + 0.03j)$	$[GV/m]$
$\rho_{poly} = 1000$	$[kg/m^3]$
$v_{poly} = 1500$	$[m/s]$
$\rho_{SADM} = 2000$	$[kg/m^3]$
$v_{SADM} = 524$	$[m/s]$
$C = 120$	$[nF]$

Using these material parameters and the impedance model for the XTM transducer given in section 2.7.1, the theoretically and experimentally obtained impedance and admittance curves are shown in figures 3.3 and 3.4.

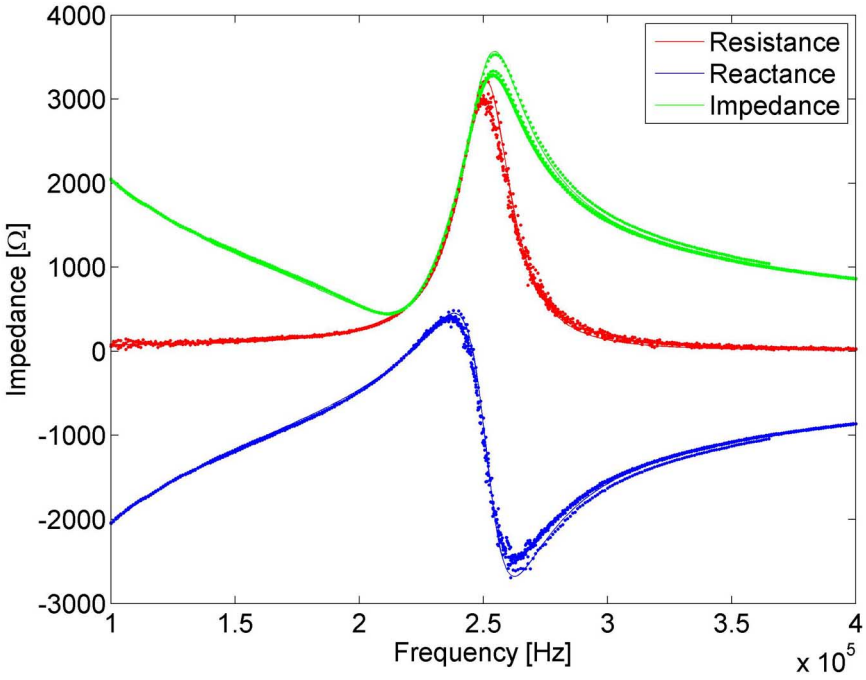

Figure 3.3: XTM 214kHz Piezoelectric Transducer Impedance

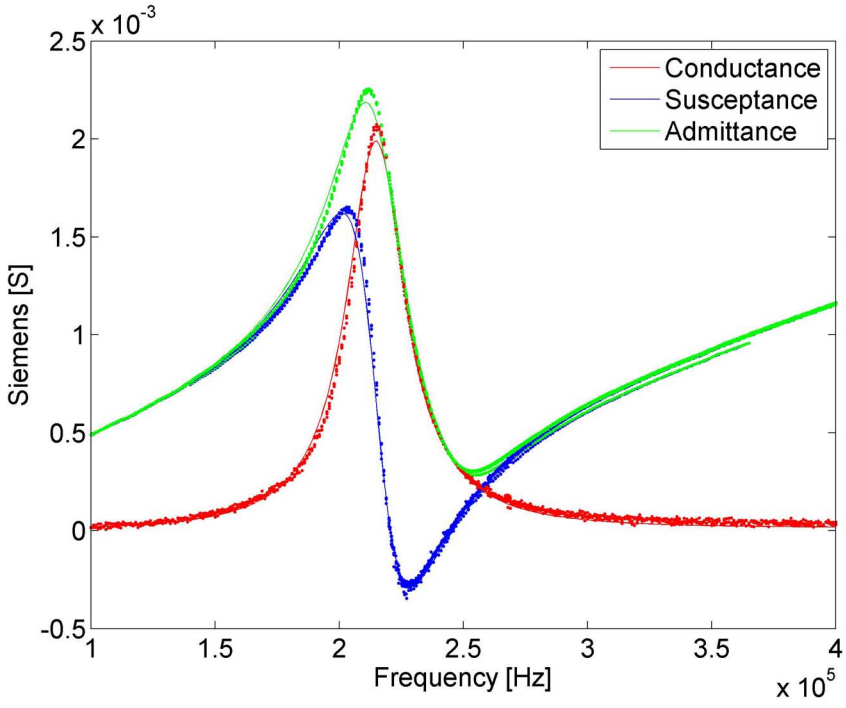

Figure 3.4: XTM 214kHz Piezoelectric Transducer Admittance

The solid lines in figures 3.3 and 3.4 represent the theoretically obtained impedance and admittance curves, whereas the dotted lines represent the experimentally obtained impedance and admittance curves.

The mechanical resonance frequency of the transducer occurs at the maximum value of the admittance curve, which occurs at a frequency of 214kHz. The mechanical anti-resonance frequency of the transducer occurs at the maximum value of the impedance curve. This occurs at a frequency of 256kHz.

In figures 3.3 and 3.4, the impedance and admittance measurements are repeated a number of times to determine the error expected when making the impedance and admittance measurements.

Since the theoretically and experimentally determined values are in very close agreement with each other, this suggests that the correct material parameter values have been determined and that the impedance model developed in section 2.7.1 is valid.

3.2.2. Impedance and Admittance of a Composite Piezoelectric Element

The theoretical input impedance and admittance models of the composite piezoelectric element, shown in figure 3.5, are verified in this section.

Figure 3.5: Single Element Piezocompsite Transducer

The experimentally determined material parameters for this element are given by:

$\rho = 7240$	$[kg/m^3]$
$c_{33}^D = (94.3 + 2.1j)$	$[GPa]$
$K_{33}^S = (476.54 - 25j)$	$[\quad]$
$h_{33} = (3.12 + 0.1j)$	$[GV/m]$
$L = 5.12$	$[mm]$
$A_o = 111.95$	$[mm^2]$

The theoretical impedance and admittance curves are determined using equation 2.131 which is included for reference below.

$$\begin{aligned} Z_{in} &= \frac{1}{j\omega C_o} - \frac{2sin(kL)N^2}{\rho c A_o \omega C_o (1 + cos(kL))} \\ &= -\frac{1}{C_o \omega}[j + \frac{2N^2 tan(\frac{kL}{2})}{\rho c A_o}] \end{aligned} \tag{3.28}$$

Note that the definitions of C_o, N, and k are given in section 2.7.1.

The theoretically and experimentally determined impedance and admittance curves are presented in figures 3.6 and 3.7.

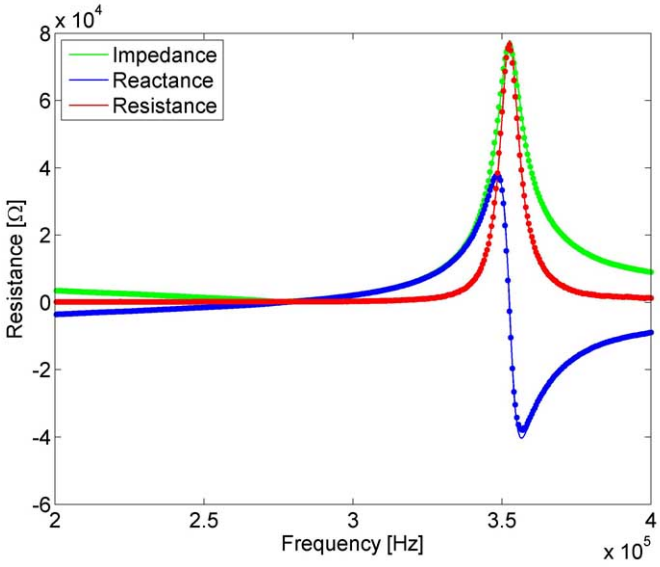

Figure 3.6: Single Element Piezocompsite Transducer Impedance

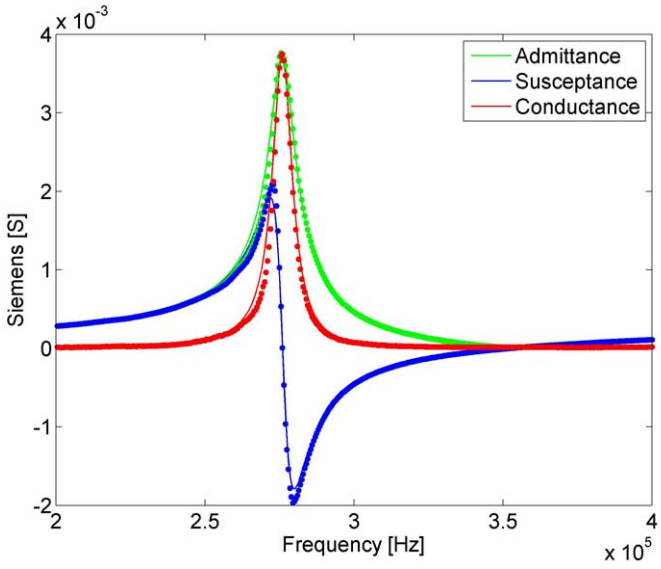

Figure 3.7: Single Element Piezocompsite Transducer Admittance

In figures 3.6 and 3.7, a very good match was obtained between the theoretically predicted and experimentally determined impedance and admittance curves. There is some variation in the susceptance and conductance curves, but these are still within the error bounds of the measurement. This variation may be caused by external noise coupling effects through the cables used to conduct the measurement.

3.2.3. Composite Piezoelectric Element with SADM Backing

The input impedance and admittance values of the transducer shown in figure 3.8 are provided in this section. The data obtained is used to determine the material parameters of the transducer, and is also compared with the values obtained from the impedance model.

Figure 3.8: Single Element Piezocompsite Transducer with SADM Backing

The experimentally determined material parameters for the transducer in figure 3.8 are given by the following:

$$
\begin{aligned}
A_o &= 111.95 && [mm^2] \\
L &= 5.12 && [mm] \\
\rho &= 7300 && [kg/m^3] \\
c_{33}^D &= (94.3 + 2.8j) && [GPa] \\
K_{33}^S &= (446.9 - 14.7j) && [\ \ ] \\
h_{33} &= (3.12 + 0.094j) && [GV/m] \\
\rho_{SADM} &= 2000 && [kg/m^3] \\
v_{SADM} &= 524 && [m/s]
\end{aligned}
$$

Using these material parameters, the theoretical impedance and admittance curves are determined using the theory developed in section 2.7.1. Note that the parameters $L_p = 0$, $L_m = 0$, $Z_L = 0$, and $Z_B = \rho_{SADM} v_{SADM} A_o$ are used to model this transducer. The theoretically predicted curves together with the experimentally measured impedance and admittance values are presented in figures 3.9 and 3.10.

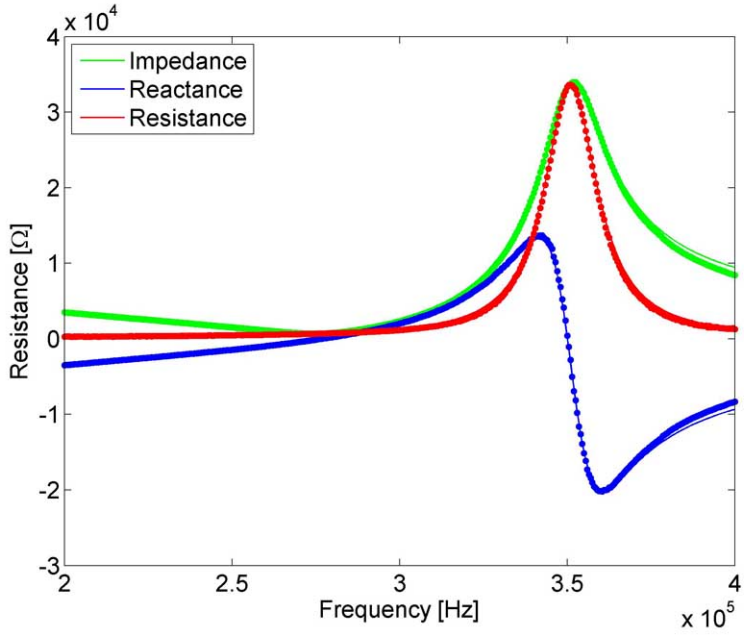

Figure 3.9: Single Element Piezocompsite Transducer with SADM Backing Impedance

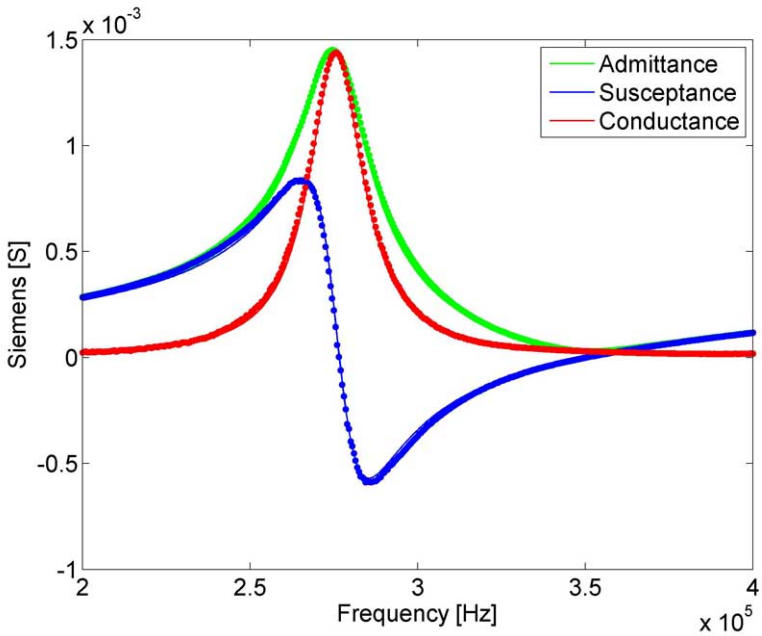

Figure 3.10: Single Element Piezocompsite Transducer with SADM Backing Admittance

As seen from figures 3.9 and 3.10, the theoretically determined and experimentally measured values are in very close agreement with each other.

Next, the same transducer structure given in figure 3.8 is used, but with the surface area A_o doubled. This is done by connecting two of the single piezocomposite elements in parallel. The following material parameters are determined for this two element structure:

$A_o = 223.89$	$[mm^2]$
$L = 5.12$	$[mm]$
$\rho = 7300$	$[kg/m^3]$
$c_{33}^D = (94.3 + 2.8j)$	$[GPa]$
$K_{33}^S = (446.9 - 20j)$	$[\ \ ]$
$h_{33} = (3.21 + 0.094j)$	$[GV/m]$
$\rho_{SADM} = 2000$	$[kg/m^3]$
$v_{SADM} = 524$	$[m/s]$

Not only is A_o different, but differences occur in h_{33} and the loss term in K_{33}^S.

The reason for these differences is that every transducer element has material variations even if they are constructed in the same way using equivalent processes. For the piezocomposite element, differences in measurement could easily be due to the concentration and orientation of the piezoelectric fibers embedded in the epoxy of the piezocomposite material.

The comparison of the theoretically determined impedance and admittance curves with the experimentally determined curves for the two element structure are shown in figures 3.11 and 3.12.

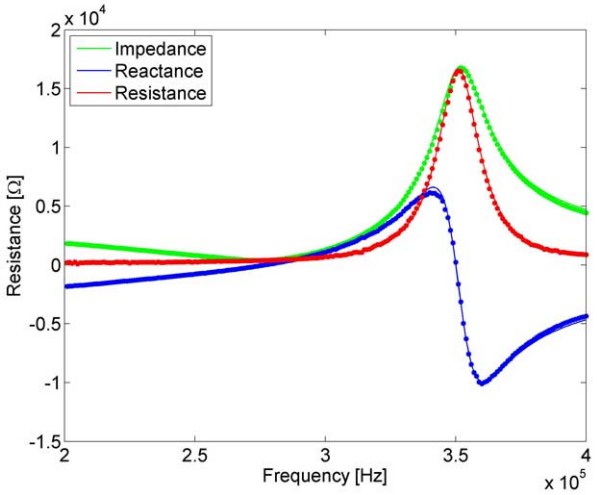

Figure 3.11: Two Element Piezocompsite Transducer with SADM Backing Impedance

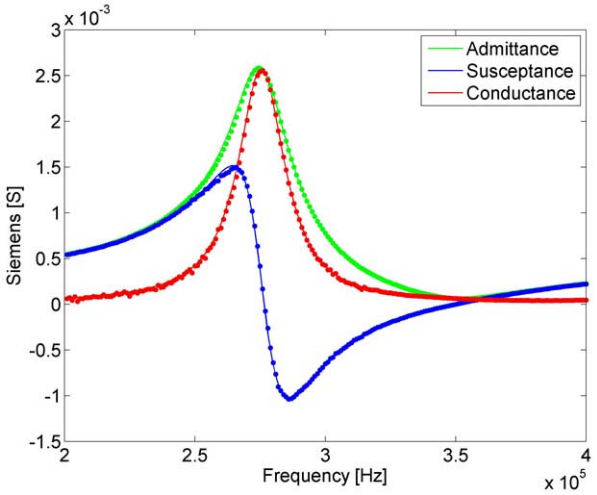

Figure 3.12: Two Element Piezocompsite Transducer with SADM Backing Admittance

As seen from figures 3.11 and 3.12, excellent agreement between the theoretically and experimentally determined values is obtained.

3.2.4. Matched Piezocomposite Transducer

A comparison is made between the theoretically and experimentally determined impedance and admittance curves for the piezocomposite transducer shown in figure 3.13.

Figure 3.13: Piezocomposite Transducer

The piezocomposite transducer illustrated in figure 3.13 contains a 3 layer structure composed of a matching layer, the piezocomposite layer, and a backing layer made of SADM. This is the same structure as that of the Matched transducer developed in section 2.7. The surrounding structure of the piezocomposite transducer is composed of polyurethane and SADM material. Since the SADM material is a very good acoustic absorber, it is assumed to act as an infinite medium. Therefore, any waves that enter this material are considered to completely dissipate.

The material parameters used to model this transducer are given by the following values:

$$A_o = 173.52 \qquad [mm^2]$$
$$\rho_{load} = 1.21 \qquad [kg/m^3]$$
$$v_{load} = 324 \qquad [m/s]$$

$\rho_{mtch} = 1300$	$[kg/m^3]$
$v_{mtch} = (4100 + 400i)$	$[m/s]$
$L_{mtch} = 3.1$	$[mm]$
$L = 5.3$	$[mm]$
$\rho = 7750$	$[kg/m^3]$
$c_{33}^D = (108 + 15j)$	$[GPa]$
$K_{33}^S = (950.9 - 50j)$	$[\ \ ]$
$h_{33} = (1.81 + 0.1j)$	$[GV/m]$
$\rho_{SADM} = 2000$	$[kg/m^3]$
$v_{SADM} = 524$	$[m/s]$

The theoretical impedance and admittance curves for the transducer in figure 3.13 are obtained using the theory developed in section 2.7.1, with $L_p = 0$.

Using the material parameters, together with the experimentally measured impedance and admittance curves, a comparison between the theoretically predicted and experimentally measured curves is shown in figures 3.14 and 3.15.

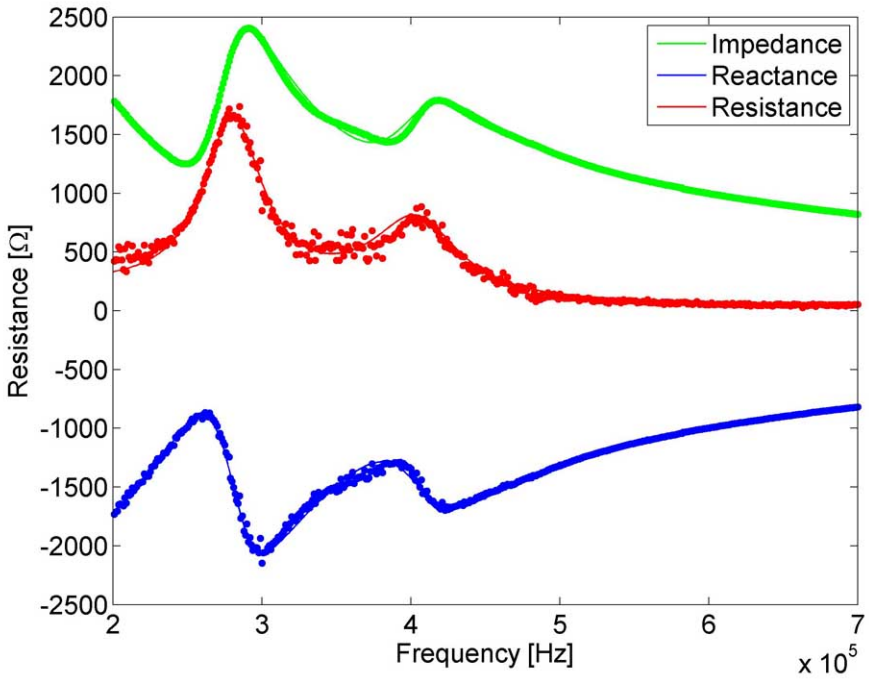

Figure 3.14: Piezocomposite Transducer Impedance

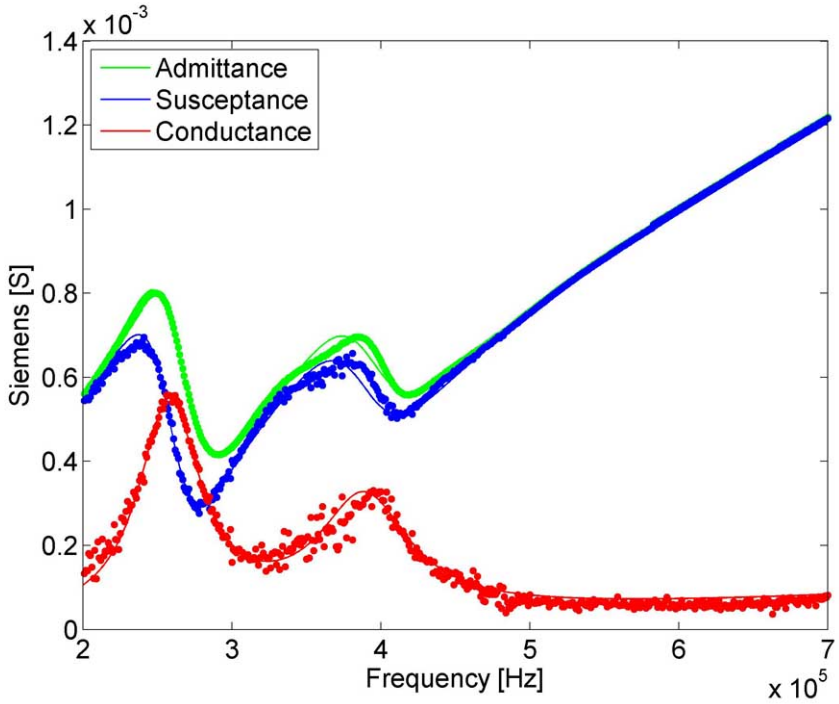

Figure 3.15: Piezocomposite Transducer Admittance

Figures 3.14 and 3.15 show that a good match is obtained between the experimentally measured and theoretically predicted curves. The admittance curve contains a minor variation between about 350kHz and 400kHz resulting from any number of factors. One such factor may be that there are other longitudinal and width modes in operation effecting the thickness mode operation of the transducer. Also, note that the SADM material is a granular structure containing rubber and lead compounds. This is not a homogeneous material; therefore, standing waves may be present at these frequencies that are not accounted for by the developed impedance/admittance equations. It is also possible that the material parameters in the transducer are frequency dependent.

3.3. Conclusion of the Experimental Validation of the Impedance Model

The impedance and admittance models developed in section 2.7.1 have been verified using the measured impedance and admittance curves for a number of different transducers. It was also successfully shown that using the impedance and admittance data with the material parameter constraints, that it is possible to determine the material

parameters of a transducer if the geometric dimensions of the transducer are known.

In order to show whether effects unrelated to the thickness mode operation are present, or if the material parameters are frequency dependent, a visual comparison of the measured and theoretical impedance and admittance values should be performed. If it is found that the theoretical values do not match the experimental values, then either the material parameters are frequency dependent, or the transducer is not operating strictly in thickness mode.

4. Sensitivity Measurement

Experimental verification of the sensitivity expression of the XTM transducer, introduced in section 2.7.4, is presented in this chapter.

Many methods can be used to experimentally measure the sensitivity of an acoustic transducer, as shown in section 4.1. However, in this case the Reciprocity Measurement method is used to determine the sensitivity of the XTM transducer since the instrumentation and transducers required for this method are available at the facility used to conduct the sensitivity measurement.

The steps necessary to conduct the Reciprocity Measurement are presented in section 4.3 and the experimental setup used for this is illustrated in section 4.4. Associated error sources, as well as methods of error reduction for measurements made are included throughout the section.

Measurements made using the Reciprocity Measurement method require complex experimental instrumentation and test facilities, motivating the need for a theoretical method to determine the sensitivity of an acoustic transducer. A detailed theoretical analysis of the Reciprocity Measurement method is therefore made in section 4.1. The theory of the Reciprocity Measurement presented clearly shows the assumptions that must be made in order to obtain accurate sensitivity measurements.

Measured values are presented in section 4.5 and it can be seen that these experimentally measured sensitivity values agree closely with the theoretically predicted sensitivity values of the XTM transducer. Therefore, it is concluded that the sensitivity theory developed in section 2.7.4 is valid.

4.1. Sensitivity Measurement Methods for Acoustic Transducers

Of the methods used to measure the sensitivity of a transducer, some require complex experimental setups, while others are easy to perform but require complicated theoretical development. Table 4.1 lists the commonly used methods to determine the sensitivity of a transducer. This table is taken from the book, Principles of Underwater Sound written by Urick [1].

Method	Advantages	Disadvantages
Reciprocity (a) Spherical (b) Cylindrical (c) Plane (d) Self-Reciprocity	Standards not required; absolute method	Lengthy; complex; requires reciprocal transducer
Pulse Calibration	Reduces effect of reflections and standing waves	Elaborate Equipment Required
Impedance Calibration	Tank or body of water not required	Complex data reduction
Comparison	Simple and fast	Not absolute method, requires calibrated transducer

Table 4.1: Methods to Measure the Sensitivity of an Underwater Acoustic Transducer

The most common method used is the Comparison Method which requires access to a calibrated transducer. Another option utilized is the Reciprocity Method, in which no calibrated transducer is necessary. To perform the sensitivity measurement, the Reciprocity method is used, but the Comparison method is also discussed since it is a popular method used for transducer sensitivity calibration.

4.2. Comparison Method

The comparison method is a relatively quick and easy method used to determine the sensitivity of a transducer. To conduct the sensitivity measurement, a calibrated omnidirectional transducer is placed a distance d from the transducer being tested. This calibrated transducer is used to create an acoustic pulse which is received by the uncalibrated transducer. The voltage output from the receiving transducer is then compared with the characteristics of the transmit voltage response of the calibrated transducer to determine the sensitivity of the uncalibrated transducer.

A serious issue with this method, however, is that one must have a transducer that is guaranteed to be calibrated. This requirement presents a problem as the properties of a transducer depend on many factors such as temperature, pressure, and time. In order to guarantee that the transducer in question is actually calibrated, it must be recalibrated regularly.

4.3. Reciprocity Method

The reciprocity method utilizes three uncalibrated transducers to determine the sensitivity of a single transducer. Since the hydrophone sensitivity is determined without a calibrated transducer, this method is an absolute calibration. The method relies on the electroacoustic reciprocity principle used to relate the receiving sensitivity M, with the transmitting response S. These quantities are related through the constant J, known as the reciprocity parameter [2]. The electroacoustic reciprocity principle is defined by equation 4.1 [1]:

$$\frac{|E|}{|v|} = \frac{|F|}{|I|} \tag{4.1}$$

The parameter $|E|$ is the open-circuit voltage magnitude obtained from the transducer when the face of the transducer is driven with a sinusoidal velocity of magnitude $|v|$. $|F|$ is the magnitude of the applied sinusoidal force on the face of the transducer, and $|I|$ is the magnitude of the closed-circuit output current from the transducer that results from the applied force $|F|$. If a transducer is reciprocal, then it must satisfy equation 4.1.

A discussion of the steps necessary to perform the reciprocity measurement method is given in section 4.3.3.

4.3.1. Reciprocity Parameter

As mentioned above, the reciprocity parameter J relates a transducer's transmit response S with its receiving sensitivity M. The book, Underwater Electroacoustic Measurements written by Bobber, gives an excellent explanation of how the parameter J is defined, as well as its characteristics [29]. As explained in Bobber, the parameter J depends on the acoustic medium, frequency, and boundary conditions of the transducer being measured. The reciprocity parameter J, is however, independent of the mechanical details of the transducer such as its dimensions and material properties. To be reciprocal, a transducer must be linear, passive, and reversible. It should be mentioned that there is presently no known way to prove if a transducer is reciprocal, however, methods do exist to ascertain the probability of a transducer being reciprocal. For the reciprocity calibration performed in this chapter, the spherical wave reciprocity parameter defined by equation 4.2 is utilized [2].

$$J_s \equiv \frac{M}{S} = \frac{2r}{\rho_o f} \tag{4.2}$$

The parameter r is the distance between the transmit transducer and the receive transducer, ρ_o is the density of the acoustic medium in which the reciprocal measurement is being done, and f is the frequency the measurement is being conducted at. In order for J_s to be valid, the pressure pattern of the transmit transducer must follow a spherical spreading law [1]. Spherical spreading occurs when the sound intensity decreases proportionally to $1/r^2$, or the pressure decreases proportionally to $1/r$. This occurs when the receive transducer is in the far-field region of the transmit transducers pressure waveform. This condition must be checked before the measurement is made.

Furthermore, for the parameter J_s to be valid, the transmit response S and receive sensitivity M must be obtained in the free-field region where no boundaries are present. The method of using a pulsed waveform to mitigate the issue of having boundaries present is discussed in section 4.4.1.

4.3.2. Reciprocity Check

The Reciprocity Method requires at least one transducer to satisfy the reciprocity condition. Bobber introduces the following test to check if the reciprocity condition fails [29]. The test requires two transducers, T_1 and T_2. The transducers are placed in the test tank and their acoustic axes are aligned to face each other. This allows the maximum transmit and receive response to be obtained from each transducer, as well as reducing the effects each transducer's beam pattern has on the measurement. T_1 is driven with a current I_1, and the open-circuit voltage V_2 obtained from T_2, is recorded. Without changing the positions or boundary conditions of the test, signal directions are switched by driving T_2 with a current I_2 and recording the open-circuit voltage V_1 from transducer T_1. If the two transducers are indeed reciprocal, then the following relationship between the measured quantities must hold:

$$\frac{V_2}{I_1} = \frac{V_1}{I_2} \tag{4.3}$$

It should be noted that this test is reliable if T_1 and T_2 are dissimilar transducers. If, for example, they are the same, they may contain the same nonlinear effects which cause the above relationship to be true, when in fact, neither transducer is reciprocal. Note that just because two dissimilar transducers satisfy the relationship above, it

does not prove that they are reciprocal, it merely suggests they are reciprocal.

4.3.3. Theory of Reciprocity Calibration

The theory necessary to perform the Reciprocity Calibration is presented in this section. The method is well known and is discussed in a number of texts [1, 2, 29]. The derivation presented in Albers is followed here [2]. In order to perform a reciprocity calibration, three transducers are required, of which at least one is reciprocal. Three transducers, H, P, and T are defined as follows; transducer H performs as a hydrophone and is only used to receive an acoustic signals, P is a projecting transducer, and T is the reciprocal transducer which both, transmits and receives signals. Three measurements are necessary to obtain enough information to find the sensitivity, M_H, of H. A fourth measurement is taken to determine the validity of the reciprocity requirement of transducer T.

Reciprocity Calibration Step#1

In the first step, P and H are aligned so their acoustic center of axes is coincident and have a separation distance of r_1. P is driven with a current I_1. The pressure on the face of H, produced from P, is p_{r_1}. The assumption is made that r_1 is large enough that when the pressure field produced by P reaches H, it satisfies the spherical spreading requirement explained in section 4.3.1. The following expressions for the transmit current response of P, and the receive sensitivity of H are given by.

$$M_H = \frac{v_H}{p_{r_1}} \tag{4.4}$$

$$S_P = \frac{p_{r_1} r_1}{I_1} \tag{4.5}$$

v_H is the open-circuit voltage produced by H from the pressure p_{r_1}. Combining the above equations, the following expression is obtained.

$$S_P M_H = \frac{p_{r_1} r_1}{I_1} \frac{v_H}{p_{r_1}} = \frac{v_H r_1}{I_1} \tag{4.6}$$

Reciprocity Calibration Step#2

P and T are aligned so their acoustic center of axes are coincident and their separation distance is r_2. P is driven with a current I_2 such that the pressure produced on the face of T is p_{r_2}. Again, r_2 is assumed large enough that when the pressure waves produced from P reach T, they obey the spherical spreading requirement. The expressions for

the sensitivity of T, and the transmit current response of P are given below.

$$M_T = \frac{v_T}{p_{r_2}} \tag{4.7}$$

$$S_P = \frac{p_{r_2} r_2}{I_2} \tag{4.8}$$

v_T is the open-circuit voltage produced by T from the pressure p_{r_2}. Combining equations 4.4 and 4.7 for M_H and M_T, the following expression is obtained.

$$\frac{M_H}{M_T} = \frac{v_H}{p_{r_1}} \frac{p_{r_2}}{v_T} = \frac{v_H}{v_T} \left(\frac{p_{r_2}}{p_{r_1}} \right) \tag{4.9}$$

Reciprocity Calibration Step#3

T and H are aligned so their acoustic center of axes are coincident and have a separation of r_3. T is driven with a current I_3 such that the pressure produced on the face of H is p_{r_3}. Once again, r_3 is assumed large enough that when the waves produced from T reach H, the spherical spreading requirement is satisfied. The following expressions for the sensitivity of H and transmit current response of T are given by.

$$M_H = \frac{v'_H}{p_{r_3}} \tag{4.10}$$

$$S_T = \frac{p_{r_3} r_3}{I_3} \tag{4.11}$$

The value v'_H is the open-circuit voltage produced from H from the pressure p_{r_3}. Combining the above expressions for M_H and S_T, the following relation is obtained.

$$S_T M_H = \frac{p_{r_3} r_3}{I_3} \frac{v'_H}{p_{r_3}} = \frac{v'_H r_3}{I_3} \tag{4.12}$$

Now using equations 4.6 and 4.12, the following expression for S_P/S_T is obtained.

$$\frac{S_P M_H}{S_T M_H} = \frac{S_P}{S_T} = \frac{v_H r_1}{I_1} \frac{I_3}{v'_H r_3} = \frac{v_H}{v'_H} \frac{r_1 I_3}{r_3 I_1} \tag{4.13}$$

With the above equations and the spherical reciprocity parameter, an expression for M_H containing M_T is determined from equation 4.9. As well, an expression for S_P is determined using equation 4.12.

$$M_H = M_T \frac{v_H}{v_T} \left(\frac{p_{r_2}}{p_{r_1}} \right) \tag{4.14}$$

$$S_P = S_T \frac{v_H}{v'_H} \frac{r_1 I_3}{r_3 I_1} \tag{4.15}$$

These equations are multiplied to obtain.

$$S_P M_H = S_T \frac{v_H}{v'_H} \frac{r_1 I_3}{r_3 I_1} * M_T \frac{v_H}{v_T} \left(\frac{p_{r_2}}{p_{r_1}} \right) \tag{4.16}$$

Now equations 4.6 and 4.16 are used to solve for the expression $S_T M_T$ as shown.

$$S_T \frac{v_H}{v'_H} \frac{r_1 I_3}{r_3 I_1} * M_T \frac{v_H}{v_T} \left(\frac{p_{r_2}}{p_{r_1}} \right) = \frac{v_H r_1}{I_1} \tag{4.17}$$

$$S_T M_T = \frac{v'_H v_T p_{r_1} r_3}{v_H I_3 p_{r_2}} \tag{4.18}$$

To determine an expression for M_T, the reciprocity requirement of T is used with equation 4.18 for $S_T M_T$ as follows.

$$J_S = \frac{M_T}{S_T} \implies S_T = \frac{M_T}{J_S} \tag{4.19}$$

$$\frac{M_T^2}{J_S} = \frac{v'_H v_T p_{r_1} r_3}{v_H I_3 p_{r_2}} \tag{4.20}$$

$$M_T = \sqrt{J_S \frac{v'_H v_T p_{r_1} r_3}{v_H I_3 p_{r_2}}} \tag{4.21}$$

An expression for M_H is determined using equations 4.14 and 4.21.

$$\begin{aligned} M_H &= \frac{v_H}{v_T} \left(\frac{p_{r_2}}{p_{r_1}} \right) \sqrt{J_S \frac{v'_H v_T p_{r_1} r_3}{v_H I_3 p_{r_2}}} \\ &= \sqrt{J_S \frac{v'_H v_H p_{r_2} r_3}{v_T I_3 p_{r_1}}} \end{aligned} \tag{4.22}$$

Notice that p_{r_1} is functionally dependent on the values of I_1 and r_1. As well, p_{r_2} is functionally dependent on the values of I_2 and r_2. To simplify the calibration procedure, all measurements are conducted using the same separation distance r, and drive current I. Therefore, $I = I_1 = I_2 = I_3$ and $r = r_1 = r_2 = r_3$ in which case $p_{r_1} = p_{r_2}$. This allows the expression of M_H to be given by equation 4.23.

$$M_H = \sqrt{J_S \frac{v'_H v_H r}{v_T I}} \tag{4.23}$$

To find the receive sensitivity of a transducer, one requires three voltage measurements, the distance between transducers, the drive current, the appropriate reciprocity parameter, and equation 4.23.

Reciprocity Calibration Step#4: Reciprocity Check

To validate the results of the measurements made in the previous steps, the reciprocity requirement of transducer T must be checked. A quick way to do this is to conduct the following measurement to determine v_P. Align transducer T and P along their acoustic center axis with a separation distance r. Now drive transducer T with a current I and record the open-circuit output voltage v_P, of transducer P. In order for transducer T and P to be considered reciprocal, the following relation must be true:

$$\frac{v_P}{I} = \frac{v_T}{I} \implies v_P = v_T \tag{4.24}$$

Note that v_T is determined in Step#2 of the Reciprocity Calibration.

4.4. Experimental Setup for Sensitivity Measurement

The reciprocity calibration was carried out in a tank with dimensions $< 4, 4, 2 >$ meters corresponding to $< \text{length}, \text{width}, \text{height} >$. The transducers used for the reciprocity calibration are presented in figure 4.1.

In order to keep the same naming convention as that used in the reciprocity calibration theory, table 4.2 shows the naming scheme for the corresponding transducers in figure 4.1.

MARPORT_182kHz_PROTO	$\Longleftrightarrow$	T
AIR 214kHz	$\Longleftrightarrow$	H
Air 212kHz	$\Longleftrightarrow$	P

Table 4.2: Naming Convention for Transducers used in Reciprocity Calibration

As a summary, the diagram in figure 4.2 shows the steps necessary to conduct the reciprocity calibration.

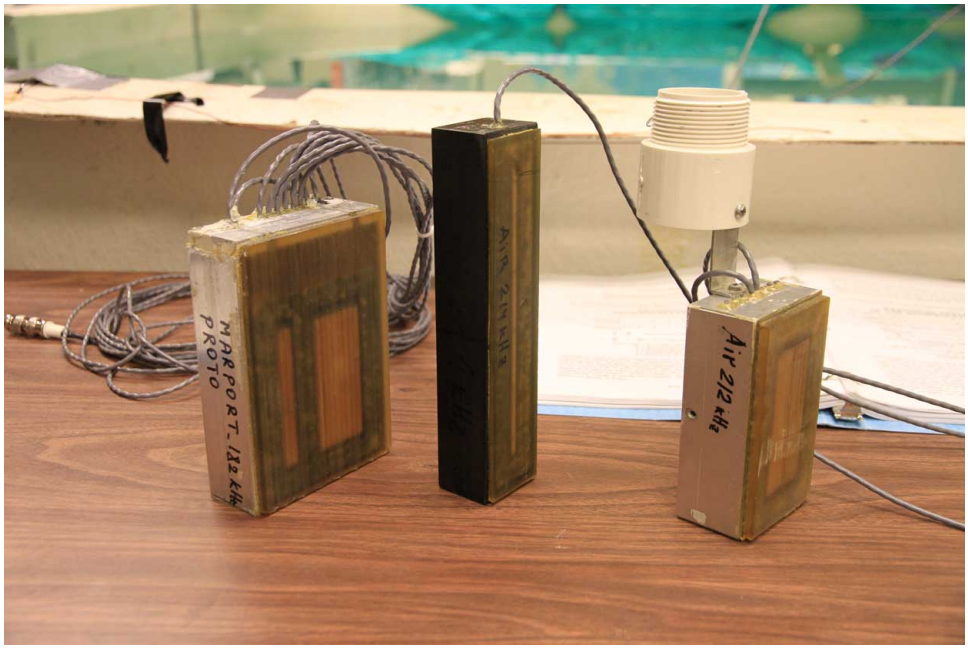

Figure 4.1: Transducers used to conduct the Reciprocity Calibration
[Left→Right: MARPORT_182kHz_PROTO, AIR 214kHz, Air 212kHz]

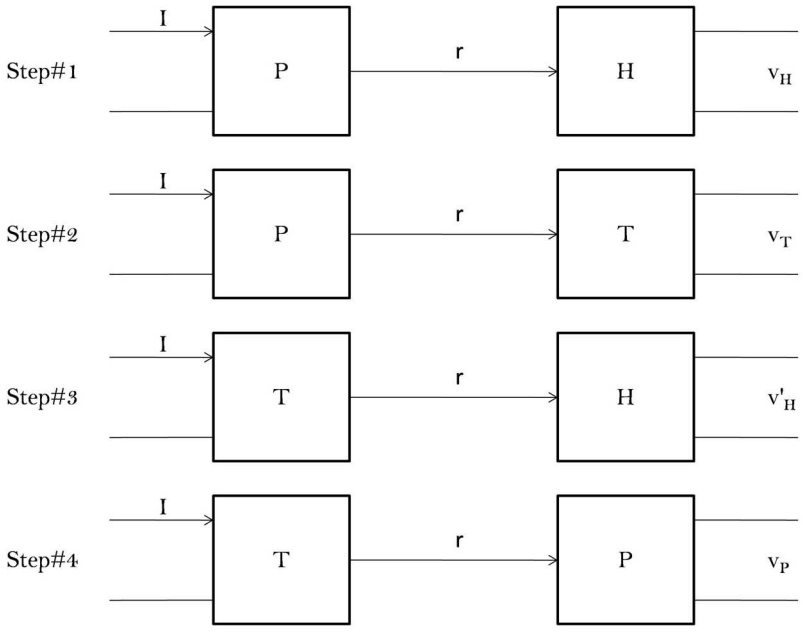

Figure 4.2: Outline of the Measurements Needed for Reciprocity Calibration

Each of the measurements in figure 4.2 is carried out using the same procedure. Therefore, only the analysis of Step#1 of the reciprocity calibration is presented in sections 4.4.1 to 4.4.4.

4.4.1. Geometric Setup

The geometric setup of the test tank and the transducer placement is important to ensure that the test is being conducted such that the free-field and far-field conditions are satisfied. In this section, experimental methods used to conduct measurements at steady-state in a finite sized test tank are presented.

For the reciprocity parameter to be valid, a medium that is homogeneous, isotropic, and free of boundaries is required. Of course, there is no such test facility available. Reflecting boundaries, temperature gradients, gas bubbles, other sources of acoustic and electromagnetic interference as well as many other effects are all present during any acoustic measurement. The goal is to set up a test condition that allows sufficiently accurate results to be obtained without the need for a large test tank. The tank used here to conduct the reciprocity calibration is not treated with anechoic material. Therefore, when conducting the measurements, reflections are present from the surface and walls of the tank.

A common method used to mitigate the problem of boundary conditions is to use a pulsed transmission and receive method. In this method, the transducer being used to project the sound is driven by a short finite cycle pure-frequency pulse. As long as the transmit transducer and receive transducer have a sufficient amount of time to reach steady-state before any reflections arrive, then the problem of a finite sized test tank can be mitigated. The theory associated with the length of the rise time and ring time of the transducer is presented in chapter 5.

4.4.2. Hydrophone Voltage Response Pattern

The hydrophone voltage response pattern is used to determine the magnitude of the steady-state output voltage from the hydrophone when excited by an incoming pressure waveform. The amount of time it takes for the hydrophone to reach a steady-state value depends on the rise time and steady-state section of the pressure waveform as well as on the hydrophone's rise time characteristics. The amount of time it takes for the hydrophone voltage response pattern to reach steady-state must be shorter than the time it takes for interference pressure waveforms from reflections to reach the hydrophone. It is useful to look at the response patterns of the receiving hydrophone

to illustrate the steady-state requirement. The response of a receive transducer when excited by a transmitted pulse is shown in figure 4.3.

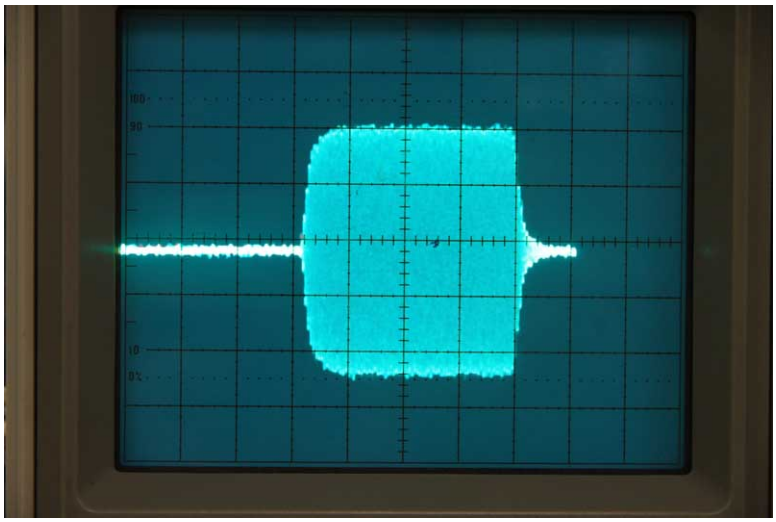

Figure 4.3: Response of Transducer when excited by a pressure wave

As seen from figure 4.3, there is an initial transitory period at the start of the waveform which increases in an approximately exponential fashion. A steady-state is then reached in which the magnitude of the signal amplitude does not vary with time. After the drive pressure has stopped, there is a relaxation period where the amplitude of the waveform decreases in an approximately exponential fashion. All of the measurements must be done in the steady-state region of the waveform where no interfering waveforms from reflections occur.

4.4.3. Geometry of the Test Tank

When a pulse is sent from the transmit transducer to the receive transducer, multiple reflections occur in the test tank. The primary pressure wave is the one which hits the hydrophone first. It has the shortest path length from the transmitter to the receiver and is the only signal that should excite the receive transducer during the measurement.

To ensure no unwanted signals resulting from reflections interfere with the measurement, major contributors that could cause interference must be determined. The amount of time it takes for these interference signals to reach the receive transducer must be larger than the amount of time it takes to complete the steady-state voltage measurement.

The interference signals are caused by signal reflections from the walls, bottom, and surface of the tank. Figure 4.4 shows how the surface and bottom reflections interfere with the primary signal.

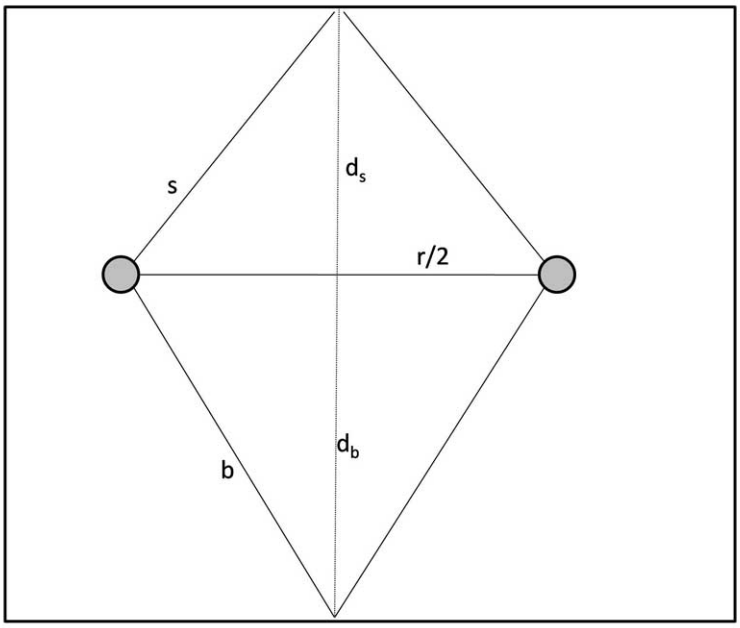

Figure 4.4: Reflections from Surface and Bottom

Table 4.3 lists the length of each acoustic path and the travel time of the pressure signals in figure 4.4.

	Route	**Distance**	**Time**
Direct Path	r	r	r/c
Surface Reflection	s	$2\sqrt{(d_s^2+(\frac{r}{2})^2)}$	$2\sqrt{(d_s^2+(\frac{r}{2})^2)}/c$
Bottom Reflection	b	$2\sqrt{(d_b^2+(\frac{r}{2})^2)}$	$2\sqrt{(d_b^2+(\frac{r}{2})^2)}/c$

Table 4.3: Bottom and Surface Reflection Times in Test Tank, c is the acoustic speed in the medium

The wall-reflections that may cause measurement inaccuracies are shown in figure 4.5.

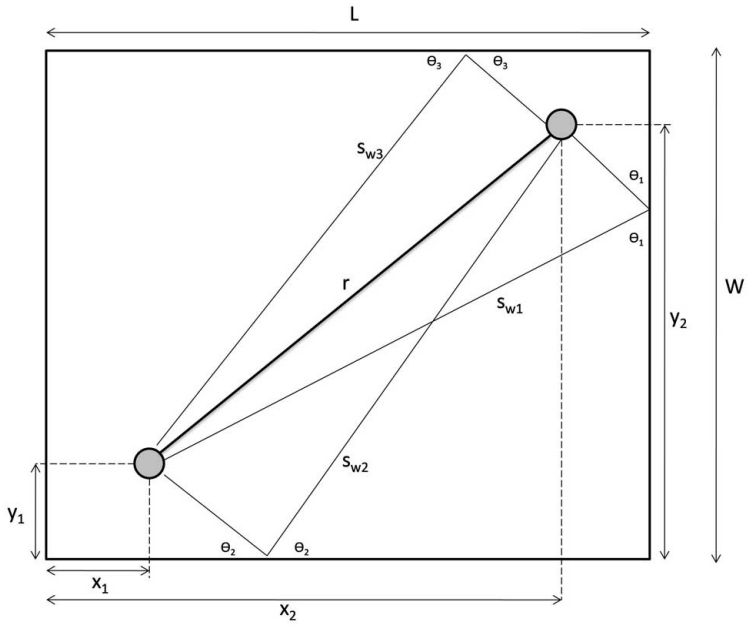

Figure 4.5: Reflections from the side walls of the tank

In order to determine the path lengths s_{w1}, s_{w2} and s_{w3}, the parameters (x_1, y_1), the position of the transmit transducer, and (x_2, y_2), the position of the receive transducer is introduced. $\theta_1, \theta_2,$ and θ_3 are the angles associated with the reflections that take place on the side walls. The equations for $\theta_1, \theta_2,$ and θ_3 and the acoustic path lengths, s_{w1} ,s_{w2} and s_{w3} are given below:

$$\theta_1 = tan^{-1}\Big(\frac{2L - x_1 - x_2}{y_2 - y_1}\Big) \tag{4.25}$$

$$s_{w1} = \frac{L - x_1}{sin(\theta_1)} + \frac{L - x_2}{sin(\theta_1)} \tag{4.26}$$

$$\theta_2 = tan^{-1}\Big(\frac{y_2 + y_1}{x_2 - x_1}\Big) \tag{4.27}$$

$$s_{w2} = \frac{y_1}{sin(\theta_2)} + \frac{y_2}{sin(\theta_2)} \tag{4.28}$$

$$\theta_3 = tan^{-1}\Big(\frac{2W - y_2 - y_1}{x_2 - x_1}\Big) \tag{4.29}$$

$$s_{w3} = \frac{W - y_1}{sin(\theta_3)} + \frac{W - y_2}{sin(\theta_3)} \tag{4.30}$$

The acoustic paths represented by s_{w1}, s_{w2} and s_{w3} limit the amount of time the primary pulse can be observed without any reflections causing interference with

the measurement. It is worth noting that if the projector has a very directional beam pattern, then the acoustic paths defined by s_{w1}, s_{w2} and s_{w3} may not effect the measurement significantly, but this is not the case for other interference paths. The next major source of error in the reciprocity method is the alignment of the transducers.

4.4.4. Alignment of the Transducers

One of the major sources of error in the reciprocity calibration is the alignment of both transducers such that their acoustic axes are coincident. Both transducer axes must be at the same depth. Since the maximum response is seen when the two acoustic axes of the two transducers are aligned, a pulse is sent through the water and the received response is observed. Then, by adjusting the orientation and height of the transducers, a search for the maximum receive response is conducted. Once found, the two transducers are aligned.

4.4.5. Determination of the Drive Current I

The instrumentation used to conduct the measurement allows a specific drive voltage to be specified for the transmit transducer. In addition, the complex input electrical impedance of each transducer can be determined by conducting a separate impedance measurement for each. Using the impedance of the transducer and the drive voltage, the current I can be determined using the following formula.

$$I = \frac{|V|}{|Z_{eq}|} \tag{4.31}$$

The parameter $|V|$ is the amplitude of the sinusoidal drive voltage, and $|Z_{eq}|$ is the magnitude of the complex impedance of the transducer being driven. Equation 4.31 is used to determine the drive voltage $|V|$ to ensure I remains constant throughout the measurement.

4.4.6. Determination of the Magnitude of the Steady-State Hydrophone Voltage Response

The open-circuit output voltage of the hydrophone is recorded beginning with the initialization of the drive pulse for the projector. A typical voltage response for the hydrophone resulting from the excitation pressure pulse is presented in figure 4.6. The instrumentation used to record the voltage response always samples the signal

at 8 times the frequency of the drive signal. In this case, the projector is being driven with a 210kHz sinusoidal pulse, which means the samples are obtained at a frequency of 1.68MHz. The Amplitude axis of figure 4.6 corresponds to the output of a 16-bit ADC converter used to measure the voltage response.

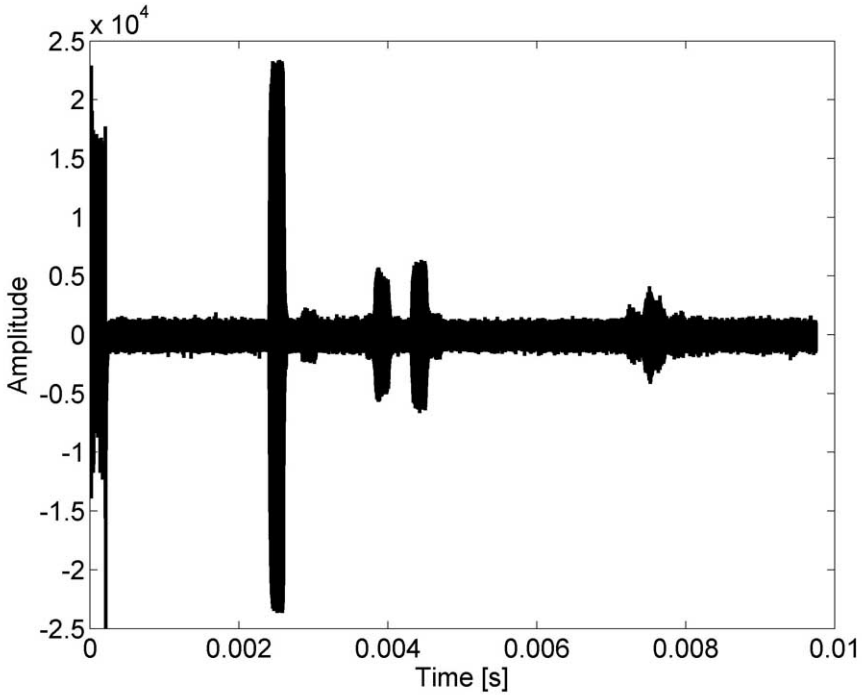

Figure 4.6: Open-Circuit Voltage response over entire test time for a 210kHz Pulse

Figure 4.6 shows that there is considerable noise present in the received signal. Note that a bandpass filter could be used to filter a significant amount of the unwanted noise. At the start of the received signal waveform, there is a large amount of interference picked up from the electromagnetic coupling between the transmit transducer cables and the receive transducers cables. This electromagnetic coupling does not effect the measurement. The largest amplitude waveform seen in the voltage response is the received signal resulting from the primary acoustic pulse. After the effects of the primary acoustic pulse have stopped, there are a number of other waveforms present in the voltage response resulting from pressure waves due to reflections. As seen, the waveform produced from the primary pressure pulse is isolated from all subsequent waveforms produced by reflections. This allows the steady-state value of the voltage waveform resulting from the primary acoustic pulse to be obtained easily.

The hydrophone response when the primary pulse reaches the hydrophone is pre-

sented in figure 4.7.

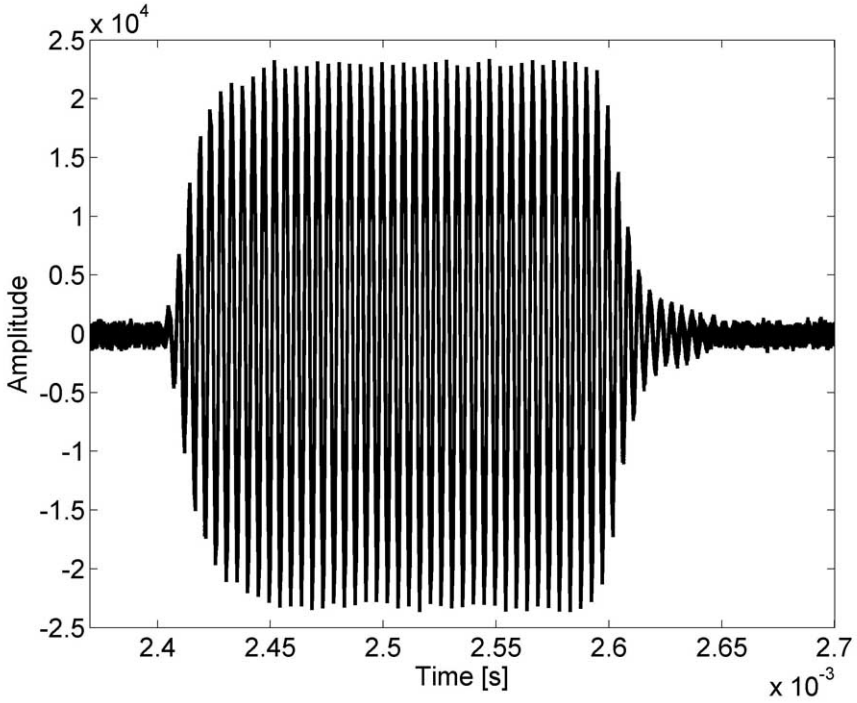

Figure 4.7: Open-Circuit Voltage response when first 210kHz Pulse reaches the hydrophone

The waveform in figure 4.7 shows the typical response of a transducer. The rise time, steady-state period, and ring time are all present and clearly visible.

The instrumentation used to send the pulse and record the hydrophone voltage response are coherent from pulse to pulse. If multiple measurements are performed at the same frequency, white noise can be significantly reduced by averaging the values over a number of trials.

The waveforms obtained by taking an average over 50 pulses are presented in figures 4.8 and 4.9.

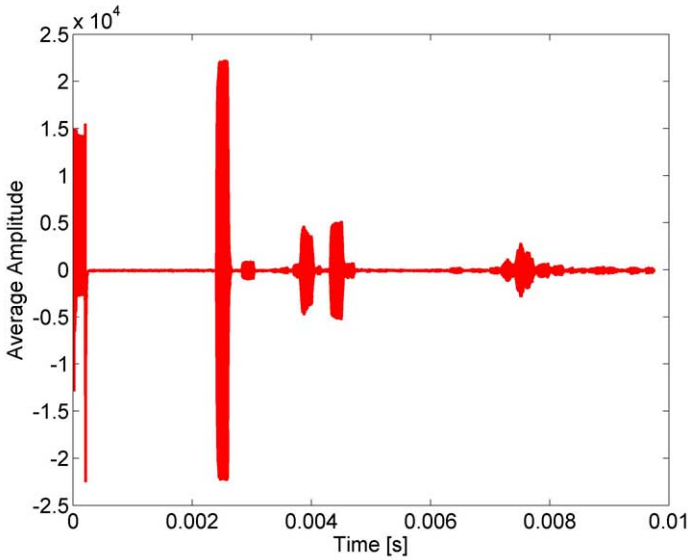

Figure 4.8: Open-Circuit Voltage response over entire test time for a 210kHz Pulse Averaged over 50 Pulses

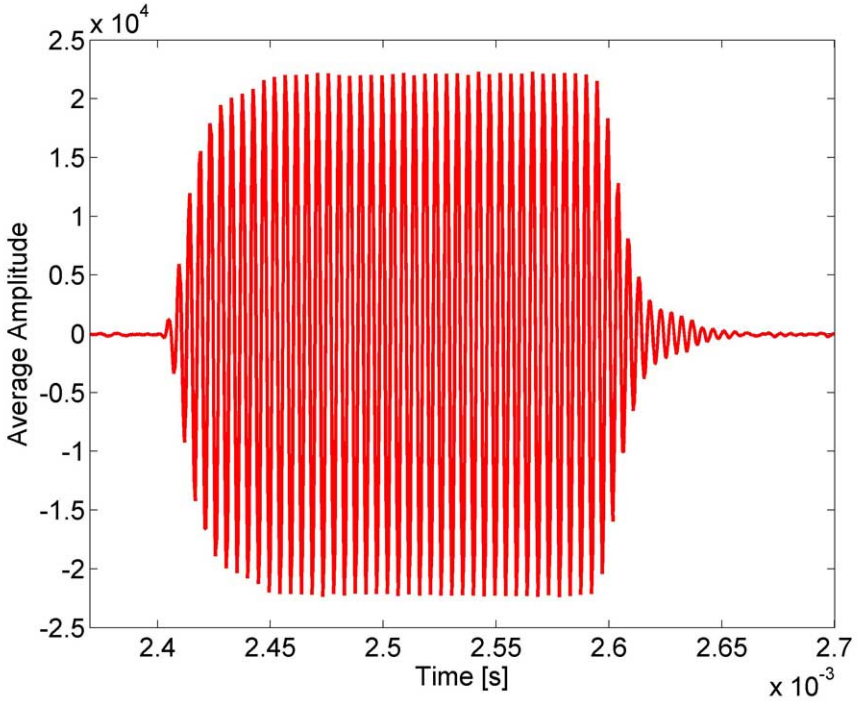

Figure 4.9: Open-Circuit Voltage response of the hydrophone for the first received Pulse at 210kHz Averaged over 50 Pulses

As seen from figures 4.8 and 4.9, better results are obtained if the measurement values are averaged over a number of pulses.

From figure 4.9, the rise time of the voltage response is about 10 cycles long and the ring time is approximately 14 cycles long.

To measure the steady-state hydrophone voltage response, two methods are used. The first method is to fit a sine curve to the steady-state region and determine the magnitude of the voltage response from the fit. The sine-fitting method is relatively simple because the frequency is known. The second method takes the magnitude of the in-phase and quadrature components of the received signal and determines the magnitude of the steady-state voltage response. The magnitude of the in-phase and quadrature components of the hydrophone voltage response resulting from a 210kHz pressure signal is given in figure 4.10.

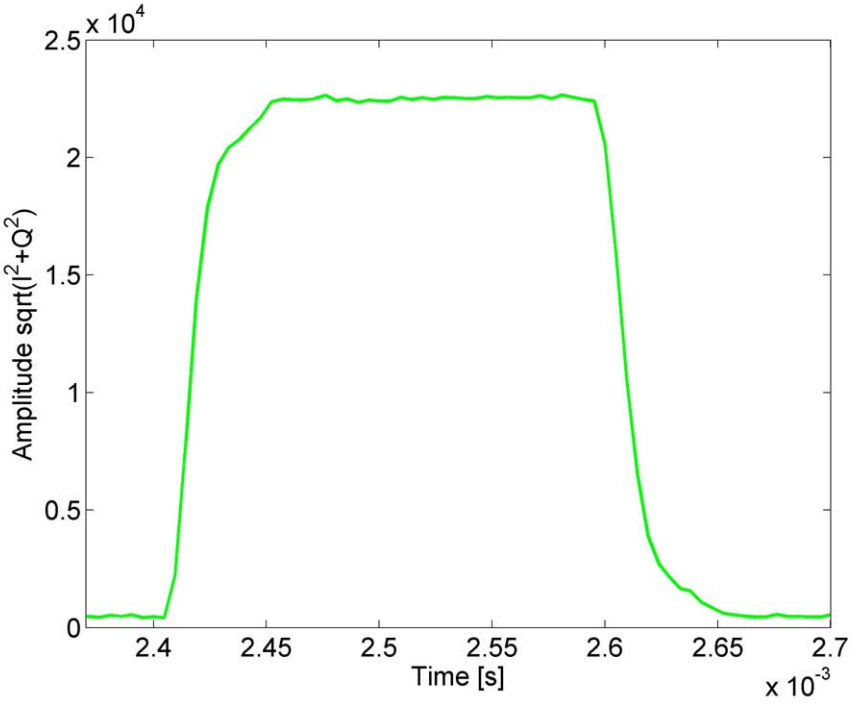

Figure 4.10: Average Magnitude of the Open-Circuit Voltage response of the hydrophone for the first received Pulse at 210kHz from the in-phase and quadrature components Averaged over 50 Pulses

Both the sine-fit and quadrature methods produce equivalent results for all frequencies measured in this sensitivity measurement.

4.4.7. Difficulties Associated with the Voltage Measurement

Situations arise which produce difficulties when conducting the steady-state voltage measurement. An example is given in figure 4.11. Here, the same transducer setup

from the previous section is used, but the measurement is made at a frequency of 260kHz.

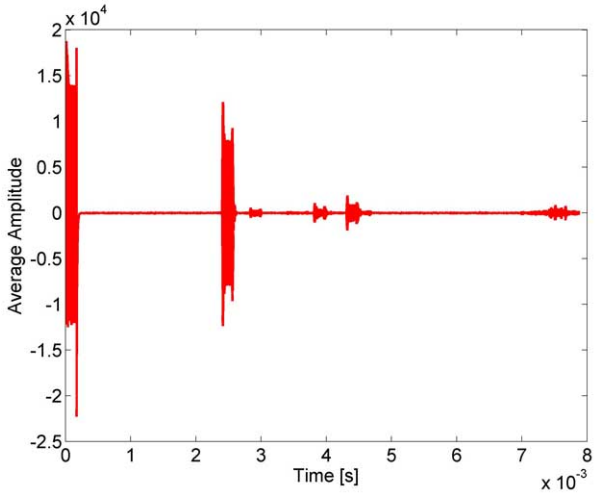

Figure 4.11: Average Magnitude of the Open-Circuit Voltage response of the hydrophone at 260kHz

The electromagnetic coupling is still present but does not interfere with the measurement. The difficulty in the voltage measurement arises because the rise time section no longer contains a uniform increase in amplitude. Therefore, care must be taken when determining the steady-state magnitude of the voltage output, as seen in figure 4.12.

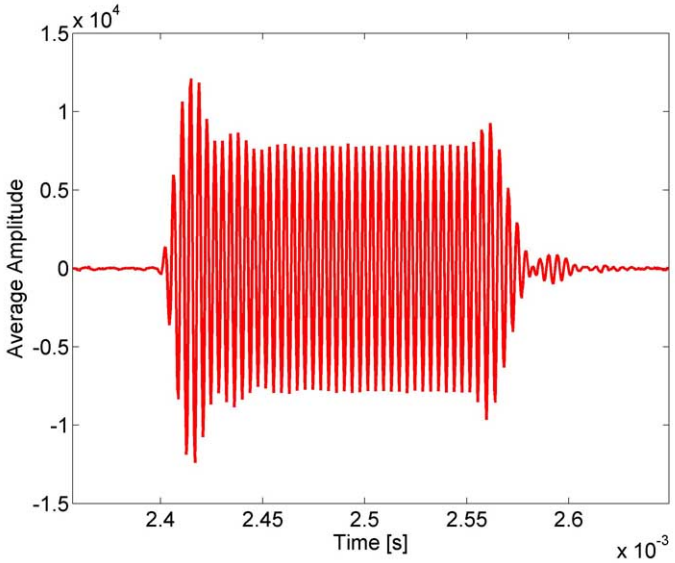

Figure 4.12: Magnitude of the Open-Circuit Voltage response of the hydrophone for the first received Pulse at 260kHz Average d over 50 Pulses

The initial rise time and ring time are clearly visible in figure 4.12. The frequency of 260kHz is located close to the anti-resonance frequency of the receive transducer. The pattern of the receive voltage is produced from the complex transient acoustic wave interactions that take place in the receive transducer from the applied pressure pulse. Although the transient effect is pronounced on the receive voltage, it is still possible to isolate the steady-state section of the waveform.

4.5. Experimental Results of Reciprocity Calibration

Having discussed the theoretical aspects of the reciprocity calibration, experimental setup, and the data acquisition methods, the results obtained from the reciprocity calibration are now presented. Figure 4.13 shows the theoretically and experimentally determined sensitivity for transducer H. The dots indicate the experimental values, and the solid lines indicate the theoretical values.

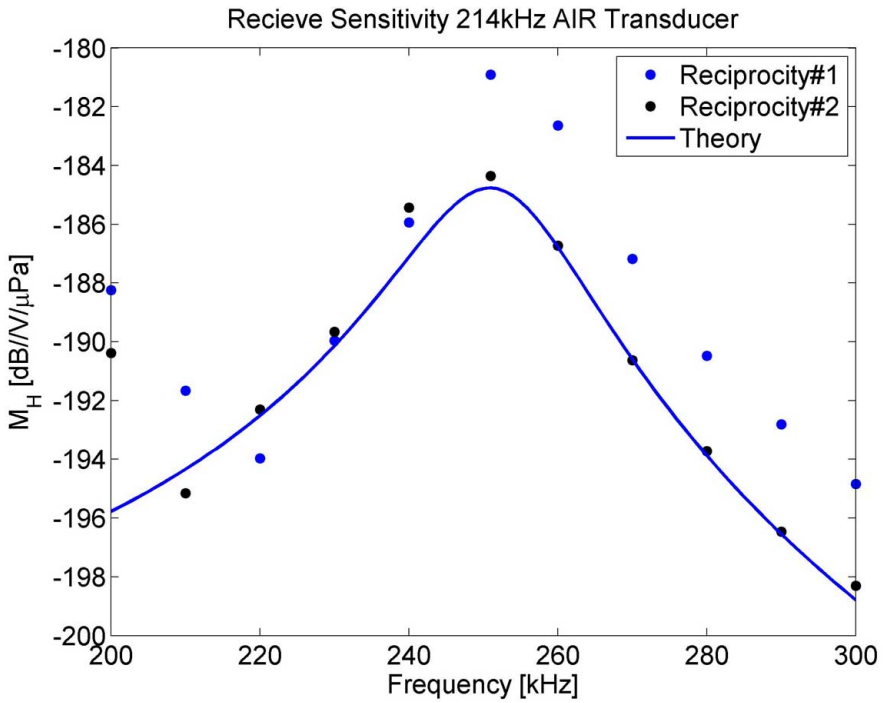

Figure 4.13: Sensitivity of Transducer H

Reciprocity#1, in figure 4.13, is determined using the measurements shown in figure 4.2 and using equation 4.23. Reciprocity#2 is determined using the same

measurements, except P is assumed to be the reciprocal transducer, in which case equation 4.32 is used to determine the sensitivity.

$$M_H = \sqrt{J_S \frac{v'_H v_H r}{v_P I}} \tag{4.32}$$

If T and P are reciprocal transducers, then the results of Reciprocity#1 and Reciprocity#2 should be equivalent.

One of the primary issues associated with the reciprocity calibration is the alignment of the acoustic axes. The acoustic axis of a single multi-element transducer is invariant as the frequency is varied. This is not the case for transducers containing a planar array of multi-element structures. Transducers P and T are both composed of a planar array of multi-element structures. Only a single multi-element structure of the multi-element array is used which causes the acoustic axis to change direction and the beam pattern to change shape when the frequency is varied. Notice that the largest deviation from the theoretical and experimental sensitivity varies by about 6dB//V/μPa. This variation can easily be caused by the misalignment of the acoustic center axis of the two transducers.

The results of the Reciprocity Check for transducers P and T is given in figure 4.14.

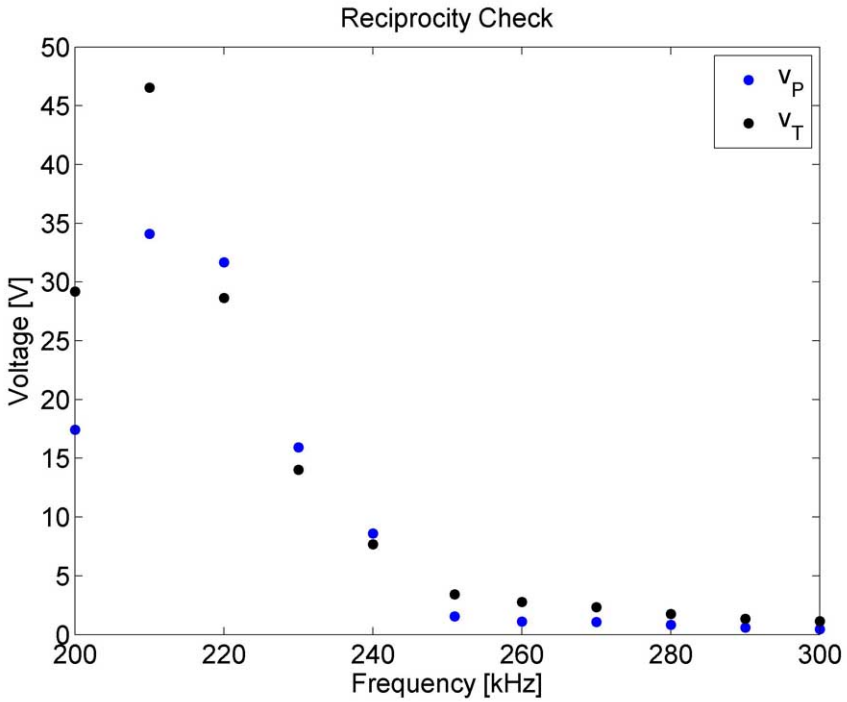

Figure 4.14: Reciprocity Check for Transducers P and T

If the two transducers are considered to be reciprocal, the values v_P and v_T in figure 4.14 must be the same. The variation between v_P and v_T may be caused by the beam pattern changing shape during the measurement. For the frequency values where the transducers P and T appear to be reciprocal, the theoretically determined and experimentally measured sensitivity are in close agreement with each other. This suggests that P and T may be reciprocal transducers, but only for a certain frequency range.

4.6. Conclusion of Sensitivity Measurement

This chapter shows the complexity associated with the conducting of sensitivity measurements. The theory and experimental techniques required to successfully measure the sensitivity using the reciprocity calibration method are presented in sections 4.3 and 4.4. The measured sensitivity is compared with the theoretically predicted sensitivity of an XTM transducer from section 2.7.4, and it is demonstrated that the sensitivity of a multi-layer acoustic transducer operating in thickness mode can be accurately obtained using the distributed sensitivity model. This allows for the rapid optimization of transducer designs, eliminating the need for sophisticated and costly experimental sensitivity measurements.

5. Transient Analysis Laplace Domain

In this chapter, the transient characteristics of a multi-layer acoustic transducer operating in thickness mode are developed in the Laplace domain. To obtain the time domain values, the numerical inverse Laplace transform routines given in appendix A are utilized.

Transient characteristics are important for transducer design and operation. For example, suppose that a transducer designer wants to maximize the obtainable resolution and wishes to utilize the resonance performance of the transducer when it is used as a transmitter and receiver. In order to increase the resolution of a transducer, the frequency of the transmit pulse must be increased [16]. Generally, the pressure pulses are sent sequentially to construct an image using the echoes of sent pulses. The difficulty is that the rise time and ring time must be small in order for the transducer to rapidly switch roles, as a transmitter and as a receiver. If the performance characteristics are defined, this allows the optimum mechanical design to be determined in order to reduce the number of cycles necessary to reach steady-state. These can then be reduced to the point where the resonance performance characteristics of the transducer can be utilized.

Not only can the mechanical design be tailored to obtain desired performance characteristics, but it also becomes possible to design the drive voltage to produce a desired output pressure. Sophisticated output pressure waveforms are required for a number of cutting-edge applications. In test facilities, pulses with low rise times and ring times are desirable [14, 15, 16]. For underwater communication, the Gaussian pulse is needed for optimum transmission through channels [15]. For Doppler tolerant applications, bionic pulses are used [30]. And, for high resolution applications, the zero-phase cosine magnitude pulse is preferred [17]. In order to output these waveforms using a multi-layer acoustic transducer operating in thickness mode, a routine is required that can account for the multi-layered structure.

The development of a novel routine that combines the versatility of a distributed model of the transducer with state-of-the-art numerical inversion routines is presented in this chapter. The Drive Voltage Design Method (DVDM) developed requires that only the material properties and geometric dimensions of the transducer need to be known in order to determine the drive voltage necessary to output a user defined pressure waveform. As is shown, this method is superior to other drive voltage design methods in that it accounts for the multi-layered structure of the transducer, is capable of outputting a general pressure waveform, and does not require any experimental measurements to be made of the transducer.

To determine the transient performance characteristics of a transducer, equations relating displacement, force, and voltage in a piezoelectric and non-piezoelectric element are used. In section 5.2, the development of the transient performance characteristics include the transient voltage output resulting from a pressure input ($TVOPI$), the transient pressure output resulting from a voltage input ($TPOVI$), and the voltage response of the transducer. The voltage response is developed because it is the easiest performance parameter to measure experimentally, and is therefore used to validate the transient theory.

The novel DVDM is derived in section 5.3.

5.1. Derivation of Transient Equations for a Piezoelectric Transducer

This section presents the basic transient equations describing the displacement and force in a non-piezoelectric element, as well as the displacement, force, and voltage occurring in a piezoelectric element. These expressions have already been developed in [6, 7]. Redwood's development is illustrated here because of the importance of these expressions in the development of the $TVOPI$, $TPOVI$, and voltage response for multi-layer acoustic transducers operating in thickness mode. To determine these expressions, Redwood uses the one-dimensional lossless wave equation and phenomenological equations of a piezoelectric element, given by equations 2.7, 2.26, and 2.27, re-presented below.

$$\frac{\partial^2 \xi(x,t)}{\partial t^2} = v^2 \frac{\partial^2 \xi(x,t)}{\partial x^2} \tag{5.1}$$

$$T_3(x,t) = c_{33}^D S_3(x,t) - h_{33} D_3(x,t) \tag{5.2}$$

$$E_3(x,t) = -h_{33} S_3(x,t) + \beta_{33}^S D_3(x,t) \tag{5.3}$$

v is the acoustic wave velocity in the material, and ξ is the displacement. To solve this set of equations, a set of boundary conditions must be specified. The most useful boundary conditions are given by the following set of equations describing the particle speed u, pressure P, and force F.

$$u(x,t) = \frac{\partial \xi(x,t)}{\partial t} \qquad \text{Particle Speed} \tag{5.4}$$

$$P(x,t) = -T_3(x,t) \qquad \text{Pressure} \tag{5.5}$$

$$F(x,t) = -A_o T_3(x,t) \qquad \text{Force} \tag{5.6}$$

Equations 5.1, 5.2, and 5.3, together with the boundary conditions, are transformed into the Laplace domain to construct the necessary equations of displacement, force, and voltage in a non-piezoelectric and piezoelectric element. Note that the non-piezoelectric element does not require an expression for voltage.

5.1.1. Laplace Domain Equation of Displacement for Non-Piezoelectric Element

To find the displacement in the non-piezoelectric element, the Laplace transform of equation 5.1 is performed.

$$\mathscr{L}[\xi(x,t)] = \bar{\xi}(x,s) = \int_0^\infty \xi(x,t) e^{-st}\, \mathrm{d}t \tag{5.7}$$

$$\mathscr{L}[\frac{\partial^2 \xi(x,t)}{\partial t^2}] = s^2 \bar{\xi}(x,s) - s\bar{\xi}(x,s) - \frac{\partial \xi(x,0)}{\partial t} \tag{5.8}$$

$$\mathscr{L}[\frac{\partial^2 \xi(x,t)}{\partial x^2}] = \frac{d^2 \bar{\xi}(x,s)}{dx^2} \tag{5.9}$$

The initial conditions of the non-piezoelectric element are set to zero, from which the Laplace domain expression of equation 5.1 is given by the following differential equation:

$$s^2\bar{\xi}(x,s) = v^2\frac{d^2\bar{\xi}(x,s)}{dx^2} \tag{5.10}$$

The general solution to this ordinary differential equation is given by equation 5.11.

$$\bar{\xi}(x,s) = A(s)\underbrace{e^{-\frac{s}{v}x}}_{\rightarrow} + B(s)\underbrace{e^{\frac{s}{v}x}}_{\leftarrow} \tag{5.11}$$

In equation 5.11, the arrow $\rightarrow$ indicates a wave traveling in the positive x direction. The arrow $\leftarrow$ indicates a wave traveling in the negative x direction. $A(s)$ and $B(s)$ are determined from the boundary conditions of the element. Note that for a non-piezoelectric element, $D_3 = 0$. The commonly used boundary conditions for a non-piezoelectric element are given by the following set of equations:

$$\bar{u}(x,s) = s\bar{\xi}(x,s) = s\Big[A(s)e^{-\frac{s}{v}x} + B(s)e^{\frac{s}{v}x}\Big] \tag{5.12}$$

$$\begin{aligned}\bar{P}(x,s) &= -Y\frac{d\bar{\xi}(x,s)}{dx} = -\frac{sY}{v}\Big[-A(s)e^{-\frac{s}{v}x} + B(s)e^{\frac{s}{v}x}\Big] \\ &= \frac{sZ}{A_o}\Big[A(s)e^{-\frac{s}{v}x} - B(s)e^{\frac{s}{v}x}\Big]\end{aligned} \tag{5.13}$$

$$\begin{aligned}\bar{F}(x,s) &= -A_o c_{33}^D\frac{d\bar{\xi}(x,s)}{dx} = -\frac{sc_{33}^D A_o}{v}\Big[-A(s)e^{-\frac{s}{v}x} + B(s)e^{\frac{s}{v}x}\Big] \\ &= sZ\Big[A(s)e^{-\frac{s}{v}x} - B(s)e^{\frac{s}{v}x}\Big]\end{aligned} \tag{5.14}$$

In equation 5.14, Z is the the characteristic acoustic impedance of the element and is given by $Z = \rho v A_o$.

5.1.2. Laplace Domain Equations of Displacement, Force, and Voltage of a Piezoelectric Element

First, the expression for $\bar{F}$ in a piezoelectric element is determined. The Laplace transform of equation 5.2 is shown below.

$$\begin{aligned}
&\mathscr{L}[T_3(x,t)] = \bar{T}_3(x,s) \\
&\mathscr{L}[S_3(x,t)] = \bar{S}_3(x,s) = \frac{d\bar{\xi}(x,s)}{dx} \\
&\mathscr{L}[D_3(x,t)] = \bar{D}_3(x,s) \\
&\bar{T}_3(x,s) = c_{33}^D \frac{d\bar{\xi}(x,s)}{dx} - h_{33}\bar{D}_3(x,s)
\end{aligned} \tag{5.15}$$

An expression for $\bar{\xi}$ and $\bar{D}_3$ is determined by utilizing the analysis presented in Redwood [6]. Then, using equation 5.2 and Newton's second law, the following formula for ξ is obtained.

$$\begin{aligned}
\rho\Big(\frac{\partial^2\xi(x,t)}{\partial t^2}\Big) &= \Big(\frac{\partial T_3}{\partial x}\Big) \\
&= c_{33}^D \frac{S_3(x,t)}{\partial x} - h_{33}\frac{D_3(x,t)}{\partial x}
\end{aligned} \tag{5.16}$$

Solving for $\partial^2\xi/\partial t^2$ in equation 5.16 and substituting the expression $S_3 = \partial\xi/\partial x$, the following formula is obtained.

$$\frac{\partial^2\xi(x,t)}{\partial t^2} = (c_{33}^D/\rho)\frac{\partial^2\xi(x,t)}{\partial x^2} - (h_{33}/\rho)\frac{\partial D_3(x,t)}{\partial x} \tag{5.17}$$

It is assumed that plane wave propagation takes place strictly in the x direction. Furthermore, it assumed that there are no free charges present inside the piezoelectric element, Gausses law states that $\nabla\cdot D = 0$. Using these assumptions, the following equation is obtained.

$$\begin{aligned}
\nabla\cdot D &= \frac{\partial D_x}{\partial x} + \frac{\partial D_y}{\partial y} + \frac{\partial D_z}{\partial z} \\
&= \frac{\partial D_x}{\partial x} + \cancelto{0}{\frac{\partial D_y}{\partial y}} + \cancelto{0}{\frac{\partial D_z}{\partial z}} \\
&\implies \frac{\partial D_x}{\partial x} = 0
\end{aligned} \tag{5.18}$$

The cancellations above are since only plane wave motion occurs only in the

x direction. By plugging equation 5.18 into equation 5.17, and noting that the x direction is identical to the 3 direction, the wave equation within the piezoelectric element is found and given by equation 5.19.

$$\frac{\partial^2 \xi(x,t)}{\partial t^2} = (c_{33}^D/\rho)\frac{\partial^2 \xi(x,t)}{\partial x^2} \tag{5.19}$$

Assuming the piezoelectric element has zero initial conditions, the Laplace domain representation of equation 5.19 is given by equation 5.20.

$$s^2 \bar{\xi}(x,s) = v\frac{\partial^2 \xi(x,s)}{\partial x^2} \tag{5.20}$$

The general solution to equation 5.20 is given by equation 5.21.

$$\bar{\xi}(x,s) = A(s)e^{-\frac{s}{v}x} + B(s)e^{\frac{s}{v}x} \tag{5.21}$$

The parameters $A(s)$ and $B(s)$ are determined from the boundary conditions of the piezoelectric element. The expression for $\bar{F}$ is obtained using equations 5.6 and 5.15 as shown below.

$$\begin{aligned}
\bar{F}(x,s) &= -A_o \bar{T}_3(x,s) \\
&= -A_o\Big[c_{33}^D \frac{d\bar{\xi}(x,s)}{dx} - h_{33}\bar{D}_3(x,s)\Big] \\
&= -A_o\Big[\frac{sc_{33}^D}{v}\big[-A(s)e^{-\frac{s}{v}x} + B(s)e^{\frac{s}{v}x}\big] - h_{33}\bar{D}_3(x,s)\Big]
\end{aligned} \tag{5.22}$$

To simplify the expression for $\bar{F}$, the following relations are utilized:

$$Z_c = \rho v A_o \tag{5.23}$$

$$\bar{D} = \frac{\bar{Q}}{A_o} \tag{5.24}$$

The expression for $\bar{D}$ is obtained from Gauss's law applied to the piezoelectric element's surface. Z_c is the characteristic acoustic impedance of the piezoelectric element. After the relations $Z_c, \bar{D}$ are inserted into equation 5.22, the simplified expression for $\bar{F}$ is given by equation 5.25.

$$-\frac{\bar{F}}{A_o} = \frac{sc_{33}^D}{v}\Big[-A(s)e^{-\frac{s}{v}x} + B(s)e^{\frac{s}{v}x}\Big] - h_{33}\frac{\bar{Q}(x,s)}{A_o}$$
$$\bar{F} = sZ_c\Big[A(s)e^{-\frac{s}{v}x} - B(s)e^{\frac{s}{v}x}\Big] + h_{33}\bar{Q} \tag{5.25}$$

Next, the equation for the voltage $\bar{V}$, developed between the piezoelectric element's electrical terminals, is determined using equation 5.26.

$$\bar{V} = \int \bar{E}\cdot \mathrm{d}\ell \tag{5.26}$$

The assumption that no electrical field is present, except in the x direction, allows the integration of $\bar{E}$ strictly in the x direction. If one end of the piezoelectric element is positioned at $x = 0$, and the element has a thickness L, then the following expression for $\bar{V}$ is obtained. Note that C_o is the clamped capacitance of the piezoelectric element.

$$\begin{aligned}
\bar{V} &= \int_{x=0}^{x=L} \bar{E}\mathrm{d}x \\
&= \int_0^L -h_{33}\frac{d\bar{\xi}}{dx} + \beta_{33}^S \bar{D}_3 \mathrm{d}x \\
&= -\int_0^L h_{33}\frac{d\bar{\xi}}{dx}\mathrm{d}x + \frac{\bar{D}_3 L}{\varepsilon_{33}^S} \\
&= -h_{33}\Big[\bar{\xi}\Big|_{x=L} - \bar{\xi}\Big|_{x=0}\Big] + \frac{\bar{D}_3 L}{\varepsilon_{33}^S} \\
&= -h_{33}\Big[\bar{\xi}\Big|_{x=L} - \bar{\xi}\Big|_{x=0}\Big] + \frac{\bar{Q} L}{A_o \varepsilon_{33}^S} \\
&= -h_{33}\Big[\bar{\xi}(L,s) - \bar{\xi}(0,s)\Big] + \frac{\bar{Q}}{C_o}
\end{aligned} \tag{5.27}$$

The mechanical boundary conditions most often used for the piezoelectric element are given by the following set of equations:

$$\bar{F}(x,s) = sZ_c\left[A(s)e^{-\frac{s}{v}x} - B(s)e^{\frac{s}{v}x}\right] + h_{33}\bar{Q} \tag{5.28}$$

$$\bar{P}(x,s) = \frac{sZ_c}{A_o}\left[A(s)e^{-\frac{s}{v}x} - B(s)e^{\frac{s}{v}x}\right] + \frac{h_{33}\bar{Q}}{A_o} \tag{5.29}$$

$$\bar{u}(x,s) = s\bar{\xi}(x,s) = s\left[A(s)e^{-\frac{s}{v}x} + B(s)e^{\frac{s}{v}x}\right] \tag{5.30}$$

Another useful boundary condition can be defined at the electrical terminals of the piezoelectric element [6]. The current I into the transducer is related to the charge Q on the electrodes by the formula $I = dQ/dt$. This formula and Ohm's Law are used to determine an appropriate boundary condition for the case when the piezoelectric element is loaded by an electrical impedance $\bar{Z}_{load}$.

$$\begin{aligned}\bar{V} &= -\bar{I}\bar{Z}_{load} \\ &= -s\bar{Q}\bar{Z}_{load}\end{aligned} \tag{5.31}$$

Equations 5.21, 5.25, and 5.27, together with the boundary conditions defined using 5.28, 5.29, 5.30, and 5.31, are used to describe the transient behavior of a piezoelectric element.

5.2. Development of *TVOPI*, Voltage Response, and *TPOVI*

The transient expressions presented in sections 5.1.1 and 5.1.2 are used to develop the *TVOPI*, voltage response, and *TPOVI*. These are important transient performance characteristics to have for any transducer design. Note that to determine the time domain expressions the numerical inverse Laplace transform routines presented in appendix A can be used.

5.2.1. Transient Voltage Output resulting from a Pressure Input

The Transient Voltage Output resulting from a Pressure Input (*TVOPI*) is a measure of the transient voltage received from an input pressure field.

It is assumed that the pressure on the face of the transducer is uniform. The

simplest case is one in which only a single piezoelectric element with no backing or matching layer is considered to illustrate how the Laplace domain expression of the *TVOPI* is determined. The mechanical setup used to determine the *TVOPI* is presented in figure 5.1.

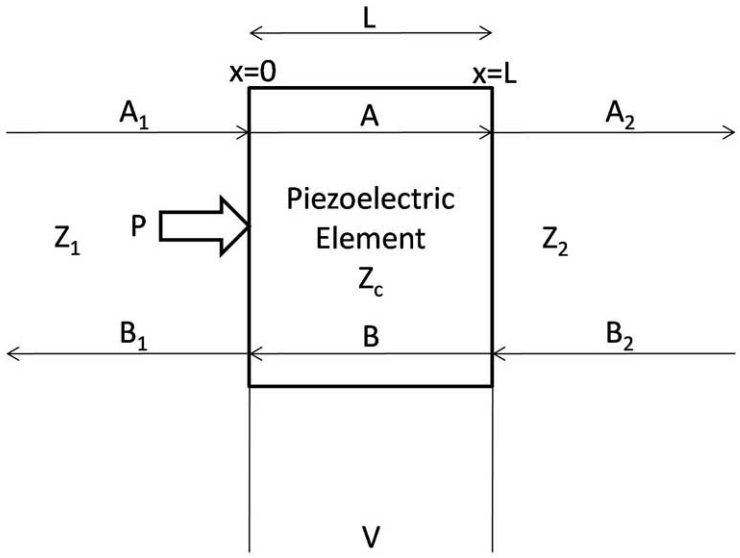

Figure 5.1: The Mechanical Setup used to determine the Open-Circuit Output Voltage of a Single Element Transducer resulting from a Pressure Input P

Equations 5.21, 5.27, 5.28 and 5.29 from section 5.1.2 are used to obtain the necessary equations to describe the transient behavior within the piezoelectric element and within the boundary mediums of the element as well. These are given by the following equations.

$$\bar{\xi}_1(x,s) = A_1 e^{-\frac{s}{v_1}x} + B_1 e^{\frac{s}{v_1}x} \tag{5.32}$$

$$\bar{F}_1(x,s) = sZ_1\left[A_1 e^{-\frac{s}{v_1}x} - B_1 e^{\frac{s}{v_1}x}\right] \tag{5.33}$$

$$\bar{\xi}(x,s) = Ae^{-\frac{s}{v}x} + Be^{\frac{s}{v}x} \tag{5.34}$$

$$\bar{F}(x,s) = sZ_c\left[Ae^{-\frac{s}{v}x} - Be^{\frac{s}{v}x}\right] + h_{33}\bar{Q} \tag{5.35}$$

$$\bar{\xi}_2(x,s) = A_2 e^{-\frac{s}{v_2}x} + B_2 e^{\frac{s}{v_2}x} \tag{5.36}$$

$$\bar{F}_2(x,s) = sZ_2\left[A_2 e^{-\frac{s}{v_2}x} - B_2 e^{\frac{s}{v_2}x}\right] \tag{5.37}$$

$$\bar{V} = -h_{33}\Big[\bar{\xi}(L,s) - \bar{\xi}(0,s)\Big] + \frac{\bar{Q}}{C_o} \tag{5.38}$$

$$\bar{P}(x,s) = \frac{sZ_1}{A_o}\Big[A_1 e^{-\frac{s}{v_1}x} - B_1 e^{\frac{s}{v_1}x}\Big] \tag{5.39}$$

This set of equations is used to find $\bar{V}$ as a function of $\bar{P}$. The parameters $\{A_1, B_1, A, B, A_2, B_2, \bar{Q}\}$ are determined by the boundary conditions of the element. The first is the continuity boundary condition for displacement and force at the boundaries of the piezoelectric element.

$$\bar{\xi}_1\Big|_{x=0} = \bar{\xi}\Big|_{x=0} \qquad \bar{\xi}\Big|_{x=L} = \bar{\xi}_2\Big|_{x=L} \tag{5.40}$$

$$\bar{F}_1\Big|_{x=0} = \bar{F}\Big|_{x=0} \qquad \bar{F}\Big|_{x=L} = \bar{F}_2\Big|_{x=L} \tag{5.41}$$

It is assumed that there are no incoming pressure waves at the back of the transducer so that $B_2 = 0$. As well, since only the open-circuit voltage is being considered, the quantity $\bar{Q} = 0$ because no current flows from the transducer [6]. Using these boundary conditions, the following set of equations is obtained.

$$A_1 + B_1 = A + B \tag{5.42}$$

$$sZ_1\Big[A_1 - B_1\Big] = sZ_c\Big[A - B\Big] \tag{5.43}$$

$$Ae^{-\frac{s}{v}L} + Be^{\frac{s}{v}L} = A_2 e^{-\frac{s}{v_2}L} \tag{5.44}$$

$$sZ_c\Big[Ae^{-\frac{s}{v}L} - Be^{\frac{s}{v}L}\Big] = sZ_2\Big[A_2 e^{-\frac{s}{v_2}L}\Big] \tag{5.45}$$

$$\bar{V} = h_{33}\Big[A(1 - e^{-\frac{s}{v}L}) + B(1 - e^{\frac{s}{v}L})\Big] \tag{5.46}$$

$$\bar{P}(x,s) = \frac{sZ_1}{A_o}\Big[A_1\Big] \tag{5.47}$$

This set of equations is used to solve for $\bar{V}$ as a function of $\bar{P}$ and is given by equation 5.48. Note that the $TVOPI = \bar{V}(\bar{P})$.

$$\bar{V} = \Big[\frac{2A_o h(e^{\frac{Ls}{v}} - 1)((Z_2 + Z_c)e^{\frac{Ls}{v}} + (Z_2 - Z_c))}{s[(Z_1 + Z_c)(Z_2 + Z_c)e^{\frac{2Ls}{v}} + (Z_1 - Z_c)(Z_c - Z_2)]}\Big]\bar{P} \tag{5.48}$$

It is of interest to determine the $TVOPI$ of a single element transducer when an

impedance load is present. For this case, the boundary condition $\bar{Q} = 0$ is no longer valid because current flows from the transducer. Figure 5.2 represents the mechanical setup used to determine the *TVOPI* when an electrical load is present.

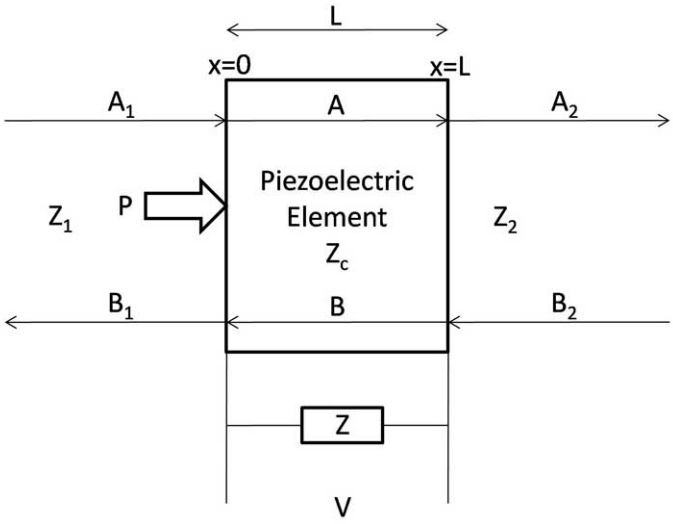

Figure 5.2: Mechanical Setup used to determine the Output Voltage of Single Element Transducer with an Electrical Load resulting from a Pressure Input P

In order to find the *TVOPI* of the transducer in figure 5.2, the boundary condition $\bar{V} = -s\bar{Q}\bar{Z}_{load}$, from equation 5.31, is utilized. Using this boundary condition, along with the equations found from the boundary conditions for the unloaded piezoelectric element, the following set of equations is obtained.

$$A_1 + B_1 = A + B \tag{5.49}$$

$$sZ_1\Big[A_1 - B_1\Big] = sZ_c\Big[A - B\Big] + h_{33}\bar{Q} \tag{5.50}$$

$$Ae^{-\frac{s}{v}L} + Be^{\frac{s}{v}L} = A_2e^{-\frac{s}{v_2}L} \tag{5.51}$$

$$sZ_c\Big[Ae^{-\frac{s}{v}L} - Be^{\frac{s}{v}L}\Big] + h_{33}\bar{Q} = sZ_2\Big[A_2e^{-\frac{s}{v_2}L}\Big] \tag{5.52}$$

$$\bar{V} = h_{33}\Big[A(1-e^{-\frac{s}{v}L}) + B(1-e^{\frac{s}{v}L})\Big] + \frac{\bar{Q}}{C_o} \tag{5.53}$$

$$\bar{V} = -s\bar{Q}\bar{Z}_{load} \tag{5.54}$$

$$\bar{P}(x,s) = \frac{sZ_1}{A_o}\Big[A_1\Big] \tag{5.55}$$

The solution of this set of equations for $\bar{V}$ as a function of $\bar{P}$ is given by equa-

tion 5.56, the *TVOPI* of a single element transducer when an electrical load is present.

$$
\begin{aligned}
C_1(s) &= 2A_oC_ohZ_1s(e^{\frac{Ls}{v}}-1)((Z_2+Z_c)e^{\frac{Ls}{v}}+(Z_2-Z_c)) \\
C_2(s) &= s[(Z_1+Z_c)(Z_2+Z_c)e^{\frac{2Ls}{v}}+(Z_1-Z_c)(Z_c-Z_2)] \\
C_3(s) &= h^2[(Z_1+Z_2-2Z_c)+4Z_ce^{\frac{Ls}{v}}-(Z_1+Z_2-2Z-c)e^{\frac{2Ls}{v}}] \\
C_4(s) &= s^2Z_1[(Z_1-Z_c)(Z_c-Z_2)+(Z_1+Z_c)(Z_2+Z_c)e^{\frac{2Ls}{v}}] \\
\bar{V} &= \left[\frac{C_1(s)}{C_2(s)+C_o(C_3(s)+C_4(s))}\right]\bar{P}
\end{aligned}
\tag{5.56}
$$

5.2.2. Transient Voltage Response for a Given Input Voltage

The transient voltage response of a transducer resulting from a given input voltage is presented in this section. The schematic representation of the setup used to determine the voltage response is given in figure 5.3.

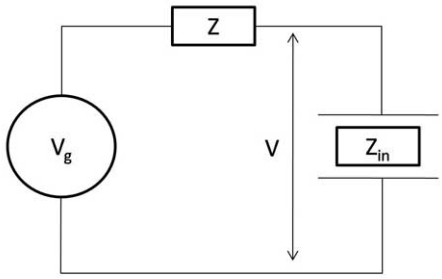

Figure 5.3: Electrical Setup Used to find Transient Voltage Response

In figure 5.3, the input voltage waveform is defined by V_g. Any loading between the voltage generator and transducer is taken into account by the impedance Z. Notice that any electrical structure can be broken down into this form using Thevenin's Theorem. The input impedance of the transducer is represented by Z_{in}. The voltage response is the expression for V as a function of V_g.

The derivation of the voltage response of a single element transducer has already been conducted by Richards [31]. Here, the theory is expanded to model the voltage response of a multi-layer transducer operating in thickness mode.

In order to obtain the voltage response, an expression for $\bar{Z}_{in}$ is required. Note that $\bar{Z}_{in}$ is the transient input impedance of the transducer in the Laplace domain. The transient input impedances of piezoelectric and non-piezoelectric elements are used

to construct the expression for $\bar{Z}_{in}$ for a multi-layer acoustic transducer operating in thickness mode.

Transient Impedance of Non-Piezoelectric Element

To determine the transient impedance of a non-piezoelectric element, note that the impedance is equal to the ratio of force to velocity. Therefore, the boundary conditions of $\bar{F}$ and $\bar{u}$ given by equations 5.14 and 5.12, can be used to determine a general expression for the impedance of a non-piezoelectric element, given by equation 5.57.

$$\bar{Z}(s,x) = \frac{\bar{F}(x,s)}{\bar{u}(x,s)} = Z_o\left[\frac{Ae^{-\frac{sx}{v}} - Be^{\frac{sx}{v}}}{Ae^{-\frac{sx}{v}} + Be^{\frac{sx}{v}}}\right] \tag{5.57}$$

The parameters A and B are found using the boundary conditions of the non-piezoelectric element. The thickness of the element is L and the load on the element is given by $\bar{Z}_L(s)$. The input transient impedance of the piezoelectric $\bar{Z}_{in}(s)$, is determined at $x = 0$ such that $\bar{Z}_{in}(s) = \bar{Z}(s,0)$. Therefore the equations used to determine the parameters A and B used to find $\bar{Z}_{in}(s)$ are given by.

$$\bar{Z}_{in}(s) = \bar{Z}(s,0) = Z_o\left[\frac{A-B}{A+B}\right] \tag{5.58}$$

$$\bar{Z}_L(s) = \bar{Z}(s,L) = Z_o\left[\frac{Ae^{-\frac{sL}{v}} - Be^{\frac{sL}{v}}}{Ae^{-\frac{sL}{v}} + Be^{\frac{sL}{v}}}\right] \tag{5.59}$$

After solving for A and B, the expression for $\bar{Z}_{in}(s)$ is given by equation 5.60.

$$\bar{Z}_{in} = Z_o\left[\frac{Z_L + Z_o tanh(\frac{Ls}{v})}{Z_o + Z_L tanh(\frac{Ls}{v})}\right] \tag{5.60}$$

If multiple non-piezoelectric elements are cascaded in series, equation 5.60 can be used recursively to find the input impedance of the layered structure. For example, consider the two layer structure given in figure 5.4.

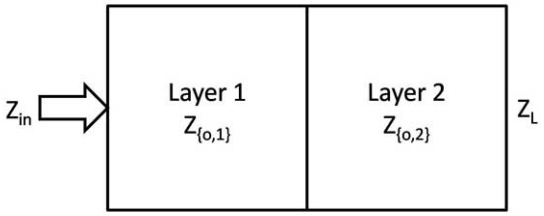

Figure 5.4: Input Impedance of Cascaded Non-Piezoelectric Elements

The input impedance of the structure in figure 5.4 is given by the following formula.

$$\bar{Z}_1 = Z_{o,2}\left[\frac{Z_L + Z_{o,2}tanh(\frac{L_2 s}{v_2})}{Z_{o,2} + Z_L tanh(\frac{L_2 s}{v_2})}\right]$$
$$\bar{Z}_{in} = Z_{o,1}\left[\frac{Z_1 + Z_{o,1}tanh(\frac{L_1 s}{v_1})}{Z_{o,1} + Z_1 tanh(\frac{L_1 s}{v_1})}\right] \tag{5.61}$$

Transient Impedance of Piezoelectric Element

The transient input impedance of a piezoelectric element is determined by using the equations of force and particle velocity together with the boundary conditions of the element. Figure 5.5 illustrates the direction of the force and particle velocity on the boundaries of the piezoelectric element.

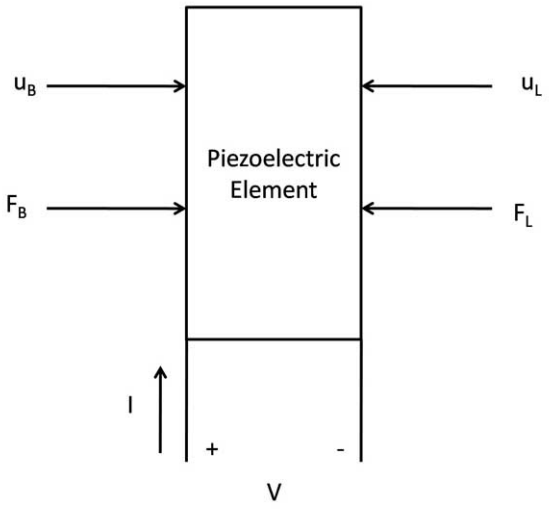

Figure 5.5: Transient Input Impedance of Piezoelectric Element

The expressions for $\bar{u}_B$,$\bar{F}_B$,$\bar{u}_L$,$\bar{F}_L$ can be determined using equations 5.30 and 5.28 and imposing the associated boundary conditions. The set of equations obtained from the boundary conditions together with the expression for the voltage, given by equation 5.27, are listed as follows.

$$\bar{u}_B(s) = s\Big[A+B\Big] \tag{5.62}$$

$$\bar{F}_B(s) = sZ_c\Big[A-B\Big] + h_{33}\bar{Q} \tag{5.63}$$

$$\bar{u}_L(s) = s\Big[Ae^{-\frac{s}{v}L} + Be^{\frac{s}{v}L}\Big] \tag{5.64}$$

$$\bar{F}_L(s) = sZ_c\Big[Ae^{-\frac{s}{v}L} - Be^{\frac{s}{v}L}\Big] + h_{33}\bar{Q} \tag{5.65}$$

$$\bar{V} = h_{33}\Big[A(1-e^{-\frac{sL}{v}}) + B(1-e^{\frac{sL}{v}})\Big] + \frac{\bar{Q}}{C_o} \tag{5.66}$$

It is convenient to use the current $\bar{I}$, instead of the charge $\bar{Q}$, in the above equations. This is done by using the following formulas and making the required substitutions.

$$I = \frac{\partial Q}{\partial t} = A_o\frac{\partial D}{\partial t} \tag{5.67}$$

$$D = \frac{Q}{A_o} \tag{5.68}$$

Converting these equations into the Laplace Domain and solving for $\bar{I}$, the following expression for the current $\bar{I}$ is obtained.

$$\bar{I} = s\bar{Q} \tag{5.69}$$

Then, using equation 5.69, together with the boundary conditions equations of the piezoelectric element, it is possible to solve for $\bar{F}_L$, $\bar{F}_B$, and $\bar{V}$ as functions of $\bar{u}_L$, $\bar{u}_B$, and $\bar{I}$. The results are summarized in matrix form given in 5.70.

$$\begin{bmatrix} \bar{F}_L \\ \bar{F}_B \\ \bar{V} \end{bmatrix} = \begin{bmatrix} Z_c coth(\frac{sL}{v}) & Z_c csch(\frac{sL}{v}) & \frac{h_{33}}{s} \\ Z_c csch(\frac{sL}{v}) & Z_c coth(\frac{sL}{v}) & \frac{h_{33}}{s} \\ \frac{h_{33}}{s} & \frac{h_{33}}{s} & \frac{1}{sC_o} \end{bmatrix} \begin{bmatrix} \bar{u}_L \\ \bar{u}_B \\ \bar{I} \end{bmatrix} \tag{5.70}$$

The transient input impedance of the piezoelectric element $\bar{Z}_{in}$, is determined by using the equations presented in 5.70 together with the following relations.

$$\bar{Z}_L = \frac{\bar{F}_L}{\bar{u}_L} \tag{5.71}$$

$$\bar{Z}_B = \frac{\bar{F}_B}{\bar{u}_B} \tag{5.72}$$

$$\bar{Z}_{in} = \frac{\bar{V}}{\bar{I}} \tag{5.73}$$

$\bar{Z}_L$ is the transient load impedance, and $\bar{Z}_B$ is the transient backing impedance of the piezoelectric element. The solution for $\bar{Z}_{in}$ is given by equation 5.76.

$$C_1(s) = Z_c(2C_o h^2 + s(Z_B + Z_L)) \tag{5.74}$$

$$C_2(s) = (C_o h^2(Z_B Z_L) + s(Z_c^2 + Z_B Z_L)) \tag{5.75}$$

$$\bar{Z}_{in}(s) = \frac{2C_o h^2 Z_c - C_1(s)cosh(\frac{Ls}{v}) + C_2(s)sinh(\frac{Ls}{v})}{C_o s^2(-Z_c(Z_B + Z_L)cosh(\frac{Ls}{v}) + (Z_c^2 + Z_B Z_L)sinh(\frac{Ls}{v}))} \tag{5.76}$$

Voltage Response to Given Input Voltage Waveform

To determine the transient input impedance of the entire transducer $\bar{Z}_{in}(s)$, notice that equations for the non-piezoelectric elements can be directly substituted into equation 5.76 for the input impedance of a piezoelectric element in order to determine $\bar{Z}_{in}(s)$.

Using the expression for $\bar{Z}_{in}(s)$ of the transducer, the voltage response is given by equation 5.77.

$$\bar{V} = \Big[\frac{\bar{Z}_{in}}{\bar{Z} + \bar{Z}_{in}}\Big]\bar{V}_g \tag{5.77}$$

Note that the parameters in equation 5.77 are equivalent to the parameters shown in figure 5.3.

5.2.3. Transient Pressure Output resulting from a Voltage Input

The Transient Pressure Output resulting from a Voltage Input (*TPOVI*) of a transducer provides the output pressure produced at the face of the transducer from a given drive voltage. The *TPOVI* is an important peformance characteristic to have

as it can be used to determine the rise time and ring time constants of a transmitted pressure waveform as well as to determine the values of the transmitted pressure waveform.

In this section the development of the *TPOVI* for two important cases are presented. The first is related to the transient pressure field produced if a pure voltage waveform is applied to the transducer and the second is related to a more realistic situation in which a function generator, with a certain impedance, provides the drive voltage to the transducer.

TPOVI for Pure Voltage Input

The expression of the *TPOVI* of a single piezoelectric element transducer with no electrical load is found by using the equations describing $\bar{\xi}, \bar{F}, \bar{P}$, and $\bar{V}$ together with the boundary conditions of the element. Figure 5.6 presents the mechanical setup used to solve for P as a function of V.

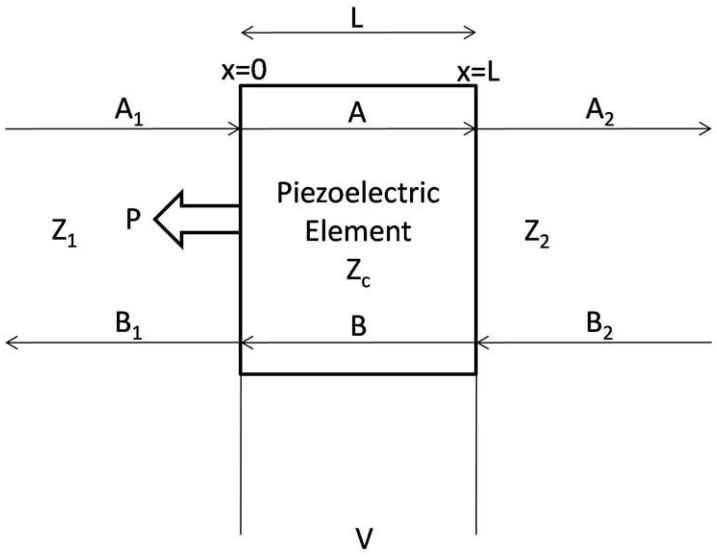

Figure 5.6: Mechanical Setup used to determine *TPOVI* from Pure Voltage Input

In figure 5.6, V is the drive voltage of the piezoelectric element, and P is the output pressure field on the face of the transducer resulting from V. The expressions for $\bar{\xi}, \bar{F}, \bar{P}$, and $\bar{V}$ in figure 5.6 are determined using equations 5.21, 5.25, 5.27, and 5.29. The obtained set of equations for these parameters are given below.

$$\bar{\xi}_1(x,s) = A_1 e^{-\frac{s}{v_1}x} + B_1 e^{\frac{s}{v_1}x} \tag{5.78}$$

$$\bar{F}_1(x,s) = sZ_1\Big[A_1 e^{-\frac{s}{v_1}x} - B_1 e^{\frac{s}{v_1}x}\Big] \tag{5.79}$$

$$\bar{\xi}(x,s) = Ae^{-\frac{s}{v}x} + Be^{\frac{s}{v}x} \tag{5.80}$$

$$\bar{F}(x,s) = sZ_c\Big[Ae^{-\frac{s}{v}x} - Be^{\frac{s}{v}x}\Big] + h_{33}\bar{Q} \tag{5.81}$$

$$\bar{\xi}_2(x,s) = A_2 e^{-\frac{s}{v_2}x} + B_2 e^{\frac{s}{v_2}x} \tag{5.82}$$

$$\bar{F}_2(x,s) = sZ_2\Big[A_2 e^{-\frac{s}{v_2}x} - B_2 e^{\frac{s}{v_2}x}\Big] \tag{5.83}$$

$$\bar{V} = -h_{33}\Big[\bar{\xi}(L,s) - \bar{\xi}(0,s)\Big] + \frac{\bar{Q}}{C_o} \tag{5.84}$$

$$\bar{P}(x,s) = \frac{sZ_1}{A_o}\Big[A_1 e^{-\frac{s}{v_1}x} - B_1 e^{\frac{s}{v_1}x}\Big] \tag{5.85}$$

To find an expression that relates $\bar{P}$ to $\bar{V}$, the following boundary conditions are used. The boundary mediums of the piezoelectric element are assumed infinite in extent allowing $A_1 = 0$, and $B_2 = 0$. The continuity boundary conditions of force and displacement are used at each boundary of the element. These boundary conditions are used to obtain the following set of equation.

$$\bar{\xi}_1\Big|_{x=0} = \bar{\xi}\Big|_{x=0}$$
$$\implies B_1 = A + B \tag{5.86}$$

$$\bar{F}_1\Big|_{x=0} = \bar{F}\Big|_{x=0}$$
$$\implies sZ_1\Big[-B_1\Big] = sZ_c\Big[A - B\Big] + h_{33}\bar{Q} \tag{5.87}$$

$$\bar{\xi}_2\Big|_{x=L} = \bar{\xi}\Big|_{x=L}$$
$$\implies A_2 e^{-\frac{sL}{v_2}} = Ae^{-\frac{sL}{v}} + Be^{\frac{sL}{v}} \tag{5.88}$$

$$\bar{F}_2\Big|_{x=L} = \bar{F}\Big|_{x=L}$$
$$\implies sZ_2\Big[A_2 e^{-\frac{sL}{v_2}}\Big] = sZ_c\Big[Ae^{-\frac{sL}{v}} - Be^{\frac{sL}{v}}\Big] + h_{33}\bar{Q} \tag{5.89}$$

The voltage $\bar{V}$ and pressure $\bar{P}$ are given by the following equations.

$$\bar{V} = h_{33}\Big[A(1-e^{-\frac{sL}{v}} + B(1-e^{\frac{sL}{v_2}})\Big] + h_{33}\bar{Q} \tag{5.90}$$

$$\bar{P} = \frac{sZ_1}{A_o}\Big[-B_1\Big] \tag{5.91}$$

To solve for $\bar{P}$ as a function of $\bar{V}$ the above set of equations are used. The solution for the output pressure $\bar{P}$, is given by equation 5.92. This is the *TPOVI* when no electrical load is present.

$$\begin{aligned}
C_1(s) &= Z_1 C_o hs(1-e^{\frac{Ls}{v}})((Z_2-Z_c)+e^{\frac{Ls}{v}}(Z_2+Z_c) \\
C_2(s) &= s[(Z_1-Z_c)(Z_2-Z_c)-(Z_1+Z_c)(Z_2+Z_c)e^{\frac{2Ls}{v}}] \\
C_3(s) &= (2Z_c-(Z_1+Z_2))-4Z_c e^{\frac{Ls}{v}}+(Z_1+Z_2+2Z_c)e^{\frac{2Ls}{v}} \\
\bar{P} &= \Big[\frac{C_1(s)}{A_o[C_2(s)+C_o h^2 C_3(s)]}\Big]\bar{V}
\end{aligned} \tag{5.92}$$

TPOVI from a General Function Generator

The *TPOVI* of a single piezoelectric element when an electrical load is present is developed in this section. Figure 5.7 illustrates the mechanical setup used to find the *TPOVI* for this case.

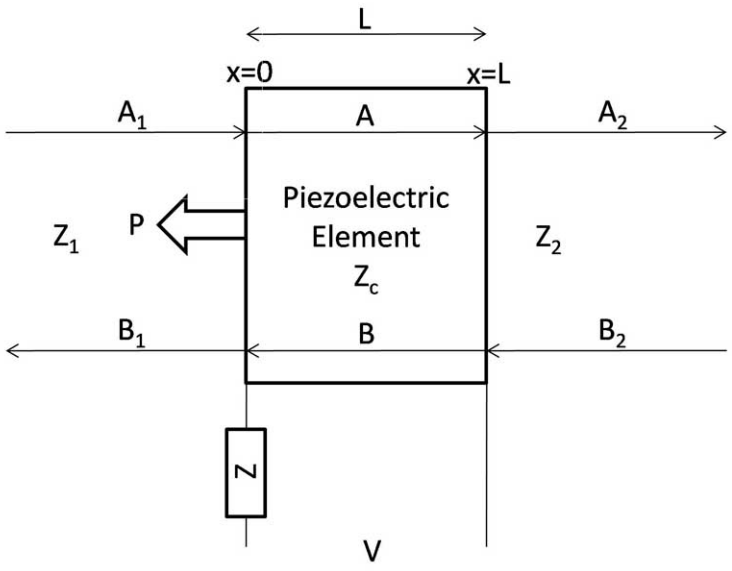

Figure 5.7: Single Element *TPOVI* with Electrical Load

In figure 5.7, notice that the only difference between this mechanical setup, and the one presented in figure 5.6, is the introduction of the impedance $\bar{Z}$. To account for $\bar{Z}$, the following boundary condition is used.

$$\bar{V} = \Big[\frac{\bar{Z}_{in}}{\bar{Z} + \bar{Z}_{in}}\Big]\bar{V}_g \tag{5.93}$$

The parameter $\bar{Z}_{in}$, is the transient input impedance of the piezoelectric element given by equation 5.76. The other boundary conditions used to find the *TPOVI* for a pure input voltage are the same as for the loaded case. The output pressure $\bar{P}$, as a function of $\bar{V}_g$, is given by equation 5.94.

$$\begin{aligned}
C_1(s) &= Z_1 C_o hs(1 - e^{\frac{Ls}{v}})((Z_2 - Z_c) + e^{\frac{Ls}{v}}(Z_2 + Z_c) \\
C_2(s) &= s[(Z_1 - Z_c)(Z_2 - Z_c) - (Z_1 + Z_c)(Z_2 + Z_c)e^{\frac{2Ls}{v}}] \\
C_3(s) &= (2Z_c - (Z_1 + Z_2)) - 4Z_c e^{\frac{Ls}{v}} + (Z_1 + Z_2 + 2Z_c)e^{\frac{2Ls}{v}} \\
\bar{P} &= \Big[\frac{C_1(s)}{A_o[C_2(s) + C_o h^2 C_3(s)]}\Big]\bar{V} \\
&= \Big[\frac{C_1(s)}{A_o[C_2(s) + C_o h^2 C_3(s)]}\Big]\Big[\frac{\bar{Z}_{in}}{\bar{Z} + \bar{Z}_{in}}\Big]\bar{V}_g
\end{aligned} \tag{5.94}$$

Equation 5.94 provides the Laplace domain solution for the *TPOVI* for a loaded piezoelectric element.

5.3. Drive Voltage Design to output a Specific Pressure Waveform

The theoretical development of a drive voltage design method (DVDM) is presented. The DVDM is used to pre-shape the drive voltage in order to obtain a specified pressure waveform from a multi-layer acoustic transducer operating in thickness mode. This is the first time a distributed model of the transducer has been used in order to determine the drive voltage necessary to output a specific pressure waveform.

A significant amount of work has focused on methods to drive a transducer to output a desired pressure waveform, but most research has concentrated on the transducer being modeled using a 2^{nd}-order lumped circuit model, which is only applicable at the resonance frequency of the transducer and does not account for the effects

caused by a multi-layered structure. Other methods have required the experimental measurement of the transfer function of the transducer in order to determine the drive voltage necessary to produce a desired pressure output. The issue with measurement of the transfer function is that not only does one require the transducer to be built, but difficulties also arise in obtaining accurate measurements of the output pressure waveform used to construct the transfer function.

The method developed in this section relies on the use of the distributed model of the transducer, given by the *TVOPI*, as well as on the use of cutting-edge numerical inversion routines. Only the geometric dimensions and material parameters of the transducer, along with the desired output pressure waveform, are required. This allows the accurate design of drive voltages to be determined for multi-layer acoustic transducers operating in thickness mode without any experimental measurements required

5.3.1. Drive Voltage Design from Transient Distributed Model

The DVDM is based on using *Inverse Filtering* and the *TPOVI* expression of the transducer. The technique of *Inverse Filtering* is also known as *Deconvolution* and *Restitution*.

To begin the development of the DVDM, the expression for the *TPOVI* is analyed in the Laplace domain. Notice that the $TPOVI = \bar{P}(\bar{V})$. Introducing the expression $POVI = \bar{P}/\bar{V}$ allows the *POVI* to be re-written as $TPOVI = [POVI] * \bar{V}$. Note that the Laplace domain expression of the *POVI* is easily obtained from the *TPOVI* because the output pressure $\bar{P}$ is linearly related to the drive voltage $\bar{V}$.

Using the technique of *Inverse Filtering* and the *POVI*, it is possible to determine the voltage $\bar{V}_{DDS}(s)$ necessary to produce the desired output pressure $\bar{P}_D(s)$ from the transducer. Figure 5.8 presents how the process of *Inverse Filtering* is applied to the *POVI* to determine the drive voltage, $\bar{V}_{DDS}(s)$, necessary to produce $\bar{P}_D(s)$.

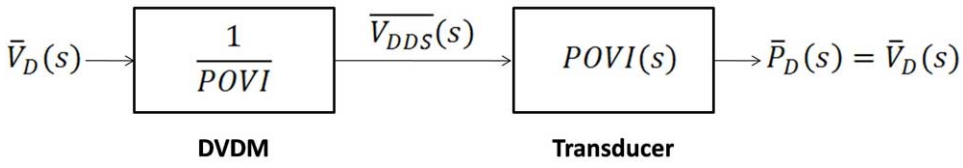

Figure 5.8: Process Diagram of how the DVDM Operates

In figure 5.8, $\bar{P}_D(s)$ is the desired pressure output of the transducer and is equal

to $\bar{V}_D(s)$. The DVDM block determines the drive voltage $\bar{V}_{DDS}(s)$ necessary to produce the output pressure $\bar{P}(s)$ from the transducer. This block represents where the technique of *Inverse Filtering* is applied to the *POVI*. As seen, when $\bar{V}_{DDS}(s)$ is used to drive the transducer, the output pressure produced is equal to $\bar{P}_D(s)$.

Specifically, the Laplace domain expression of $\bar{V}_{DDS}(s)$ is given by equation 5.95.

$$\bar{V}_{DDS}(s) = \Big[\frac{1}{POVI(s)}\Big] * \bar{P}_D(s) \tag{5.95}$$

To determine a time domain solution of the drive voltage given by equation 5.95, the numerical inversion routines presented in appendix A are used.

In order for the DVDM method to produce a bounded drive voltage, the poles of the expression $1/POVI$ must all be negative. This occurs if the real parts of the zeros of the *POVI* are all negative. Note that even if this condition is not met, it is still possible to obtain the output pressure waveform, but the time duration is limited to the maximum amplitude capabilities of the drive voltage electronics.

5.4. Conclusion of Laplace Domain Formulation

A number of Laplace domain solutions for the transient characteristics of a transducer are presented in the preceding sections. The transient equations for displacement and force in a non-piezoelectric element are found in section 5.1.1 and the transient equations for displacement, force, and voltage in a piezoelectric element are found in section 5.1.2. These equations are used to determine the *TVOPI*, voltage response, and *TPOVI* of a transducer, as shown in section 5.2.

The expressions developed in sections 5.1 and 5.2 provide a designer with the ability to rapidly evaluate different transducer geometries and materials without the need for elaborate experimental setups and sophisticated instrumentation.

In section 5.3, a novel method, DVDM, is derived that is used to pre-shape the drive voltage in order to output a desired pressure waveform from a multi-layer acoustic transducer operating in thickness mode. This method requires the geometric dimensions and material parameters of the transducer as well as the desired pressure waveform be known prior to the determination of the necessary drive voltage.

6. Theoretical and Experimental Analysis of Transient Theory

The transient theory introduced in chapter 5 is validated in this chapter using theoretical and experimental methods.

A method for testing the validity of the *TVOPI* using Snell's Law is developed in section 6.1 and it is shown that accurate predictions of the *TVOPI* for single element and multi-element transducers operating in thickness mode can be obtained.

No simple methods exist to validate the *TPOVI*. Instead, the steady-state TVR is used to make a partial validation of the *TPOVI*. If the transducer is being driven with a unity magnitude sinusoidal drive voltage, then the steady-state region of the output pressure waveform must have the same magnitude as the TVR. This allows for the partial validation of the *TPOVI*, as shown in section 6.2.

A similar procedure of driving the transducer with a unity magnitude sinusoidal pressure together with the steady-state sensitivity may be used as a validation check of the *TVOPI*, as shown in section 6.2.

The state-of-the-art Drive Voltage Design method (DVDM) developed in section 5.3, is validated in section 6.3. It is conclusively shown that the developed method, when applied to a lumped circuit model, obtains a perfect match between the analytic and numerically found drive voltages. Subsequently, an in depth discussion is given of the results of the DVDM for a single piezoelectric element and an XTM transducer. This analysis provides sufficient detail to validate the accuracy and robustness of the developed routine for the purpose of outputting a general pressure waveform from a multi-layer acoustic transducer operating in thickness mode.

Having conducted the theoretical validation of the transient theory, it is necessary to determine a practical method for verifying the transient theory that does not involve elaborate experimental setups and instrumentation. The easiest transient performance characteristic to measure is the voltage response, developed in section 5.2.2.

Determination of the capability of the voltage response to be used to validate the

transient theory is shown in section 6.4. This is done by analyzing the effect material parameter variation has on the obtained voltage response.

Voltage response is a suitable expression for validating the transient theory. Experimental measurement of the voltage response is the topic of section 6.5, in which the voltage response of a piezocomposite material is analyzed for a number of different drive voltages. The experimentally measured and theoretically determined voltage responses are compared throughout the analysis. For the first time, it is demonstrated that the theoretical voltage response can accurately predict the voltage response obtained experimentally from a piezocomposite element.

6.1. Validation of *TVOPI* using Established Theory of Reflection and Transmission

A method suitable for testing the validity of the *TVOPI*, developed in section 5.2.1, is presented in this section.

The method utilizes the application of a Dirac delta (δ) function pressure to the face of the transducer, and since the acoustic speed in the material is known, it is possible to determine the arrival of the delta pressure pulse at a boundary. Using Snell's law of reflection and transmission, determination of the change in voltage after the incident delta pressure reflects or enters a boundary of the piezoelectric element can be made. This method is explained in detail for a single layer and 2-Layer XTM transducer to validate the *TVOPI* equation.

6.1.1. Validation of Single Element *TVOPI*

First Snell's law of reflection, R and transmission, T relative to the boundary in figure 6.1 are determined. P_R signifies the reflected pressure, P_T signifies the transmitted pressure, and P_I signifies the incident pressure.

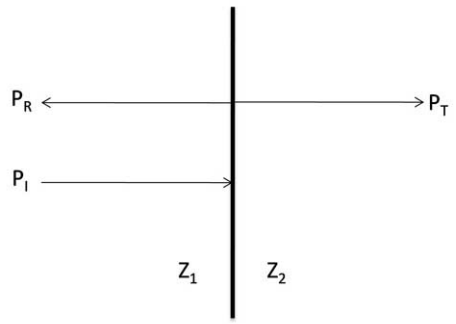

Figure 6.1: Diagram used to illustrate Snell's Law of Reflection and Transmission

The equations describing R and T at the boundary in figure 6.1 are given by equations 6.1 and 6.2.

$$R = \frac{Z_2 - Z_1}{Z_2 + Z_1} \tag{6.1}$$

$$T = \frac{2Z_2}{Z_2 + Z_1} \tag{6.2}$$

The mechanical arrangement of the piezoelectric element is presented in figure 6.2.

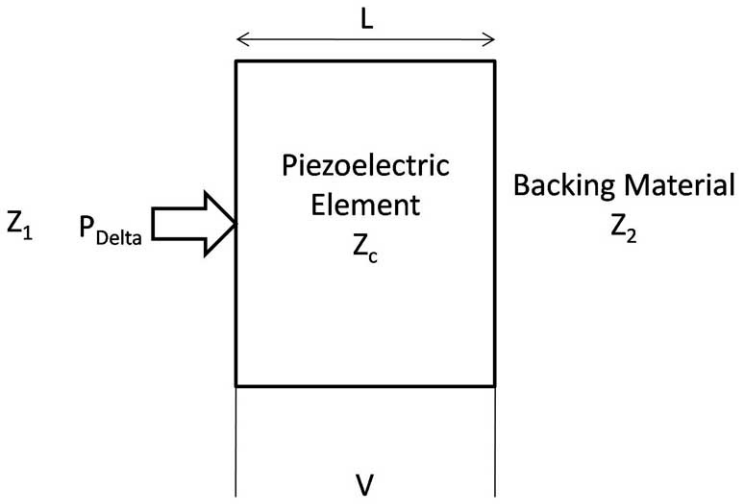

Figure 6.2: Incident Delta Plane Pressure Wave on a Single Element Transducer

The characteristic impedance of a single piezoelectric element is defined as Z_c. The front material has an impedance Z_1, and the backing material has an impedance Z_2. The transducer is assumed to have no losses. Therefore, when the delta pressure P_{Delta}, is applied to the face of the transducer, the expectation is to observe a constant voltage output while the pulse travels through the it.

When P_{Delta} enters the transducer, an immediate jump in the output voltage occurs and remains constant until the pulse reaches the backing layer of the transducer. At this point, the voltage reverses sign and is reduced by the factor R_2 according to Snell's law. The voltage then remains constant until it reaches the front layer boundary of the transducer where it changes sign and is reduced by the factor R_1. Thereafter the voltage remains constant until the pulse is once again reflected at the backing layer boundary R_2. This process of internal reflection repeats itself an infinite number of times.

The value R_1 is the reflection coefficient associated with a wave from medium Z_c about to reflect off the boundary of material Z_1. The value R_2 is the reflection coefficient associated with a wave fro medium Z_c about to reflect off the boundary of material Z_2. The values, R_1 and R_2, are given by the following equations.

$$R_1 = \frac{Z_1 - Z_c}{Z_1 + Z_c} \tag{6.3}$$

$$R_2 = \frac{Z_2 - Z_c}{Z_2 + Z_c} \tag{6.4}$$

The reflection coefficients R_1 and R_2 are utilized to determine the voltage output of the transducer from the pressure input P_{Delta}.

In order to determine the time domain expression of the voltage output using the distributed model of the transducer, the *TVOPI* expression of the element, given by equation 5.48, is utilized. Notice that the Laplace domain expression of P_{Delta} is equal to $\bar{P} = 1$. Therefore, using $\bar{P} = 1$ and equation 5.48, the Laplace domain expression for the output voltage is given by equation 6.5.

$$\bar{V} = \frac{2A_o h_{33}(e^{\frac{Ls}{v}} - 1)((Z_2 + Z_c)e^{\frac{Ls}{v}} + Z_2 - Z_c)}{s(Z_1 + Z_c)(Z_2 + Z_c)e^{\frac{2Ls}{v}} + s(Z_1 - Z_c)(Z_c - Z_2)} \tag{6.5}$$

In order to conduct the analysis of the voltage output resulting from P_{Delta}, the following set of material parameters are used as they provide a good approximation to real world values:

$$\begin{aligned} A_o &= 1 && [m^2] \\ L &= 1 && [\text{mm}] \\ h_{33} &= 1 * 10^9 && [V/m] \\ Z_1 &= 1 * 10^6 && [kg/s] \\ Z_2 &= 0.5 * 10^6 && [kg/s] \\ Z_c &= 2 * 10^6 && [kg/s] \\ v &= 4000 && [m/s] \end{aligned}$$

These material parameters are used to find the values of R_1 and R_2. Additionally, the parameter τ is introduced to represent the time it takes for the pulse to travel

from one side of the element to the other.

$$R_1 = -\frac{1}{3} \tag{6.6}$$

$$R_2 = -\frac{3}{5} \tag{6.7}$$

$$\tau = \frac{L}{v} = 2.5 * 10^{-7} s \tag{6.8}$$

To conduct the numerical inversion of equation 6.5, Iseger's and the DAC Method from appendix A are used. The voltage values obtained are given in figure 6.3.

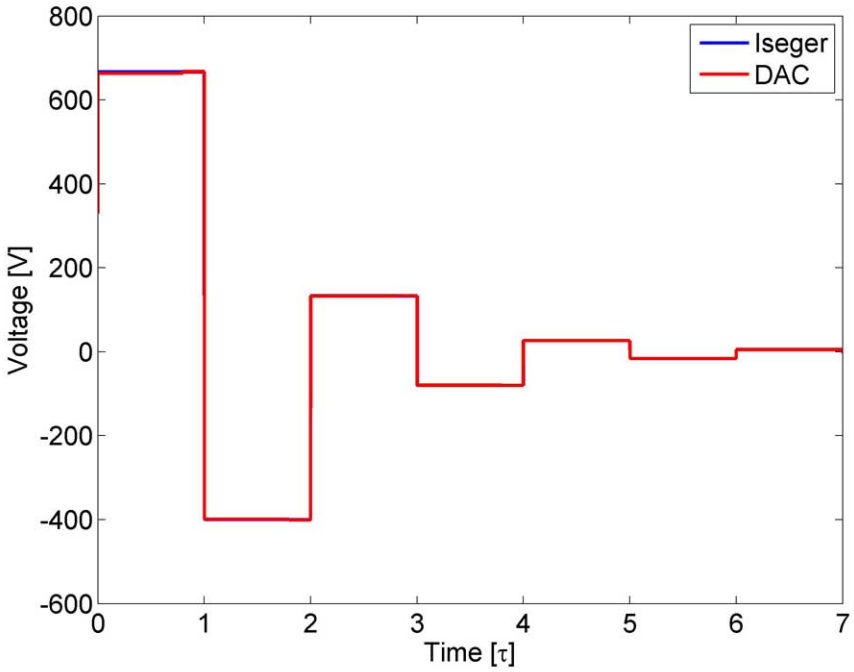

Figure 6.3: Open-Circuit Voltage Output from Delta Pressure Input for Single Element Transducer

Visually, the voltage output is as expected. The voltage jumps occur at integer multiples of τ, and the voltage values after each jump are a multiple of $-R_1$ or $-R_2$. A detailed comparison of the voltage values is presented in table 6.1.

Time	$TVOPI$ for P_{Delta}	R_1 and R_2 Coefficients
0.5τ	666.6662999510171	666.6662999510171
1.5τ	-399.9993500621985	-399.9999441506848
2.5τ	133.3333107465898	133.3333147168949
3.5τ	-79.99972976984275	-79.999988830136957
4.5τ	26.66686957687763	26.666662943378984
5.5τ	-15.99961901853426	-15.999997766027390
6.5τ	5.33390107405914	5.333332588675797

Table 6.1: Single Element Delta Pressure $TVOPI$

Table 6.1 shows that the voltage output obtained using the numerical inversion of equation 6.5 and that obtained using the R_1 and R_2 coefficients are nearly equal. Note that the voltage output at time 0.5τ from both methods in table 6.1 are set equal because there is no way to determine the initial value without resorting to numerical techniques.

6.1.2. 2-Layer XTM Transducer $TVOPI$ Validation

The validation of the $TVOPI$ for a 2-Layer transducer is conducted using the same method as presented in section 6.1.1.

The 2-Layer XTM transducer is shown in figure 6.4.

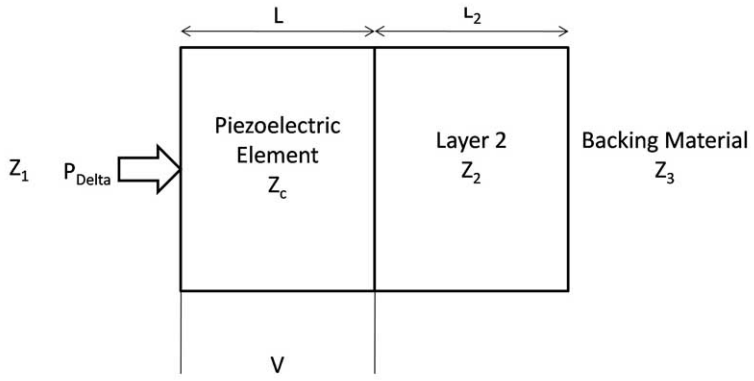

Figure 6.4: Mechanical Setup of 2-Layer XTM Transducer

The material parameters of the 2-Layer XTM transducer are provided below. These are typical values for materials used to construct underwater acoustic transducers. Additionally, it should be noted that mechanical, piezoelectric, and dielectric loss terms are not included, thereby allowing the use of the validation method developed in section 6.1.1.

$$
\begin{aligned}
A_o &= 445 && [mm^2] \\
L &= 5 && [\text{mm}] \\
\rho &= 7550 && [kg/m^3] \\
v &= 4000 && [m/s] \\
h_{33} &= 2.68 * 10^9 && [V/m] \\
Z_c &= \rho v A_o = 13439 && [kg/s] \\
Z_1 &= \rho_1 v_1 A_o = (1000)(1500) A_o = 667.5 && [kg/s] \\
v_2 &= 1500 && [m/s] \\
Z_2 &= \rho_2 v_2 A_o = (3000) v_2 A_o = 2002.5 && [kg/s] \\
L_2 &= 1 && [\text{mm}] \\
Z_3 &= \rho_3 v_3 A_o = (2000)(524) A_o = 466.36 && [kg/s] \\
\tau &= \frac{L}{v} = 1.25 && [\mu s] \\
\tau_2 &= \frac{L_2}{v_2} = 2/3 = (8/15) * \tau && [\mu s]
\end{aligned}
$$

Using these values, and the theory developed in section 5.2.1, it is possible to predict the voltage output from a delta pressure input on the face of the transducer using the Laplace domain expression for $\bar{V}$, given by equation 6.9.

$$
\begin{aligned}
P(s) &= 1 \\
C_1(s) &= (Z_2 + Z_3)((Z_2 - Z_c) + (Z_2 + Z_c) e^{\frac{Ls}{v}}) \\
C_2(s) &= (Z_3 - Z_2)((Z_2 + Z_c) + (Z_2 - Z_c) e^{\frac{Ls}{v}}) + C_1(s) e^{\frac{2Ls}{v_2}} \\
C_3(s) &= (Z_2 + Z_3)(Z_1 - Z_c)(Z_2 - Z_c) e^{\frac{2(L+L_2)s}{v_2}} \\
C_4(s) &= (Z_2 - Z_3)(Z_2 - Z_c)(Z_1 + Z_c) e^{\frac{2Ls(v+v_2)}{vv_2}} \\
C_5(s) &= (Z_2 - Z_3)(Z_1 - Z_c)(Z_2 + Z_c) e^{\frac{2Ls}{v_2}} \\
C_6(s) &= (Z_2 + Z_3)(Z_1 + Z_c)(Z_2 + Z_c) e^{\frac{2(L(v_2+v)+vL_2)s}{vv_2}}
\end{aligned}
$$

$$\bar{V} = \left[\frac{2A_o e^{\frac{2Ls}{v_2}}(e^{\frac{Ls}{v}} - 1)h_{33}C_2(s)}{s(C_3(s) + C_4(s) - C_5(s) - C_6(s))}\right]\bar{P} \tag{6.9}$$

The numerical inversion of equation 6.9, with $\bar{P} = 1$, is conducted using Iseger's and the DAC method from appendix A. The voltage values are given in figure 6.5.

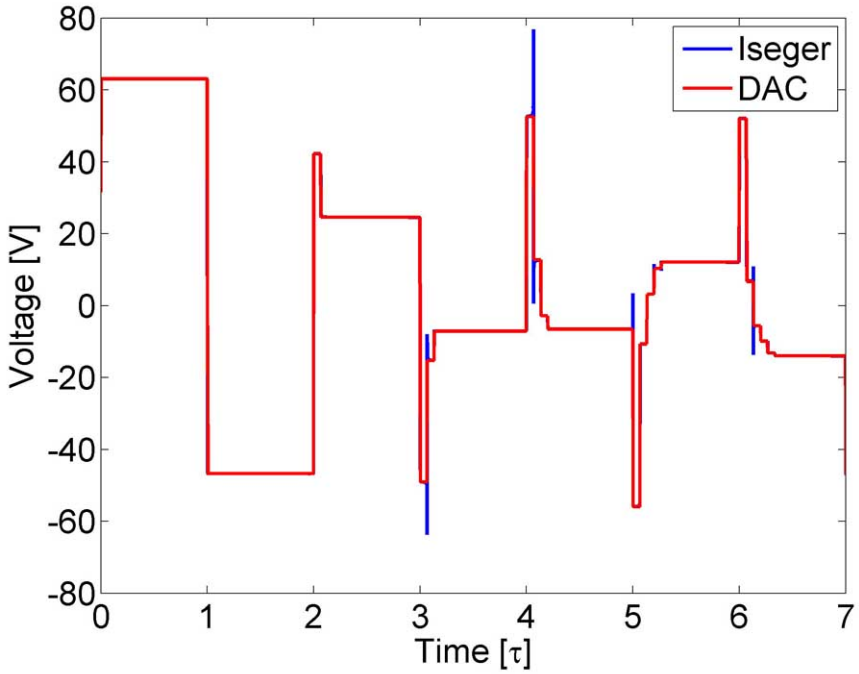

Figure 6.5: 2-Layer XTM Transducer Open-Circuit Voltage Output from Delta Pressure Input

From figure 6.5, it can be seen that the Iseger method produces large spikes at locations of certain discontinues of $V(t)$, whereas the DAC method does not. These spikes are a product of the Iseger inversion method and are not present in the actual values of $V(t)$. Away from the discontinuities, the Iseger and DAC methods are in excellent agreement. Using the values τ and τ_2, it can be observed that the voltage discontinuities in figure 6.5 occur at the correct locations.

Since the DAC method gives the best results for inverting equation 6.9 with $\bar{P} = 1$, the voltage values obtained from this method are compared with the expected values obtained using the method of reflection and transmission coefficients, similar to what is done in section 6.1.1. To conduct the comparison, the following set of reflection and transmission coefficients are required:

$$R_1' = \frac{Z_1 - Z_c}{Z_1 + Z_c} = -0.905363$$
$$R_2 = \frac{Z_2 - Z_c}{Z_2 + Z_c} = -0.740634$$
$$R_2' = \frac{Z_c - Z_2}{Z_2 + Z_c} = 0.740634$$
$$T_2 = \frac{2Z_2}{Z_2 + Z_c} = 0.259366$$
$$T_2' = \frac{2Z_c}{Z_2 + Z_c} = 1.74063$$
$$R_3' = \frac{Z_3 - Z_2}{Z_3 + Z_2} = -0.622206$$

Table 6.2 provides a detailed comparison of the voltage values obtained from the numerical inversion of the *TVOPI* to the voltage values obtained using the reflection and transmission coefficients.

Time	***TVOPI* for P_{Delta}**	**R,T Equation**	**R,T Voltage**
0.5τ	63.090242764529421	V_o	63.090242764529421
1.5τ	-46.726296207779782	$V_o R_2$	-46.726778859664485
$1.5\tau + \tau_2$	42.304368015266235	$V_o R_2 R_1'$	42.304696688722416
$2\tau + \tau_2$	24.581447092376433	$V_o[R_2 R_1' + T_2 R_3' T_2']$	24.582567343147030
$2.5\tau + \tau_2$	-49.054598752475862	$V_o[R_2 R_1' R_2' + T_2 R_3' T_2']$	-49.054426072930625
$1.5\tau + 3\tau_2$	-15.286994515063656	$V_o[R_2 R_1' R_2' + T_2 R_3' T_2' R_1']$	-15.287336536657069

Table 6.2: 2-Layer XTM Transducer Delta Pressure *TVOPI*

As can be seen from table 6.2, a very good match was found between the values obtained from the transmission and reflection coefficients and those obtained using the *TVOPI*.

6.1.3. Conclusion of the Validation of *TVOPI* using Established Theory of Reflection and Transmission

In this section the transient voltage output resulting from a Dirac delta function pressure input obtained from the *TVOPI* for both single element and multi-element transducers is discussed. A comparison is made between the voltage output resulting from a delta function pressure input using the *TVOPI* to the expected voltage output

using Snell's law of reflection and transmission as well as the travel times of the input pressure pulse. The voltage outputs obtained from the two methods are in very good agreement; therefore, validation of the *TVOPI* for single and multi-layer acoustic transducers operating in thickness mode has been completed.

6.2. Partial Validation of Transient Response of Matched Transducer

The partial validation of the *TPOVI* of the Matched transducer presented in section 3.2.4 is determined in this section. Unfortunately, no simple methods to validate the entire response obtained from the *TPOVI* exist. It is possible, however, to utilize the steady-state TVR of the Matched transducer from section 2.7.5 in order to conduct a partial validation. If the Matched transducer is driven with a finite cycle unity magnitude sinusoidal drive voltage, then the steady-state region of the *TPOVI* must have the same magnitude as the TVR. Therefore, validation within the steady-state region of the *TPOVI* using the TVR is presented.

The *TVOPI* was already validated in section 6.1, but as a check, a comparison, similar to that conducted previously, between the sensitivity and steady-state magnitude of the *TVOPI* is made. The result found was that if the Matched transducer is driven by a finite cycle unity magnitude sinusoidal pressure wave, then the magnitude of the steady-state region of the *TVOPI* must have the same value as the sensitivity. The sensitivity of the Matched transducer is determined in section 2.7.4.

To begin the analysis an expression for the *TPOVI* is determined for the Matched transducer in section 6.2.1. This is followed in section 6.2.2 by the partial validation, as described above, for the *TPOVI*. Then, having completed the analysis of the *TPOVI*, a derivation of the *TVOPI* of the Matched transducer is made in section 6.2.3. The comparison between the sensitivity and steady-state region of the *TPOVI* is completed in section 6.2.4.

The mechanical structure of the Matched transducer is presented in figure 6.6. The parameters $\{A_1, B_1, A, B, A_2, B_2, A_3, B_3\}$ are explicitly shown because they are used to derive the *TPOVI* and *TVOPI*.

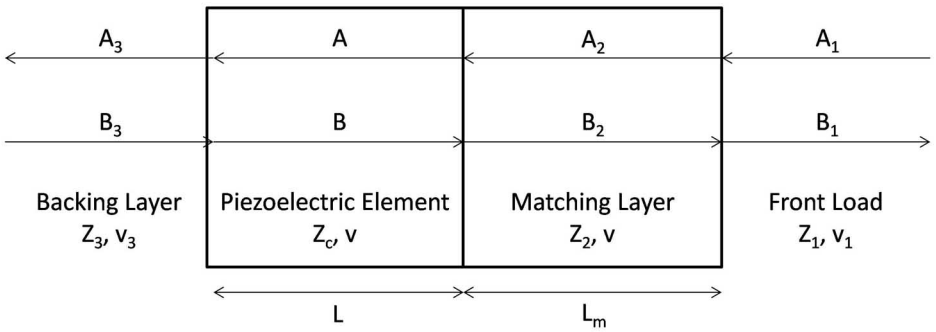

Figure 6.6: Mechanical Structure of Matched Transducer

The material parameters of the Matched transducer used in this section can be found in section 3.2.4.

6.2.1. Derivation of the *TPOVI* of the Matched Transducer

An expression for the *TPOVI* of the Matched transducer presented in figure 6.6 is determined using the theory developed in sections 5.1.1 and 5.1.2. The following set of equations describe the displacements and forces in the Matched transducer.

$$\bar{\xi}_1(x,s) = A_1 e^{-\frac{s}{v_1}x} + B_1 e^{\frac{s}{v_1}x} \tag{6.10}$$

$$\bar{F}_1(x,s) = sZ_1\Big[A_1 e^{-\frac{s}{v_1}x} - B_1 e^{\frac{s}{v_1}x}\Big] \tag{6.11}$$

$$\bar{\xi}_2(x,s) = A_2 e^{-\frac{s}{v_2}x} + B_2 e^{\frac{s}{v_2}x} \tag{6.12}$$

$$\bar{F}_2(x,s) = sZ_2\Big[A_2 e^{-\frac{s}{v_2}x} - B_2 e^{\frac{s}{v_2}x}\Big] \tag{6.13}$$

$$\bar{\xi}_(x,s) = A e^{-\frac{s}{v}x} + B e^{\frac{s}{v}x} \tag{6.14}$$

$$\bar{F}(x,s) = sZ_c\Big[A e^{-\frac{s}{v}x} - B e^{\frac{s}{v}x}\Big] + h_{33}\bar{Q} \tag{6.15}$$

$$\bar{\xi}_3(x,s) = A_3 e^{-\frac{s}{v_3}x} + B_3 e^{\frac{s}{v_3}x} \tag{6.16}$$

$$\bar{F}_3(x,s) = sZ_3\Big[A_3 e^{-\frac{s}{v_3}x} - B_3 e^{\frac{s}{v_3}x}\Big] \tag{6.17}$$

The equation for the voltage $\bar{V}$ is illustrated below.

$$\bar{V} = h_{33}\Big[A e^{-\frac{s}{v}L_m}(1 - e^{-\frac{s}{v}L}) + B e^{\frac{s}{v}L_m}(1 - e^{\frac{s}{v}L})\Big] + \frac{\bar{Q}}{C_o} \tag{6.18}$$

Boundary conditions are introduced to solve for the parameters $\{A_1, B_1, A_2, B_2, A, B, A_3, B_3, Q\}$. It is assumed that the backing layer and front load

are of infinite extent. This allows $B_3 = A_1 = 0$. The continuity boundary conditions for force and displacement are also used. These boundary conditions provide enough information to solve for $\{B_1, A_2, B_2, A, B, A_3, Q\}$ using the following set of equations.

$$B_1 = A_2 + B_2 \tag{6.19}$$

$$sZ_1[-B_1] = sZ_2[A_2 - B_2] \tag{6.20}$$

$$A_2 e^{-\frac{L_m s}{v_2}} + B_2 e^{\frac{L_m s}{v_2}} = A e^{-\frac{L_m s}{v}} + B e^{\frac{L_m s}{v}} \tag{6.21}$$

$$sZ_2[A_2 e^{-\frac{L_m s}{v_2}} - B_2 e^{\frac{L_m s}{v_2}}] = sZ_c[A e^{-\frac{L_m s}{v}} - B e^{\frac{L_m s}{v}}] + h_{33}\bar{Q} \tag{6.22}$$

$$A e^{-\frac{(L_m+L)s}{v}} + B e^{\frac{(L_m+L)s}{v}} = A_3 e^{-\frac{(L_m+L)s}{v_3}} \tag{6.23}$$

$$sZ_c[A e^{-\frac{(L_m+L)s}{v}} + B e^{\frac{(L_m+L)s}{v}}] = sZ_3[A_3 e^{-\frac{(L_m+L)s}{v_3}}] \tag{6.24}$$

$$\bar{V} = h_{33}\Big[A e^{-\frac{s}{v}L_m}(1 - e^{-\frac{s}{v}L}) + B e^{\frac{s}{v}L_m}(1 - e^{\frac{s}{v}L})\Big] + \frac{\bar{Q}}{C_o} \tag{6.25}$$

$$\bar{P} = \frac{sZ_1}{A_o}[-B_1] \tag{6.26}$$

The equation for $\bar{P}$ as a function of $\bar{V}$ is found using the above set of equations, and is given by equation 6.27. Note that the $TPOVI = \bar{P}(\bar{V})$.

$$C_1(s) = (Z_3 - Z_c) - (Z_3 + Z_c)e^{\frac{Ls}{v}}$$

$$C_2(s) = (Z_1 + Z_2)(Z_2 - Z_c)(Z_3 - Z_c)e^{\frac{(Lv_2 + 2L_m(v+v_2))s}{vv_2}}$$

$$C_3(s) = (Z_1 - Z_2)(Z_3 - Z_c)(Z_2 + Z_c)e^{\frac{(L+2L_m)s}{v}}$$

$$C_4(s) = (Z_1 - Z_2)(Z_2 - Z_c)(Z_3 + Z_c)e^{\frac{(3L+2L_m)s}{v}}$$

$$C_5(s) = (Z_1 + Z_2)(Z_2 + Z_c)(Z_3 + Z_c)e^{\frac{(3Lv_2 + 2L_m(v+v_2))s}{vv_2}}$$

$$C_6(s) = (Z_1 - Z_2)(Z_2 - Z_3 - 2Z_c)e^{\frac{(3L+2L_m)s}{v}}$$

$$C_7(s) = (Z_1 + Z_2)(Z_2 + Z_3 - 2Z_c)e^{\frac{(Lv_2 + 2L_m(v+v_2))s}{vv_2}}$$

$$C_8(s) = 4(Z_1 - Z_2)Z_c e^{\frac{2(L+L_m)s}{v}} - 4(Z_1 + Z_2)Z_c e^{\frac{2(L_m(v+v_2)+Lv_2)s}{vv_2}}$$

$$C_9(s) = (Z_1 - Z_2)(Z_2 - Z_3 + 2Z_c)e^{\frac{(L+2L_m)s}{v}}$$

$$C_{10}(s) = (Z_1 + Z_2)(Z_2 + Z_3 + 2Z_c)e^{\frac{(3Lv_2+2L_m(v+v_2))s}{vv_2}}$$
$$C_{11}(s) = C_2(s) + C_3(s) - C_4(s) - C_5(s)$$
$$C_{12}(s) = C_6(s) - C_7(s) + C_8(s) - C_9(s) + C_{10}(s)$$
$$\bar{P} = \left[\frac{2C_o h_{33} s Z_1 Z_2 (1 - e^{\frac{Ls}{v}}) e^{\frac{(Lv_2+L_m(2v_2+v))s}{vv_2}}}{A_o(sC_{11}(s) + C_o h_{33}^2 C_{12}(s))}\right]\bar{V} \tag{6.27}$$

To determine the time domain pressure output for the Matched transducer, the numerical inverse Laplace routines presented in appendix A are applied to equation 6.27.

6.2.2. Partial Validation of the *TPOVI* of the Matched Transducer

In order to perform the partial validation of the *TPOVI* of the Matched transducer given by equation 6.27, it is necessary to determine where the steady-state region of the *TPOVI* is located. To do this, a number of pressure output waveforms obtained from the *TPOVI* are examined when the Matched transducer is driven with a 1V 40 cycle sinusoidal drive voltage at a frequency f.

Figure 6.7 shows the result obtained by numerically inverting the *TPOVI* using Iseger's method when the drive voltage is at the resonance frequency of the transducer, which occurs at $f = 241.5$kHz.

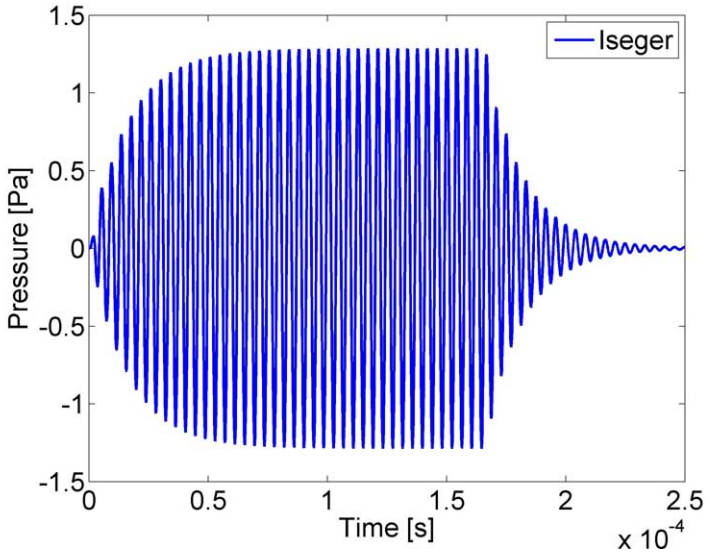

Figure 6.7: *TPOVI* for 1V 40 cycles Sinusoidal Driving Voltage at 241.5kHz

The rise time of the waveform in figure 6.7 shows an exponential like increase in magnitude until the steady-state portion of the signal is reached. After the 40 cycle drive voltage is complete, an exponential like decay in the pressure output of the transducer is obtained. This type of response is characteristic when the transducer is being driven at its resonance frequency.

Now the determination of the pressure output when the Matched transducer is driven at a frequency away from its resonance frequency is determined. The resultant *TPOVI* for the drive voltage at a frequency of 200kHz and 500kHz is presented in figure 6.8.

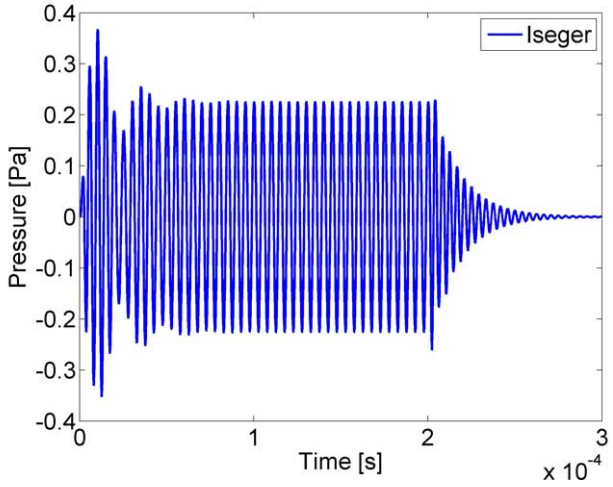

(a) $f = 200kHz$

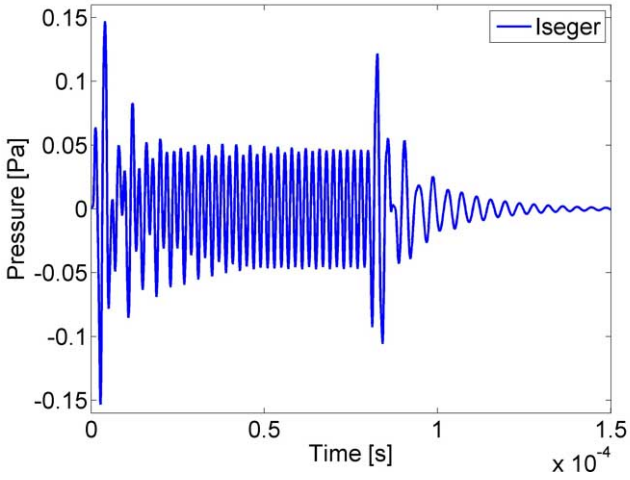

(b) $f = 500kHz$

Figure 6.8: *TPOVI* for 1V 40 cycles Sinusoidal Driving Voltage

In figure 6.8, the steady-state sections of the transient pressure output have a lower magnitude than the steady-state portion of the pressure output when the Matched transducer is driven at its resonance frequency. It may also be noted from figure 6.8 that the rise time and ring time sections of the pressure output no longer follow an exponential-like increase or decrease in magnitude. This characteristic occurs because of the complex internal acoustic wave interactions and reflections occuring within the transducer.

Using figures 6.7 and 6.8, the transducer is assumed to have reached a steady-state value after completion of the first 30 cycles of the drive voltage. Therefore, in order to determine the steady-state magnitude, the maximum value of the transient pressure waveform must be taken after the first 30 cycles of the drive voltage have been completed.

The comparison of the steady-state region of the *TPOVI* to the TVR of the transducer is presented in figure 6.9

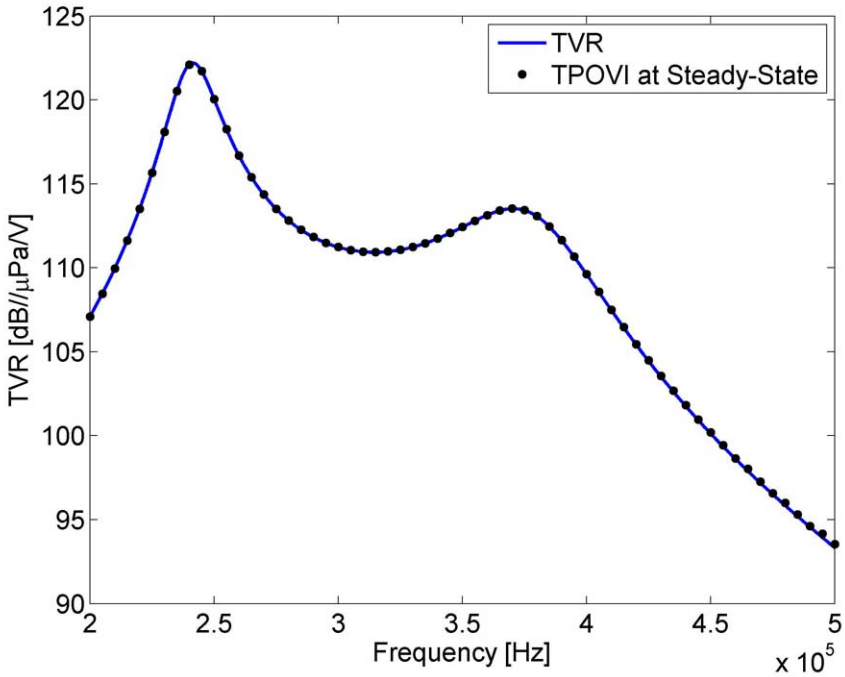

Figure 6.9: *TPOVI* at Steady-State and TVR Comparison for Matched Transducer

As figure 6.9 shows, excellent agreement is obtained between the steady-state section of the *TPOVI* and the TVR when the input sinusoid is a unity magnitude sinusoidal drive voltage. Therefore, it is illustrated that an accurate estimate occurs

between the established TVR theory, and the steady-state magnitude of the *TVOPI*.

6.2.3. Derivation of the *TVOPI* of the Matched Transducer

The *TVOPI* expression of the Matched transducer is derived in this section. As before, the equations describing the displacement, force, and voltage at the terminals of the transducer are used. These are given by equations 6.10 to 6.18. The expression for the *TVOPI* is found with these equations using the appropriate boundary conditions.

First, since there is no electrical load connected to the Matched transducer, this allows the setting of $Q = 0$. In addition, since the backing layer is composed of SADM, an acoustic absorber, any acoustic waves entering the backing layer are absorbed. Therefore $B_3 = 0$. Additional boundary conditions are determined from the continuity condition of displacement and force on the boundaries of the elements. Dependant on these boundary conditions, $\{A_1, B_1, A_2, B_2, A, B, A_3\}$ may now be solved using the following equations.

$$A_1 + B_1 = A_2 + B_2 \tag{6.28}$$

$$sZ_1[A_1 - B_1] = sZ_2[A_2 - B_2] \tag{6.29}$$

$$A_2 e^{-\frac{s}{v_2}L_m} + B_2 e^{\frac{s}{v_2}L_m} = Ae^{-\frac{s}{v}L_m} + Be^{\frac{s}{v}L_m} \tag{6.30}$$

$$sZ_2[A_2 e^{-\frac{s}{v_2}L_m} - B_2 e^{\frac{s}{v_2}L_m}] = sZ_c[Ae^{-\frac{s}{v}L_m} - Be^{\frac{s}{v}L_m}] \tag{6.31}$$

$$Ae^{-\frac{s}{v}(L_m+L)} + Be^{\frac{s}{v}(L_m+L)} = A_3 e^{-\frac{s}{v_3}(L_m+L)} \tag{6.32}$$

$$sZ_c[Ae^{-\frac{s}{v}(L_m+L)} - Be^{\frac{s}{v}(L_m+L)}] = sZ_3[A_3 e^{-\frac{s}{v_3}(L_m+L)}] \tag{6.33}$$

$$\bar{V} = h_{33}\Big[Ae^{-\frac{s}{v}L_m}(1 - e^{-\frac{s}{v}L}) + Be^{\frac{s}{v}L_m}(1 - e^{\frac{s}{v}L})\Big] \tag{6.34}$$

$$\bar{P} = \frac{sZ_1}{A_o}[A_1] \tag{6.35}$$

Solving this set of linear equations for $\bar{V}$ as a function of $\bar{P}$, the following expression for the *TVOPI*is obtained and given by equation 6.36.

$$C_1(s) = (Z_3 - Z_c) + (Z_3 + Z_c)e^{\frac{Ls}{v}}$$
$$C_2(s) = (Z_1 + Z_2)(Z_2 - Z_c)(Z_3 - Z_c)e^{\frac{2L_m(v+v_2)s}{vv_2}}$$
$$C_3(s) = (Z_1 - Z_2)(Z_3 - Z_c)(Z_2 + Z_c)e^{\frac{2L_m s}{v}}$$
$$C_4(s) = (Z_1 - Z_2)(Z_2 - Z_c)(Z_3 + Z_c)e^{\frac{2(L+L_m)s}{v}}$$
$$C_5(s) = (Z_1 + Z_2)(Z_2 + Z_c)(Z_3 + Z_c)e^{\frac{2(L_m(v+v_2)+Lv_2)s}{vv_2}}$$
$$\bar{V} = \left[\frac{4A_o h_{33} Z_2 e^{\frac{L_m(2v_2+v)s}{vv_2}}(1 - e^{\frac{Ls}{v}})C_1(s)}{s(C_2(s) + C_3(s) - C_4(s) - C_5(s))}\right]\bar{P} \tag{6.36}$$

Equation 6.36 is used to find the voltage output resulting from a pressure input for the Matched transducer.

6.2.4. *TVOPI* Validity Test for the Matched Transducer

In this section the *TVOPI* of the Matched transducer is tested. If the Matched transducer is driven with a finite cycle unity magnitude sinusoidal pressure, then the magnitude of the steady-state portion of the voltage output must be equal to the sensitivity of the transducer. The *TVOPI* has already validated in section 6.1. Therefore, a comparison of the steady-state portion of the *TVOPI* and the sensitivity of the transducer can be used to test the validity of *TVOPI* of the Matched transducer, not establish it.

The drive pressure used to conduct this study is a 40 cycle unity magnitude sinusoid at a frequency f. Iseger's numerical inversion routine from appendix A is used to obtain the time domain solution of the *TVOPI*.

Initially, a number of transient voltage waveforms are produced when the transducer is driven at various frequencies f. The first waveform is presented in figure 6.10. The frequency of the drive pressure producing this voltage waveform is at the anti-resonance frequency of the transducer, which occurs at $f = 270.5$kHz.

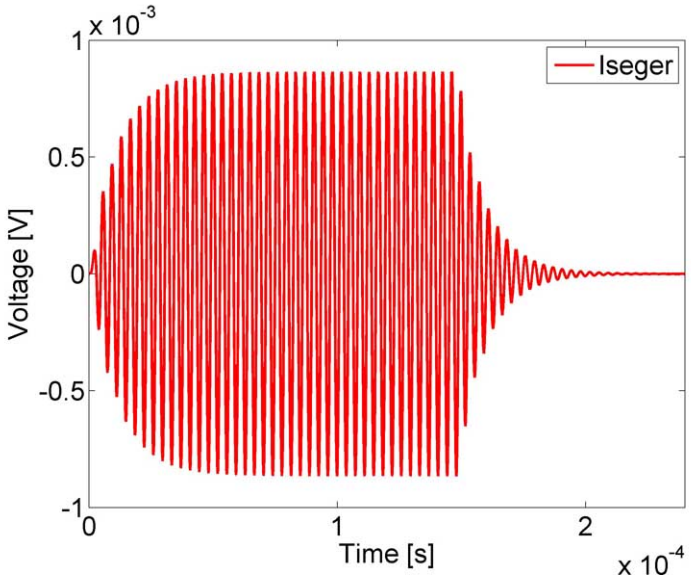

Figure 6.10: *TVOPI* for 1Pa 40 cycles Sinusoidal Driving Pressure at 270.5kHz

Figure 6.10 shows an exponential-like increase in magnitude for the rise time portion of the voltage output until the steady-state value is reached. After the drive pressure has completed, the ring time follows an exponential-like decay. This characteristic is common when the transducer is receiving a sinusoidal pressure excitation at its anti-resonance frequency.

Figures 6.11 and 6.12 show the voltage outputs obtained when the drive pressure is applied away from the anti-resonance frequency of the transducer.

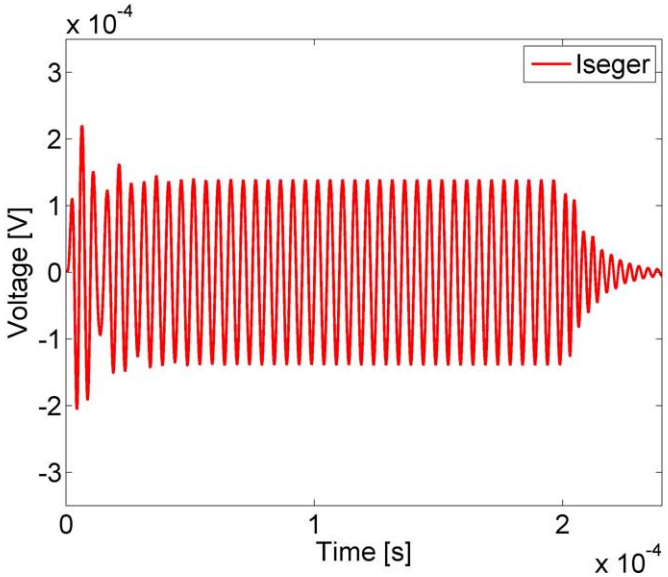

Figure 6.11: *TVOPI* for 1Pa 40 cycles Sinusoidal Driving Pressure at 200kHz

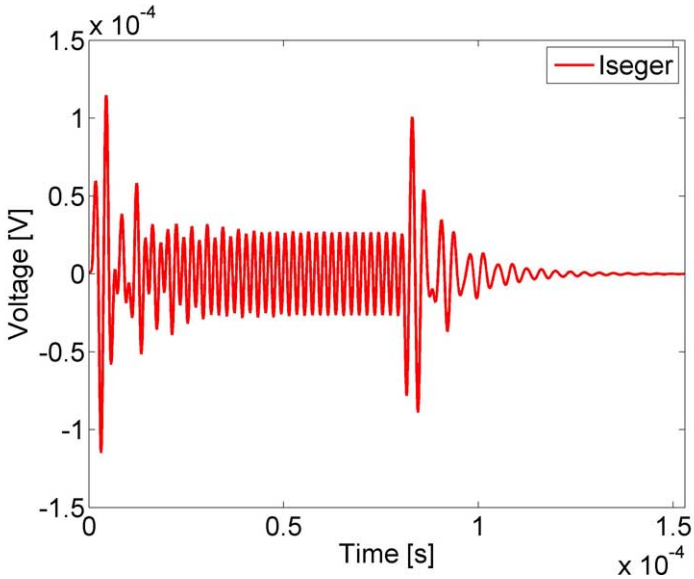

Figure 6.12: *TVOPI* for 1Pa 40 cycles Sinusoidal Driving Pressure at 500kHz

In figures 6.11 and 6.12, notice that the magnitude of the steady-state sections of the output voltages have a smaller magnitude than the magnitude of the steady-state sections of voltage obtained when the transducer is driven at its anti-resonance frequency, seen in figure 6.10. Additionally, the exponential-like behavior in the rise time and ring time sections of the transient voltage are no longer present. The transient characteristics seen in the rise time and ring time are a result of the complex acoustic wave interactions that take place inside the Matched transducer.

Using figures 6.10, 6.11 and 6.12, it is determined that after 30 cycles of the drive pressure have completed the steady-state value of the output voltage is reached. The maximum magnitude of the voltage waveform produced by the last 10 cycles of the drive pressure are used to determine the steady-state value of the *TVOPI*.

The sensitivity equation from section 2.7.4 is used to test the validity of the steady-state values obtained from the *TVOPI*, and the comparison between the sensitivty and steady-state values obtained from the *TVOPI* are presented in figure 6.13.

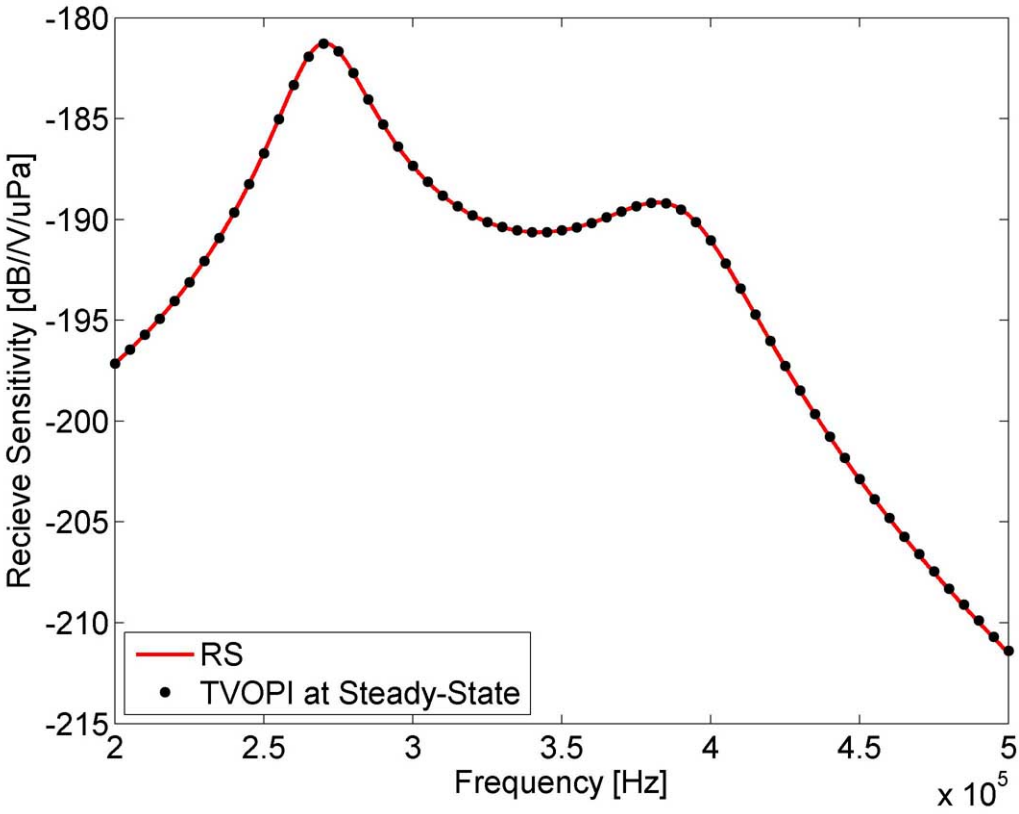

Figure 6.13: Steady-State *TVOPI* and the Receive Sensitivity for the Matched Transducer

Figure 6.13 shows that excellent agreement is obtained between the values of the *TVOPI* measured at steady-state resulting from a 1Pa sinusoidal pressure input as compared with the sensitivity of the transducer. Therefore, the validation of the *TPOVI* done in section 6.1 is correct.

6.3. Theoretical Validation of Transient Waveform Design

Given the novelty of the Drive Voltage Design method (DVDM), developed in section 5.3, creative methods are required to validate the DVDM.

The simplest way to validate the DVDM is to use the results obtained from Piquette. Piquette developed an analytic expression for the drive voltage necessary to produce a pure finite cycle sinusoidal pressure output from a spherical transducer

using a lumped circuit model of the transducer [10, 11]. The developed drive voltage is known as the transient suppression waveform. The study of this thesis focuses on the thickness mode transducer, but it is possible to utilize the results of Piquette to validate our numerical inversion methods and the *Inverse Filtering* technique. This analysis is completed in section 6.3.1.

Subsequently, an analytic expression for the drive voltage necessary to produce a pure finite cycle sinusoidal pressure waveform from a thickness mode transducer is modeled using the BVD model. A comparison is made of the results obtained using the DVDM to the analytic expression developed in order to show the robustness of the DVDM. This analysis is presented in section 6.3.2.

Having established the DVDM for 2^{nd}-order lumped circuit models of a transducer, the DVDM's performance is determined using the state-of-the-art distributed model, *TVOPI*, to model a transducer.

An in depth analysis of the drive signals obtained from the DVDM for a single element and an XTM transducer to output a finite duration square pulse of unity magnitude is completed in section 6.3.3.The analysis shows the flexibility of the DVDM to accurately output any desired pressure waveform from a multi-layered thickness mode acoustic transducer.

6.3.1. Lumped Circuit Transient Suppression Waveform Design of Spherical Transducer

The analytic drive voltage equation obtained from Piquette is utilized here to output a finite cycle pressure waveform from a spherical transducer in order to validate the numerical inversion routines and the theory of *Inverse Filtering* [10, 11]. This analysis is used to establish the DVDM when the transducer is modeled using a lumped circuit model.

The analytic drive voltage found by Piquette is based upon modeling the spherical transducer using a 2^{nd}-order lumped circuit model presented in figure 6.14.

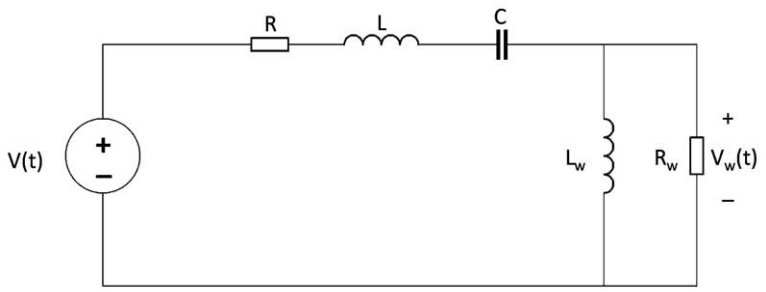

Figure 6.14: Lumped Circuit Model of Spherical Transducer

The voltage $V_w(t)$ is equivalent to the pressure waveform output of the spherical transducer. Therefore, $V_w(t)$ must be defined as a finite cycle sinusoidal waveform. Then, using circuit theory, the waveform $V_w(t)$ is used to determine, working backwards, the voltage input $V(t)$ needed to produce this waveform. The derivation of $V(t)$ has been completed in [10].

In order to conduct the comparison, the analysis is restricted to a 4 cycle sinusoidal waveform with frequency $\omega = 2\pi f$. The analytic equations for the output pressure, and input voltage producing this output pressure, are presented in equations 6.37 and 6.40.

$$V_w(t) = \begin{cases} 0 & \text{if } t < 0 \\ \frac{V_o}{R_w} sin(\omega t) & \text{if } 0 \leq t \leq \frac{4}{f} \\ 0 & \text{if } t > \frac{4}{f} \end{cases} \tag{6.37}$$

$$I(t) = \frac{V_o}{L_w \omega}[1 - cos(\omega)t)] + \frac{V_o}{R_w} sin(\omega t) \tag{6.38}$$

$$q(t) = \frac{V_o t}{L_w \omega} - \frac{V_o}{L\omega^2} sin(\omega t) + \frac{V_o}{R_w \omega}[1 - cos(\omega t)] \tag{6.39}$$

$$V(t) = \begin{cases} 0 & \text{if } t < 0 \\ L\frac{dI}{dt} + \frac{q}{C} + IR + V_o sin(\omega t) & \text{if } 0 \leq t \leq \frac{4}{f} \\ \frac{q(4/f)}{C} & \text{if } t > \frac{4}{f} \end{cases} \tag{6.40}$$

Then, in order to validate the numerical inversion routines, a Laplace domain expression is required which relates $V(t)$ to $V_w(t)$. Using the circuit model in figure 6.14, the necessary Laplace domain expressions are given by the following equations.

$$Z_{LCR} = R + sL + \frac{1}{sC} \tag{6.41}$$

$$\bar{V}_w(s) = \left[\frac{V_o\omega}{\omega^2 + s^2}\right]\left[1 - e^{-(4/f)s}\right] \tag{6.42}$$

$$\bar{V}(s) = \left[\frac{sL_wR_w}{R_wZ_{LCR} + sL_wZ_{LCR} + sL_wR_w}\right]\bar{V}_w(s) \tag{6.43}$$

The values listed below for $\{L, C, R, R_w, L_w, V_o\}$ are used to conduct the comparison between the results obtained using the numerical inversion of equation 6.43 and the analytic values obtained by Piquette. These are the same values used by Piquette to model the spherical transducer [11]:

$$\begin{aligned} L &= 5.79 && [mH] \\ C &= 30 && [\mu F] \\ R &= 5.04 && [\Omega] \\ R_w &= 114 && [\Omega] \\ L_w &= 5.55 && [mH] \\ V_o &= 1 && [V] \end{aligned}$$

Before the comparison of the analytic expression of the drive voltage given by equation 6.40 to what is obtained after doing the Laplace domain inversion of 6.43 is conducted, the output pressure obtained resulting from a sinusoidal drive voltage is shown. The output pressure waveform produced from a pure sinusoidal voltage input of 4 cycles at a frequency of 12kHz is shown in figure 6.15.

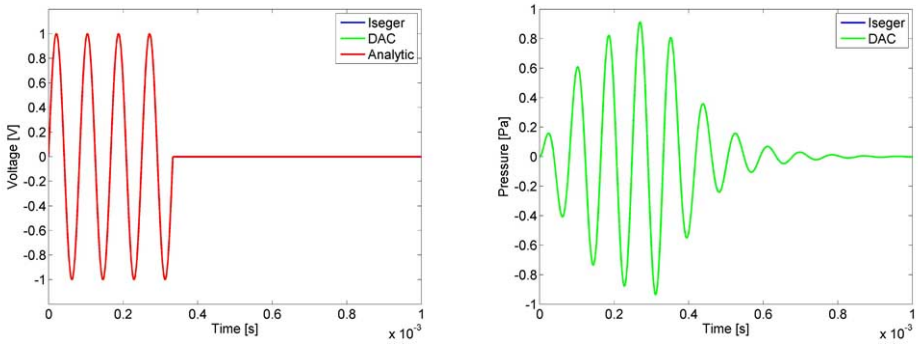

(a) Drive Voltage

(b) Pressure Output of Spherical Transducer

Figure 6.15: Drive Signal and Pressure Output of Spherical Transducer

Figure 6.15 shows the output signal obtained if the transducer was simply driven without doing any pre-shaping of the drive voltage. The pressure waveform contains no steady-state value because the 4 cycle drive voltage is too short to allow the steady-state value of the output pressure waveform to be reached.

A comparison is made of what is obtained from the analytic transient suppression waveform from equation 6.40 to the transient suppression waveform obtained using Iseger's and the DAC numerical inversion of equation 6.43. The comparison is given in figure 6.16.

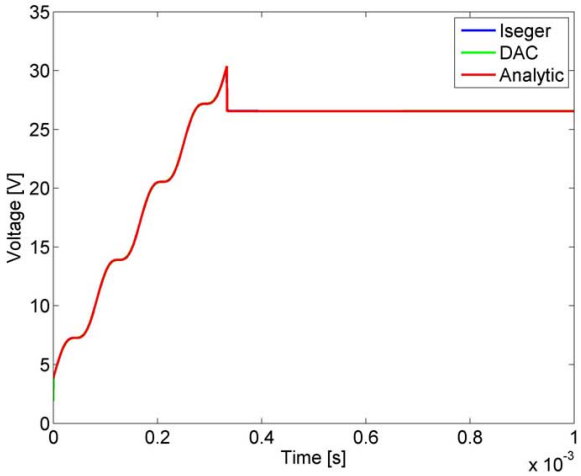

(a) Drive Signal

Figure 6.16: Transient Supression Waveform for $f = 12$kHz

As figure 6.16 shows, excellent agreement is obtained between the analytic values found by Piquette, and the results obtained from the numerical inversion of equation 6.43. This establishes that the numerical inversion routines are accurate and the DVDM is valid for spherical transducers modeled using a lumped circuit model.

6.3.2. Lumped Circuit Transient Suppression Waveform Design of Thickness Mode Transducer

In this section the same analysis as in section 6.3.1 is performed, but the BVD model of a thickness mode transducer is used instead of a lumped circuit model of a spherical transducer.

The analytic equation for the drive voltage necessary to produce a finite cycle sinusoidal pressure output is derived using the same method as that used by Piquette, which is to define the desired output pressure, and then use circuit theory to obtain an expression for the input voltage necessary to produce the output pressure.

The lumped circuit representation of a thickness mode transducer is presented in figure 6.17.

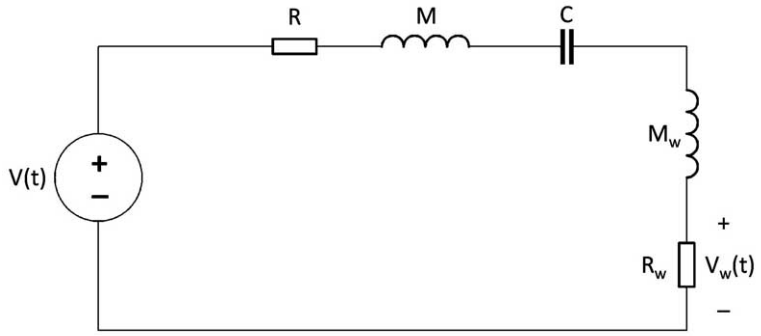

Figure 6.17: Lumped Circuit Model of Thickness Mode Transducer

The pressure output of the transducer is equivalent to the voltage $V_w(t)$ across the resistor R_w. Therefore, $V_w(t)$ is defined as a 4 cycle sinusoidal voltage with frequency f. Circuit theory is used to obtain the equation for $V(t)$ necessary to produce $V_w(t)$. $V(t)$ is given by equation 6.44.

$$V(t) = \begin{cases} 0 & \text{if } t < 0 \\ (\frac{RV_o}{R_w} + V_o)sin(\omega t) + (\frac{MV_o\omega}{R_w} + \frac{M_wV_o\omega}{R_w})cos(\omega t) + \frac{V_o}{CR_w\omega}[1 - cos(\omega t)] & \text{if } 0 \leq t \leq \frac{4}{f} \\ 0 & \text{if } t > \frac{4}{f} \end{cases} \tag{6.44}$$

The Laplace domain equation for $V(t)$, found from the circuit shown in figure 6.17, is given by equation 6.45.

$$\begin{aligned} \bar{V}_w(s) &= \left[\frac{V_o\omega}{\omega^2 + s^2}\right]\left[1 - e^{-(4/f)s}\right] \\ \bar{V}(s) &= \left[\frac{R_w}{R + sM + sM_w + R_w + 1/sC}\right]\bar{V}_w(s) \end{aligned} \tag{6.45}$$

To conduct the analysis, the following values are used for the circuit elements in figure 6.17:

$$\begin{aligned} M &= 2.94 && [H] \\ C &= 112.8 && [pF] \\ R &= 1611 && [\Omega] \\ R_w &= 2389 && [\Omega] \\ M_w &= 0.12 && [H] \\ V_o &= 1 && [V] \end{aligned}$$

The comparison of the drive voltage obtained from equation 6.44 to the drive voltage obtained by numerically inverting equation 6.45 to produce a 4 cycle 8.5kHz output pressure waveform, is shown in figure 6.18. Note that 8.5kHz is the resonance frequency of the transducer.

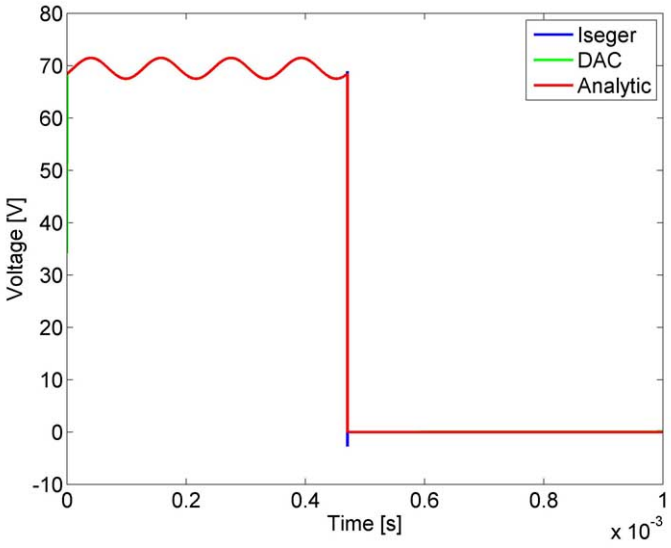

Figure 6.18: Lumped Circuit Thickness Mode Drive Voltage for $f = 8.5$kHz

Figure 6.18 shows that excellent agreement is obtained between the values found from the analytic expression, and the values obtained by numerically inverting equation 6.45.

The drive voltage obtained from the analytic and numerical routines to output a 4 cycle pressure waveform at a frequency of 5kHz and 20kHz is shown in figure 6.19.

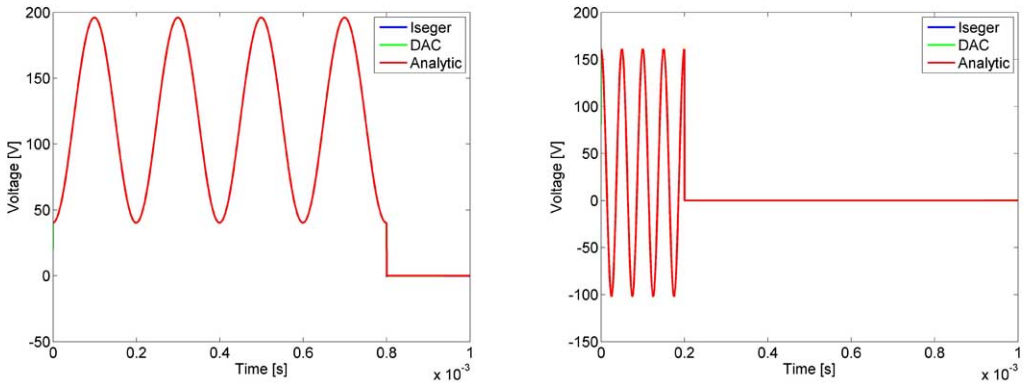

(a) Drive Voltage for $f = 5$kHz

(b) Drive Voltage for $f = 20$kHz

Figure 6.19: Lumped Circuit Transient Suppression Waveforms for Thickness Mode Transducer

As seen from figure 6.19, an excellent match between the analytic expression and the values found from the numerical routines occurs. Hence it is concluded from this

analysis that the *Inverse Filtering* works and that the numerical inversion routines are accurate. Furthermore, it is concluded that the DVDM is valid for thickness mode transducers modeled using a BVD lumped circuit model.

6.3.3. Distributed Model Transient Waveform Design

The DVDM developed in section 5.3 is used to produce a pure finite duration square output pressure from a single element transducer and an XTM transducer. The DVDM requires the *TPOVI* expression of the transducer, as well as the desired pressure output in the Laplace domain, defined by $\bar{P}$.

The single element transducer is analyzed first using equation 5.92 to obtain the *TPOVI* of the transducer. The desired finite duration square output pressure is defined, in the Laplace domain, by equation 6.46.

$$\bar{P} = \frac{1 - e^{-\tau T s}}{s} \tag{6.46}$$

The material parameters of the single element transducer are given by the following values:

$$\begin{aligned}
A_o &= 445.1 && [mm^2] \\
L &= 7.65 && [mm] \\
h_{33} &= 2.68 && [GV/m] \\
C_o &= 365.3 && [pF] \\
v_{pzt} &= 4003.3 && [m/s] \\
Z_{pzt} &= 13454.9 && [kg/s] \\
Z_1, Z_2 &= (1000)(1500)Ao && [kg/s] \\
\tau &= \frac{L}{v_{pzt}} = 1.9109 && [\mu s]
\end{aligned}$$

Z_1, Z_2 represent the backing and load impedance of the piezoelectric element. This list of material parameters is the same as for the piezoelectric element used in the XTM transducer from section 3.2.1, except that the mechanical, dielectric, and piezoelectric loss terms have been deliberately omitted. These loss terms are neglected

to simplify the analysis of the obtained drive voltages.

In order to conduct the analysis, two drive voltages are found for the piezoelectric element. The first is the drive voltage necessary to produce a square output pressure of unity magnitude for a duration of $T = 3.5\tau$. The second is the drive voltage necessary to produce a square output pressure of duration $T = 4\tau$. The necessary drive waveforms to produce the associated pressure outputs are presented in figures 6.20 and 6.21.

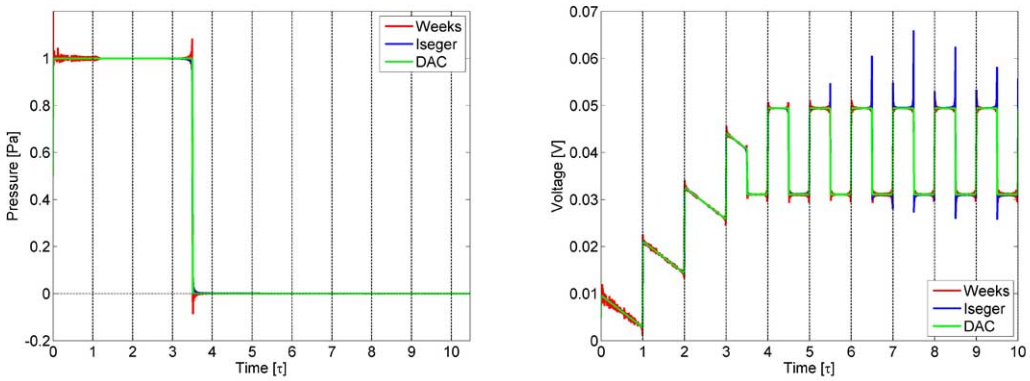

(a) Output Pressure $T = 3.5\tau$ [s] (b) Drive Voltage for T=3.5τ [s]

Figure 6.20: Distributed Model Transient Waveform Design $T = 3.5\tau$

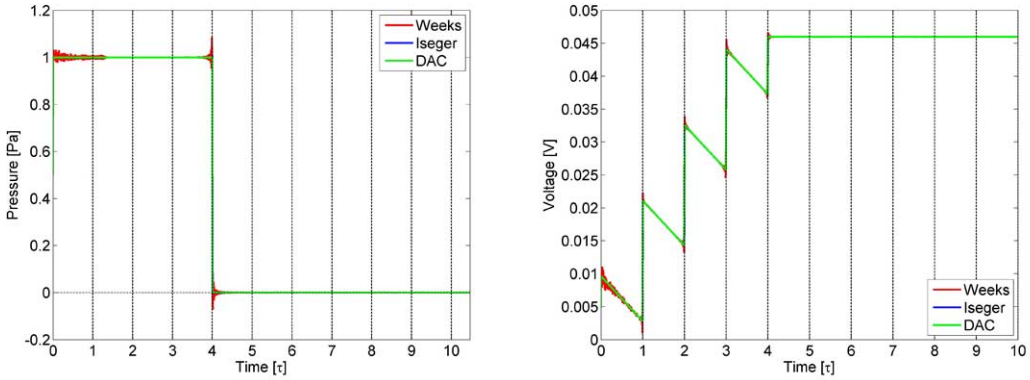

(a) Output Pressure $T = 4.0\tau$ [s] (b) Drive Voltage for T=4.0τ [s]

Figure 6.21: Distributed Model Transient Waveform Design $T = 4\tau$

Week's, Iseger's, and the DAC method are used to obtain the time domain solution of the drive voltage to determine if the numerical inversion routines are being performed correctly.

Referring to figures 6.20 and 6.21, it can be seen that Week's method contains many transients in the neighborhood $t = 0$ and, subsequently, wherever any discontinuities in the drive voltage occur. This is a common characteristic of the Week's method. Moreover, Iseger's method is similarly not accurate at points of discontinuity. This inaccuracy is a well known characteristic of this inversion routine. The DAC method is the only method that is accurate at determining the values at points of discontinues, as seen from figures 6.20 and 6.21. It should be noted, however, that the three inversion routines are in good agreement in regions away from the points of discontinuities. Therefore, it can be conclude that the numerical inversions have been calculated correctly, with the DAC method producing accurate results for the entire drive voltage waveform.

Referring to figure 6.20, an immediate jump in the drive voltage waveform occurs at time $t = 0$. This indicates the unity pressure output from the transducer. The jump at $t = \tau$ occurs due to the drive voltage acoustic wave interactions. The drive voltage must cancel the original produced acoustic wave produced from the back layer of the piezoelectric element.

More specifically, whenever a drive pulse is sent to the transducer, both the front layer and back layer are displaced in opposite directions. This causes each to produce an acoustic pulse of opposite sign. The acoustic pulse produced from the back layer reaches the front layer at time τ, the acoustic travel time in the element. Therefore, the drive voltage must cancel this acoustic pulse while maintaining the pressure output that is defined by $\bar{P}$.

The repeating square waveform seen in the drive voltage after 3.5τ is necessary to cancel the acoustic waves that occur in the piezoelectric layer. When the front layer is used to cancel an incoming acoustic pulse, the back layer is producing an acoustic pulse which must be canceled by the front layer at a time τ later. This illustrates the complex nature of the wave interactions occurring within the piezoelectric element.

From figure 6.21, notice that the drive voltage is held constant after a period of time 4τ. This occurs because there are no acoustic waves traveling in the piezoelectric element at that time. The transducer therefore is held in a fixed position whereby no more acoustic waves are produced.

Next the drive voltage necessary to produce a finite cycle unity magnitude pressure at a frequency f from the XTM transducer presented in section 3.2.1 with no mechanical, dielectric, and piezoelectric loss terms.

The *TPOVI* of the XTM transducer is given by equation 6.9 and the Laplace domain equation for the desired pressure is given by equation 6.46. The mechanical properties and dimensions for the XTM transducer are given by the following parameters:

$A_o = 445.1$	$[mm^2]$
$L = 7.65$	$[mm]$
$h_{33} = 2.68$	$[GV/m]$
$C_o = 365.3$	$[pF]$
$v = 4003.3$	$[m/s]$
$Z_c = 13454.9$	$[kg/s]$
$\tau = 1.9109$	$[\mu s]$
$Z_1 = 667.74$	$[kg/s]$
$Z_2 = 667.74$	$[kg/s]$
$L_2 = 0.9562$	$[mm]$
$v_2 = 4003.3$	$[m/s]$
$Z_3 = 466.52$	$[kg/s]$

Enough information is now presented to use Week's, Iseger's, and the DAC method to numerically invert equation 6.47 which describes the drive voltage, $\bar{V}(s)$, necessary to produce the finite duration square pulse from the XTM transducer.

$$\bar{V}(s) = \Big[\frac{1}{POVI}\Big] * \bar{P} \tag{6.47}$$

Figure 6.22 shows the drive voltage necessary to produce a square pulse of duration $T = 3.5\tau$, shown in figure 6.20(a), from the XTM transducer.

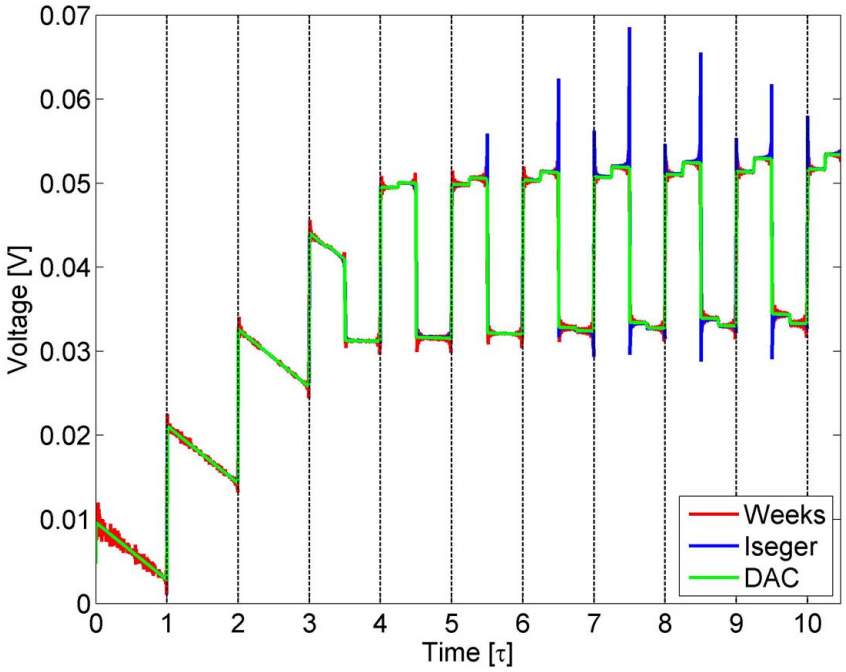

Figure 6.22: Distributed Model Transient Waveform Design for XTM Pressure Output of $T = 3.5\tau$

The drive voltage in figure 6.22 is similar to the drive voltage obtained for the single element case in figure 6.20(b), but there are noticeable differences. The first is that transients are now introduced from the second layer of the XTM transducer on the drive voltage. The drive voltage is more sophisticated than the one used for the single element transducer because of the complex acoustic wave interactions that take place in the multi-layer structure of the XTM transducer.

Thus, the state-of-the-art method of designing a drive voltage that can produce any desired output pressure waveform has been verified. The robustness of the method is shown by using the DVDM on both a single element and multi-element thickness mode acoustic transducer. The only inputs necessary to find the drive voltage are the desired pressure, the material parameters of the transducer, and its geometric dimensions.

Using the DVDM, transducer designs can be optimized to simplify the drive voltage necessary to output a specific pressure waveform. This method can also enhance the use of existing transducers by allowing outputs of sophisticated pressure waveforms, and since only the drive voltage needs to be modified, a single transducer can

be used for a number of different applications requiring complex pressure waveforms.

6.4. Variation in Voltage Response resulting from Material Parameter Variations

The easiest transient performance characteristic to measure experimentally is the voltage response, presented in section 5.2.2. Consequently, the voltage response is the preferred performance characteristic to use for the validation of the transient theory; however, before the voltage response can be used to validate the theory, it must be determined if the voltage response is effected by material parameter variations.

In this section the potential effect material parameter variations have on the voltage response of a single piezoelectric element is analyzed.

First the voltage response for a piezoelectric element lacking a backing or load material is developed. This model is used to show the effect any variations in the stiffness coefficient, mechanical loss, clamped permittivity, density, and drive frequency may have on the voltage response obtained.

6.4.1. Voltage Response of Single Piezoelectric Element

To find the voltage response of a single piezoelectric element, the Laplace domain equation of the electrical impedance of the element $\bar{Z}_{in}$, given by equation 5.76, is required. Note that the piezoelectric element is being tested in air, in which case $Z_B, Z_L = 0$ in the impedance equation.

The piezoelectric element is connected to a function generator with an internal impedance of $R = 50\Omega$ and the function generator is used to produce a pure N cycle unity magnitude sinusoidal pulse, $\bar{V}_g(s)$.

Equation 5.77 is used to obtain the voltage response of the piezoelectric element when driven with the function generator.

$$\bar{Z}_{in}(s) = \frac{1}{sC_o} - \frac{2h_{33}^2 tanh(\frac{Ls}{2v})}{s^2 Z_c} \tag{6.48}$$

$$\omega = 2\pi f \tag{6.49}$$

$$\bar{V}_g(s) = \frac{\omega}{s^2 + \omega^2}\left[1 - e^{-\frac{N}{f}s}\right] \tag{6.50}$$

$$\bar{V}(s) = \left[\frac{\bar{Z}_{in}}{R + \bar{Z}_{in}}\right]\bar{V}_g \tag{6.51}$$

The parameter N indicates the number of cycles the drive voltage has, and f indicates the frequency of the drive voltage.

To find the time domain solution of the voltage response, $\bar{V}(s)$, the numerical inversion routines presented in appendix A are used.

The original material parameters of the piezoelectric element are given by:

$$
\begin{aligned}
A_o &= 111.95 && [mm^2] \\
L &= 5.12 && [\text{mm}] \\
\rho &= 7240 && [kg/m^3] \\
\varepsilon_{33}^S &= (400.54 + i0.0) * 10^{-8} && [C/mV] \\
c_{33}^D &= (94.3 + i0.0) * 10^9 && [\text{Pa}] \\
h_{33} &= (3.2 + i0.0) * 10^9 && [V/m]
\end{aligned}
$$

The resonance frequency of the transducer occurs at 287kHz. Both the Iseger and DAC numerical inversion routines are used to determine the time domain voltage response of the transducer.

Figure 6.23 shows the voltage response obtained when the original material parameters of the transducer are used with an applied drive voltage at 287kHz.

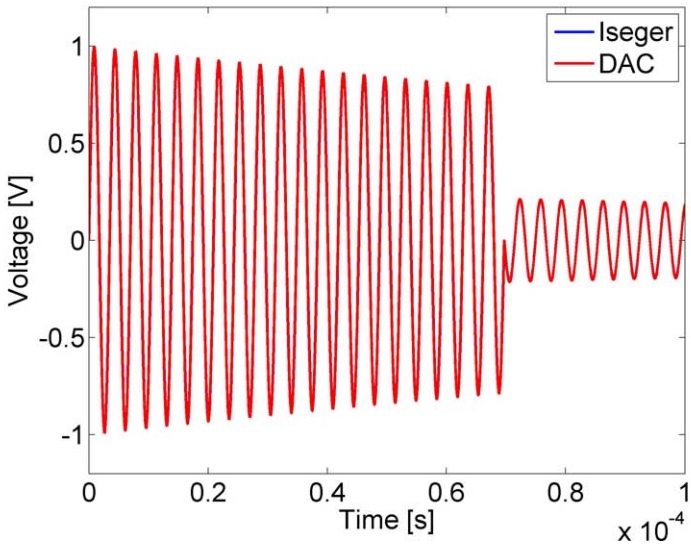

Figure 6.23: Voltage Response of Original Piezoelectric Element f=287kHz $N = 20$

Voltage Response resulting from c_{33}^D Variations

An analysis of how changes to c_{33}^D effect the voltage response of the piezoelectric element is conducted in this section. The stiffness coefficient c_{33}^D is the ratio of the force acting on the piezoelectric element to its displacement from equilibrium.

Figure 6.24 presents the voltage response of the transducer for a number of values of the parameter c_{33}^D. Note that figure 6.24(a) is the same as figure 6.23.

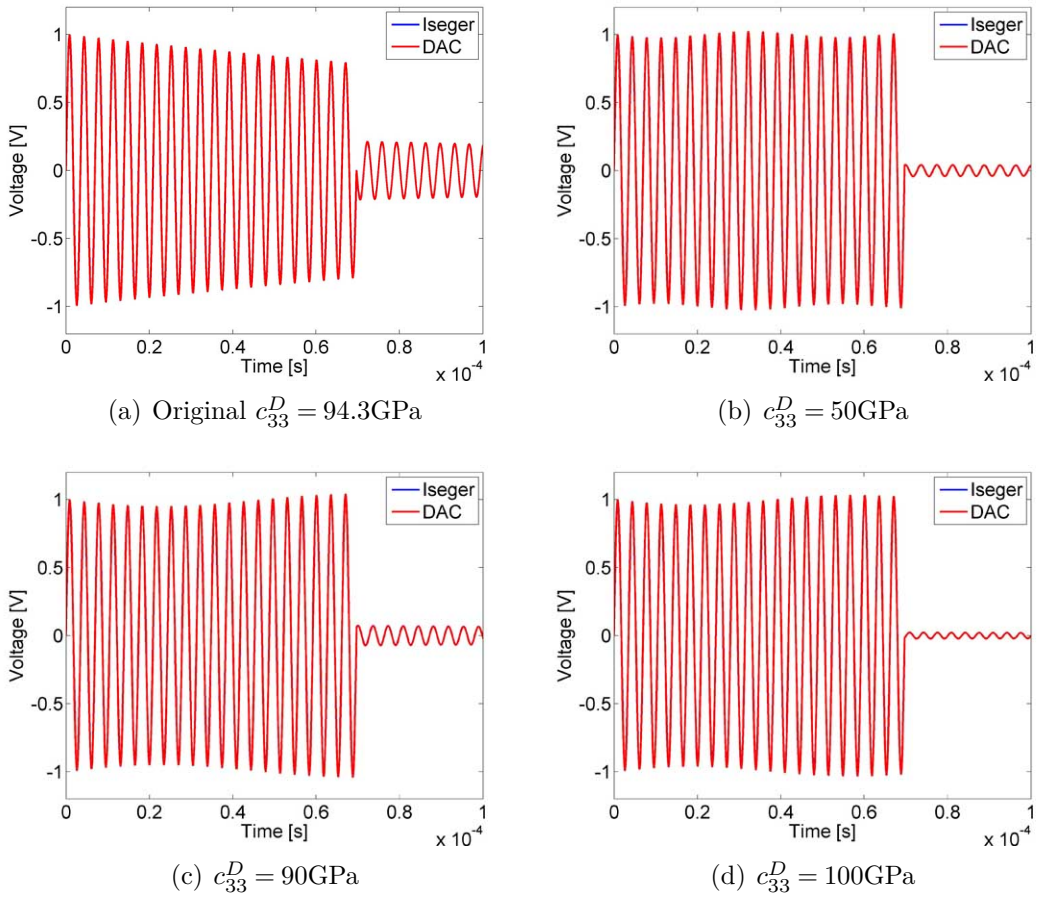

(a) Original $c_{33}^D = 94.3$GPa

(b) $c_{33}^D = 50$GPa

(c) $c_{33}^D = 90$GPa

(d) $c_{33}^D = 100$GPa

Figure 6.24: c_{33}^D variations effect on voltage response f=287kHz $N = 20$

Figure 6.24 shows that the ring time and the drive voltage portion of the voltage response is effected by the variation of c_{33}^D. The magnitude of the ring time is largest at the original value of c_{33}^D because this is the resonance frequency of the transducer. If the value of c_{33}^D changes, so does the resonance frequency of the transducer. Therefore, since the drive voltage is always at a frequency of 287kHz, if c_{33}^D changes, then the magnitude of the ring time decreases.

Voltage Response resulting from Mechanical Loss Variations

Mechanical losses may also effect the voltage response of the transducer. Figure 6.25 presents the voltage response for a number of different mechanical loss values which are introduced with the complex term in the stiffness coefficient. Note that figure 6.25(a) is equivalent to figure 6.23.

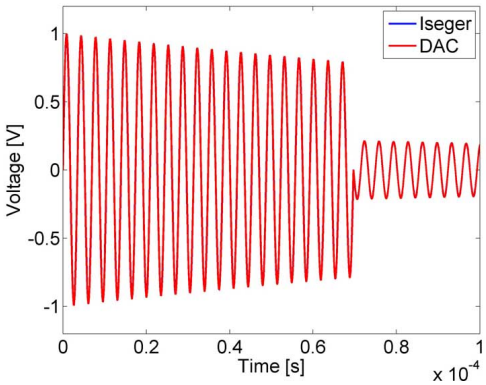

(a) Original with No Losses

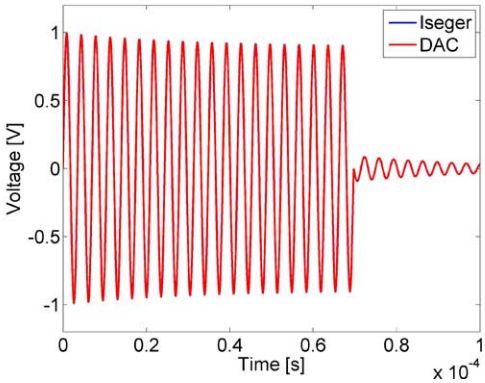

(b) $c_{33}^D = (65.4 + i2.0)$GPa

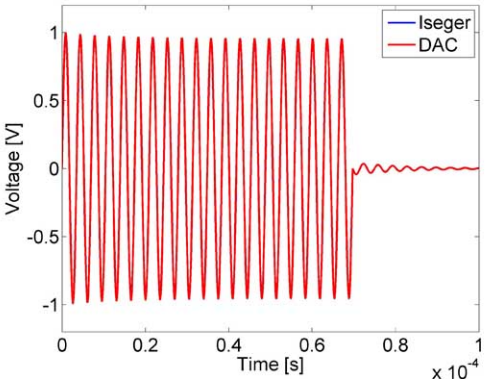

(c) $c_{33}^D = (65.4 + i5.0)$GPa

Figure 6.25: Mechanical Loss Variations effect on the voltage response f=287kHz $N = 20$

It is noticed that mechanical loss increases cause ring time decreases. This is illustrated in figure 6.25(a) and figure 6.25(c). This makes sense since increasing the amount of mechanical loss in the transducer causes faster dissipation of the energy stored in the transducer. The drive section of the voltage response also becomes more uniform in magnitude as the mechanical loss in the transducer is increased, as seen in figure 6.25.

Voltage Response resulting from Clamped Permittivity Variations

The effect making variations to the clamped permittivity K_{33}^S have on the voltage response of the transducer is analyzed in this section.

Figure 6.26 shows the voltage response for a number of values of K_{33}^S. Note that figure 6.26(a) is equivalent to figure 6.23.

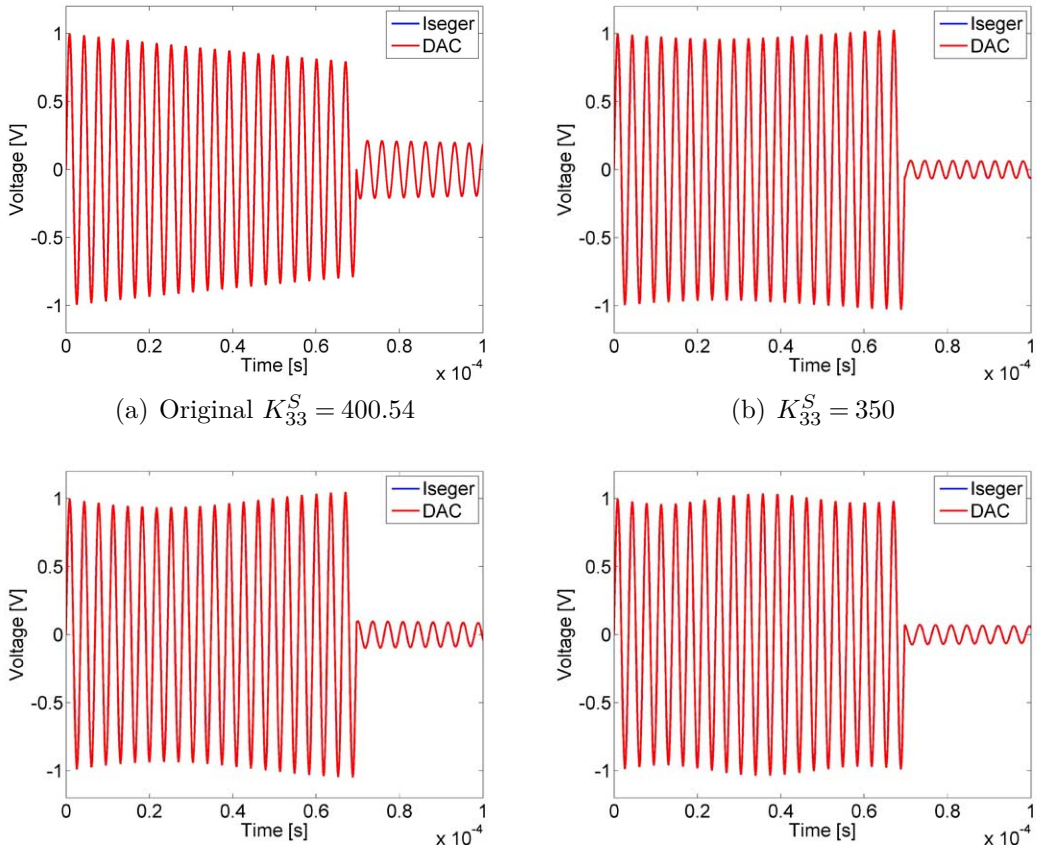

(a) Original $K_{33}^S = 400.54$ (b) $K_{33}^S = 350$

(c) $K_{33}^S = 450$ (d) $K_{33}^S = 500$

Figure 6.26: K_{33}^S Variations effect on the voltage response f=287kHz $N = 20$

Figure 6.26 shows that the value of K_{33}^S effects the shape and amplitude of the driving voltage section as well as the ring time section of the voltage response. The reason for this is that the resonance frequency of the transducer depends upon the value of K_{33}^S. Therefore, since the drive voltage of the transducer is always at f=287kHz, any modifications to K_{33}^S from the original value in figure 6.23 result in an immediate decrease in the magnitude of the ring time.

Voltage Response resulting from Density Variations

To determine how making changes to the density effects the voltage response, figure 6.27, which shows the voltage response obtained for a number of values of ρ, is used. Note that the original value of ρ is $7240kg/m^3$.

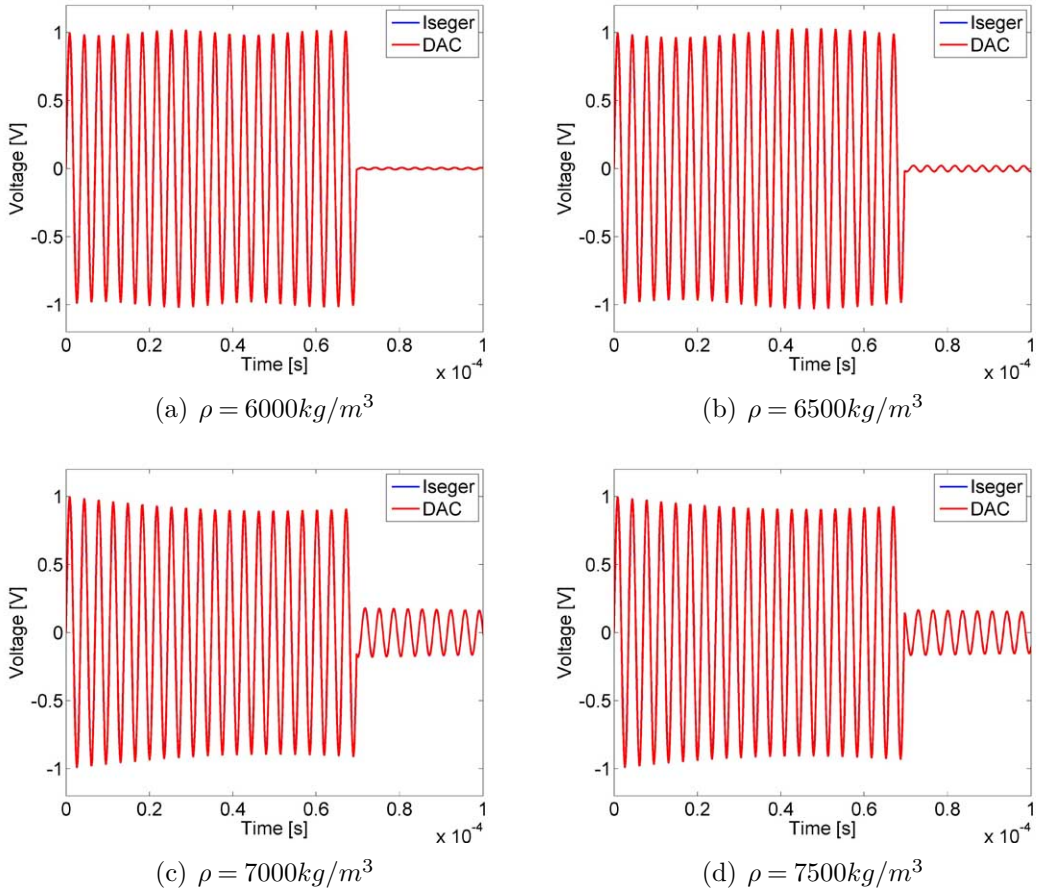

(a) $\rho = 6000kg/m^3$ (b) $\rho = 6500kg/m^3$

(c) $\rho = 7000kg/m^3$ (d) $\rho = 7500kg/m^3$

Figure 6.27: ρ Variations effect on the voltage response f=287kHz $N = 20$

Notice that the driving voltage section of the voltage response changes resulting from changes to the value of ρ, as seen from figures 6.27(d) and 6.27(e) as compared with figure 6.23.

Large variations in the value of ρ cause noticeable changes between the ring time sections of figures 6.27(b) and 6.27(c) as compared with the ring time section in figure 6.23. In this case the transducer is being driven with a drive voltage at a frequency of 287kHz, the resonance frequency of the original transducer. If the value ρ is varied, the resonance frequency of the transducer also varies. Therefore, when ρ

is varied from its original value, a reduction in ring time is expected.

Voltage Response resulting from Drive Frequency Variations

It is clear that variations to the drive frequency would effect the voltage response, but what effects are present is not clear from the complex nature of the wave interactions in the material. To gain insight into how the frequency variation effects the voltage response, a number of voltage responses are determined for different driving frequencies.

Figure 6.28 shows the voltage response obtained for a number of different driving frequencies. Note that the orginal drive frequency occurs at $f = 287\text{kHz}$.

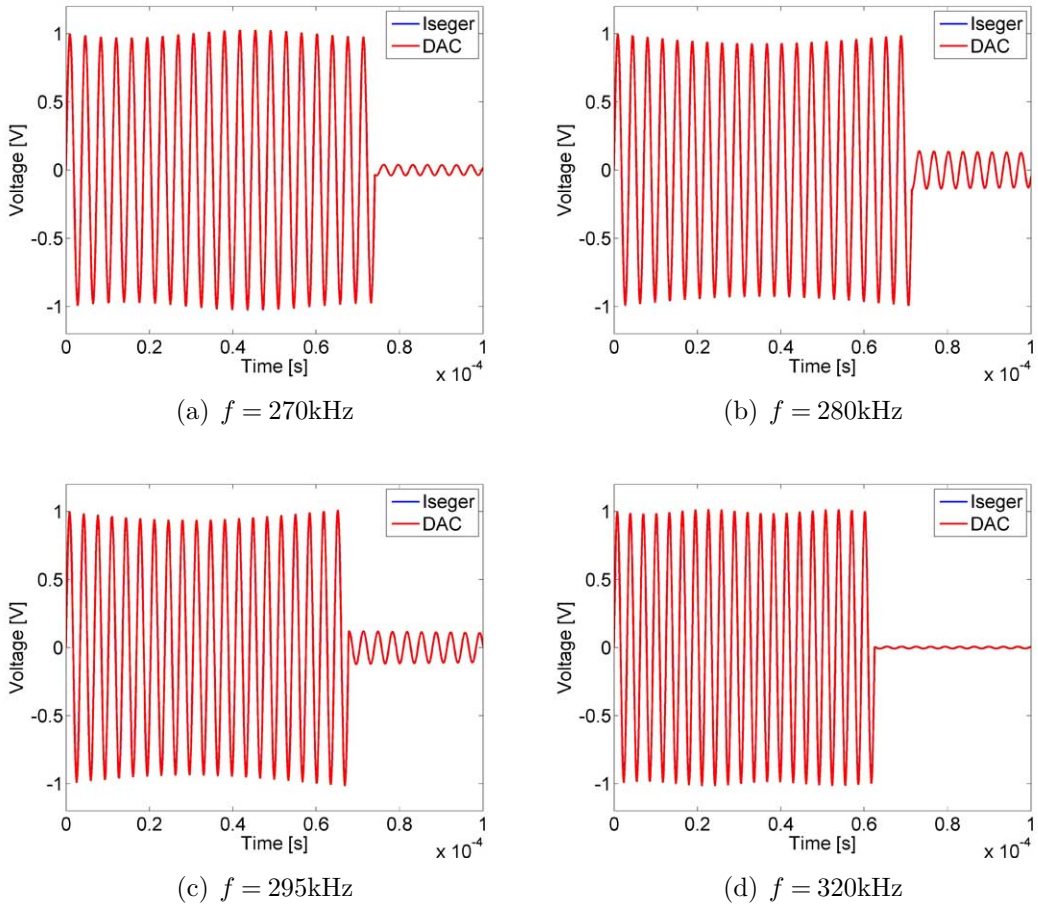

(a) $f = 270\text{kHz}$ (b) $f = 280\text{kHz}$

(c) $f = 295\text{kHz}$ (d) $f = 320\text{kHz}$

Figure 6.28: f Variation effect on the voltage response $N = 20$

Figure 6.28 shows that if f is varied, the shape of the drive section, and the ring section of the voltage response, also vary.

If figure 6.23 is compared with figures 6.28(b) and 6.28(e), it is noticed that as the frequency of the drive voltage is moved away from the resonance frequency of the transducer, the magnitude of the ring time decreases, as expected.

6.4.2. Conclusion of Sensitivity of Voltage Response to Parameter Variation

The analyses above show that the parameters c_{33}^{D}, K_{33}^{S}, and ρ all effect the voltage response of the transducer. When the frequency of the drive voltage is varied away from the resonance frequency of the transducer, a noticeable decrease occurs in the magnitude of the ring time. It is established, therefore, that the voltage response is both material and frequency dependent. The voltage response may therefore be used to experimentally verify the transient theory.

6.5. Experimental Validation of the Voltage Response

Experimental verification of the voltage response of a single piezoelectric element transducer indicates that the distributed transient models developed are accurate. The validation of the transient voltage response provides indirect validation of the other transient performance characteristics because they all rely on the equations of displacement, force, and voltage, which are all used to model the piezoelectric element as seen in chapter 5. The piezoelectric element used is composed of a piezocomposite material. This is the first time that the transient voltage response is being used to model a piezocomposite material.

An in depth study is performed to verify the accuracy of the theoretically developed voltage response. The analysis begins by driving the piezoelectric element at its resonance frequency. The drive voltage used is finite cycle sinusoid. A number of drive cycles, and amplitudes, are used to validate the accuracy of the voltage response when the transducer is being driven at its resonance frequency. This analysis is conducted in section 6.5.1.

Then, an analysis of the voltage response is conducted when the drive signal is delivered at the anti-resonance frequency of the piezoelectric element. A number of drive cycles are used to validate the accuracy of the voltage response at the anti-resonance frequency of the transducer. This analysis is done in section 6.5.2.

In order to verify the linear response of the piezoelectric element, the drive voltage

is adjusted at a constant frequency and the theoretically and experimentally obtained data are compared. If the transducer is linear, the voltage response from theory, and from experimentation, must remain equal. All that should change is the amplitude of the voltage response waveform. This linearity check is conducted in section 6.5.3.

The analysis is concluded with a study of what takes place when the frequency of the drive voltage is varied away from the resonance and anti-resonance frequencies of the piezoelectric element. This analysis is conducted in section 6.5.4.

Initially, the material parameters of the piezocomposite element must be determined. It has already been established that the impedance and admittance curves can be used to obtain the material parameters of the piezocomposite element, as shown in section 3.1. Therefore, they are used in this regard. The fit used to obtain the material parameters is presented in figures 6.29(a) and 6.29(b).

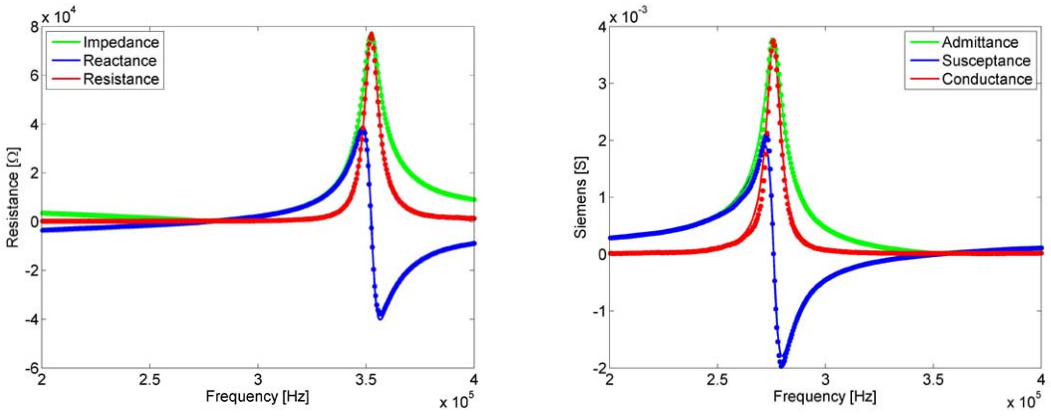

(a) Impedance (b) Admittance

Figure 6.29: Impedance and Admittance of Single Element Piezocomposite Material

The material parameters of the piezocomposite element are given by:

$$A_o = 1.1195 * 10^{-4} \quad [m^2]$$
$$L = 5.12 * 10^{-3} \quad [\mathrm{m}]$$
$$\rho = 7240 \quad [kg/m^3]$$
$$\varepsilon_{33}^S = (400.54 + i15.739) * 10^{-8} \quad [C/mV]$$

$$c_{33}^{D} = (94.3 + i2.22) * 10^{9} \quad [\text{Pa}]$$
$$h_{33} = (3.20 + i0.092) * 10^{9} \quad [V/m]$$
$$Co = (8.7576 - i0.34412_{*}10^{-11} \quad [\text{F}]$$
$$v = 3609.2 + i42.47 \quad [m/s]$$

Note that all the experimental measurements are done in air. Other details of the experimental setup used to conduct the voltage response analysis are presented in figure 6.30.

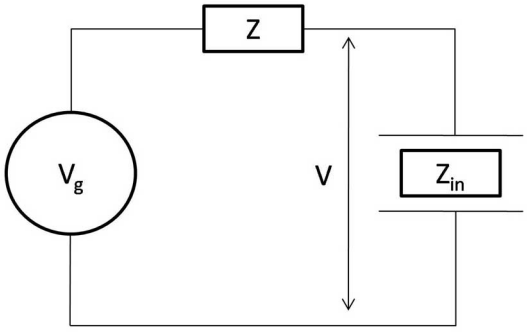

Figure 6.30: Experimental Setup for Voltage Response

In figure 6.30, the parameter V_g represents the input voltage from a Tektronix AFG-310 Function Generator. Z is the internal impedance of the function generator and is equal to 50Ω. V is the voltage response of the piezocomposite element. The voltage V, in figure 6.30, is measured by a Tektronix TDS-3034B Oscilloscope.

A number of voltage response cases are considered in this analysis and the Laplace domain expression describing the voltage response is given by equation 6.55.

$$\bar{Z}_{in}(s) = \frac{1}{sC_o} - \frac{2h_{33}^{2} tanh(\frac{Ls}{2v})}{s^{2} Z_c} \tag{6.52}$$
$$\omega = 2\pi f \tag{6.53}$$
$$\bar{V}_g(s) = A\frac{\omega}{s^{2} + \omega^{2}}\Big[1 - e^{-\frac{cyc}{f}s}\Big] \tag{6.54}$$
$$\bar{V}(s) = \Big[\frac{\bar{Z}_{in}}{R + \bar{Z}_{in}}\Big]\bar{V}_g \tag{6.55}$$

A is the amplitude of the drive signal. f is the frequency of the drive signal, and cyc is the number of cycles of the input sinusoidal drive voltage.

6.5.1. Piezocomposite Element Voltage Response at Resonance

The theoretically and experimentally obtained voltage responses for a number of different drive voltages centered at the resonance frequency of the piezocomposite element are compared. Since the drive voltage is at the resonance frequency of the piezocomposite element, the ring time of the obtained waveform is expected to be large. Using figure 6.29(b), the resonance frequency of the transducer occurs at $f = 276\text{kHz}$.

Figure 6.31 shows the voltage response of the piezocomposite element resulting from a 30 cycle sinusoidal drive voltage with an amplitude of 8V at a frequency of 276kHz.

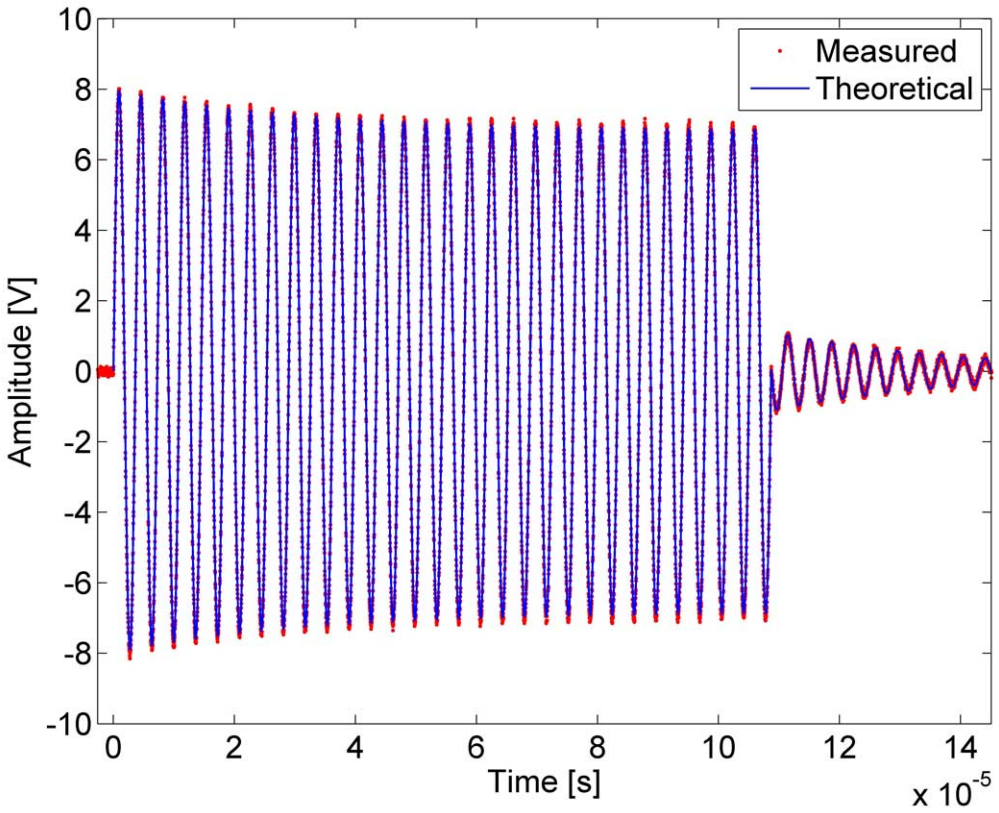

Figure 6.31: 276kHz Sinusoidal Pulse with 30 cycles at 8V

Initially there is a drop in magnitude of the measured voltage V. This magnitude eventually reaches a steady-state value after approximately 12 cycles. Refer to fig-

ure 6.31. Immediately after the 30 cycle pulse is complete, the magnitude drops, but does not decay very quickly. This is in agreement with the expectation that the ring time would be large at the resonance frequency of the transducer. Figure 6.31 shows that the experimentally measured and theoretical predicted voltage responses of the piezocomposite element are in close agreement with each other.

Next, a drive voltage with an amplitude of 10V and 20 cycles is used. The voltage response for this case is presented in figure 6.32.

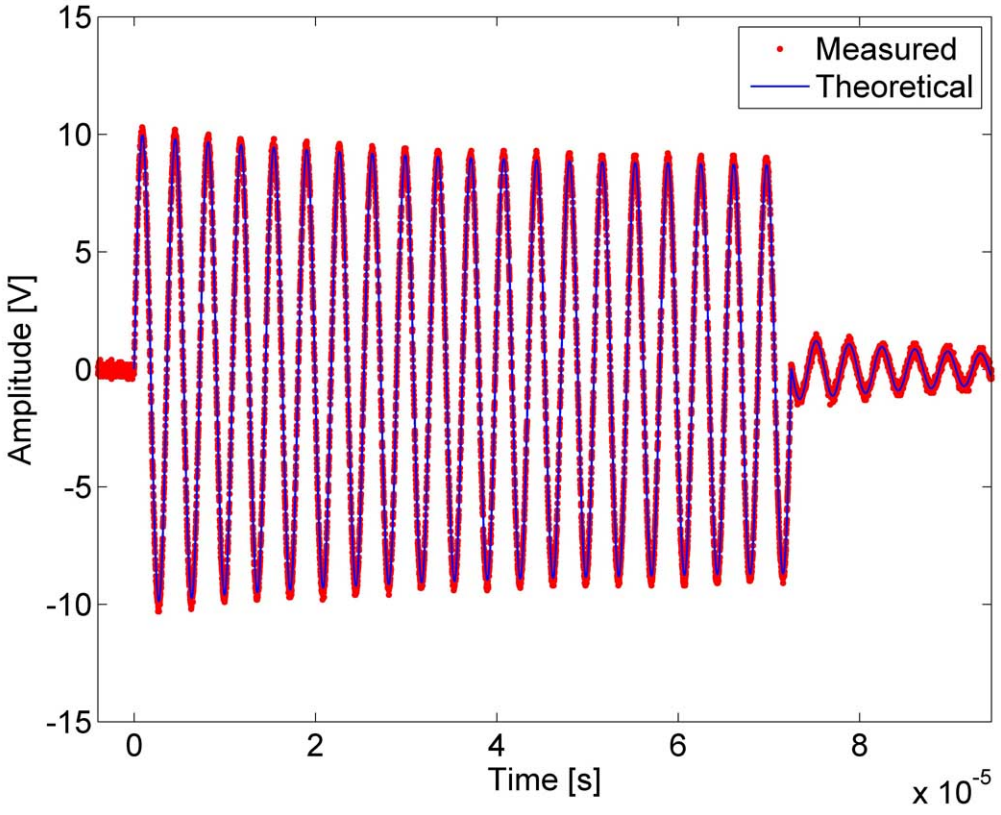

Figure 6.32: 276kHz Sinusoidal Pulse with 20 cycles at 10V

Figure 6.32 shows that the theoretically predicted and experimentally measured voltage responses are in very good agreement for the drive voltage section of the voltage response. In order to determine the accuracy of the ring time section, the attention must be focused more closely on the ring time section of figure 6.32. This is presented in figure 6.33.

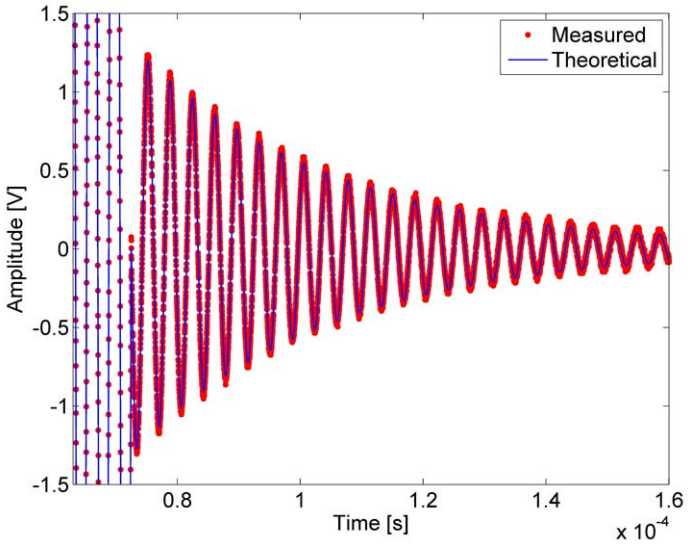

Figure 6.33: 276kHz Sinusoidal Pulse with 20 cycles at 10V Ring Section

Figures 6.32 and 6.33 illustrate a good match between the theoretically predicted voltage response and the experimental measured voltage response for a drive voltage of 20 cycles.

Figures 6.34 and 6.35 show the voltage response obtained for a 10V 10 cycle drive voltage. Note that figure 6.35 is the ring time of the voltage response shown in figure 6.34.

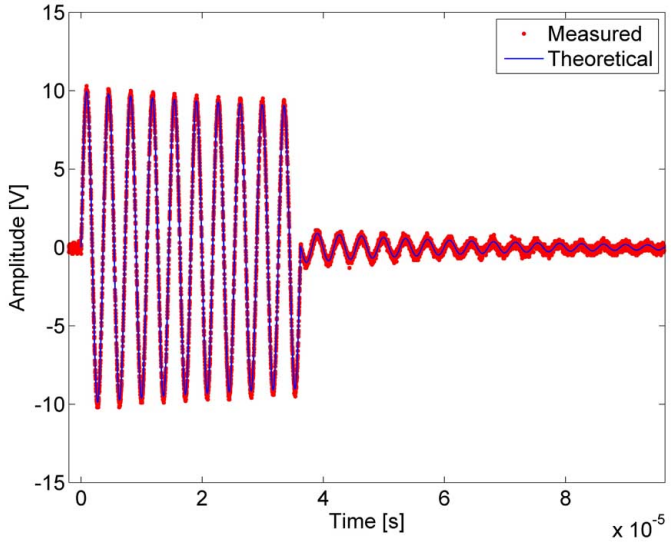

Figure 6.34: 276kHz Sinusoidal Pulse with 10 cycles at 10V

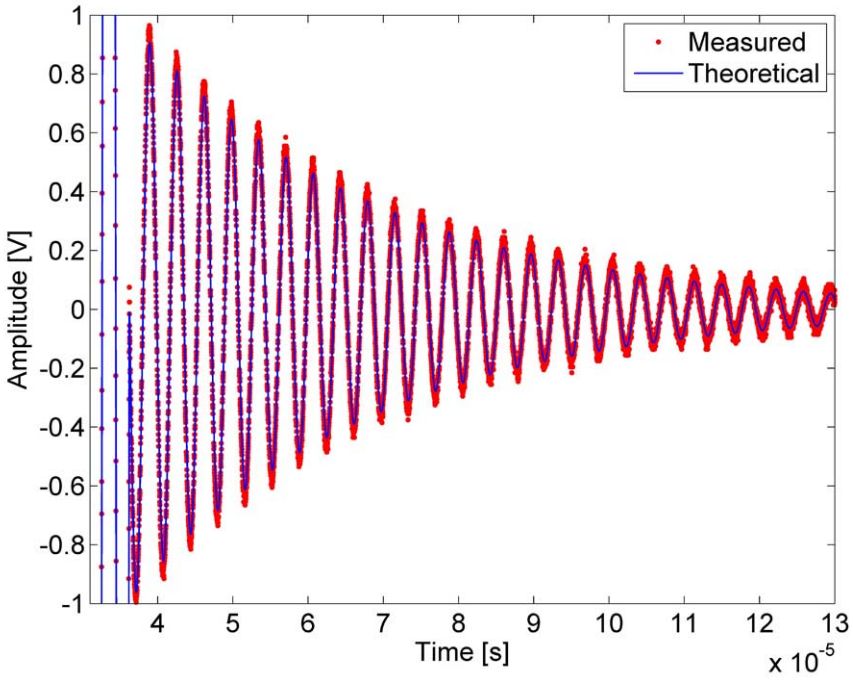

Figure 6.35: 276kHz Sinusoidal Pulse with 10 cycles at 10V Ring Section

It takes about 12 cycles for the voltage response to reach its steady-state value at the resonance frequency of the transducer. Therefore, when the drive voltage is only 10 cycles long, the steady-state section of the voltage response is not reached. Figures 6.34 and 6.35 show that excellent agreement is obtained between the experimentally measured and theoretically predicted voltage response of the piezocomposite element.

The voltage response obtained when a drive voltage of 1 cycle with an amplitude of 8V is shown in figures 6.36 and 6.37. Note that figure 6.37 is the ring time for the 1 cycle drive voltage.

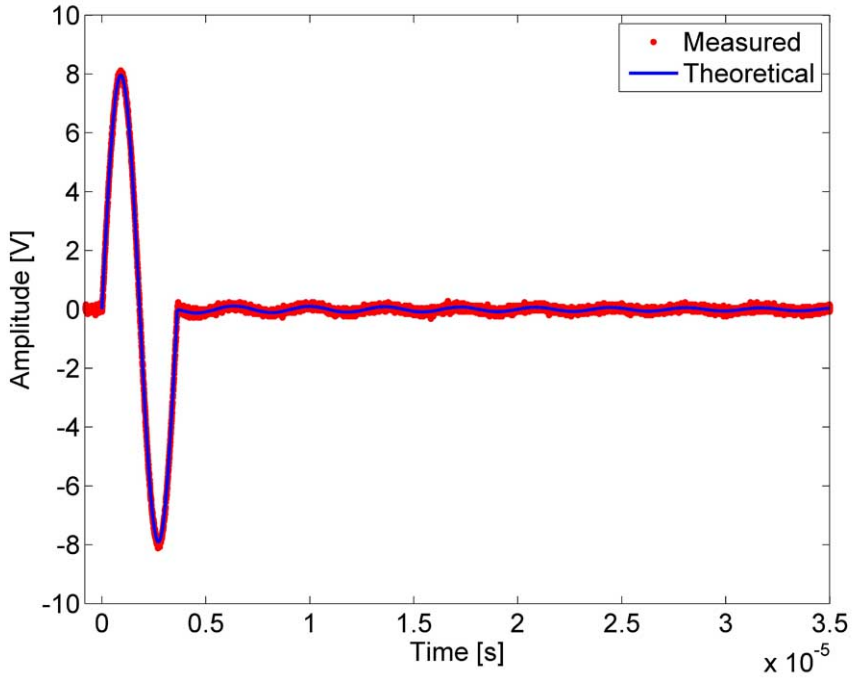

Figure 6.36: 276kHz Sinusoidal Pulse with 1 cycle at 8V

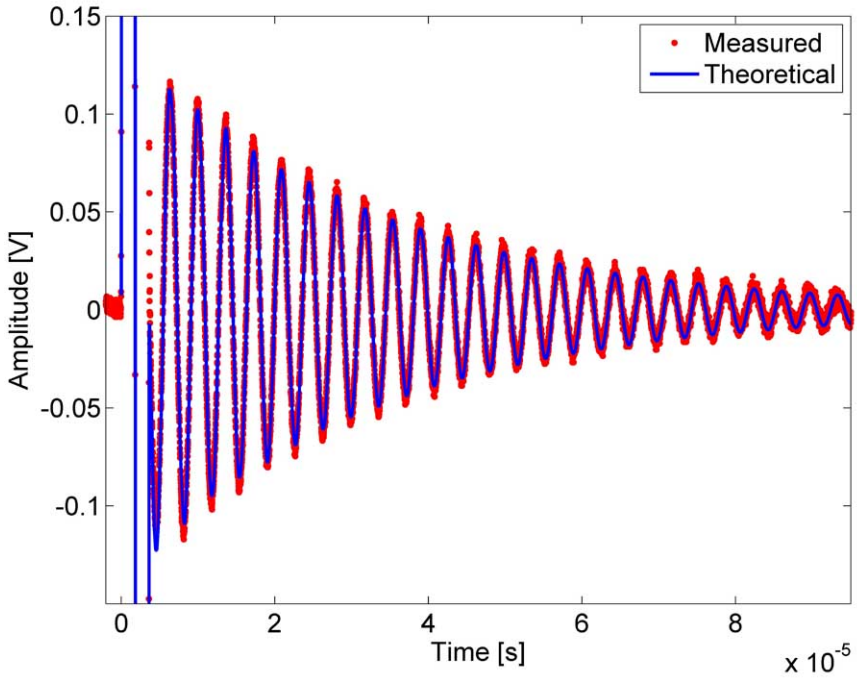

Figure 6.37: 276kHz Sinusoidal Pulse with 1 cycle at 8V Ring Section

Figures 6.36 and 6.37 show once again that the measured and theoretically obtained voltage responses of the piezocomposite element are in excellent agreement with each other.

6.5.2. Piezocomposite Element Voltage Response at Anti-Resonance

In this section the drive voltage is driven at the anti-resonance frequency of the piezoelectric element, which occurs at $f = 352.5$kHz. At the anti-resonance frequency of the transducer, a very short ring time is expected in the voltage response. Furthermore, a very sharp drop in magnitude after the drive voltage is stopped is also expected.

A 10V 30 cycle drive voltage is used and the corresponding voltage response is shown in figure 6.38.

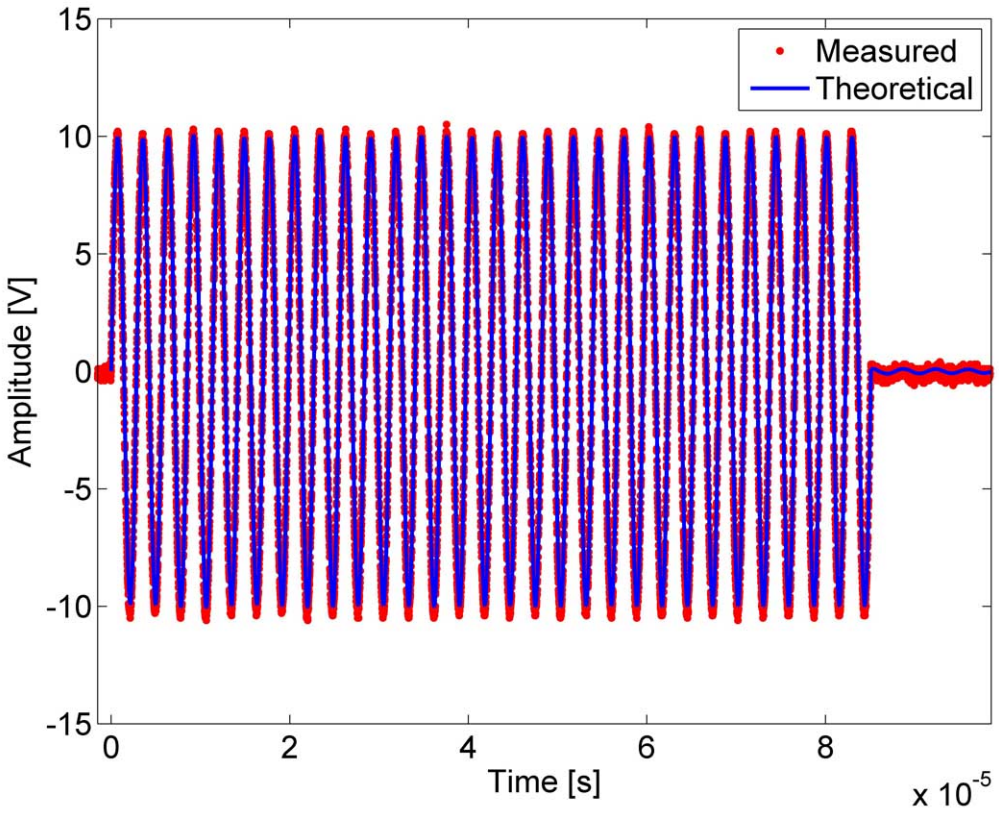

Figure 6.38: 352.5kHz Sinusoidal Pulse with 30 cycles at 10V

As expected, there is almost no variation in the magnitude of the voltage response,

as seen from figure 6.38. Figure 6.39 illustrates the ring time section of the voltage waveform shown in figure 6.38.

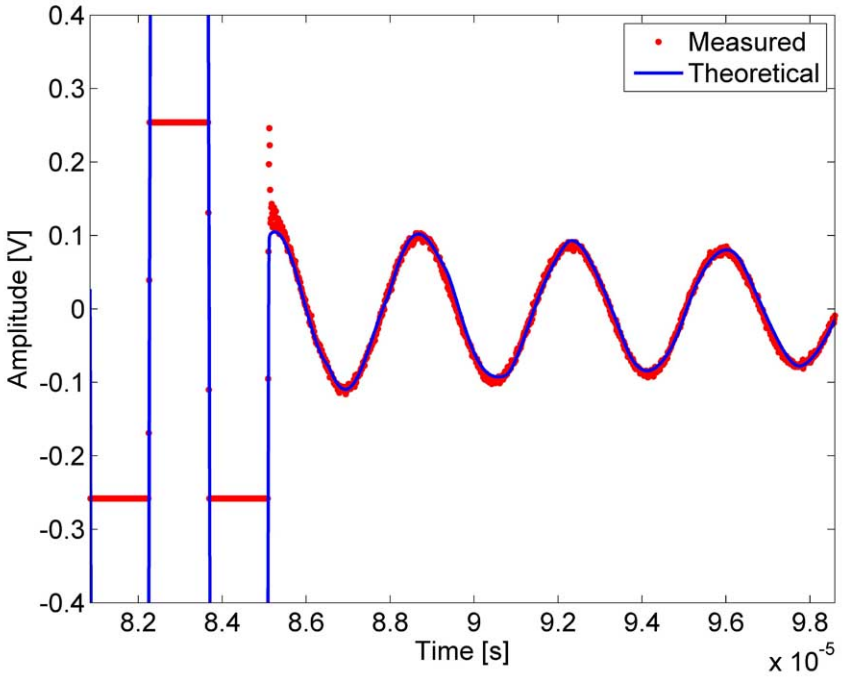

Figure 6.39: 352.5kHz Sinusoidal Pulse with 30 cycles at 10V Ring Section

Note that the horizontal red lines in figure 6.39 are caused by the saturation of the oscilloscope at this voltage resolution. As seen from figures 6.38 and 6.39, the experimentally measured voltage response is well matched with the theoretically predicted voltage response for both the voltage drive section and ring section of the waveform.

Next, the voltage response obtained from a 10V 1 cycle drive voltage is analyzed. An illustration of the corresponding voltage response waveform is shown in figures 6.40 and 6.41 .

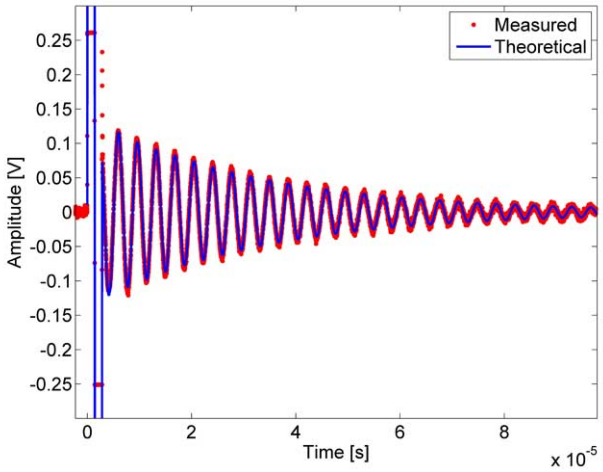

Figure 6.40: 352.5kHz Sinusoidal Pulse with 1 cycle at 10V

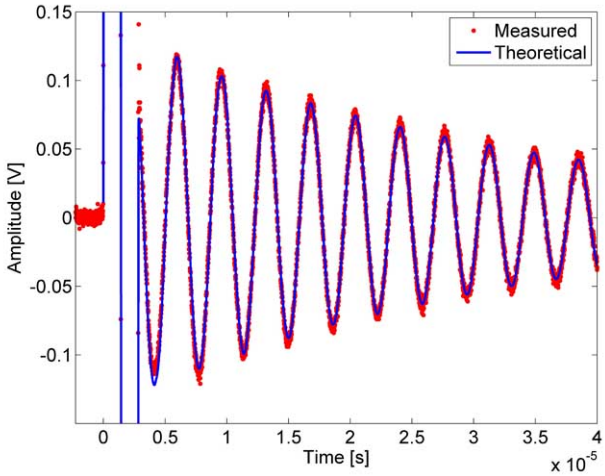

Figure 6.41: 352.5kHz Sinusoidal Pulse with 1 cycle at 10V Start of Ring Section

In figures 6.40 and 6.41, notice that after the drive voltage stops, the magnitude of the ring time is very close to the value that was obtained with the 30 cycle pulse presented in figure 6.38. The ring time is also similar to the magnitude of the ring time occurring immediately after a 1 cycle drive voltage is used at the resonance frequency of the transducer, as shown by comparing figures 6.37 and 6.41. Note that the waveform in figure 6.37 is produced from an 8V drive voltage.

The reason the magnitude of the ring time is small is that the transducer stores very little energy when these drive voltages are used. At the anti-resonance frequency, the acoustic waves in the piezocomposite element interfere destructively. Also, very

little energy is delivered to the transducer when only a single cycle drive voltage is used.

6.5.3. Piezocomposite Element Voltage Response at Constant Frequency with Amplitude Variation

The resultant effects of drive amplitude variation upon the voltage response of the piezocomposite element are analyzed in this section. The study is conducted at the resonance frequency of the transducer. This analysis is used to determine if the piezocomposite element is operating linearly for over a range of drive voltages. Note that only the ring time of the waveform is presented for this analysis because the transient characteristics are clearly apparent when one looks at the ring time.

The results of the amplitude variation of the drive voltage are presented in figure 6.42.

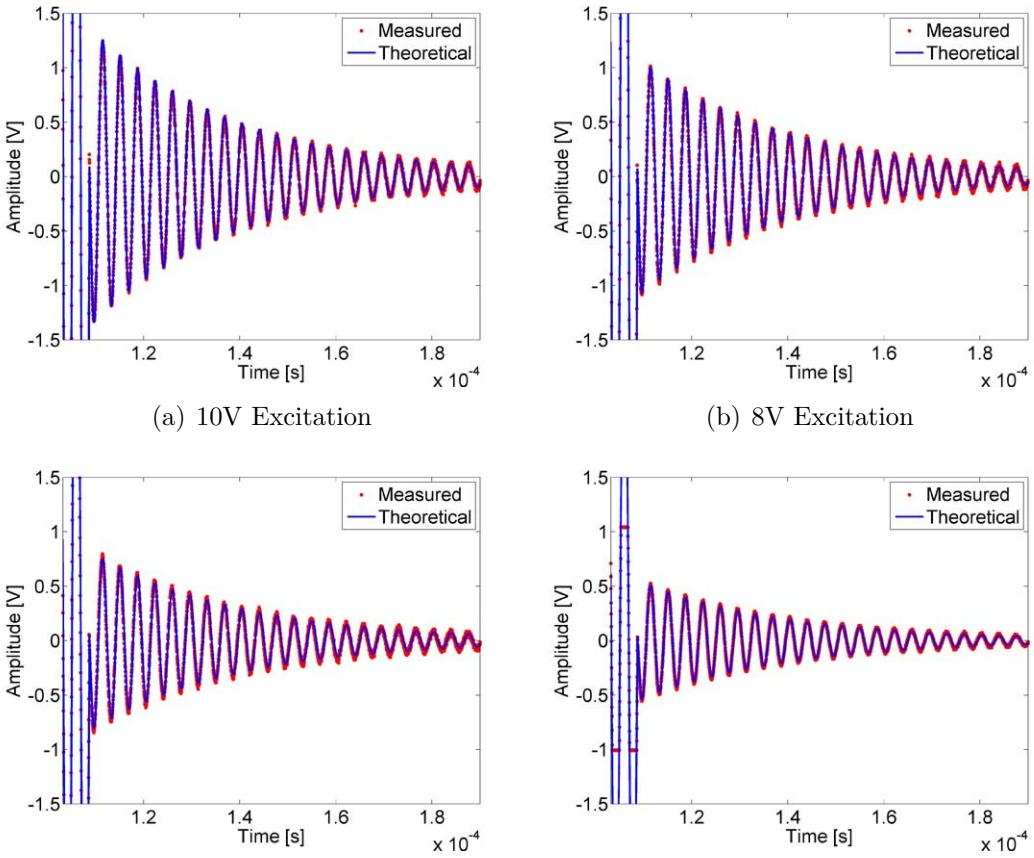

(a) 10V Excitation

(b) 8V Excitation

(c) 6V Excitation

(d) 4V Excitation

Figure 6.42: Voltage Response of transducer to 30 cycle sinusoidal driving voltages at a frequency of 276kHz

From figure 6.42, the theoretical voltage responses are nearly equal to the experimentally measured voltage responses. Therefore, it is concluded that the piezo-composite element acts linearly when the drive voltage has an amplitude between 4-10V.

It is of interest to lower amplitude of drive voltage to determine if the linearity condition is still met. The voltage responses resulting from lower amplitude drive voltages are shown in figure 6.43.

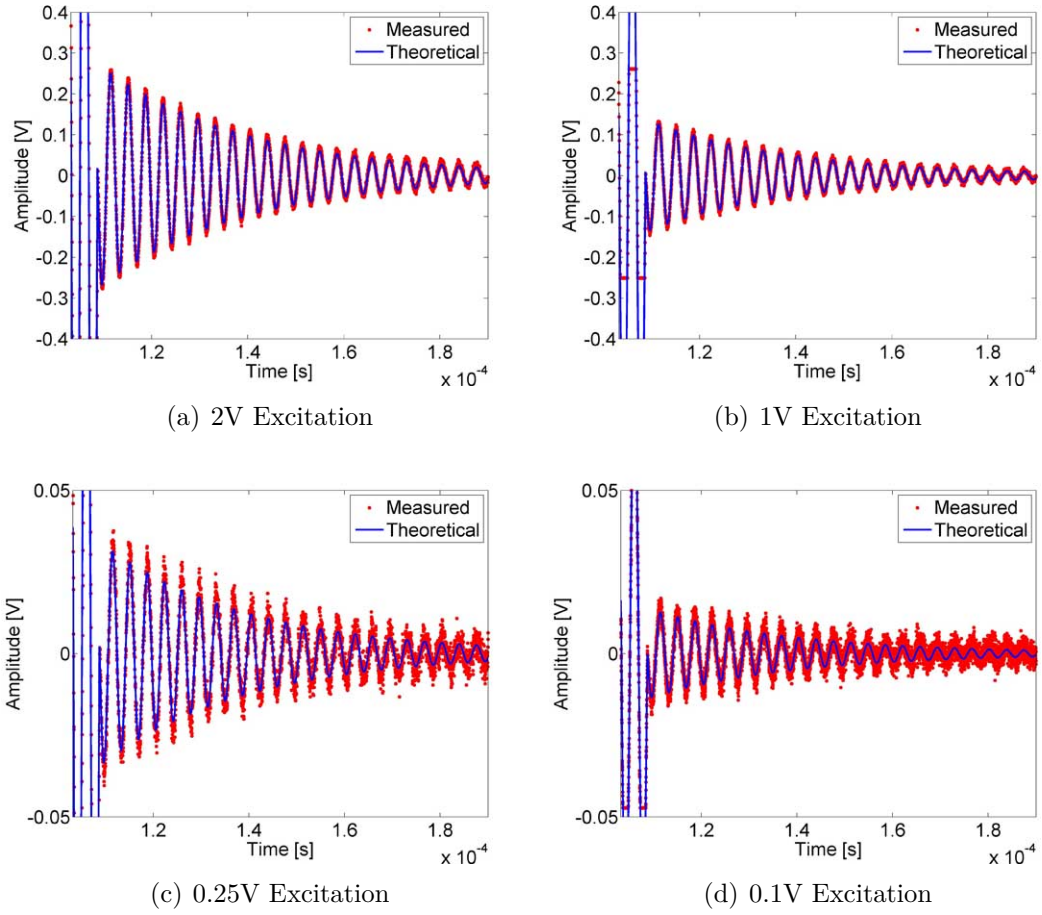

(a) 2V Excitation

(b) 1V Excitation

(c) 0.25V Excitation

(d) 0.1V Excitation

Figure 6.43: Voltage Response of transducer to 30 cycle sinusoidal driving voltages at a frequency of 276kHz

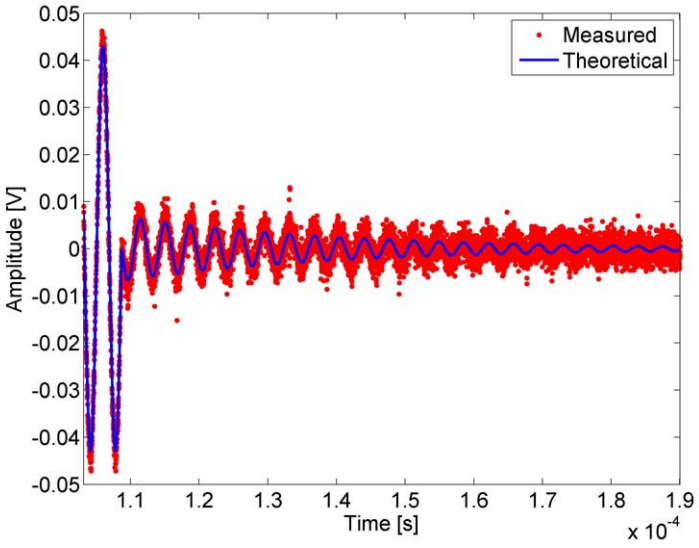

Figure 6.44: Voltage Response of transducer to 30 cycle sinusoidal drive voltage of 0.05V at a frequency of 276kHz

Figures 6.43 and 6.44 show that an extremely good match between the theoretically predicted and experimentally obtained voltage responses over a range of drive voltages, from 2V down to 50mV, at the resonance frequency of the transducer.

From this analysis, it is concluded that the piezocomposite transducer acts linearly in the voltage range 50mV-10V.

6.5.4. Piezocomposite Element Voltage Response at Constant Amplitude with Frequency Variation

An analysis of the effect variations of the driving voltage frequency have on the voltage response of the piezocomposite element are shown in this section. For this analysis, the magnitude of the drive voltage is always 10V. A number of voltage response waveforms of the piezocomposite element have already been presented in previous section; namely at the resonance frequency, $f = 276$kHz, and the anti-resonance frequency, $f = 352.5$kHz.

The result of driving the transducer below the resonance frequency with a 30 cycle sinusoidal pulse at a frequency of 200kHz is presented in figure 6.45. Note that only the ring time sections are presented since the magnitudes of the drive voltage sections are relatively constant.

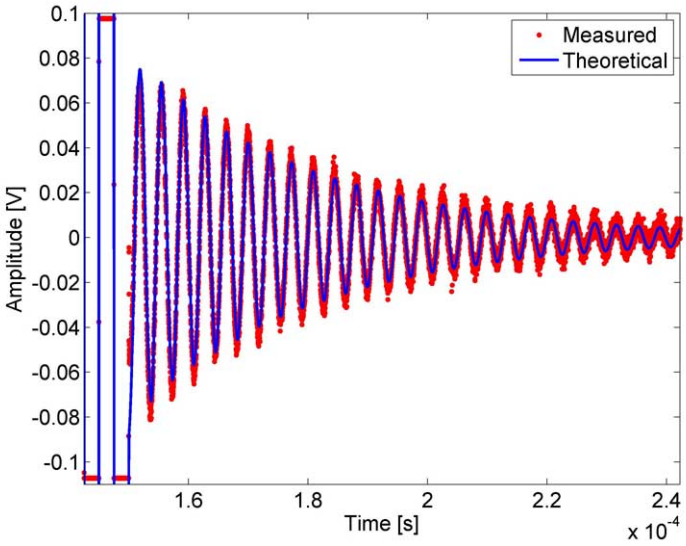

Figure 6.45: 200kHz Sinusoidal Pulse with 30cycles at 10V

Figure 6.45 shows that a fairly accurate match between the theoretically predicted and experimentally measured voltage response is obtained at a frequency of 200kHz.

The voltage response obtained by driving the transducer with a frequency of 320kHz is presented in figure 6.46. Note that this frequency is between the resonance and anti-resonance frequencies of the piezocomposite element.

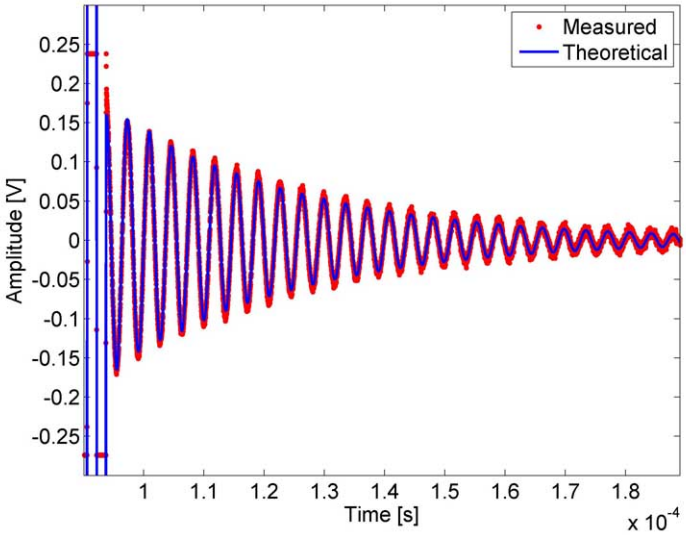

Figure 6.46: 320kHz Sinusoidal Pulse with 30cycles at 10V

Again, as shown in figure 6.46, a close match is obtained between the theoretically

predicted and the experimentally measured voltage response.

Finally, a drive frequency far beyond the anti-resonance frequency of the piezoelectric element is used. The voltage response obtained for a drive frequency of 500kHz is shown in figure 6.47.

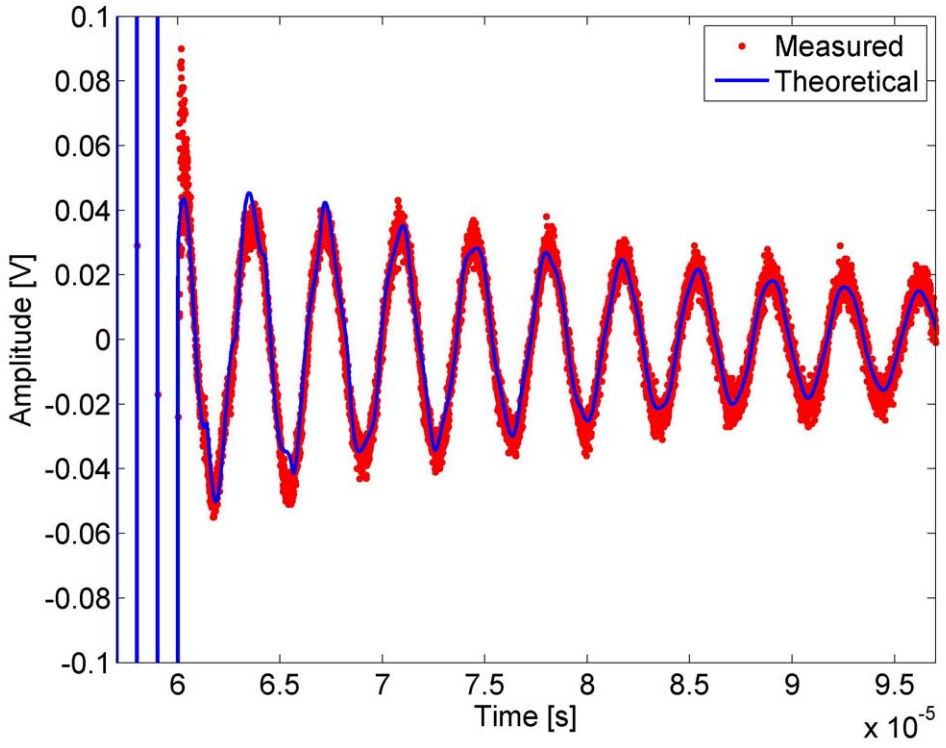

Figure 6.47: 500kHz Sinusoidal Pulse with 30cycles at 10V

At the beginning of figure 6.46, it can be noticed that there are small transient characteristics in the theoretically determined voltage response exist that are not present in the experimentally measured voltage response. These may be due to the transients being masked by the noise introduced from the experimental measurement system, or due to other effects not accounted for by the theoretical voltage response developed for transducers operating in thickness mode.

There are a number of possible causes for these transients. The first could be that the material properties are frequency dependent and have changed value. Notice that is is assumed that the material parameters are frequency invariant. Another cause could be that the linear assumption may break down when the drive voltage frequency moves far beyond the regular operating frequency of the transducer element.

The transients may also be the result of other resonances from the width and length mode of the piezoelectric element.

As indicated in section 3.3, it is possible to use the impedance and admittance data of the piezocomposite element to determine if other effects not related to the thickness mode are present.

The experimentally measured impedance and admittance curves, together with the theoretically determined impedance and admittance curves, are shown in figures 6.48 and 6.49.

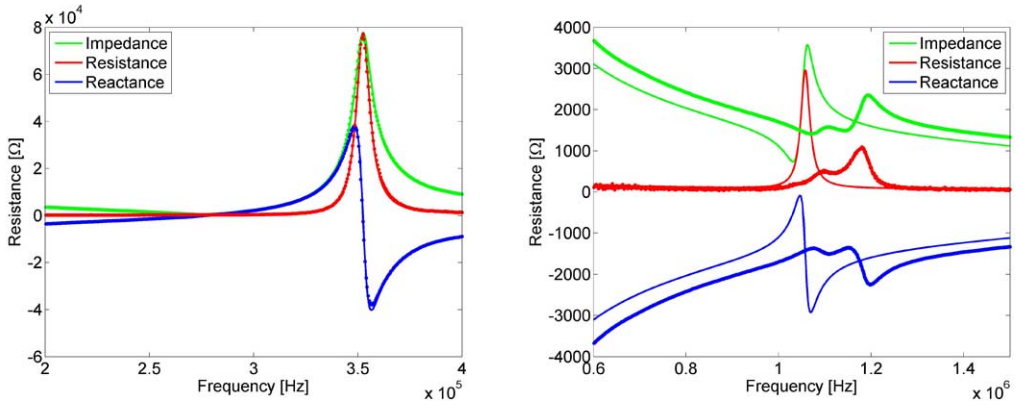

(a) Low Frequency (b) High Frequency

Figure 6.48: Detailed Impedance Curves of Piezocomposite Element

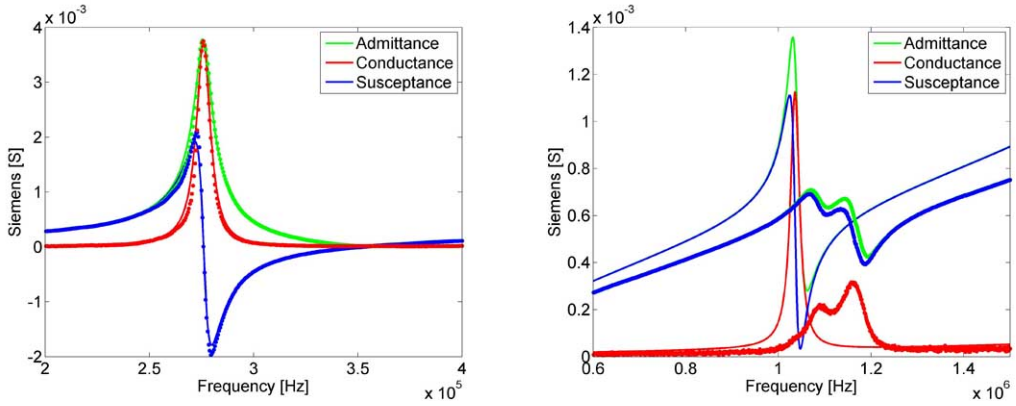

(a) Low Frequency (b) High Frequency

Figure 6.49: Detailed Admittance Curves of Piezocomposite Element

As can be seen from figures 6.48 and 6.49, the theoretical values obtained for the impedance and admittance are accurate for low frequencies, but clearly as the frequency is increased past 600kHz, the theoretically predicted impedance and admittance curves do not match the experimentally determined values. Therefore, either the material parameters have changes value or other effects not related to the thickness mode operation of the piezocomposite element are present at higher frequencies. Since the theory for the impedance and admittance depends upon exactly the same parameters as the transient theory, there is no surprise that if one of the theories fails to be accurate, the other fails as well because both models depend on the same material parameters and assumptions.

6.6. Conclusion of Theoretical and Experimental Analysis of the Transient Theory

An in depth validation of the distributed transient performance characteristics developed in chapter 5 was presented in this chapter.

The successful validation of the *TVOPI* was conducted using a method developed using the theory of Snell's Law of reflection and transmission for both single and multi-element acoustic transducers operating in thickness mode.

Currently, no method exists to validate the *TPOVI* without the use of complex experimental equipment or sophisticated finite element numerical routines. A partial validation of the *TPOVI* was successfully conducted, however, using the steady-state TVR. Although not a complete validation, it showed the accuracy of the *TPOVI* when used to predict the steady-state behavior of a transducer driven by a sinusoidal voltage.

A validation check of the *TVOPI* was performed by driving a transducer with a unity magnitude sinusoidal pressure and comparing the obtained steady-state amplitude with the sensitivity of the transducer. The values obtained from the sensitivity and the steady-state sections of the *TVOPI* are in very close agreement, as expected.

The DVDM developed in section 5.3 was successfully validated by comparing the analytic expression obtained from 2^{nd}-Order lumped circuit model to what is obtained from the DVDM when using a 2^{nd}-Order lumped circuit model. A detailed discussion of the results obtained when the output pressure waveform is a finite duration square pulse for a single and multi-layer acoustic transducer operating in thickness mode was also given to further validate the method.

Having completed a number of theoretical validations of the transient theory, the last part of this chapter focused on the experimental validation of the transient theory using the voltage response. For the first time, it was proved conclusively that the theoretical voltage response accurately predicts the voltage response of a piezocomposite element. This is a significant find as it illustrates the flexibility of the transient theory to model any type of multi-layer acoustic transducer operating in thickness mode.

7. Example Application and Concluding Summary

If a choice between two backing layer materials must be made for a transducer both, steady-state impedance and sensitivity methods, as well as the developed *TVOPI* models, could be used to do this.

Assume that an XTM transducer receives a sinusoidal pressure pulse at a frequency of 260kHz, and that the material selection of two backing materials, Z_{M1} and Z_{M2} are to be tested. The rise time constant and ring time constant, as well as the corresponding sensitivity values, need to be determined. Refer to section 3.2.1 for details regarding the material parameters and geometric structure of the XTM transducer.

Note that, short rise and ring time constants of the voltage output provide the best receive performance as long as sufficient steady-state sensitivity is maintained. To determine the steady-state impedance and sensitivity, the expressions developed in sections 2.7.1 and 2.7.4 are utilized, and in order to determine the rise time and ring time constants of the transducer, the expression developed for the TVOPI in section 6.1.2 is used.

The specific acoustic impedances of Z_{M1} and Z_{M2} are given by:

$$Z_{M1} = 2096 \qquad \text{[Mrayls]}$$
$$Z_{M2} = 524 \qquad \text{[Mrayls]}$$

When using Z_{M1} and Z_{M2}, the impedance and sensitivity of the XTM transducer are illustrated in figures 7.1 and 7.2.

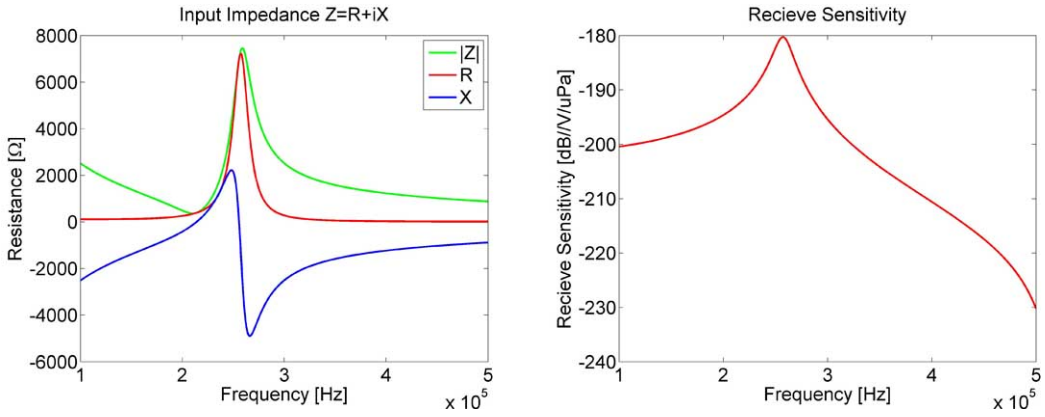

(a) Impedance (b) Sensitivity

Figure 7.1: Steady-State Performance Parameters of XTM Transducer with Z_{M1}

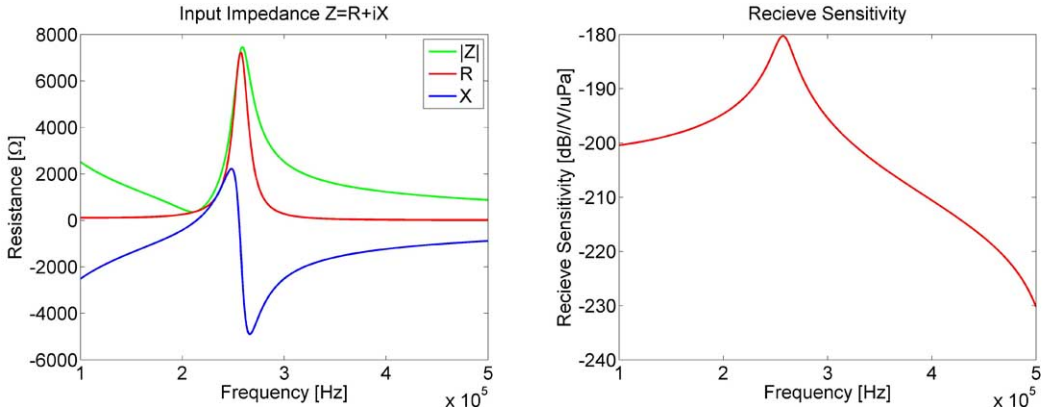

(a) Impedance (b) Sensitivity

Figure 7.2: Steady-State Performance Parameters of XTM Transducer with Z_{M2}

From figures 7.1 and 7.2, the sensitivity of the transducer at a frequency of 260kHz when using material Z_{M1} is $-180.7dB//V/\mu Pa$, and when using material Z_{M2} is $-183.4dB//V/\mu Pa$.

To determine the rise time and ring time of the receive pulse, a qualitative measurement is made using the time constants τ_{rise} and τ_{ring}. These parameters are found by fitting the function $\underline{\mathrm{V}}(t)$ to the magnitude of the voltage output.

$$\underline{\mathrm{V}}(t) = \begin{cases} V_{SS}(1 - e^{-t/\tau_{rise}}) & 0 \leq t \leq t_f \\ V_{SS}(e^{-(t-t_f)/\tau_{rise}}) & t_f \leq t \end{cases} \tag{7.1}$$

V_{SS} is the steady-state value of the voltage output and is determined from the sensitivity. t_f is the time when the drive pressure stops. The values of τ_{rise} and τ_{ring} for materials Z_{M1} and Z_{M2} are shown in figures 7.3 and 7.4. Note the vertical dashed-black lines indicate the location of t_f.

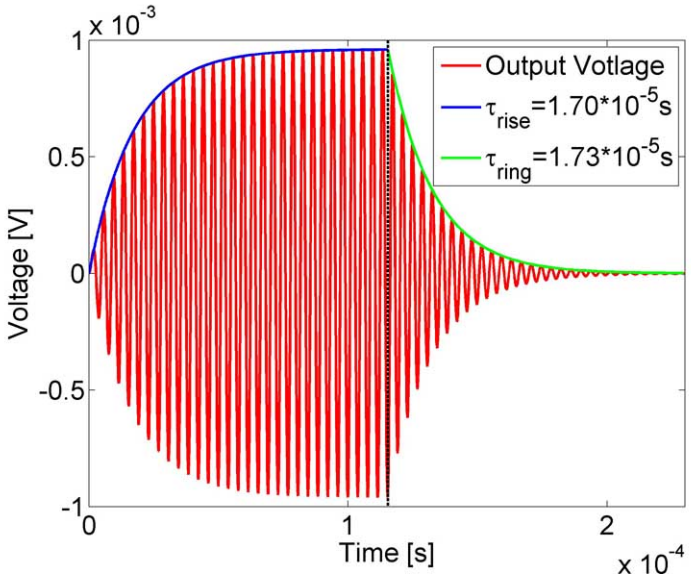

Figure 7.3: Voltage Output due to 30 cycle Sinusoidal Pressure Input of Unity Magnitude at a frequency of 260kHz for Z_{M1}

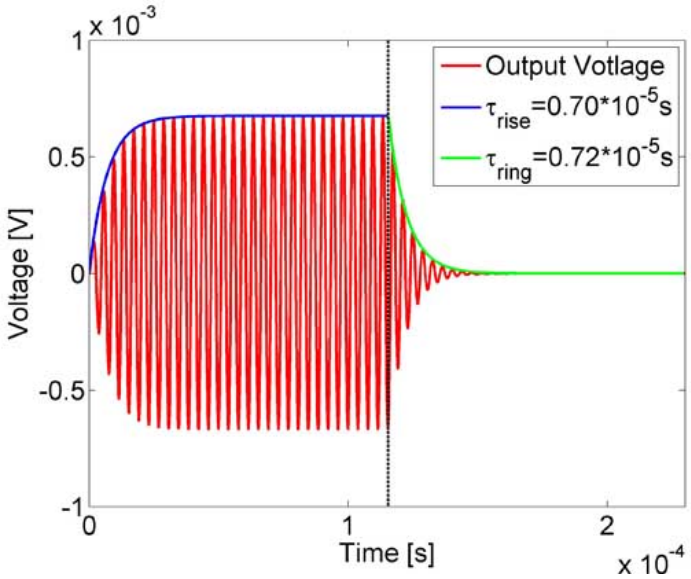

Figure 7.4: Voltage Output due to 30 cycle Sinusoidal Pressure Input of Unity Magnitude at a frequency of 260kHz for Z_{M2}

From the steady-state and transient analysis, the parameters used to evaluate which particular backing material to use are given in table 7.1.

	Material		
	Z_{M1}	Z_{M2}	**Symbol [Unit]**
Sensitivity	-180.7	-183.4	M $[dB//V/\mu Pa]$
Rise Time Constant	17.0	7.0	τ_{rise} $[\mu s]$
Ring Time Constant	17.3	7.2	τ_{ring} $[\mu s]$
Input Impedance	6670-j3283	4811-j298.1	Z_{in} $[\Omega]$

Table 7.1: Parameters used to Evaluate Receive Performance of XTM Transducer with Backing Materials Z_{M1} or Z_{M2} when $f = 260$kHz

Based upon the values in table 7.1, the material Z_{M2} is the preferred alternative for the backing layer of the XTM transducer since it has the lowest rise time and ring time constants. The sensitivity obtained when Z_{M2} is used is slightly lower than that obtained when using Z_{M1}; however, the sensitivity is not sufficiently different to counteract the negative effects caused by the increase in the rise and ring time constants. Therefore, Z_{M2} is the backing material preferred for this application.

This thesis presents the development of distributed models of multi-layered acoustic transducers operating in thickness mode. The distributed models were used to determine the steady-state and transient performance characteristics of a transducer and may be used in future applications to provide practical, cost-effective, and convenient alternatives to design through experimentation.

The steady-state performance characteristics developed include the impedance, sensitivity, transmit voltage response, efficiency, and acoustic impedance; the most convenient of these, in terms of measurement, being the impedance.

An entire chapter was dedicated to the verification of the impedance and admittance as they can be used to determine the material parameters of the transducer. Also, it was demonstrated that the impedance/admittance data can be used to determine whether the transducer's material parameters are invariant, as well as to determine whether other effects not related to the thickness mode operation are present over the frequency range of interest.

Measuring the sensitivity of a transducer is very difficult. A number of methods are widely used, but their accuracy is generally poor or requires sophisticated instrumentation and laboratory setups. In this thesis it was verified that the distributed

sensitivity model for a multi-layer acoustic transducer operating in thickness mode accurately predicts its sensitivity. This verification was conducted by comparing the experimentally measured sensitivity values obtained from the reciprocity calibration method with theoretically determined values. Since close agreement exists between these values, the developed sensitivity expression may be used and innovative designs can be rapidly optimized without the need for complex and time consuming experimentation.

In a number of practical applications, the transient performance characteristics of a transducer are also important. These characteristics may be used to determine the rise and ring time constants, as well as the sophisticated waveforms that occur when a transducer receives a pressure pulse or when it is driven to output a pressure pulse.

Cutting-edge distributed transient models were developed in this thesis that describe the pressure output resulting from a voltage input (TPOVI), the voltage output resulting from a pressure input (TVOPI), and the voltage response of multi-layer acoustic transducers operating in thickness mode. These models were developed in the Laplace domain and required state-of-the-art numerical inversion routines to find the time domain solutions. These methods are easy to implement on any standard computer and allow transducer designers to rapidly evaluate the performance of transducer designs. As well, the expressions can be used to create novel signal processing routines that can be used to enhance the performance of existing transducers.

Modern drive electronics for transducers are now capable of outputting arbitrary waveforms. This has motivated the design of software routines capable of outputting desired pressure waveforms by pre-shaping the drive voltages of the transducer. In this thesis, a novel routine was developed for pre-shaping the drive voltage that is based on modeling the transducer using a distributed transient model. This method is superior to other methods as it is accurate and only requires the material parameters and geometric dimensions of the transducer to be defined. This allows for the optimization of a transducer to simplify the input drive voltage necessary to output a sophisticated pressure waveform. As well, the flexibility of the method allows existing transducers to be used in a number applications where intricate waveforms are required. This reduces the necessity of having to design and build new transducers for specific applications. Both, the transient performance characteristics and the drive voltage design method for multi-layer acoustic transducers operating in thickness mode were developed and validated using theoretical and experimental methods.

Transducer design is both, an art and a science requiring a good understanding of the physical phenomena that take place in a transducer. The state-of-the-art performance characteristics developed in this thesis provide transducer designers with the necessary tools to make informed design decisions and facilitate the optimization of multi-layer underwater acoustic transducers operating in thickness mode.

References

[1] R. J. Urick, *Principles of Underwater Sound*. Blacklick, Ohio, U.S.A.: McGraw-Hill, Inc., 3 ed., 1983.

[2] V. M. Albers, *Underwater Acoustic Handbook II*. University Park, Pennsylvania: Pennsylvania State University Press, 1965.

[3] C. H. Sherman and J. L. Butler, *Transducers and Arrays for Underwater Sound*. Springer.

[4] K. W. Kwok, H. L. W. Chan, and C. L. Choy, "Evaluation of the material parameters of piezoelectric materisl by various methods," *IEEE Transactions on Ultrasonics, Ferroelectrics, and Frequency Control*, vol. 44, no. 4, pp. 733–742, 1997.

[5] Y. Dong, Z. Wu, H. Hu, B. Wu, and G. Xu, "A novel method for characterization of piezoelectric material parameters by simulated annealing optimization," *IEEE Transactions on Ultrasonics, Ferroelectrics, and Frequency Control*, vol. 87, no. 12, pp. 2613–2615, 2010.

[6] M. Redwood, "Transient performance of a piezoelectric transducer," *The Journal of the Acoustical Society of America*, vol. 33, no. 4, pp. 527–536, 1961.

[7] O. M. Stuetzer, "Multiple reflections in a free piezoelectric plate," *Acoustical Society of America*, vol. 42, no. 2, pp. 502–508, 1967.

[8] H. L. Zhang, M. X. Li, and C. F. Ying, "Complete solutions of the transient behavior of a transmitting thickness-mode piezoelectric transducer and their physical interpretations," *Acoustical Society of America*, vol. 74, no. 4, pp. 1105–1114, 1983.

[9] D. Hazony and T. Kocher, "Finite impulse response ultrasonic transducers," *Acoustical Society of America*, vol. 71, no. 1, pp. 203–206, 1982.

[10] J. C. Piquette, "Method for transducer transient suppression. I: Theory," *Journal of the Acoustical Society of America*, vol. 92, no. 3, pp. 1203–1213, 1991.

[11] J. C. Piquette, "Method for transducer transient suppression. II: Experiment," *Journal of the Acoustical Society of America*, vol. 92, no. 3, pp. 1214–1221, 1991.

[12] J. C. Piquette, "Approximate transducer transient suppression with increased output amplitude," *Journal of the Acoustical Society of America*, vol. 128, no. 5, pp. 2543–2548, 2010.

[13] J. C. Piquette and S. E. Forsythe, "Transducer transient suppression: Generalized methods of analysis," *Acoustical Society of America*, vol. 100, no. 3, pp. 1577–1583, 1996.

[14] B. Change and T. Chang, "Enhancing ultrasonic imaging with low transient pulse shaping," *IEEE Transactions on Ultrasonics, Ferroelectrics, and Frequency Control*, vol. 54, no. 3, pp. 627–635, 2007.

[15] P. Cobo, "Application of shaping deconvolution to the generation of arbitrary acoustic pulses with conventional sonar transducers," *Journal of Sound and Vibration*, vol. 188, no. 1, pp. 131–144, 1995.

[16] P. Cobo, C. Ranz, and M. Cervera, "Increasing the vertical resolution of conventional sub-bottom profilers by parametric equalization," *Geophysical Prospecting*, vol. 50, no. 2, pp. 139–149, 2002.

[17] P. Cobo, C. Ranz, A. Fernandez, M. Cuesta, D. K. Anthony, and M. Siguero, "Waveform shaping of sonar transducer for improving the vertical resolution in sub-bottom sediments profiling," *Marine Geophysical Research*, vol. 26.

[18] A. A. Vives, *Piezoelectric Transducers and Applications.* Heidelberg, Germany: Springer, 2008.

[19] R. G. Ballas, *Piezoelectric Multilayer Beam Bending Actuators: Static and Dynamic Behavior and Aspects of Sensor Integration.* Microtechnology and MEMS, Heidelberg, Germany: Springer, 2007.

[20] R. Pastore, A. Ballato, J. Kosinski, and H. Cui, "Theoretical and experimental studies of loss in piezoelectric ceramic resonators," *IEEE/EIA International Frequency Control Symposium and Exhibition*, 2000.

[21] M. Lethiecq, L. P. Tran-Huu-Hue, F. Patat, and L. Pourcelot, "Measurement of losses in five piezoelectric ceramics between 2 and 5 mhz," *IEEE Transactions on Ultrasonics, Ferroelectrics, and Frequency Control*, vol. 40, no. 3, pp. 232–237, 1993.

[22] L. P. Tran-Huu-Hue, O. Audrain, F. Levassort, and M. Lethiecq, "Influence of the different loss parameters on piezoelectric material performances," *Ferroelectrics*, vol. 224, no. 1, pp. 177–184, 1999.

[23] Y. Chen, Y. Wen, and P. Li, "Loss mechanisms in piezoelectric transducers and its response to stress," *IEEE Proceedings of 2004 International Conference on Information Aquisition*, 2004.

[24] R. Holland, "Representation of dielectric, elastic, and piezoelectric losses by complex coefficients," *IEEE Transactions on Sonics and Ultrasonics*, vol. SU-14, no. 1, pp. 18–20, 1976.

[25] S. Sherrit and B. K. Mukherjee, "The use of complex material constants to model the dynamic response of piezoelectric materials," *1998 Ultrasonic Symposium*, 1998.

[26] J. G. Smits, "Influence of moving domain wall and jumping lattice defects on complex material coefficients of piezoelectrics," *IEEE Transactions on Sonics and Ultrasonics*, vol. SU-23, no. 3, pp. 168–174, 1976.

[27] K. Uchino and S. Hirosei, "Loss mechanisms in piezoelectrics: How to measure different losses separately," *IEEE Transactions on Ultrasonics, Ferroelectrics, and Frequency Control*, vol. 48, no. 1, pp. 307–321, 2001.

[28] K. L. Kaiser, *Transmission Lines, Matching and Crosstalk.* Michigan, U.S.A.: CRC Press, Taylor & Francis Group, 2006.

[29] R. J. Bobber, *Underwater Electroacoustic Measurements.* Los Altos, California, U.S.A.: Peninsula Publishing, 1988.

[30] R. A. Altes and W. D. Reese, "Doppler-tolerant classification of distributed targets - a bionic sonar," *IEEE Transactions on Aerospace and Electronic Systems*, vol. 11, no. 5, pp. 708–724, 1975.

[31] R. E. Challis and J. A. Harrison, "Rapid solutions to the transient response of piezoelectric elements by z-transform techniques," *The Journal of the Acoustical Society of America*, vol. 74, no. 6, pp. 1673–1680, 1983.

[32] J. A. C. Weideman, "Algorithms for parameter selection in the weeks method for inverting the laplace transform," *Society for Industrial and Applied Mathematics*, vol. 21, no. 1, pp. 111–128, 1999.

[33] S. Ghnimi, A. Rajhi, and A. Gharsallah, *Optimal Algorithm for the Numerical Inversion Laplace Transforms Method in a Multiconductor Transmission Line System*. 2008.

[34] C. Cunha and F. Viloche, "The laguerre functions in the inversion of the laplace transform," *Inverse Problems*, vol. 9, no. 57, pp. 57–68, 1993.

[35] B. Davies and B. Martin, "Numerical inversion of the laplace transform: a survey and comparison of methods," *Journal of Computational Physics*, vol. 33, no. 1, pp. 1–32, 1979.

[36] J. Abate and P. P. Valko, "Multi-precision laplace transform inversion," *International Journal for Numerical Methods in Engineering*, vol. 60, no. 5, pp. 979–993, 2004.

[37] B. S. Garbow, G. Giunta, and J. N. Lyness, "Software for an implementation of week's method for the inverse laplace transform problem," *ACM Transactions on Mathematical Software*, vol. 14, no. 2, pp. 163–170, 1988.

[38] J. N. Lyness and G. Giunta, "A modification of the weeks method for numerical inversion of the laplace transform," *Mathematics of Computation*, vol. 47, no. 175, pp. 313–322, 1986.

[39] J. Abate, C. L. Choudhury, and W. Whitt, "On the laguerre method for numerically inverting laplace transforms," *Informs Journal on Computing*, vol. 8, no. 4, pp. 413–427, 1996.

[40] J. Abate, G. L. Choudhury, and W. Whitt, "On the laguerre method for numerically inverting laplace transforms," *Informs Journal of Computing*, vol. 8, no. 4, pp. 413–427, 1996.

[41] G. Giunta, G. Laccetti, and M. R. Rizzardi, "More on the weeks method for the numerical inversion of the laplace transform," *Numerical Mathematics*, vol. 54, no. 2, pp. 193–200, 1988.

[42] P. D. Iseger, "Numerical transform inversion using gaussian quadrature," *Probability in the Engineering and Informational Sciences*, vol. 20, no. 1, pp. 1–44, 2006.

[43] J. Toutain, J. Battaglia, C. Pradere, J. Pailhes, A. Kusiak, W. Aregba, and J. C. Batsale, "Numerical inversion of laplace transform for time resolved thermal characterization experiment," *Journal of Heat Transfer*, vol. 133, no. 4, pp. 1–3, 2011.

[44] W. Gautschi, *Orthogonal Polynomials: Computation and Approximation (Numerical Mathematics and Scientific Computation)*. Oxford Science Publications, 2004.

[45] K. S. Crump, "Numerical inversion of laplace transforms using a fourier series approximation," *Journal of the ACM*, vol. 23, no. 1, pp. 89–96, 1976.

[46] F. Durbin, "Numerical inversion of laplace transforms: an efficient improvement to dubner and abate's method," *International Journal for Numerical Methods in Engineering*, vol. 17, no. 4, pp. 371–376, 1974.

Appendix

Appendix A.
Numerical Inversion of Laplace Transform

To determine the time domain function $f(t)$, from the Laplace Domain function $F(s)$, the Bromwich Integral is used [32], as shown by equation A.1.

$$f(t) = \frac{1}{2\pi i} \int_{\sigma-i\infty}^{\sigma+i\infty} F(s) e^{st} ds \tag{A.1}$$

In practice, the value σ is chosen to be greater than the largest real part of all the singularities of $F(s)$. This ensures that the integral in equation A.1 exists. If $F(s)$ is a simple function, then the theory from complex analysis can be used to find a closed form analytic solution of $f(t)$. But, for the Laplace domain expressions considered in this thesis, there are no closed form analytic solutions. Therefore, numerical methods must be used to obtain the time domain values from the Laplace domain expressions.

There are now over 100 different algorithms that can be used for the numerical inverse Laplace transform of $F(s)$ [33]. However, since the inverse Laplace transform is *ill-posed*, no universal algorithm exists [34]. To determine an appropriate inversion routine to use, the following criteria are considered [35]:

a) Applicability to Problem
b) Numerical Accuracy
c) Computational Time and Stability
d) Implementation Difficulties

An excellent overview of a number of inversion routines can be found in the paper by Abate and Valko [36]. The expressions $F(s)$ being considered in this thesis represent time domain functions with a number of discontinuities or functions that are

smooth. Therefore, using the criteria above, the following numerical inverse Laplace transform routines have been selected:

1) Weeks Method
2) Isegers Method
3) Crump's Method
4) Dubner-Abate-Crump (DAC) Method

Method 1 is based on the expansion of $F(s)$ using Laguerre functions, and then performing the numerical inversion with these functions. Method 2 is based on using the Poisson Summation Formula and then approximating the infinite summation using a Gaussian Quadrature rule. Methods 3-4 are based on the Fourier-Series Method for computing the inverse Laplace transform.

Each of these routines is summarized in the following sections. Comments are made regarding the estimated error associated with using each routine, as well as which methods are suitable for specific expressions of $F(s)$.

Note that the *ill-posed* nature of the numerical inverse Laplace transform necessitates the fact that a number of inversion techniques be used and subsequently compared to increase the confidence of the time domain solution obtained [35]. The reason for doing this is that one can ascertain if peculiar behavior exists in the values obtained and whether this is due to the actual values or to problems associated with the inversion routine used [35].

A.1. Week's Method

Week's method is a well known method to numerically invert a Laplace domain expression. This method is computationally efficient if a number of time domain points are used [32]. Furthermore, high accuracy is obtainable using Week's method when the time domain function is continuous [35].

A well known weakness of Week's method, however, is its inability to give accurate results if discontinuities are present in the function f(t) [32, 35, 37]. Another issue with Week's method is that it requires the parameters, σ and b, to be chosen close to their optimal value in order for accurate results to be obtained. The choice of the parameters, σ and b, is not trivial, but there are methods available to determine the values of σ and b close to their optimum values for special functions of $F(s)$ [32].

One of the main reasons that this method is is used here is that it provides a good

numerical check for the results of the other numerical inversion routines. It does not, however, perform well when losses are present in the Laplace domain solutions of the *TVOPI*, *TPOVI*, and the voltage response of the transducer.

The main idea of Week's method is to expand the time domain function $f(t)$ using a set of Orthogonal Laguerre Polynomials $l_n(t)$. The Laplace transform of $l_n(t)$ is known analytically. Then, the function $F(s)$, is expanded using the Laplace domain expressions of the Orthogonal Laguerre Polynomials. The Laguerre Coefficients, q_n, produced from these expansions are used to relate the function $F(s)$ to $f(t)$. The Laguerre Generating Function, $Q(z)$, is used to determine the values of q_n from $F(s)$.

A detailed derivation of Week's Method is given in [38, 39], and further details related to Week's method can be found in [32, 37, 39, 40, 41]. The final solution of Week's method that can be implemented on a computer, is given by the following equations [32]:

$$f(t) = e^{\sigma t} \sum_{n=0}^{N-1} q_n l_n(bt) \tag{A.2}$$

$$l_n(bt) = e^{-bt/2} L_n(bt) \tag{A.3}$$

$$L_n(bt) = \Big[\sum_{k=0}^{n} \binom{n}{k} \frac{(-bt)^k}{k!} \Big] \tag{A.4}$$

$$Q(z) = \sum_{n=0}^{\infty} q_n z^n = \frac{b}{1-z} F\Big[\frac{b(1+z)}{2(1-z)} + \sigma \Big] \tag{A.5}$$

$$q_n = \frac{e^{\frac{ik\pi}{2N}}}{2N} \sum_{k=-N}^{N-1} Q\Big(e^{\frac{i(k+0.5)\pi}{N}} \Big) e^{in(\frac{k\pi}{N})} \tag{A.6}$$

The parameter, N, is related to the number of terms used in the midpoint rule to approximate q_n.

A.1.1. Sources of Error

One of the major problems with Week's method is the choice of parameters, σ and b [39, 41]. These parameters greatly effect the numerical accuracy obtainable from the inversion routine. Also, errors associated with the truncation performed in both, the Laguerre series expansion and the evaluation of the coefficients q_n exist. The Week's method performs very poorly if discontinuities exist in the time domain function $f(t)$ [37]; however, this is only true if the discontinuities do not occur at $t = 0$.

An example of the Laplace domain function is given by equation A.7.

$$F(s) = \frac{1}{s} \tag{A.7}$$

This is the well known unit step function. The expression of $Q(z)$ for this function is given by equation A.8.

$$\begin{aligned} Q(z) = \sum_{n=0}^{\infty} q_n z^n &= \frac{b}{1-z} F\Big[\frac{b(1+z)}{2(1-z)} + \sigma\Big] \\ &= \frac{b}{1-z}\Big[\frac{2(1-z)}{b(1+z)+2\sigma(1-z)}\Big] \\ &= \frac{2b}{(b+2\sigma)+z(b-2\sigma)} \\ &= \Big(\frac{2b}{b+2\sigma}\Big)\Big[\frac{1}{1+z((b-2\sigma)/(b+2\sigma)}\Big] \\ &= \Big(\frac{2b}{b+2\sigma}\Big)\sum_{n=0}^{\infty}(-1)^n\Big(\frac{b-2\sigma}{b+2\sigma}\Big)^n z^n \\ &\implies q_n = (-1)^n\Big(\frac{b-2\sigma}{b+2\sigma}\Big)^n \end{aligned} \tag{A.8}$$

As seen from equation A.8, the Laguerre coefficients rapidly decline as long as b and σ are chosen correctly. It can be concluded, therefore, when a discontinuity exists at the origin, the accuracy of the inversion routine is not effected.

A.2. Iseger's Method

Iseger's Method is a Gaussian Quadrature rule method used to compute the numerical inverse Laplace transform.

This method was selected because it is easy to implement and it gives near machine accuracy for smooth functions [42]. This method is also fairly accurate when discontinuities are present in the time domain function [43]; however, it provides inaccurate results at the points of discontinuity.

Iseger's method uses the Fourier Series and the Poisson's Summation Formula to obtain an expression for the numerical inverse Laplace transform. The Poisson Summation Formula is given by equation A.9.

$$\sum_{k=-\infty}^{+\infty} F(a+2\pi i(k+v)) = \sum_{k=0}^{+\infty} e^{-ak} f(k) e^{-2\pi i k v} \tag{A.9}$$

Iseger's method is based on the evaluation of the sum on the left hand side of equation A.9 using a Gaussian Quadrature rule. After this is completed, the Discrete Inverse Fourier Transform is used to solve for specific values of the time domain function $f(k)$.

The derivation of Iseger's method is shown in [42], and the final result is presented below.

$$f(k\Delta) \approx \frac{e^{ak}}{N} \sum_{j=0}^{N-1} f_j e^{\frac{2\pi k j}{N}} \tag{A.10}$$

$$f_j = \begin{cases} \frac{1}{2\Delta} \sum_{k=1}^{n} \beta_k \left[F(\frac{a+i\lambda_k}{\Delta}) + F(\frac{a+i\lambda_k+2\pi i}{\Delta}) \right] & \text{if } j = 0 \\ \frac{1}{\Delta} \sum_{k=1}^{n} \beta_k F(\frac{a+i\lambda_k+2\pi i v}{\Delta}) & \text{if } j > 0 \end{cases} \tag{A.11}$$

In equation A.11, the parameters β_k and λ_k are defined by:

$$\lambda_k = \frac{1}{i\mu_k^{0.5}} - i\pi \tag{A.12}$$

$$\beta_k = \frac{\alpha_k^{0.5}}{|\mu_k^{0.5}|^2} \tag{A.13}$$

The values μ_k^v are the zeros of the polynomial $q_n^v(s)$ presented in equation A.14, and α_k^v are the positive Christoffel numbers given by equation A.16 [44].

$$q_n^v(s) = p_n(s) - (-1)^n e^{-2\pi i v} p_n(-s) \tag{A.14}$$

$$p_n(s) = \sqrt{2n+1} \sum_{k=0}^{n} \frac{(k+n)!}{(n-k)!} \frac{(-s)^k}{k!} \tag{A.15}$$

$$\alpha_k^v = \frac{1}{\sum_{j=0}^{n} |q_j^v(\mu_k^v)|^2} \tag{A.16}$$

A method used to implement Iseger's routine is presented in [42].

A.2.1. Iseger Error Analysis

There are two parameters that determine the magnitude of the error associated with Iseger's method. The first is the time discretization parameter N. In theory, as proven by Iseger for smooth functions, the larger the value of N, the more accurate the results. The same effect is obtained if one chooses a smaller Δ value since if the time interval of interest of $f(t)$ is fixed, then an increase in Δ causes a corresponding increase in N.

The other parameter that effects the accuracy is the choice of n, the number of points used for the Quadrature Rule. A value of $n = 16$ gives fairly good results, but since a higher accuracy is preferred, a value of $n = 48$ is used. For smooth functions, $n = 48$ gives results near machine precision [42].

There is a numerical stability problem with Iseger's method for certain functions $F(s)$. This problem is associated with the sample points s, given by equation A.17, used in Iseger's method.

$$s = \frac{1}{\Delta}\left[a + i\lambda_j + \frac{2\pi ik}{M}\right] \tag{A.17}$$

To see the numerical stability problem, consider the numerical inversion of the time-shifted unit step given by equation A.18.

$$F(s) = \frac{1}{s}e^{\tau s} \tag{A.18}$$

Notice that if the real part of the ratio of Δ and τ is large, then the value of $e^{\tau/\Delta}$ is extremely large. This is a particularly important problem to be aware of since these types of exponential terms are present in a number of the expressions developed in this thesis, where the values of τ can be many magnitudes larger than the values of Δ.

A.3. Crump's Method

Crump's Method is an easy to implement numerical inverse Laplace transform routine, and is useful for the inversion of a wide range of functions which are smooth and contain discontinuities [35]. This method is accurate and has stood the test of time as modified versions of it are still widely used today [35].

Crump's Method is based on the properties of the Fourier Series and Laplace transform to perform the numerical inversion. The derivation of Crump's Method is

given in [45]. The final result of Crump's method is given by equation A.19.

$$f(t) = \frac{e^{at}}{T}\left[\frac{1}{2}Re[F(a)] + Re[\sum_{k=1}^{N-1} F(a+\frac{ik\pi}{T})e^{\frac{ik\pi t}{T}}]\right] \tag{A.19}$$

The parameter a is chosen such that a is larger than any of the real singularities of the Laplace domain function $F(s)$ being inverted. The parameter T is chosen such that $t < T$, for the values of $f(t)$ being determined.

A.3.1. Crump's Method Error Analysis

The errors associated with Crump's method are discussed in [45]. An estimate of the error associated with using Crump's Method is given by equation A.20.

$$\begin{aligned} E_n &= e^{at}\sum_{n=1}^{\infty} g_n(t) \\ &= e^{at}\sum_{n=1}^{\infty}\left[e^{-a(2nT+t)}f(2nT+t)\right] \\ &= \sum_{n=1}^{\infty} e^{-2naT}f(2nT+t) \end{aligned} \tag{A.20}$$

Since the function $f(t)$ is bounded, it is possible to obtain the relation $|f(t)| \leq Me^{\alpha t}$ for some bounded value M and substituting this relation into the above geometric series, the following error bound is obtained [45]:

$$E_n \leq \frac{Me^{\alpha t}}{e^{2(a-\alpha)T} - 1} \tag{A.21}$$

Notice that α, shown in equation A.1, represents the real part of the largest singularity of $F(s)$. Note that $t < T$ and $a > \alpha$, which allows the inversion routine to be as accurate as needed by making $a - \alpha$ sufficiently large.

Another source of error occurs as a result of the truncation of the infinite Fourier series to obtain a numerical solution for $f(t)$; therefore, at points of discontinuity, Gibbs phenomenon is present. The effect of Gibbs phenomena can be reduced by increasing the number of terms in the truncated series.

A.4. Dubner-Abate-Crump Method

The Dubner-Abate-Crump (DAC) method is summarized in this section. This method uses the same principle as Crump's method, but increases both the computational accuracy and speed of Crump's method.

The DAC method is based on evaluating the sum given in equation A.19 using the Fast-Fourier Transform. The derivation of how to do this is presented in [46]. The DAC method is given by equation A.26.

$$W = e^{\frac{2\pi i}{N}} \tag{A.22}$$

$$W^{jk} = W^{j(k+lM)} \quad \text{for } l = 0, 1, 2, \ldots \tag{A.23}$$

$$A(k) = \sum_{l=0}^{L} F(a + i(k + lN)\frac{2\pi}{T}) \tag{A.24}$$

$$t_j = j\Delta t = j\frac{T}{N} \text{ for } j = 0, 1, 2, ..., N-1 \tag{A.25}$$

$$f(t_j) = \frac{2e^{aj\Delta t}}{T}\Big[-\frac{1}{2}Re[F(a)] + Re[\sum_{k=0}^{N-1} A(k)W^{jk}]\Big] \tag{A.26}$$

Equation A.26 can be evaluated very quickly using the Inverse Fast-Fourier Transform. Note that when using equation A.26, the constraint $t < T/2$ must be true.

A.4.1. Error Analysis of DAC Methods

Since the DAC method is based on the same method as Crump's method, the following error bound for the DAC inversion routine is obtained.

$$E_n \leq \frac{Me^{\alpha t}}{e^{2(a-\alpha)T} - 1} \tag{A.27}$$

Note that this result is obtained using the property that $f(t)$ is bounded such that $|f(t)| \leq Me^{\alpha t}$. The benefit of using the DAC method is that it is numerically faster to compute and is more stable than Crump's Method.